PHYSICAL AND CHEMICAL INSIGHTS INTO COMPLEX FERROELECTRIC OXIDES THROUGH MACHINE LEARNING APPROACHES

A Dissertation
Presented to
The Academic Faculty

By

Lee A. Griffin

In Partial Fulfillment
of the Requirements for the Degree
Doctor of Philosophy in the
School of School of Electrical and Computer Engineering

Georgia Institute of Technology

August 2020

PHYSICAL AND CHEMICAL INSIGHTS INTO COMPLEX FERROELECTRIC OXIDES THROUGH MACHINE LEARNING APPROACHES

Approved by:

Dr. Nazanin Bassiri-Gharb, Co-Advisor
G.W. Woodruff School of Mechanical Engineering
Georgia Institute of Technology

Dr. Asif Khan, Advisor
School of Electrical Engineering
Georgia Institute of Technology

Dr. Levent Degertekin
School of Electrical Engineering
Georgia Institute of Technology

Dr. Todd Sulchek
G.W. Woodruff School of Mechanical Engineering
Georgia Institute of Technology

Dr. Matthieu Bloch
School of Electrical Engineering
Georgia Institute of Technology

Dr. Mark Davenport
School of Electrical Engineering
Georgia Institute of Technology

Date Approved: January 11, 2000

Nothing whatsoever takes place in the universe in which some relation of maximum and minimum does not appear

Leonhard Euler

For Melisa.

ACKNOWLEDGEMENTS

First and foremost, I extend a heartfelt thank you to Prof. Bassiri-Gharb. The impact of her guidance and support on this thesis and myself personally is incalculable. Her passion for and dedication to science and knowledge is truly inspiring. Since we met, she has served as a paragon of professional and personal integrity, which continues to encourage me today.

I would like to express my great appreciation for Dr. Iaroslav Gaponenko, who has served as an invaluable source of knowledge and who I have come to respect and admire. I also thank Dr. Shujun Zhang who provided many of the samples used throughout this thesis. Additionally, I thank the members of my dissertation committee: Profs. Khan, Degertekin, Sulchek, Bloch, and Davenport, for volunteering their time and expertise, particularly in such tumultuous times.

I thank my family for all of the support and encouragement they have provided. In particular, my wife Melisa has been exceptionally supportive, patient, and encouraging. Without her, I would not have been able to finish this degree nor would I have come remotely this far.

Finally, I thank all those who have aided me in this work by assisting with sample preparation, characterization, analysis, tool development, and intellectual discussions. In addition, I thank these same people for simply being good encouraging people that were a pleasure to be around and work with. This thesis would not exist without them: Kerisha Williams, Evelyn Chin, Yulian Yao, Samuel Williams, Mohammed Aamir, and Micah Terrell.

TABLE OF CONTENTS

LIST OF TABLES

LIST OF FIGURES

LIST OF ABBREVIATIONS

PE	Polarization vs. Electric field
T_c	Curie Temperature
MPB	Morphotropic Phase Boundary
PZT	$Pb(Zr_xTi_{1-x})O_3$
PMN-xPT	$(1-x)Pb(Mg_{1/3}Nb_{2/3})O_3$-$xPbTiO_3$
PMN	$Pb(Mg_{1/3}Nb_{2/3})O_3$
PT	$PbTiO_3$
T_B	Burns Temperature
PNR	Polar Nano Region
T_d	Depolarizing Temperature
T_m	Dielectric Peak Temperature
Relaxor-FE	Relaxor-Ferroelectric
CNR	Chemical Nano Regions
TEM	Transmission Electron Microscopy
SPM	Scanning Probe Microscopy
PFM	Piezoresponse Force Microscopy
AFM	Atmoic Force Microscopy
BE	Band Excitation
DR	Dimensionality Reduction
PCA	Principle Component Analysis

NMF	Non-Negative Matrix Factorization
DL	Dictionary Learning
NN	Neural Network
R-PFM	Resonant Piezoresponse Force Microscopy
A_0	Piezoresponse amplitude at resonance
ϕ	Piezoresponse phase
Q	Quality factor
ω_0	Resonance Frequency
PR	Piezoresponse
SS-PFM	Switching Spectroscopy PFM

SUMMARY

Due to their exceptional piezoelectric properties, ferroelectric materials are extensively used for electromechanical applications, ranging from medical ultrasound transducers, to speakers, micro and nano-positioners, etc.. In particular, solid solutions of ferroelectric perovskites are the most widely used materials, due to their order of magnitude larger response when compared to other ferroelectrics. The large response of these materials is attributed to a wide range of physical and chemical phenomena, including: the influence of a morphotropic phase boundary (MPB), the presence of chemical and polar heterogeneties, extrinsic contributions from ferroelectric domain walls and phase boundaries, and more. While these individual phenomena have been studied for decades, much about them remains poorly understood.

Concurrently, increasing computational power has brought to prominence a set of complex statistical approaches commonly referred to as machine learning (ML) techniques. In recent years, these ML approaches have been combined with advanced *in-situ* characterization techniques, capable of producing unprecedented amounts of data, to accelerate the assessment of ferroelectrics and many other functional materials. However, the shortcomings of ML, such as their "interpretability" and lack of physical constraints, have become increasingly apparent and hindered many ML based studies.

This work addresses the electromechanical response of ferroelectric perovskite solid solutions and the effectiveness of ML techniques applied to this field. In particular, lead zirconate titanate (PZT) and lead manganese niobate-lead titanate (PMN-xPT), which exhibit some of the largest reported piezoelectric properties, are investigated. Characterization is achieved *via* piezoresponse force microscopy (PFM), and an open-source wide bandwidth PFM variant is developed to expand the capabilities of the technique. Insight into the obtained data is achieved with a variety of unsupervised ML approaches, the limitations of which are addressed through use of a quantitative methodology developed here.

First, the local piezoresponse of (1-x)PMN-xPT is investigated as a function of space, time, applied electric-field, and for a range of compositions at x=0, 0.28, 0.40. Due to a lack of physical and/or chemical constraints, ML analysis of such a multi-parameter characterization is difficult, as behaviors cannot be correlated across the various parameters. To facilitate such an analysis, dimensional stacking, a method for imposing constraints and allowing for correlation of the various measurement parameters, was developed. With this approach, the evolution of time- and voltage-dependent electromechanical behaviors were tracked across different chemical compositions and a glassy phase associated with the relaxor end member was identified. Furthermore, the glassy relaxor-like behavior was shown to persist into compositions with large amounts of the ferroelectric end-member,

including those traditionally considered simply “ferroelectric”.

Expounding upon dimensional stacking, a scientifically consistent procedure for applying ML was developed. This procedure utilizes constraints provided by dimensional stacking, but also minimizes user bias and the effects of overfitting by advocating a quantitative and reproducible approach to model selection. The procedure was demonstrated on previously reported data characterizing the voltage-dependent piezoresponse in PZT films over a micron-scale area. The results were compared to two previous ML-based reports assessing this data, which identified exotic physical phenomena. We demonstrate that the experimental data are well-described by classical ferroelectric theory and that limitations with the data set and biased application of previously reported ML-methodologies can result in substantial misinterpretation of data and analysis output.

Lastly, the voltage-dependence of the local piezoresponse in 0.60PMN-0.40PT was investigated, probing the effect of ferroelectric domain walls. Ferroelectric domain walls contribute from 40 to 80% of the overall piezoelectric response in ferroelectric solid solutions, however it is unclear if such contributions persist at smaller length scales. Through application of ML approaches, proximity to domain walls was not found to impact the piezoresponse. Yet, when traditional statistical analysis was applied to the same data a limited impact was identified, highlighting an unavoidable limitation in ML: comparatively weak statistical trends can be ignored. This

weak dependence of the switching behavior on domain walls was suggested to be due to underlying material heterogeneities acting as nuclei for polarization reversal, effectively curtailing the impact of domain walls. These results suggest that future work should concentrate on controlling these heterogeneities as opposed to the traditional approach of domain engineering.

The studies presented in this thesis highlight the power and limitations of "off-the-shelf" ML-based analysis applied to materials science. Through development of the instrumentation and the application of ML methodologies discussed here (namely, systematic clustering and dimensional reduction approaches augmented by data set stacking guided through physical and chemical understanding of the existing phenomena), significant contributions to the scientific understanding of the electromechanical response in complex ferroelectric oxides were achieved. Namely, new understandings of how composition and a glassy domain state affect the piezoresponse behavior in PMN-xPT were discovered and a composition previously purely considered to be "ferroelectric" was shown to exhibit glassy relaxor-like behavior. However, physically meaningful and unbiased results were found to require appropriate methodology and physical/chemical constraints. Additionally, the final study underscored a remaining limitation in these off-the-shelf ML approaches, specifically: these approaches can be limited when attempting to identify complex and statistically weak behavior. However, by supplementing ML with traditional statistical techniques, the final study

also highlighted that increased sub-micron heterogeneities could reduce the impact of domain walls.

CHAPTER 1

INTRODUCTION AND LITERATURE REVIEW

Piezoelectric materials are electromechanically coupled, i.e. an applied stress or strain yields a polarization and an applied electric field results in a stress or strain in the material. This coupling is due to an asymmetric electric dipole moment in the material and is the fundamental physical process at the heart of technologies such as sensors, actuators, ultrasound transducers, and energy harvesters.[1,2,3,4,5,6] Naturally, the limitations of these technologies are directly impacted by the efficacy of this physical process and improvement in the functional response of these materials has resulted in corresponding improvement in these technologies.[7,8] Typically, the strength (or magnitude) of the piezoelectric response of a material is quantified with the piezoelectric coefficient.

Specifically, the piezoelectric effect for an unconstrained material and for small electric fields is described by:

$$D_i = d_{ijk}\sigma_{jk} \quad or \quad D_i = e_{ijk}x_{jk} \tag{1.1}$$

where D_i is the electric displacement field generated by an applied stress (σ_{jk}) or strain (x_{jk}) and d_{ijk} and e_{ijk} are the piezoelectric coefficients, a third rank tensor. Conversely, the stress or strain generated by an applied

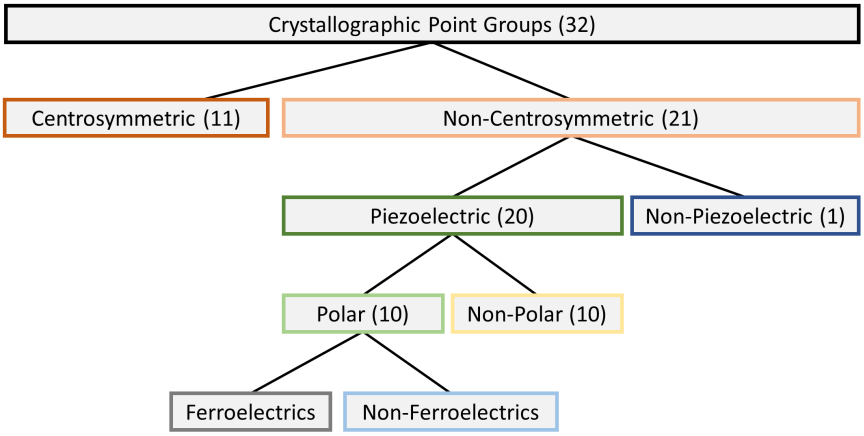

Figure 1.1: Schematic of the crystallographic point groups that illustrates the relationship between piezoelectricity and ferroelectricitiy.

electric field is given by:

$$x_{jk} = d_{kij}E_k \quad or \quad \sigma_{jk} = e_{kij}E_k \tag{1.2}$$

The same equations can be expressed in reduced notation:

$$\begin{aligned} D_i &= d_{ij}\sigma_j \quad or \quad D_i = e_{ij}x_j \\ x_i &= d_{ij}E_j \quad or \quad \sigma_i = e_{ij}E_j \end{aligned} \tag{1.3}$$

Here, σ_{ii} and x_{ii} are reduced to σ_i and x_i, respectively. The shear stresses (and similarly strains) are replaced with σ_4 , σ_5, and σ_6. For example, consider an electric field applied uniformly in the thickness direction of a piezoelectric sample (E_3), strain along the thickness direction (x_3) would be $x_3 = d_{33}E_3$ and in-plane strain (assuming $x_1 = x_2$) would be $x_1 = d_{31}E_3$. These coefficients (d_{33} and d_{31}) are the most commonly reported piezoelectric coefficients and are referred to as the longitudinal piezoelectric coeffi-

cient and the transverse piezoelectric coefficient, respectively.

The values of these coefficients can span several orders of magnitude, over a wide range of materials. Of the 32 crystallographic point groups, 21 are non-centrosymmetric, with 20 of those demonstrating piezoelectricity (Fig. 1.1). These 20 point groups can be further divide into polar and non-polar groups. Those which exhibit a spontaneous polarization are called polar materials and those that do not are non-polar materials. In some polar materials an applied electric field can reorient the spontaneous polarization, while in others the field required to reorient the polarization exceeds the dielectric strength of the material. These "re-orientable" materials are ferroelectrics,[9,10] and ferroelectric perovskites (of the form ABO_3) are the most widely used piezoelectric materials.

1.1 Ferroelectrics

A material can be classified as ferroelectric if: 1. the material exhibits a spontaneous polarization and 2. the polarization is switchable by application of a sufficiently large electric field.[10,11] The quintessential polarization dipoles begin to form at sufficiently low temperatures (below the Curie temperature, T_c), while at high temperatures, ferroelectrics are in a cubic non-ferroelectric paraelectric phase (Fig. 1.2a). In general, the polarization directions are based upon the minimization of the electrostatic (e.g. depolarizing fields) and mechanical energy (e.g. strain during the phase tran-

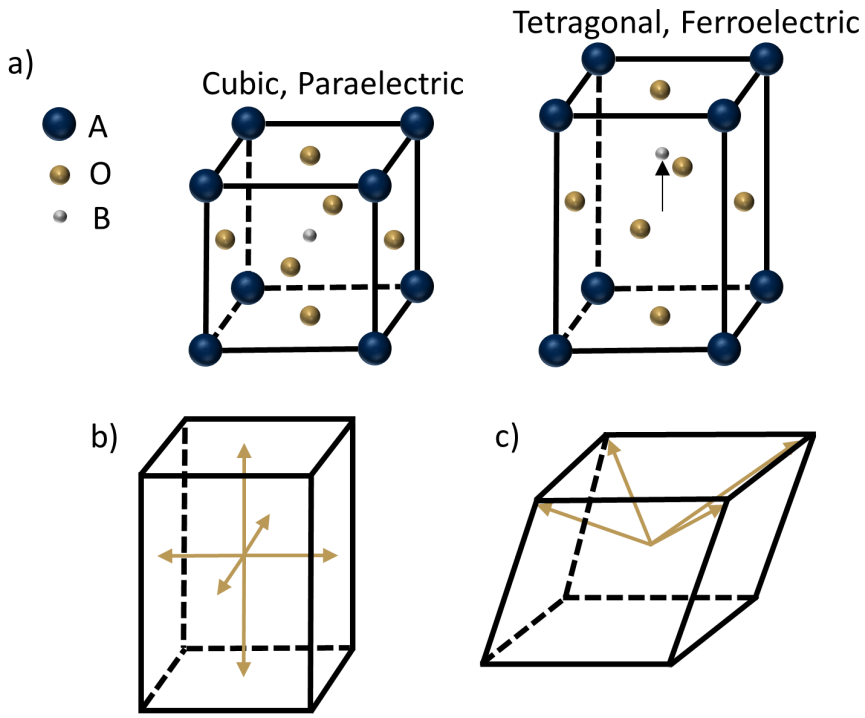

Figure 1.2: Illustration of a) the cubic paraelectric phase and a tetragonal ferroelectric phase for a perovskite material, b) the available polarization directions for a (001) tetragonal crystal, and c) the available polarization directions for a (001) rhombohedral crystal. T For simplicity, only upward polarization directions are indicated for the rhombohedral distortion in (c).

sition)[9,10] and limited to the directions available for the particular crystal distortion (e.g. Fig. 1.2b and c). During cooling, regions of nearly uniform polarization directions typically coalesce and form ferroelectric domains, which are divided by ferroelectric domain walls. Domain walls are named according to the angle between the two separated domains, e.g. for a tetragonal crystal (Fig. 1.2b), if domain A's polarization points "up" and domain B's points "down" then the wall separating them would be a 180° domain wall. The switching of these domains and movement of domain walls are the physical drivers of the quintessential ferroelectric curve, the hysteretic

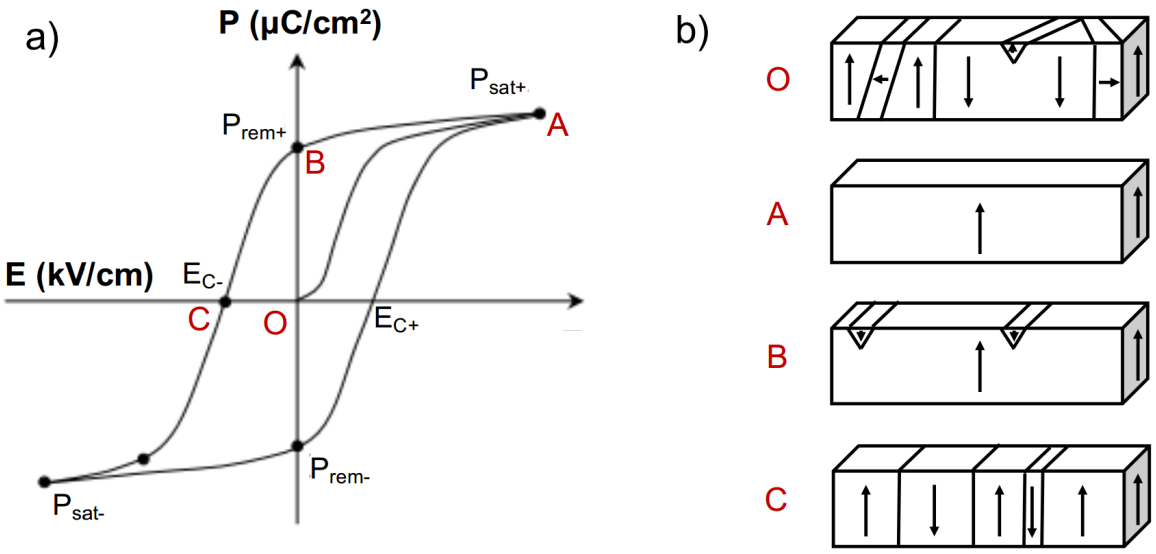

Figure 1.3: Schematic representation of the (a) polarization-electric field (P-E) loop and (b) domain states at important points along the hysteresis loop[12,13,14]

polarization vs. electric field (PE) curve (Fig. 1.3), which describes the non-linear behavior in response to appropriately large electric fields.

Upon application of an electric field (E_j) to a virgin material, polarization (P_i) initially increases linearly with electric field. As the electric field continues to increase, the aforementioned ferroelectrics domains that are poorly aligned with the applied field switch through nucleation of new domains and domain wall motion to increase alignment. Eventually, the polarization response saturates (point A) (P_{sat^+}) (Fig. 1.3) as the domains become ”maximally aligned”. Subsequently, as the magnitude of the electric field is reduced, some domains begin to return to their initial polarization direction, due to the influence of effects such as mechanical and electrical boundary conditions. However, at zero field a spontaneous polarization (the remanent polarization, P_{rem^+}) persists at point B. The process then repeats

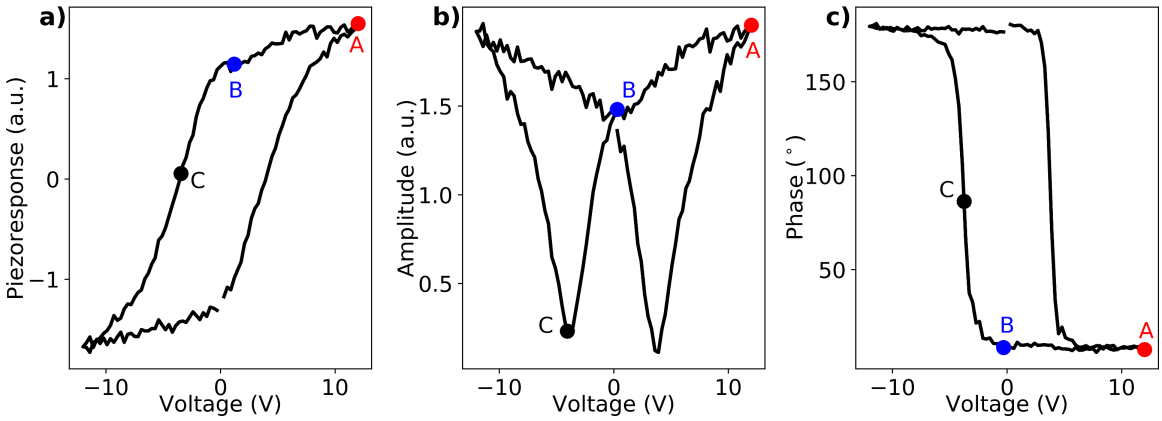

Figure 1.4: Example of strain-electric field (or piezoresponse) hysteresis loops. a) The piezoresponse hysteresis loop. b) The amplitude of the piezoresponse. c) The phase of the piezoresponse, which is measured relative to the applied field. The inset letters correspond to those in Fig. 1.3 and represent A. the positive saturation values, B. the positive remnant values, and C. the negative coercive

from this remanent state as negative fields are applied and domains of the opposite polarity begin to nucleate. An eventual net zero polarization is reached at point C, referred to as the negative coercive field (E_{c^-}), where the polarization is said to have "switched". This process then proceeds from coercive to the negative saturation (P_{sat^-}) value and finally to the negative remnanet ((P^-_{rem}). Another cycle would then continue from P^-_{rem} to the positive coercive (E_{c^+}) and back to P_{sat^+}. In an ideal and perfectly symmetric polarization-field loop, this process follows the outer-path in Fig. 1.3 ad-infinitum never returning to the origin.

Due to the piezoelectricity of ferroelectrics, this hysteretic behavior is also present in the strain-electric field behavior (i.e. the piezoresponse), as demonstrated in Fig. 1.4a. This hysteretic piezoresponse exhibits all of the same parameters as the PE loop of Fig. 1.3, i.e. saturation values, remnant

Table 1.1: Comparison of select piezoelectric coefficients in selected ferroelectric/non-ferroelectric materials in thin film form[9,15]

Material	Class	d_{33} (pC/N)	d_{31} (pC/N)
$Pb(Zr_xTi_{1-x})O_3$	Ferroelectric	80 to 593	-94 to -274
$BaTiO_3$	Ferroelectric	190	78
PVDF	Ferroelectric	-35	23
ZnO	Non-Ferroelectric	6 to 12	-4.7
AlN	Non-Ferroelectric	5	3

values, and coercive values. Often the piezoresponse is represented as an amplitude (Fig. 1.4b) and phase (Fig. 1.4c), informing on the magnitude of the piezoelectric coefficient and the polarization state of the material, respectively.

The ubiquity of ferroelectrics in electromechanical applications is due to the fact that they boast some of the largest piezoelectric coefficients. In particular, ferroelectric perovskites demonstrate a piezoelectric coefficient an order of magnitude larger than non-ferroelectrics (Table 1.1).[9,15] This advantageous property has naturally led to ferroelectrics being the center of intense research aimed at discovering the source of the enhanced properties. In the 70+ years since the discovery of the first ferroelectric perovskite,[16] chemistries with increasing piezoelectric properties have been discovered and contributing physical phenomena have been investigated, including: extrinsic contributions,[17,18,19,20,21] morphotropic phase boundaries (MPB),[22,23] field-induced phase transitions,[24,25] heterogeneities (structural, chemical, and/or polar),[26,27] and more. These phenomena are discussed below.

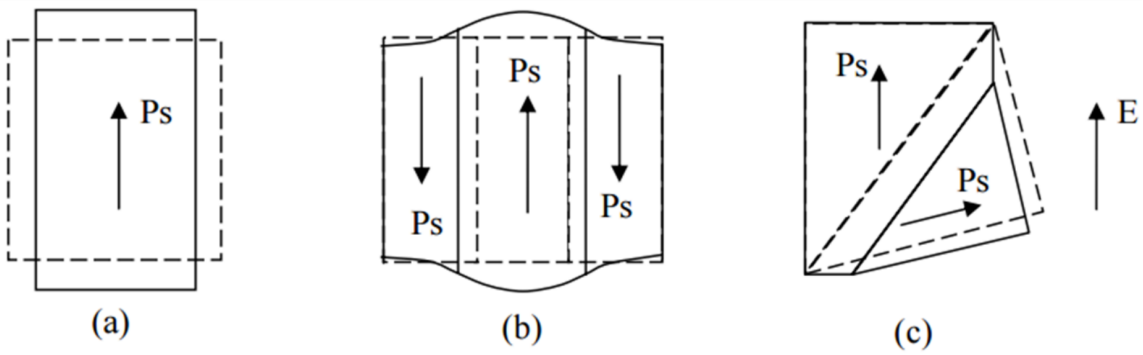

Figure 1.5: Illustration of a) the intrinsic contribution of a single domain, b) extrinsic contribution from the motion of a 180° domain wall, and c) the extrinsic contribution of a non-180° domain wall. The dashed lines represent the initial state and the solid line represents the state when under the shown electric field (E).[13]

1.2 Extrinsic and Intrinsic Contributions

The physical contributions to the piezoelectric response in a typical ferroelectric consists of intrinsic and extrinsic phenomena. The intrinsic contributions are the direct consequence of the deformation of the crystal lattice (Fig. 1.5a), i.e. the average response of a single domain. This category includes electrostriction, a quadratic effect that is due to the slight displacement of ions in the crystal lattice when under an applied field. While electrostriction and applies to all dielectrics, some ferroelectrics present extraordinarily large electrostrictive coefficients (e.g. relaxors).[28]

Extrinsic contributions consist of contributions from domain wall motion (Fig. 1.5b and c) and phase boundary motion, as well as the displacement of defects.[29] A variety of methods for separating and quantifying intrinsic and extrinsic effects have been developed, such as Rayleigh Law based analysis,[30,13] and these phenomena have been investigated as a function of tem-

perature,[31,32] excitation frequency,[33,34] and aging (time dependence).[35,36]

In particular, extrinsic contributions of domain walls are routinely assessed macroscopically.[37,38,39,40] Such macroscopic studies often average contributions from numerous internal interfaces and coordinated motion thereof. With the continued trend towards device miniaturization, systematic studies of the effects of domain walls on the electromechanical response at the microscale have become necessary and increasingly prevalent.[41,42,43,44,45]

Most of these studies have concentrated on the nucleation and growth dynamics of domains.[17,18,19] A limited number of studies have addressed domain walls' influence on characteristic parameters, e.g. nonlinearity in piezoresponse,[20] and strain-electric field switching.[21,46,47] Most notably, in $LiNbO_3$, the nucleation voltage was found to be continuously affected by the presence of a domain wall, up to two micrometers away. Specifically, the nucleation voltage increased by an order of magnitude in absence of a domain wall. However, the results were in contrast to prior models suggesting that the influence of a domain wall extends to at most 100's of nanometers.[48]

It should be noted that these and many previous studies concentrated on user-written domains, which can be largely metastable.[22,49] As such, the effects of domain wall proximity and eventual *instability* of a "written" domain wall are often convoluted. Such instabilities could be particularly strong in materials with complex chemistries, such as relaxor-ferroelectric

Table 1.2: Comparison of select piezoelectric coefficients in selected single crystal ferroelectric materials[50]

Material	d_{33} (pC/N)	d_{15} (pC/N)
PMN-28PT	100	3500
PMN-32PT	200	3500
PMN-37PT	500	2000
$PbZr_{0.5}Ti_{0.5}O_3$	200	400

solid solutions.

Notably, extrinsic effects alone do not fully explain the large piezoelectric properties in ferroelectrics and large variation in piezoelectric coefficients across ferroelectrics can be seen, e.g. $Pb(Zr_xTi_{1-x})O_3$ or PZT exhibits significantly larger coefficients when compared to prototypical ferroelectric $BaTiO_3$ (Table 1.1).

1.3 Morphotropic Phase Boundaries and Structural Phase Transitions

Unlike $BaTiO_3$, PZT is a *solid solution* combining two materials. For example, PZT consists of $PbZrO_3$ (an anti-ferroelectric) and $PbTiO_3$ (a ferroelectric). Similarly, (1-x)$Pb(Mg_{1/3}Nb_{2/3})O_3$-x$PbTiO_3$ (or PMN-xPT) combines $Pb(Mg_{1/3}Nb_{2/3})O_3$ (a relaxor, see below) and $PbTiO_3$. In practical electromechanical applications, some of the most widely used ferroelectrics are solid solutions, because they exhibit some of the highest electromechanical properties among ferroelectrics. However, the piezoelectric properties and others (e.g. structure and dielectrics properties) are highly dependent on composition, x (Table 1.2).

This strong compositonal-dependence is best illustrated in the phase dia-

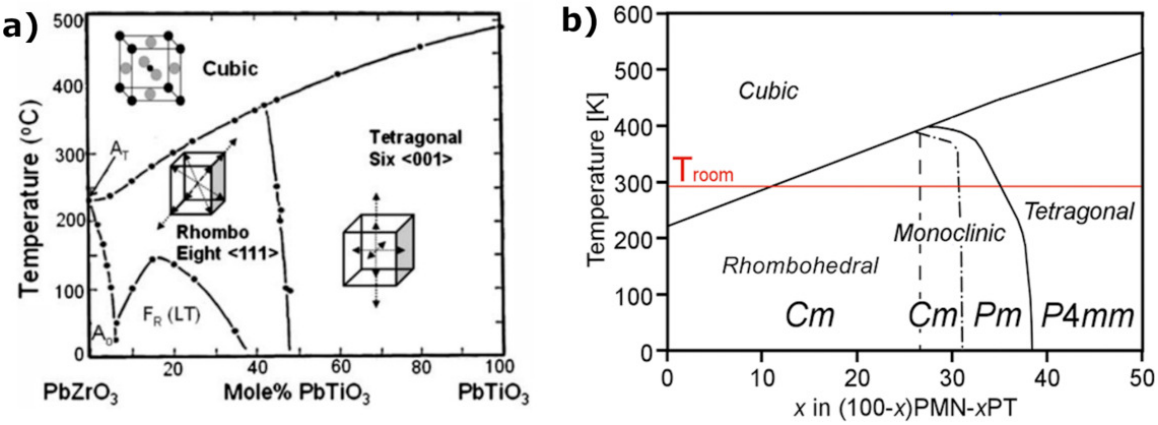

Figure 1.6: Phase diagrams for a) PZT and b) PMN-xPT.[51,52]

gram of these materials (Fig. 1.6[51,52]). For instance, in PZT, as the percentage of $PbTiO_3$ is increased the material structure transitions from rhombohedral to tetragonal, where the boundary between these two is at $x = 52\%$. This boundary is called the morphotropic phase boundary (MPB) and is mostly temperature independent. Notably, PMN-xPT exhibits three MPB's, one dividing a rhombohedral and monoclinic phase ($x \approx 28$), one two monoclinic phases ($x \approx 31$), and one a monoclinic and tetragonal phase ($x \approx 38$).

In particular, near-MPB compositions (on the rhombohedral side) of PZT and PMN-xPT exhibit the highest reported piezoelectric coefficients for the respective chemistry, given the correct crystallographic orientation and poling where necessary.[53,54,55] This observed improvement is often attributed to increased "polarizability", i.e. a wide array of available polarization directions afforded by the coexistence of rhombohedral, tetragonal, and monoclinic phases (e.g. see Figure 1.2) allowing for better alignment with an

applied field.[56,57,58] Additionally, this structural heterogeneitiy around the MPB has been shown to facilitate field-induced phase transition,[59,57,56,58,60,61,62] further contributing to the functional properties. However, even among MPB-based materials there is a sizable disparity in the reported piezoelectric coefficients, Table 1.2, with relaxor-ferroelectric solid solutions (e.g. PMN-xPT) exhibiting the highest coefficients.

1.4 Relaxor-Ferroelectrics

Relaxor-ferroelectrics (relaxor-FE) are a solid solution of a relaxor and a ferroelectric (e.g. $PbTiO_3$). These materials exhibit the largest reported piezoelectric coefficients among ferroelectrics (Table 1.2). In particular, the largest response is found in single crystal PMN-xPT for compositions near the rhombohderal side of the MPB and when cut and poled along the 001 crystallographic axis.[63] This exceptional response has been attributed to the aforementioned phenomena: extrinsic contributions, the influence of an MPB, structural phase transitions, and comparatively large shear response[50] (d_{15} in Table 1.2) and electrostrictive effects.[64] In addition, relaxor-ferroelectrics exhibit increased heterogeneity, attributed to the relaxor end-member, that is often cited as a key contributor to the piezoresponse.

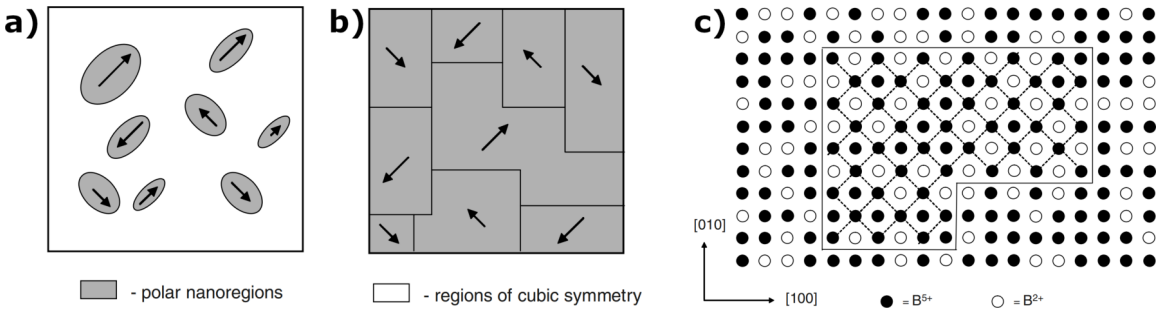

Figure 1.7: Illustrations of PNRs and CNRs. a) and b) show two different models of PNRs. In a), PNRs are considered polar "islands" embedded in a non-polar matrix. In b), the entire material is shown as polarized, with various domains divided by domain walls, however, here the "domains" are nanoscopic. c) Illustration of a chemically ordered region (i.e. CNR) within a disordered region.[65]

1.5 Relaxors: Polar Nano Regions and Chemical Nano Regions

Relaxors (e.g. $Pb(Mg_{1/3}Nb_{2/3})O_3$ or PMN) are a non-proper ferroelectric, with a dielectric peak temperature T_m that increases with the measuring frequency and which exhibit a large amount of disorder and/or heterogeneity. At high temperatures relaxors are in a paraelectric state quite similar to the one observed in typical ferroelectics. However, upon cooling relaxors begin to exhibit behavior that distinguishes them from typical ferroelectrics. Most notably, there is no well-defined temperature at which relaxors transition from a paraelectric to ferroelectric state. Instead, when relaxors are cooled below the Burns temperature (T_B) nanoscopic polar regions (or polar nano regions (PNRs, Fig. 1.7a and b) form, which then freeze into a disordered glassy state below the depolarizing temperature T_d. These PNRs range in size from 1.5 nm to 6 nm and in volume fraction from 0% to 30%,[66,67] for high (600's K) and low (10's K) temperatures, respectively. Below T_d, re-

laxors can be forced into a ferroelectric state with poling.

PNRs are a unique properties of relaxors and an example of their increased disorder. As such, PNRs are considered to have a strong influence on the piezoelectric properties of relaxors and, subsequently, relaxor-FEs. Their influence have been confirmed in a wide range of studies and have been shown to contribute to the large shear response of relaxors,[68,69,70] as well as the polarizability.[26,71,72]

Another unique feature of relaxors (and example of disorder) are chemical nano regions (CNRs, Fig. 1.7c), i.e. nanoscopic variations of chemical ordering. Specifically, in PMN, the B-site cations (Mn and Nb) exist in ordered regions with $Mg : Nb = 1 : 1$, that are surrounded by regions where Mn and Nb are randomly distributed with a ratio of $Mg : Nb < 1 : 2$.[73,74] This compositional disorder not only impacts the properties of relaxors, but are a necessity for their existence, as it has been demonstrated that when this disorder is removed relaxors can transition to an antiferroelectric.[75]

1.6 Remaining Challenges

Despite the identification and study of the numerous above contributors, we lack a *complete* physical and chemical understanding of the piezoelectric response in ferroelectrics, hindering advancements in piezoelectric materials. This is evident when considering the development of novel ferroelectric compositions. Since informed design of materials would require a complete

and thorough understanding of the piezoelectric response in ferroelectrics, new compositions have continued to be developed with a trial-and-error based doping of pre-existing chemistries.[76,77,78,79] The gaps in our understanding are varied. Of particular interest in this thesis is the impact of the individual contributors on the various characteristic behaviors of ferroelectrics.

For instance, in some ferroelectrics, the piezoelectric properties have been shown to be strongly influenced by extrinsic effects.[38,39,40] One report performed at the macroscopic scale, showed that smaller domains (higher domain wall density) yielded significantly higher piezoelectric coefficients.[80] However, recent studies have begun to challenge this relationship, with a notable report demonstrating that a high domain wall density is not required when designing materials with very high piezoelectric coefficients.[81]

Similarly, the source of the exceptional electromechanical properties of relaxor-ferroelectrics remains contentious. One theory suggests that polarization rotation aided by the monoclinc phases present around the MPB is the significant contributor,[57] while the "adaptive phase" theory questions the very existence of the monoclinic phase. In this model, the monoclinic phase is considered to locally be higher-symmetry (e.g. tetragonal) nanodomains with very low domain wall energy and domain wall motion is thought to be responsible for the high piezoelectricity.[82] Still others attribute the response to the unique heterogeneous polar states of relaxor ferroelectrics at

the nanoscale (PNRs).[50,83]

To address these issues (among many more), researchers have become increasingly reliant upon advanced characterization techniques, as well as big data/machine learning analyses.

1.7 *In-situ* and *Operando* Characterization of Ferroelectrics

Due to advances in characterization techniques, *in-situ* and *operando* observations of materials at nano- to micrometer length scales has become increasingly more accessible.[84,85,86,87,88,40] With these advanced techniques, it has finally become possible to address the evolution of the electromechanical response in ferroelectrics and relaxor-FEs at the length scale at which the response is born. For instance, advances in high-resolution transmission electron microscopy (TEM) have enabled investigations of the structure and electromechanical properties of relaxor-ferroelectrics under the influence of mechanical stress,[89,90] electric field,[91,92] or temperature.[93] Further, diffraction techniques have been used to study the evolution of polar structures[94,95] and even confirmed the existence of PNRs.[26]

1.8 Piezoresponse Force Microscopy

An increasingly popular method for local characterization of ferroelectrics is by scanning probe microscopy (SPM).[96,97,98,99,100,101] SPM measurements benefit from the ability to spatially map functional behavior and collect large

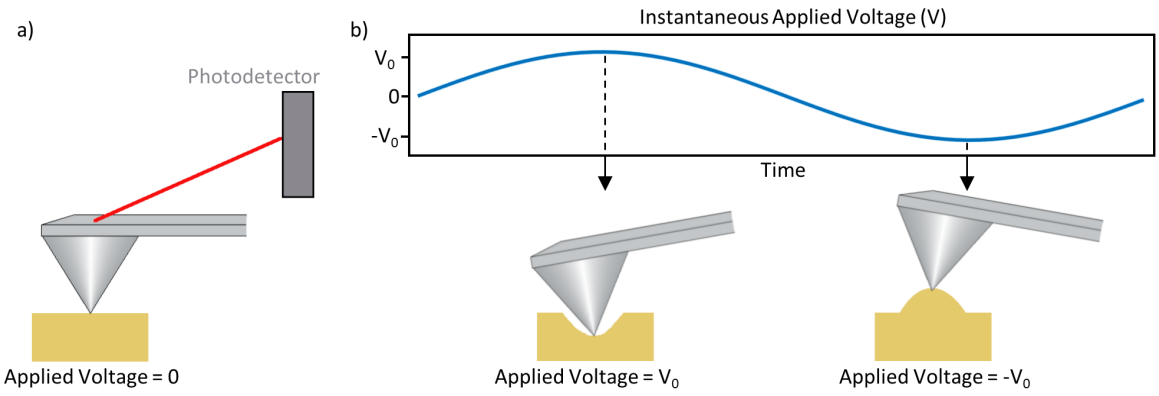

Figure 1.8: Illustration of single frequency PFM. A conductive tip is placed in contact with the sample, a laser focused onto the back of the tip, and deflections of the tip are measured via a photodetector. a) Tip and sample when the applied voltage is zero. The sample exhibits no strain and a baseline for tip deflections is established. b) Tip and sample at various applied voltages. The sinusoidal applied voltage causes a sinusoidal strain, which is extracted from the tip deflections via the photodetector. The amplitude (A) of the piezoresponse corresponds to the amplitude of the deflections and the phase of the piezoresponse (ϕ) is the phase difference between the applied voltage and the deflections.

high-dimension spectroscopic information, all with atomic to nanometer resolution. One such technique is piezoresponse force microscopy (PFM), a variant of atomic force microscopy (AFM). In this technique, a conductive tip is placed in contact with an electromechanically activate material. A laser is focused onto the back of the tip and the reflection of the laser is collected with a photodetector (illustrated in Fig. 1.8a). Then, an sinusoidal electric field is applied to the material through the tip and the material strains due to the piezoelectric effect (Fig. 1.8b). Ideally, the frequency of the applied field is the resonant frequency of the tip-surface interactions, increasing the response and decreasing noise. The deflections of the tip and, thus, the material strain is collected via the photodetector. The amplitude (A) of the deflections correspond to the piezoelectric coefficient. While, the

polarization direction of the material (ϕ) can be obtained from the phase difference in the applied voltage and the measured deflections (Fig. 1.8b).

In this way PFM maps the local electromechanical response with a spatial resolution that roughly corresponds to tip radius (at best on the order of $10\ nm$). This approach has been widely used to study mesoscale domain configuration of FE materials and has informed on mesoscale phase transitions,[102] as well as domain configuration dependence on chemistry and temperature.[103,104,105,106,107] Additionally, PFM is capable of probing the electromechanical response as a function of time and/or voltage, enabling measurement of local switching behavior or other time/field- dependent electromechanical behaviors.[108,109,110,109,41]

1.8.1 Wide Band Probing of the Response-Frequency Behavior

However, traditional PFM is limited by the fact that it is "single-frequency", i.e. the material response is only probed at one frequency. Thus, significant tip-surface resonance shifts, which can be caused by surface topography and phase transitions,[65] can result in material response being completely lost to noise. Further, probing only a single frequency results in an underspecified system. For instance, a common assumption is that the tip-surface interactions are well-described by a simple harmonic oscillator (SHO):

$$f(x) = \frac{Ae^{i\phi}\omega^2}{x^2 - \frac{ix\omega}{Q} - \omega^2} \tag{1.4}$$

Where A is the piezoresponse amplitude at resonance, ϕ is the piezoresponse phase, Q is the quality factor of the tip-surface contact, and ω is the resonant frequency of the tip-surface contact. With this *a priori* assumption, it becomes clear that single frequency PFM, yielding only the amplitude and phase, does not specify a unique solution for the system and this ambiguity leads to spurious image contrast.[111,112]

Numerous extensions to PFM and SPM in general have been developed to measure the response–frequency behavior. Techniques like dual AC resonance[113] employ a control scheme to follow resonance, while others seek to capture the response–frequency behavior over a wide range of frequencies. These approaches include thermal excitation,[114] fast lock-in sweeps,[115] pulse excitation,[116,117] and band excitation.[118] Among them, band excitation (BE) stands as a particularly attractive option due to a comparatively faster measurement rate, higher signal intensities, and reduced topological cross-talk.[119] Although, spectroscopic BE-PFM measurements suffer from a strict limit on acquisition time, often limiting the amount of available data points.

1.9 Machine Learning

The continuous progress in available characterization techniques has also resulted in considerable complexity and substantial increase in the size of generated data, effectively limiting the insights obtainable through traditional statistical analysis. As a result, more advanced analysis methods based on

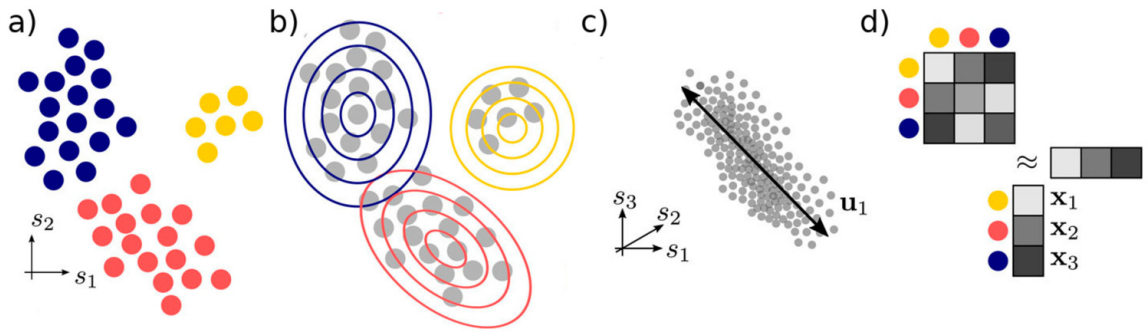

Figure 1.9: Illustration of various machine learning techniques. a) Illustration of clustering. The dots represent data points in some arbitrary space and the color of the dots represent three clusters that can be identified. b) Illustration of a distribution-based clustering technique (e.g. *k*-means) applied to the data in (a). c) Illustration of a dimensionality reduction technique that attempts to find the "direction of maximum variance" (shown as u_1). d) Many dimensionality reduction techniques can be conceptualized as a matrix factorization.[120]

machine learning algorithms have been developed to overcome these challenges.[121,122,123,124,125,126,127] Specifically, dimensional reduction (DR) and clustering techniques have been hailed as a groundbreaking paradigm in materials science,[128] and used to identify superimposed physical and chemical contributors to functional behavior within multidimensional datasets in fields as diverse as multiferroics,[129,130] superconductors,[131] oxide interfaces,[132] and electromechanically active materials.[41,49,133,134]

1.9.1 Dimensionality Reduction and Clustering

Clustering techniques seek to identify N (a user-defined parameter) clusters within a data space (or data set), e.g Fig. 1.9a. A common approach for achieving this is by making an assumption about the underlying distribution of the clusters. For instance, by assuming the distribution within a cluster

is Gaussian, the probability a given point belongs to a given cluster can be determined and, by maximizing this probability, data points can be assigned to various clusters (Fig. 1.9b).

DR techniques, seek to represent a given dataset (D) as set of N eigenvectors, U, and corresponding eigenvalues, V. In principle component analysis (PCA), one of the simplest DR techniques, eigenvectors are found by determining the "directions of maximum variance" within the data space (Fig. 1.9c). Here the eigenvalues are the individual data points projected onto these eigenvectors. Other common DR techniques (non-negative matrix factorization and dictionary learning) essentially represent a matrix factorization (i.e. $D \approx UV$, Fig. 1.9d) and are implemented by simply minimizing some error metric. A common error metric is the norm-squared of the residuals: given a two-dimensional dataset ($D(z, v)$) and N separate U-V pairs, the norm-squared of the residuals is given by Equ. 1.5.

$$(U(v), V(z)) = \frac{1}{2} \left\| D(v, z) - U(v)V(z) \right\|_2^2 \tag{1.5}$$

In typical applications, the eigenvectors ($U(v)$) can be interpreted as the "fundamental behaviors" identified across the v-dimension and the eigenvalues ($V(z)$) are the "weightings" of those behaviors across the z-dimensions. However, the exact interpretation of the results and performance of these approaches are strongly dependent on the technique used. For instance, non-negative matrix factorization (NMF) assumes that the data and result-

ing behaviors/weightings are strictly non-negative, non-ideal for the typical piezoresponse loops Fig. 1.4a. Dictionary learning (DL) includes an additional sparsity term in Eq. 1.5, allowing for probed points to be represented as both a superposition of behaviors and as single unique behaviors. Neural network (NN) based auto-encoders are non-linear and capable of representing non-linear combinations of behaviors, but require substantial computational time and sophisticated hardware.[135]

1.9.2 Intepretability Concerns

Despite their advantages, there is significant concern about the applicability of ML techniques to materials science. This concern is related to ML's strictly mathematical nature, i.e. they inherently provide results lacking a physical basis, which has resulted in an "interpretability" challenge. Specifically, a "black-box" mentality in the scientific community has often lead to challenging interpretation of outputs, which often results into incorporation of noise, and description of spurious contributions as physical phenomena.[136,137,138] In recent years, concerns over these interpretability issues have become a central focus of recent publications,[139,140,141] with some researchers highlighting a need for a means to impose physical or chemical constraints to the analysis.[138]

1.10 Thesis Goals and Organization

Through a series of studies, this thesis addresses various contributors to the electromechanical response of complex ferroelectric oxides and the effectiveness of ML techniques when applied in materials science. Furthermore, techniques for improved application of ML are developed and demonstrated on studies addressing the fundamental physics within ferroelectrics. In addition, a novel open-source wide band PFM techniques (Resonant PFM, R-PFM), is developed.

The thesis is organized as follows:

Chapter 2: Experimental Approach.

The chapter discusses the methods of sample preparation and characterization.

Chapter 3: Resonant Piezoresponse Force Microscopy.

This chapter details the specifics of RPM.

Chapter 4: Dimensional Stacking Enabled Multivariate Assessment of the Electromechanical Relaxation in Relaxor-Ferroelectrics

This chapter presents a study of the time-dependent relaxation of the piezoresponse amplitude in 001-cut single crystal PMN-xPT. The relaxation is probed across the phase diagram, for various applied voltages, and over microns square areas. A technique for imposing physical/chemical con-

straints onto ML analyses is developed to aid this multi-dimensional study.

Chapter 5: Addressing Electromechanical Switching in Ferroelectric Thin Films with Better, Faster, and Less Biased Machine Learning

In this chapter, the developed ML technique is applied to previously reported data on the electromechanical switching of a PZT thin film. A methodology for applying ML (including the technique developed in Chapter 4) to material science studies, which reduces user bias and increases interpretability, is developed.

Chapter 6: Effects of Domain Wall Proximity on Polarization Switching in Relaxor-Ferroelectric Single Crystals

In this chapter, the methodology derived in Chapter 5 is applied to study the impact of domain walls on the switching of the piezoresponse in relaxor-FE PMN-40PT. Here, out-of-the-box ML techniques are found lacking, while a traditional statistical approach is found to be effective.

Chapter 7: Conclusions and Future Work

Here, conclusions are drawn and recommendations for future work are provided.

CHAPTER 2

EXPERIMENTAL APPROACH

The chapter discusses procedure of sample preparation, characterization, and analysis.

2.1 Sample preparation

There were two categories of samples used here: 001-cut single crystals of solid solution PMN-xPT (Chapters 4 and 6) and a thin film of PZT (Chapter 5).

All PMN-xPT samples were grown by collaborator Shujun Zhang via the Modified Bridgeman Method.[142,143] The PZT thin film data was previously reported data,[144,145] as such, no first hand knowledge of the film's preparation is available. What follows is a brief summary of the sample preparation as provided by the original authors.[144,145]The PZT thin film data was a 400 nm thick $PbZr_{0.8}Ti_{0.2}O_3$ film, synthesized via pulsed-laser deposition using a KrF excimer laser (248 nm, LPX 300, Coherent), with a 60 mm target-to-substrate spacing. A 30 nm substrate of $Ba_{0.5}Sr_{0.5}RuO_3$-buffered $NdScO_3$ was used.

2.2 Piezoresponse Force Microscopy

Two forms of PFM were used for characterization of the samples: the aforementioned band excitation (BE) PFM and resonant PFM (R-PFM). R-PFM is an open-source, wide-bandwidth PFM measurement approach developed for this thesis, and is conceptually based on BE-PFM[119] and discussed in Chapter 3. Both techniques probe the frequency response of the tip-material contact by applying an electric field through the cantilever to the sample within a band of frequencies (often ≈ 50 kHz) and acquiring the resulting tip deflections within the same band of frequencies. Widely available National Instruments (NI) hardware is used for generation of the user-defined waveform and acquisition of the response (an NI-6124 is used here). Functional parameters are then extracted from the obtained frequency response by fitting to a damped-driven harmonic oscillator, i.e Eq. 1.4.

where A is the piezoresponse amplitude, ϕ is the piezoresponse phase, ω is the contact resonance frequency, and Q is the quality factor. These collective parameters inform on the electromechanical and viscoelastic properties of the sample. Specifically, A is related to the magnitude of the out-of-plane displacement, informing on the magnitude of the piezoelectric coefficients. ϕ informs on whether the surface deformations of the sample are in-phase or out-of-phase with respect to the applied voltages, and is related to the polarization state of the material. The contact resonance, ω, is related to the

visco-elastic tip-material contact properties and, unless the tip substantially changes during the measurement, it can provide information with respect to variations in the material's mechanical properties. Similarly, Q provides information on the energy absorption/dissipation. The sample's piezoresponse, PR, can be calculated using Equation 2.1.

$$PR = A\cos(\phi + \theta_{opt}), \tag{2.1}$$

where θ_{opt} is the optimum rotation angle to maximize the real component of the response, $\cos(\phi + \theta_{opt})$, with respect to the imaginary one ($\sin(\phi + \theta_{opt})$. This rotation angle accounts for phase shifts introduced by the internal capacitance of the tool.

Furthermore, two types of PFM measurements were obtained: scan measurements and grid measurements. Scan measurements raster the conductive tip over a sample area, while probing the response (e.g. A, ϕ, Q, and ω for BE and R-PFM), effectively "mapping" the state of these variables with some resolution (typically 256x256 points). For instance, a phase scan is shown underneath the tip in Fig. 2.1a. Grid measurements divided the sample area into a grid (Fig. 2.1a) and probe the piezoresponse in response to some applied waveform, where the specific waveform applied depends on the characteristic behavior of interest (e.g. strain-electric field switching, non-linearity in the piezoresponse, relaxation of the piezoresponse etc.). In particular, this thesis probes the switching behavior of the piezoresponse (in

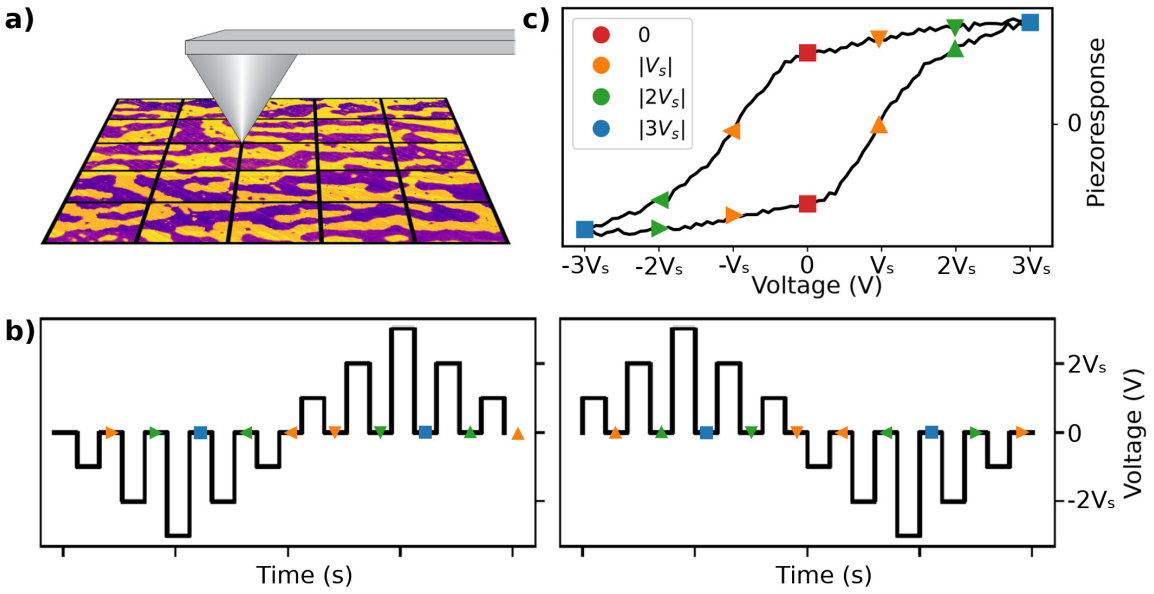

Figure 2.1: Schematic illustration of the experimental set up for grid-based PFM measurements. a) The probed area is divided into a grid (here a 4 x 4 point grid is illustrated) and at each point some waveform is applied and the piezoresponse is probed. b) For instance, when probing the switching behavior of the piezoresponse, a bipolar triangular waveform (illustrated for both positive and negative starting voltages) is applied, and the off-field piezoresponse amplitude, phase, contact resonant frequency, and quality factor are recorded. The triangles and squares are the points where the off-field response is probed. c) The probing points shown in (b) superimposed onto their corresponding locations in a typical piezoresponse hysteresis loop.

BE this is called switching spectroscopy PFM, SS-PFM)[146] and the relaxation of the piezoresponse amplitude.

When probing the switching behavior, a bipolar triangular waveform with some voltage step size (V_s) is applied. Fig. 2.1b illustrates a single "cycle" of this waveform, which yields the piezoresponse hysteresis loop (e.g. Fig. 2.1c or Fig. 1.4). Note that it is standard practice in SS-PFM to apply multiple cycles, often averaging the numerous obtained hysteresis loops together or omitting the first cycle[146, 147]. When probing the relaxation of the piezoresponse, a DC pulse is applied for some time period

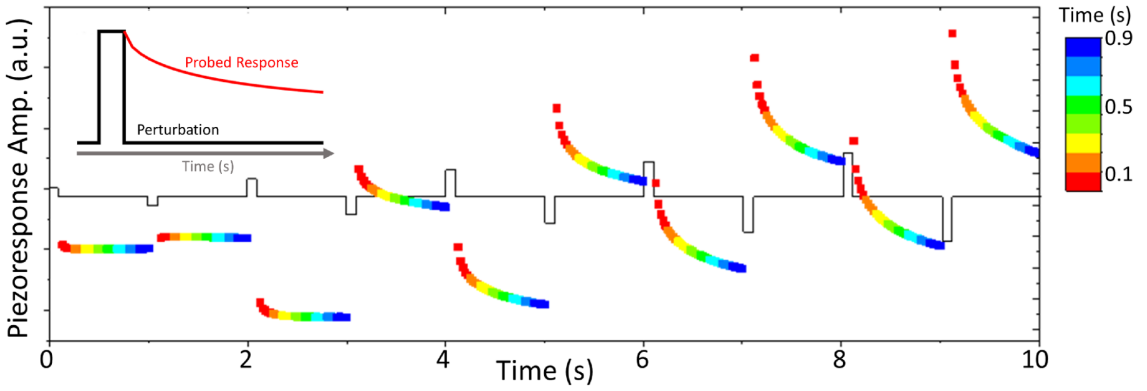

Figure 2.2: Illustration of the waveform used to probed the relaxation of the piezoresponse amplitude. The inset illustrates the response to a single DC pulse.

(Δt_{DC}) and the piezoresponse is probed over time upon removal of the DC voltage (as illustrated in the inset of Fig. 2.2). Here, a series of DC pulses with increasing magnitude and alternating polarity is used (Fig. 2.2), probing the relaxation as a function of time, applied field magnitude, and applied field polarity.

2.3 Probing the Electromechanical Relaxation Across the Phase Diagram of PMN-xPT

In Chapter 4, the local relaxation of electromechanical response of $(1-x)Pb(Mg_{1/3}Nb_{2/3})O_3 - xPbTiO_3$ single crystals was studied by band excitation piezoresponse force microscopy (BE-PFM), following the procedure previously reported in reference.[49] The BE-PFM was performed on an *Asylum Research Cypher S*, in ambient conditions. The tips used were metal-coated *Budget Sensors* ($k \approx 1N/m$) with a free in-air resonance of $\approx 75kHz$. The measurements were performed over a 50 x 50 points grid,

covering a 2 μm x 2 μm area. At each point, a BE-PFM waveform was overlaid with a voltage, and applied to the tip. The evolution of the piezoresponse was probed both as a function of time up to 0.9 s in time steps of 0.025s, and perturbation voltage. The specific time, voltage and composition dependent response $D^{p_v,p_c}(t,z)$ was measured out-of-field, after the application of each of the 10 alternating increasing positive and negative voltages, equal to and above the coercive voltage. The measurements were repeated for the three compositions studied, 001-cut PMN, PMN-0.36PT, and PMN-0.40PT. Big Data analytics were implemented in a *Jupyter* notebook, using the *Python* programming language. The standard open source machine learning and dimensionality reduction libraries were used for the analysis.

2.4 Switching PFM of a PZT Thin Film

In Chapter 5, the switching behavior of a 400 nm (110) $PbZr_{0.2}Ti_{0.8}O_3$ thin film with a 30 nm $Ba_{0.5}Sr_{0.5}RuO_3$ bottom electrode was probed. As-grown, the samples show stripes of *c/a* domains separated by a_1/a_2 stripes, resulting in a hierarchical sawtooth-like topography: $\approx$ 4 nm peaks with a peak-to-peak spacing of $\approx$ 900 nm corresponding to the stripes, and smaller $\approx$ 0.5 nm periodic surface corrugations with a $\approx$ 30 nm peak-to-peak spacing, corresponding to domain variants within each stripe.

Switching spectroscopy (SSPFM) data were acquired through band-excitation

piezoresponse force microscopy (BE-PFM) on a pre-poled 2 μm x 2 μm area of the sample. BE-PFM measurements provide information with respect to the amplitude (A), phase (ϕ), cantilever resonance frequency (ω), and Q-factor (Q) of the piezoresponse, through point-by-point fitting of the frequency-dependent electromechanical response to a simple harmonic oscillator (SHO) model. Two full cycles of SSPFM data were collected with the above method in a 60x60 point grid. However, consistent with previous reports, only the second cycle is considered in the present study. Additionally, a hard limit was applied to the resonance curves prior to analysis, enabling poor SHO fits to be removed from further processing. Furthermore, the piezoresponse curves were calculated with the as-provided amplitude and phase, by using the mean of the provided rotation angles in order to remove the instrumental phase offset. The full description of data preprocessing steps is provided in Appendix B.

2.5 Switching PFM of a PMN-40PT Single Crystal

In Chapter 6, A 001-cut 0.60PMN-0.40PT relaxor-FE single crystal grown via the modified Bridgemann method was probed via resonant PFM (R-PFM). Out-of-plane response with information on the amplitude (A), phase (ϕ), contact resonance (ω), and quality factor (Q) of the electromechanical response was characterized for a 10 μm x 10 μm and an 8 μm x 8 μm area of the surface (Figure C.1 and C.2). Switching piezoresponse (via R-

PFM) was performed in a grid of 50x50 points over approximately the same locations of the original R-PFM scan. Due to an errant spatial shift during switching spectroscopy characterization, the 8 μm x 8 μm area scans and the switching spectroscopy grid did not fully overlap. When correlating the switching spectroscopy data to the initial area scans, this shift was manually corrected. The shift was corrected by referencing the the after switching spectroscopy scans, in which the drift of the nucleated domain "dots" is clearly visible. For the 10 μm x 10 μm area, a two cycle bipolar triangular switching waveform beginning with negative voltages was applied. For the 8 μm x 8 μm area, a single cycle bipolar triangular switching waveform beginning with positive voltages was applied.

For the 10 μm x 10 μm, a Budget Multi75E-G tip with a stiffness of $\approx$ 2.4N/m was used, and for the 8 μm x 8 μm area, an Olympus AC240 with a stiffness of $\approx$ 2.2N/m was used. Furthermore, the contact force in the 8 μm x 8 μm area was increased from $\approx$ 100 nN in the 10 μm x 10 μm area to $\approx$ 400 nN in the 8 μm x 8 μm area, in order to reduce the influence of electrostatic contributions. Details of the setup and experimental technique are further discussed in Appendix C.

For the machine learning analysis, various pre-processing steps were performed on the data prior to analysis. First, the point-by-point mean was removed and data was divided by the standard deviation (z-normalization). Second, resonance values greater than 4 standard deviations away from

the mean were removed and backfilled, using the previous data point in the curve. Finally, the piezoresponse and resonance data were dimensionally stacked for the analysis, allowing for the derivation of physically correlated piezoresponse and resonance curves.[22] Model parameters were selected with a quantitative analysis of the root mean squared model error.[148] The appropriate number of components, N, and sparsity parameter (α) were estimated at $N = 3$ to 5, and $\alpha = 1$ to 1.3 for the 10 μm x 10 μm area; and $N = 4$ to 5, and $\alpha = 1$ to 1.3 for the 8 μm x 8 μm area (Figure C.5). Additional analyses corresponding to the other $N - \alpha$ pairs are discussed in Figures C.6 and C.7.

Characteristic switching parameters were extracted from the piezoresponse hysteresis curves (C.9) and binned as a function of distance to the nearest domain wall (every $80nm$ for the 10 μm x 10 μm and every $60nm$ for the 8 μm x 8 μm). The rationale for the selected bin sizes is described in the Supporting Information. Bins with less than 5 points were omitted due to a lack of statistical relevance. Figures with these omitted bins are available in the Supporting Information, as are Figures with other parameters defining the hysteresis curve (Figure C.10). The data were divided according to the initial polarization state, and distances are shown along a double positive horizontal axis, centered at a domain wall (distance = 0).

CHAPTER 3

RESONANT PIEZORESPONCE FORCE MICROSCOPY

In this chapter, the concept's behind RPFM are described.

Resonant PFM (RPFM) is the generation and application of a band of frequencies and subsequent collection of the material response within a reasonable time frame. Thus, RPFM can be conceptually divided into two ”paths”: the application path (Fig. 3.1 path a), which applies a waveform, and the collection path (Fig. 3.1 path b), which collects the response of the material to the applied waveform and extracts parameters from a fitting to Eq. 1.4.

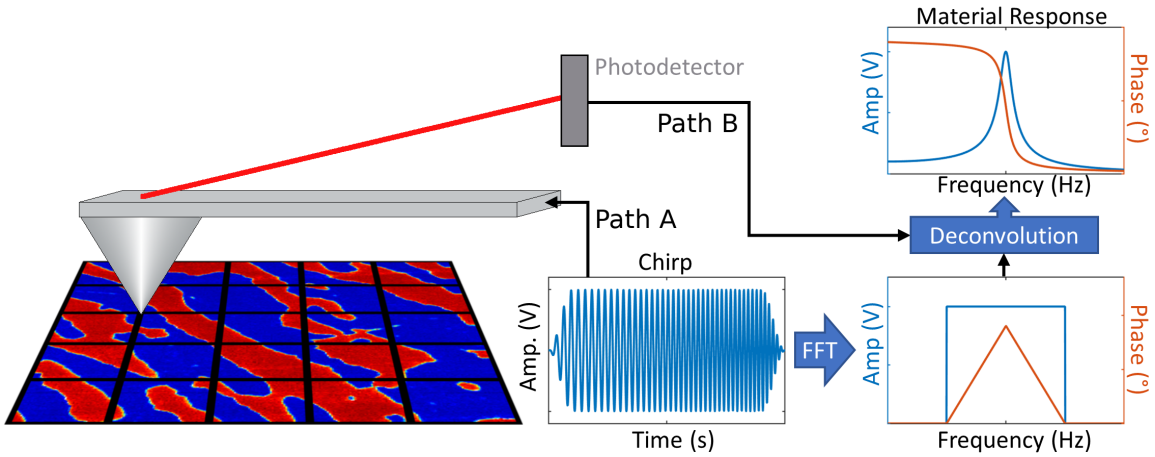

Figure 3.1: Illustration of resonant piezoresponse force microscopy (R-PFM) for application of a single chirp. First the excitation waveform is generated according to user specifications and applied to the material through the tip. Then, the AC deflections of the tip are collected from the photodetector. Finally, the AC deflections are deconvolved with the applied chirp and the material's response is obtained.

3.1 Application path

Strictly speaking, in RPFM (and any wide band probing technique) only the excitation or driving waveform is necessary to probe the material response (Fig. 3.1 path a). However, important information on the ferroelectric properties of materials is obtained from DC-field and/or time dependent

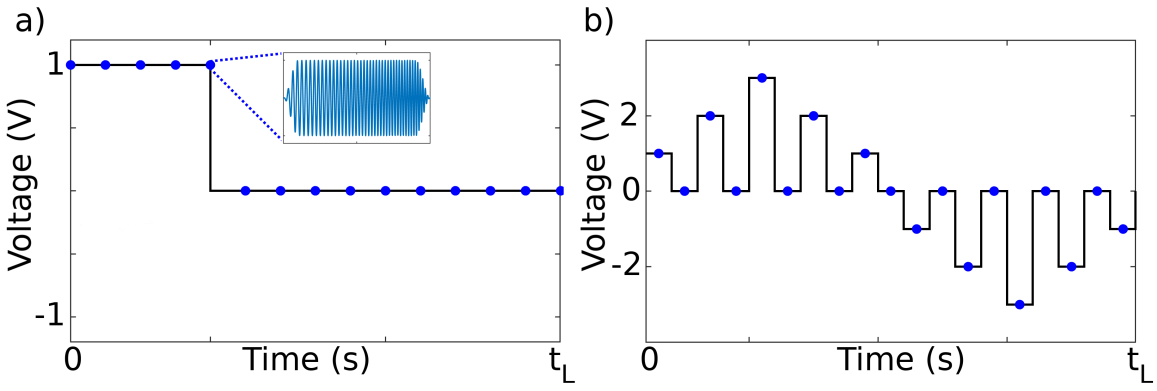

Figure 3.2: Illustrations of a) a relaxation measurement waveform and b) a switching spectroscopy measurement waveform. a) A simple relaxation measurement waveform where five consecutive chirps are applied with an added DC voltage of 1V and a subsequent 10 consecutive chirps are applied with no DC bias. In this way, the material is probed for five points while being poled by 1V and the resulting electromechanical relaxation upon removal of the 1V is probed for 10 points. b) A simple switching spectroscopy measurement waveform where the materials is probed from -3V to 3V. Blue dots represent a single chirp and the black line represents the DC voltage.

probings, such as in switching spectroscopy and relaxation measurements. Thus, a necessary functionality of RPFM is to overlay the excitation waveform with an arbitrary and user-definable waveform (e.g. Fig. 3.2), enabling such electric field based spectroscopy. Here, we will first discuss the excitation waveform and then move onto how the excitation waveform can be overlaid an arbitrary waveform to enable spectroscopic probings.

3.1.1 The Excitation Waveform

In single frequency PFM, the material is excited with a single frequency sinudsoid. The fundamental idea behind RPFM is to instead excite the materials with a *band* of frequencies. Thus, the ideal frequency spectrum of a RPFM excitation waveform is simply a constant amplitude within the

desired band of frequencies with an amplitude of zero outside the band, illustrated in Fig. 3.1. In the RPFM system described here, the excitation waveform is based on a linear swept-frequency sinusoidal (or "chirp")[149], defined as:

$$x(t) = A_0 sin((f_0 + kt)t) = sin(f_0 t + kt^2) \tag{3.1}$$

Where t is time, f_0 is the initial frequency, A_0 is the amplitude, and k is the sweep rate (also known as chirpyness). This chirp waveform indeed exhibits the desired frequency response. However, ringing in the frequency response occurs when the chirp is finite in time, due to the discontinuities occurring at the beginning and end of the waveform. This ringing can be minimized or eliminated by tapering the chirp, which gradually reduces the amplitude at the beginning and ending of the chirp. Thus, the final excitation waveform used here is a chirp tapered via a Tukey window[150], Fig. 3.3 provides an illustration.

The user dictates the excitation chirp by specifying: amplitude A, lower frequency f_L, upper frequency f_H, sampling rate f_s, and chirp duration Δt. The chirp is calculated by determining the parameters for Eq. 3.1 from these user specified parameters as shown in Eq. 3.2 and the chirp is tapered.

$$A_0 = A \tag{3.2a}$$

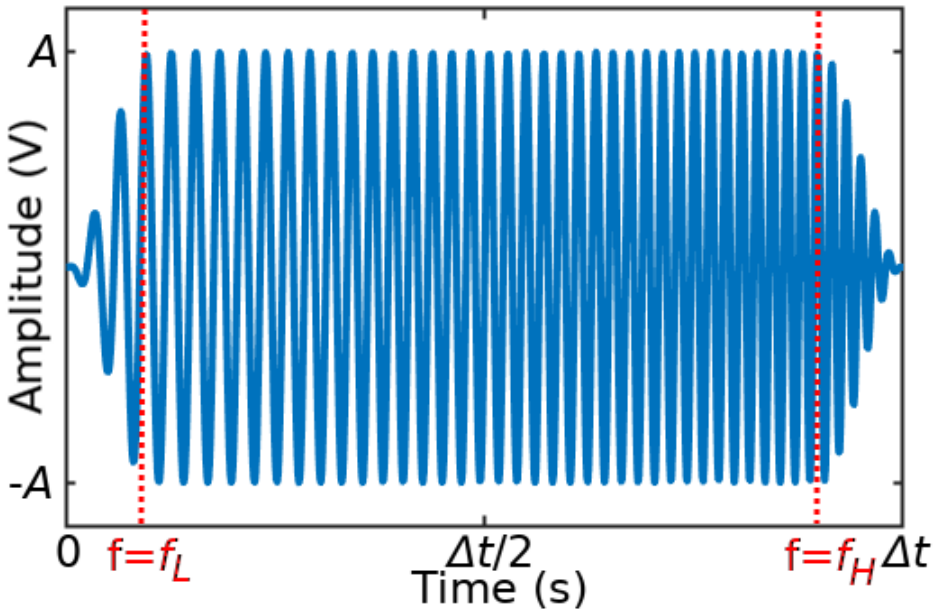

Figure 3.3: Illustration of the excitation waveform, or chirp, annotated with the user specified parameters. The chirp is calculated from the user-specified chirp amplitude (A), lower and upper frequencies (f_L and f_H), sample rate, and chirp duration (Δt). Here, A is the peak value of the chirp, Δt is the time length of the chirp, and f_L and f_H are the desired low and high frequencies of the chirp. The specified f_L and f_H are automatically adjusted to account for the windowing of the chirp, which reduces the amplitude at the beginning and ending of the waveform.

$$f_0 = 0.98 * f_L \tag{3.2b}$$

$$k = \frac{1.02 * f_H - 0.98 * f_L}{\Delta t} \tag{3.2c}$$

Note that in Eq. 3.2, the low frequency is decreased by 2% and the high frequency is increased by 2%. This is to account for the tapering and maintains a constant amplitude throughout the user-specified band. What follows is an

in depth description of each parameter, with an illustration of the parameters in Fig. 3.3.

- *Chirp Amplitude:* The Chirp Amplitude is the peak voltage of the chirp (A_0 in eq. 3.1) and should be specified in volts.

- *Lower and Upper Frequency:* The Lower and Upper Frequency are the frequencies bounds of the measurement (f_L and f_H in eq. 3.1), specified in Hz. **Note that the user specified frequencies are automatically adjusted by 2% to account for the windowing, as illustrated in eq. 3.2 and Fig. 3.3**.

- *Sampling Rate:* The Sampling Rate is frequency at which the waveform is generated and the response sampled (f_s in eq. 3.1), specified in Hz, and is dictated by Nyquist-Shannon sampling theory.

- *Chirp Duration:* The Chirp Duration is the time length of the excitation waveform, in seconds. This parameter is the defacto time step of the entire measurement, as a functional fitting is ultimately applied to the frequency response of individual chirps to extract parameters. An important relationship to consider here is the inverse relationship between the time step and frequency resolution of the ultimately obtained frequency response (i.e. material response in Fig. 3.1), or $\Delta f = \frac{1}{\Delta t}$. Δf must be reasonably small to produce an adequate fit.

3.1.2 Electric field and time dependent spectroscopy

While it is the RPFM excitation waveform (or chirp) that probes the material response and is the core of RPFM, a means of field- and time- dependent probings is necessary for a functional PFM system. Typical PFM based spectroscopic probing can be roughly categorized into DC-field dependent measurements, AC-field dependent measurements, and time-dependent measurements. For instance, switching spectroscopy would be considered DC-field dependent measurements, while electromechanical non-linearity measurements would be AC-field dependent. Further, often the higher order harmonics of the electromechanical response is investigated to inform on phenomena such as electrostriction. Thus, to fully enable common spectroscopic measurements a wide bandwidth PFM system must allow users to specify:

1. A series of an arbitrary number of consecutive chirps, enabling time dependent measurements.

2. Individual DC field offsets for each chirp within the series, enabling DC-field dependent measurements.

3. Individual Chirp Amplitudes for each chirp within the series, enabling AC-field dependent measurements.

4. The harmonic of interest for each chirp within the series, enabling in-

vestigation of higher order harmonics

In RPFM, spectroscopic measurements are enabled by allowing the user specify each of the above parameters in any order or combination. This near-complete control of measurement specification not only enables all of the common measurements (e.g. field-dependent switching spectroscopy, field- and harmonic- dependent electromechanical non-lineariy measurements, and time- and field- dependent electromechanical relaxation measurements), but also streamlines development of alternative measurement schemes. Note that, *excitation waveform* (e.g. Fig. 3.3) is used to refer to the chirp and *measurement waveform* (e.g. Fig. 3.2) is used to refer to the user-specified series of chirps, DC- and AC- offsets, etc that represent a specific measurement scheme (e.g. a switching spectroscopy measurement).

3.2 Collection Path

Once the measurement waveform is applied to the material, all that remains is to capture the material response (Fig. 3.1 path b). First, the raw AC deflections are captured as a time series at the sampling rate specified by the user. With the knowledge of the exact measurement waveform, the deflections due to individual chirps can be extracted and transformed to the frequency domain via a fast Fourier transform (FFT). Then, the effects of the chirp are removed from the frequency response by deconvolution, yielding the material's frequency response (illustrated in Fig. 3.1 path b). A func-

tional fitting of the frequency response to a damped driven oscillator (Eq. 1.4) can then used to extract the response parameters (amplitude A, phase ϕ, resonant frequency ω_0, and quality factor Q). Note that as discussed in the previous section, the user can specify which harmonic the fitting is applied to. Finally, the initial measurement waveform is again consulted to determine the conditions under which individual chirps were applied (e.g. time step, DC-field, and AC-field), allowing the resulting parameters (A, ϕ, ω_0, and Q) to be investigated as a function of these conditions.

3.2.1 AFM-Agnosticism

In order to maintain an AFM-agnostic system, RPFM limits the communication with the AFM to only the absolute necessities. Communication between any RPFM system and an AFM must, at a minimum, consist of two signals. First, the measurement waveform generated by the RPFM system must be passed to the AFM and, second, the AFM must provide the raw tip deflections for the RPFM system to process. However, the RPFM system must also be informed *when* the measurement waveform should be applied and raw tip deflections acquired and, thus, communication cannot be limited to these 2 signals. To circumvent this timing issues, a third trigger signal must be used as well. The trigger signal is simply a rising edge signifying that the RPFM system should begin outputting the measurement waveform and acquiring the raw AC deflections. For each rising edge, Ex-

cite will output the measurement waveform and acquire the response to the waveform only once. This single acquisition is referred to as an *Acquisition*.

An important consequence this AFM-agnosticism is a lack of knowledge about the tip movement. RPFM simply provides the specified measurement waveform and acquires the raw response whenever the AFM requests, i.e. whenever the AFM sends the trigger signal. This means that the user must be careful to keep track of how the measurement was performed on the AFM, so that results can be properly interpreted.

3.2.2 The Measurement Waveform and Acquisitions

Each time the RPFM system receives a trigger from the AFM, the measurement waveform is applied and the response acquired, with a single acquisition being referred to as an *Acquisition*. During operation of the RPFM system, the user provides the system with the number of acquisitions (i.e. number of triggers) that can be expected, and RPFM collects, processes, and stores the results in terms of these acquisitions. Thus, operation of RPFM is fundamentally based upon the measurement waveform.

3.3 Summary and Illustration

In summary, RPFM has a AFM-agnostic, trigger activated, and measurement-based scheme, which is best illustrated with a brief example. For instance, consider performing a point-by-point 10x10 grid based piezoresponse switch-

ing measurement (e.g, [146]). From the RPFM system's perspective, the user would specify a chirp, a switching measurement waveform to be overlaid the chirp, and $10 \times 10 = 100$ acquisitions. The system would then wait for 100 triggers from the AFM. Upon each trigger, the RPFM system will apply the switching measurement waveform and collect, process, and store the individual switching curves. This is all performed without any knowledge from the system about how the AFM tip is moving. Further information on RPFM is provided in the Appendix.

CHAPTER 4

DIMENSIONAL STACKING ENABLED MULTIVARIATE ASSESSMENT OF THE ELECTROMECHANICAL RELAXATION IN RELAXOR-FERROELECTRICS

This work was published in.[22]

4.1 Summary

In this work, an approach to encode meaningful chemical and physical boundary conditions in ML and DR analysis of multidimensional datasets is formally presented. While the conventional DR approach employs independent analysis of data slices, here we stack, or concatenate, the slices along appropriate dimensions (axes), before DR is applied. Physical and chemical constraints are thus implicitly imposed as correlation across parameters used for stacking of data slices. Compared to other techniques, such as averaging, the proposed approach offers a quantitative and lossless comparison of behaviors (*eigenvectors*) across measurement parameters. Its versatility and ease-of-use are demonstrated through the analysis of the electromechanical response in (1-x)PMN-xPT solid solutions as a function of electric field and composition, revealing the evolution and interplay of the mechanisms un-

derpinning the observed local functionality. A poling-like, and a relaxation-like behavior with a domain glass state are identified, and their evolution is tracked across the phase diagram. The proposed dimensional stacking technique, guided by the knowledge of the underlying physics of correlated systems, is valid for the analysis of any multidimensional dataset, opening a spectrum of possibilities for multidisciplinary use.

4.2 The Relaxation Data

The local electromechanical response of 001-cut pure relaxor PMN, near-MPB PMN-0.36PT and relaxor ferroelectric PMN-0.40PT single crystals was probed by band excitation piezoresponse force microscopy (BE-PFM) in order to investigate the evolution of the piezoresponse amplitude as a function of time, voltage, and composition across the phase diagram. A 50 x 50 grid (2500 different locations) were probed by BE-PFM for each composition over a 2 μm x 2 μm sample area. Each measurement was made with application of a pulse train of alternating polarity and increasing voltage pulses, spanning below and above the coercive voltage. The time-dependent relaxation of the electromechanical response was measured at the trailing edge of each voltage pulse. This measurement approach is illustrated in Chapter 2.

The complete experiment resulted in a five-dimensional dataset $D(t, x, y, p_v, p_c)$ of over a million individual data points, as a function of time t, the two spatial dimensions x, y describing the sampled areas, applied voltage p_v, and composition p_c. Henceforth, the two spatial dimensions are reduced to a single location identifier (i.e. $z = [x, y]$) for ease of handling. In the past, such datasets have been analyzed with conventional DR by slicing the data into voltage datasets for each composition, $D^{p_v,p_c}(t, z)$, and analyzing the two-dimensional slices independently.[41,49,133,134] Conversely, applying DR with

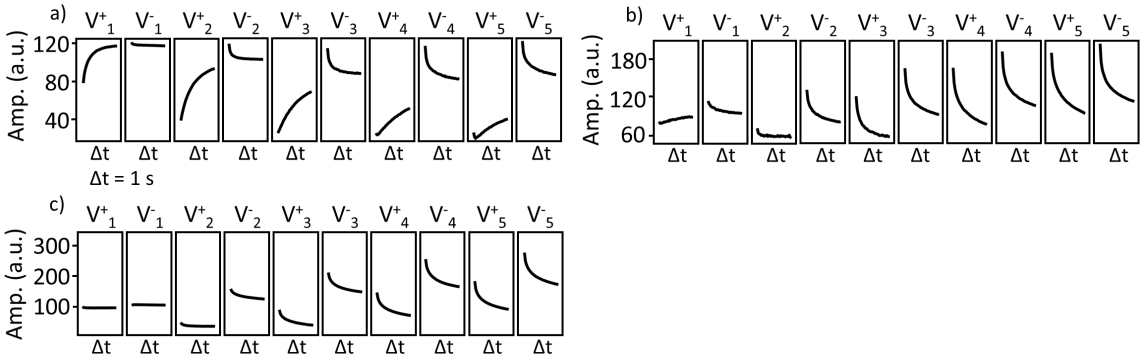

Figure 4.1: The average change in piezoresponse amplitude. The amplitude of the piezoresponse averaged across all 2500 spatial points for each voltage is shown for a) PMN b) PMN-0.36PT c) PMN-0.40PT. The response is acquired over $0.9\ s$. The total shown time lapse is for $1\ s$.

dimensional stacking concatenates the $D^{p_v,p_c}(t,z)$ slices along appropriate axes prior to DR analysis, based on physical and chemical understanding of the material. Here, we compare the resulting phenomenological insights obtained through traditional statistical analysis, the conventional DR approach, and DR with dimensional stacking.

4.3 Statistical analysis

The simplest approach to a quantitative comparison between the various compositions (p_c) and applied voltages (p_v) is to average the response $D^{p_v,p_c}(t,z)$ over the spatial dimensions, resulting in a time-dependent piezoresponse $D^{p_v,p_c,\bar{z}}(t)$ for any given voltage and composition (Figure 4.1). In PMN (Figure 4.1a), two fundamentally different behaviors are observed, correlated with the voltage polarity: for positive voltages, the piezoresponse increases over time; for negative voltages, it decays over time. Based on their

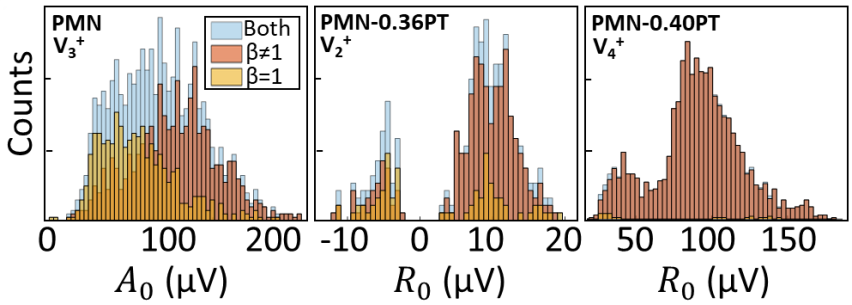

Figure 4.2: Distributions of: PMN's A_0 for the response to V_3^+, PMN-0.36PT's R_0 for the response to V_2^+, and PMN-0.40PT's R_0 for the response to V_4^+. A_0 is the piezoresponse amplitude at saturation, R_0 is the overall amplitude change over time, and β is the stretch exponential.

similarity with existing processes in ferroelectric materials, the decay and increase will henceforth be referred to as *relaxation* and *poling*, respectively.

A comparison of the averaged response across all voltages and compositions, shows that the poling behavior is observed almost exclusively in the pure relaxor end member. Such relaxation and poling behaviors in relaxor-ferroelectric systems have been previously analyzed through a stretched exponential decay, or Kohlrausch-William-Watts (KWW) function:[49,151]

$$KWW(t) = A_0 + R_0 e^{(-(t/\tau)^\beta)} \tag{4.1}$$

Where A_0 is the response at saturation, R_0 is the amplitude of the change over time, τ is the characteristic time constant, and β is the stretch exponential, describing the width of the time constant distribution. When $\beta \to 0$, the time constant distribution is the widest, and when $\beta \to 1$, the τ distribution is the tightest - with a simple exponential decay at the limit of $\beta = 1$. The KWW functional has been successfully applied to many out-of-

equilibrium systems, with an anticorrelation between the disorder and β.[152] The fitting coefficients for a KWW analysis of the averaged piezoresponse over time for each composition and voltage are reported in Figure A.1 of the Appendix. However, whilst such an approach benefits from the reduced statistical noise due to spatial averaging, it results in a loss of any spatial information and therefore possible local chemical heterogeneities.

In order to retain the spatial information, KWW fitting can be performed individually for all of the probed points for each sample, albeit with greater error margins. The distribution of select KWW coefficients, samples, and at specific applied voltages are shown in Figure 4.2. All of the distributions are show in Figures A.2-A.7 in the Appendix (Figures A.2 and A.3 plot PMN's response to positive and negative applied voltages respectively, Figures A.4 and A.5 plot PMN-0.36PT's response to positive and negative applied voltages, respectively; and Figures A.6 and A.7 plot PMN-0.40PT's response to positive and negative applied voltages, respectively). The observed bimodal distributions - e.g. in the R_0 coefficients for the V_4^+ voltage of PMN-0.40PT - highlight the presence of more than one relaxation behavior for a single voltage. The coexistence of differing contributors to the response is obviously lacking in the information provided by averaging. Furthermore, while both the averaged response and the statistical distributions identify the presence of different fundamental behaviors across compositions and voltages, they also fail to identify direct quantitative commonalities and/or any spatial

correlation. This fundamental limitation can be resolved through use of data analytics techniques and specifically dimensional reduction approaches.

4.4 Dimensional reduction

Dimensional reduction applies nonlinear statistical and algebraic methods to the input dataset D in order to extract a basis that describes it in a user-specified number, N, of *eigenvectors* (also called components), ε_i, and their associated weights (also called loading maps or mixing matrices), w_i, yielding:

$$D = \sum_{i=0}^{N} w_i \varepsilon_i + error \tag{4.2}$$

with a residual error that will depend on the dataset quality, method used, convergence criterion, and N. In the ideal case, once this decomposition has been successfully performed, ε_i will describe specific fundamental behaviors (physical and/or chemical), and their relative abundance at different spatial points over the sample areas will correspond to w_i.

As discussed, it is possible to apply the dimensional reduction methods to the four-dimensional relaxation dataset $D(t, z, p_v, p_c)$. As the probed physical quantities are time-dependent, the resulting behaviors (or components) will have to be expressed as a function of time, $\varepsilon_i(t)$. Similarly, the weights should depend on space, $w_i(z)$, enabling their representation as spatial *weight maps* for simple visual inspection of the relative contribution of the resulting behaviors to the response over the probed area. This

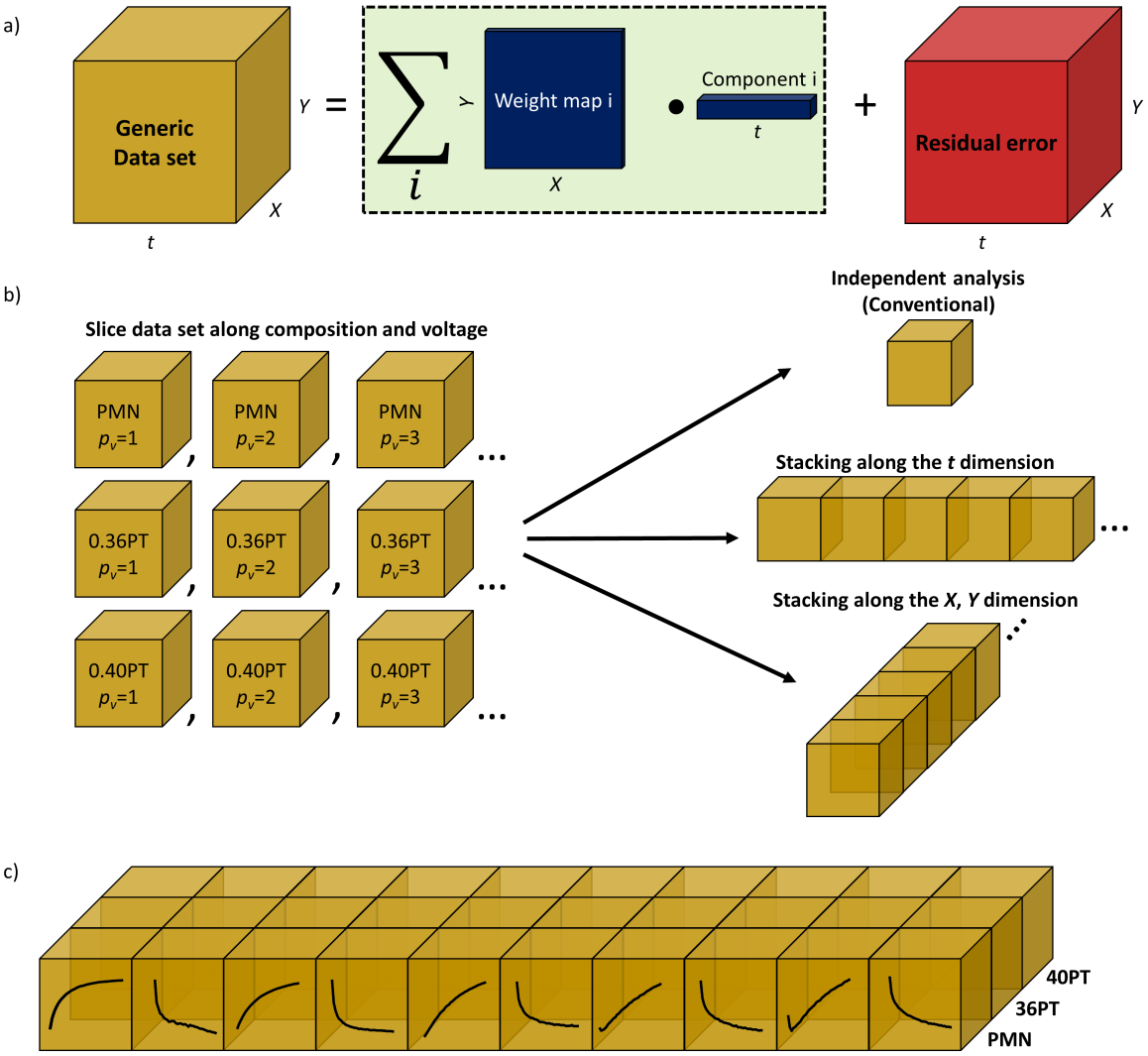

Figure 4.3: Illustrations of a) the desired outcome of dimensional reduction for a generic dataset dependent on space and time, b) the various approaches to performing dimensional reduction on the $D(t, z, p_v, p_c)$ dataset, and c) the voltage and composition dimensionally stacked data. a) In general, the goal in this work is to identify time-dependent fundamental behaviors and spatial weightings of those behaviors. This is complicated by the inclusion of additional measurement parameters, p_v and p_c. b) However, the dataset can be sliced into subsets and analyzed independently (top arrow), as is done conventionally. Alternatively, dimensional stacking can be performed along the spatial or temporal axis (middle and bottom arrows, respectively). c) Dimensional stacking can be extended to both the p_v and p_c parameters. Here the composition parameter (p_c) is spatially stacked and the voltage parameter (p_v) is temporally stacked.

is illustrated in Fig. 4.3a. Therefore, the data is divided into 2 dimensional slices of individual voltage and composition combinations to be analyzed independently, i.e:

$$D^{p_v,p_c}(t,z) = \sum_{i=0}^{N} w_i^{p_v,p_c}(z)\varepsilon_i^{p_v,p_c}(t) + error \tag{4.3}$$

Equation 4.3 expresses in its simplest form a conventional dimensional reduction approach for the acquired relaxation dataset, resulting in a total of $N \times 10p_v \times 3p_c = 30 \times N$ components with a corresponding *weight map* for each component. The conventional approach is illustrated by the top arrow in Fig. 4.3b.

For the analysis, the number of components $N = 2$, was selected to account for the bimodal behavior evidenced in the previous statistical analysis. Non-negative matrix factorization (NMF) was chosen as the specific method of dimensional reduction. This method is well suited to this work, as the component/weight pairs that it produces are strictly non-negative - reflecting the inherent additive behavior of the data, and thus enabling a clear separation of *relaxation* and *poling* behaviors.

Figure 4.4 depicts the resulting first and second components and their respective *weight maps* for all samples at a single selected applied voltage $p_v \approx 2V_c^- 3V_c^-$ (where V_c^- is the negative coercive voltage identified through initial piezoresponse force switching spectroscopy measurements for each sample), and the red lines represent the KWW fit to each curve. It

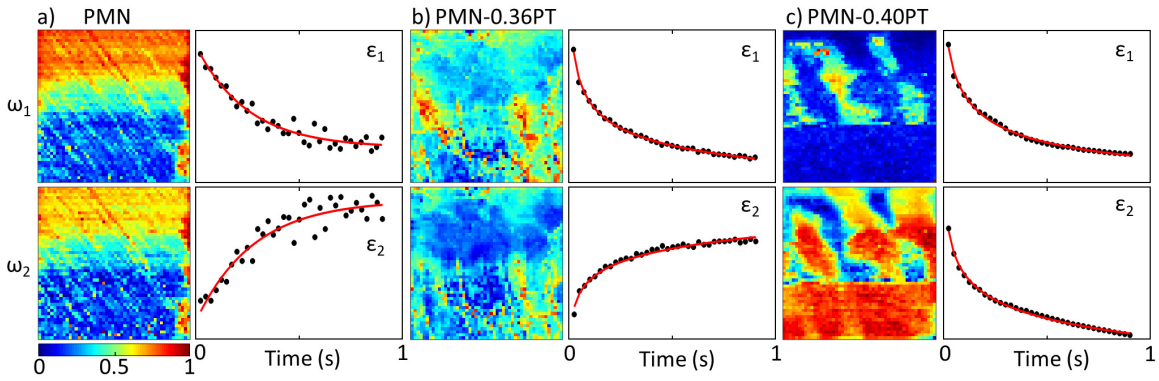

Figure 4.4: Two component conventional NMF analysis. *Eigenvectors* and *weight maps* are shown for conventional dimensional reduction, NMF for (a) PMN (b) PMN-0.36PT (c) PMN-0.40PT at an applied voltage of $\approx 2 - 3V_c^-$. The *weight maps* (ω_1 and ω_2) represent the abundance of the corresponding *eigenvectors* (ε_1 and ε_2) over the probed sample areas, i.e. the x and y directions in the *weight maps* represent the x and y directions in the sampled area. The red lines represent the KWW fit to each curve.

is worth noting that NMF identifies a co-presence of *poling* and *relaxation* behavior in the PMN sample, whereas the average response in Figure 4.2a showed only a relaxation for PMN in response to negative voltages (V_i^-). Such a behavior can either come from a discrete physical process or from over-parametrization due to the number of components N being too large. Subsequent KWW analysis was performed on each extracted component ε_i to quantitatively compare the response contributors across the compositions. The fitting parameters are reported within in Tables S1 and S2 in the Appendix A. The specific value of the time-dependent piezoresponse of the relaxor end member PMN in Figure 4.4a corresponds to simple exponential decay ($\beta = 1$) for both components. This behavior substantially changes with the addition of ferroelectric $PbTiO_3$ end-member to the solid solution. For both PMN-0.36PT and PMN-0.40PT, illustrated in Figure 4.4b and c re-

spectively, the β exponents range from 0.50 to 0.63, suggesting wide decay time distributions. It is noteworthy that such stretch exponents are characteristic of domain glasses.[153,154]

Additional inspection shows that both PMN in Figure 4.4a and PMN-0.36PT in Figure 4.4b exhibit *poling* behavior in the NMF analysis. However, each of the $30 \times N$ component-weight pairs (3 compositions, 10 voltages) is independently generated, disregarding any p_v (voltage), or p_c (composition) correlation. Therefore, even simple comparisons of results across different voltages and/or compositions is made impossible by lack of common behavior: due to the pair-wise nature of the DR (*weight map* and its corresponding component), a direct comparison between two or more ε_i is hindered by "scaling" through the corresponding ω_i. Whilst indirect comparison by proxy is possible through fitting of individual components to a physical model, this intrinsic limitation hinders more advanced analysis of correlations. In brief, conventional dimensional reduction provides a behavioral–spatial correlation lacking in traditional statistical analysis, but a method for analyzing the data as a whole is necessary for correlation across all parameters.

4.4.1 Dimensional Stacking

Quantitative comparative analysis of the entire dataset can be achieved through dimensional stacking prior to dimensional reduction. Dimensional stacking

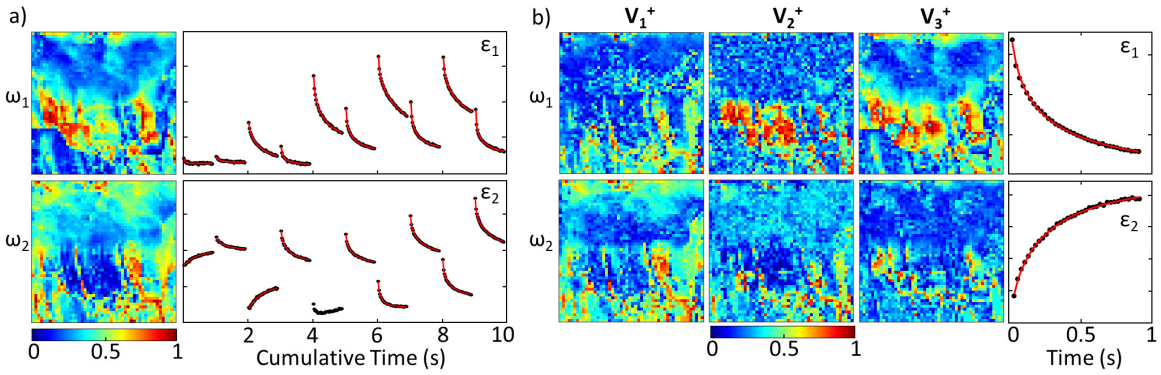

Figure 4.5: Components (ε_1 and ε_2) and *weight maps* (ω_1 and ω_2) obtained from a two component NMF analysis of PMN-0.36PT with voltage stacking along the (a) time or (b) spatial dimension, with *weight maps* representing the abundance of the corresponding components over the probed sample area. Note that in (b) only the *weight maps* for the first three positive pulses are shown. The voltage stacking results in a (a) spatial or (b) temporal correlation at the different voltages. (a) Voltage stacking along the time dimension implies that the material in a single location responds in a correlated way to the train of voltages seen over time (i.e. correlated sub- and super-coercive response). Here, the *eigenvector* components inherit the p_v dependence, thus, material response to all p_v is collectively derived as a series of concatenated behaviors. (b) Voltage stacking along the space dimension implies a single (eigenvector) underlying physical response across all the voltages, which can develop differently across the sampled area at each applied voltage. Here, the *weight maps* inherit the p_v dependence, i.e. the *eigenvectors* are voltage-independent, but a *weight map* is generated for each p_v value. The red lines represent a KWW fitting.

is performed by concatenating the $D^{p_v,p_c}(t,z)$ slices prior to analysis, as shown previously by Vasudevan et al..[49] Such data-slice concatenations can be realized if the materials is known to exhibit correlative behavior across the physical or chemical parameters involved. Here, we formally define dimensional stacking and demonstrate how the constraints are imposed and affect the subsequent interpretation of the resulting *eigenvectors* and *weight maps*.

To demonstrate the proposed method, we start by considering for an example PMN-0.36PT: the choice of a single composition translates into se-

lection of the data slice with $p_c = 2$ i.e. $D^{p_v,p_c=2}(t,z)$. The p_v slices in this dataset can be concatenated into a single dataset by stacking them along either the temporal or the spatial dimension, illustrated in the middle and bottom arrow of Fig. 4.3b, respectively. This approach inherently imposes constraints to the DR analysis: concatenation of datasets along the temporal dimension will impose a spatial constraint, and concatenation along the spatial dimension will impose a temporal correlation. For instance, let's consider concatenation of p_v slices along the time dimension (middle arrow of Fig. 4.3b):

$$D^{p_c=2}(t,z) = \begin{bmatrix} D^{p_v=1,p_c=2}(t,z) \\ D^{p_v=2,p_c=2}(t,z) \\ \cdots \\ D^{p_v=10,p_c=2}(t,z) \end{bmatrix} \tag{4.4}$$

Dimensional reduction analysis of this dataset results in the *eigenvectors* inheriting a p_v dependence. Thus, the material's response is collectively derived as a series of concatenated p_v behaviors:

$$D^{p_c=2}(t,z) = \sum_{i=0}^{N} w_i^{p_c=2}(z)\varepsilon_i^{p_c=2}(t,p_v) + error \tag{4.5}$$

Such a concatenation implies that at every location, the material responds in a correlated way to the train of voltages ($p_v = 1$ to 10) seen over time (i.e. the electromechanical response of the material is correlated at sub-

and super-coercive probing voltages). This physical correlation would seem not only possible, but indeed logical, as fundamental contributors to the observed piezoresponse (e.g. nonlinear, ferroelectric behavior, charge injection, etc.) are all expected to show specific electric field-dependent behaviors.

Figure 4.5a shows the results of the p_v dimensional stacking along the time dimension for the 2 component NMF analysis of PMN-0.36PT: the time-dependent components, ε_i, now encode the voltage dependence alongside the time evolution thereof. Component 1, ε_1 shows only *relaxation* across all voltages with an increasing baseline and amplitude. However, the second component ε_2 shows *relaxation* at negative applied voltages and higher positive voltages only, with *poling* being present at lower positive voltages. Additionally, while the first component's *relaxation* behavior tends to saturate as voltage magnitude increases (at both positive and negative polarity), the second component's response is far from saturation and grows continuously over the voltage range studied. Lastly, we note that the *weight maps* differ from those shown in Figure 4.4 for the same composition, as the results encompass spatial correlation of the behavior across all voltages.

Alternatively, we can consider a concatenation of p_v slices along the spa-

tial dimension (bottom arrow of Fig. 4.3b):

$$D^{p_c=2}(t,z) = \left[D^{p_v=1,p_c=2}(t,z) \quad D^{p_v=2,p_c=2}(t,z) \quad ... \quad D^{p_v=10,p_c=2}(t,z) \right] \tag{4.6}$$

Dimensional reduction analysis of this dataset results in the *weight maps* inheriting a p_v dependence, with *eigenvectors* in common for all p_v values:

$$D^{p_c=2}(t,z) = \sum_{i=0}^{N} w_i^{p_c=2}(z,p_v)\varepsilon_i^{p_c=2}(t) + error \tag{4.7}$$

Hence the DR analysis is constrained to consider that the response of the material to all voltages is temporally correlated. This implies that a single (*eigenvector*) physical behavior underlies across all the voltages, and can develop differently across the sampled area at each applied voltage. Here, the *weight maps* inherit the p_v dependence, i.e. the *eigenvectors* are voltage-independent, but a *weight map* is generated for each p_v value.

Figure 4.5b shows the results of the p_v dimensional stacking along the spatial dimension for the 2 component NMF analysis of PMN-0.36PT. Similar to the conventional DR approach above (Fig. 4.4), component 1 and component 2 (ε_1 and ε_2) show *relaxation* and *poling* respectively. The *weight maps* (shown for the first three positive voltages) depict an expansion of the areas with high-contributing component 1 (*relaxation*) at increasing voltage magnitude, accompanied by a contraction of the areas where com-

ponent 2 (*poling*) is contributing. Note that the ε_1 and ε_2 in Fig. 4.5 are presented with Y axis values in the Appendix Figures A.8 and A.9 in Appendix A.

In order to further identify behaviors associated with the presence of relaxor PMN and ferroelectric $PbTiO_3$ end members, it is also possible to apply dimensional stacking to the composition parameter. Specifically, in our case, composition dimensional stacking was performed along the spatial dimension in order to obtain *weight maps* with an inherited chemical composition-dependence. Such a dimensional stacking imposes a behavioral constraint across the phase diagram in the solid solution. Additionally, combining chemical composition stacking with voltage stacking along the time dimension allows us to explore the evolution of the physical processes not only as function of voltage but also across different compositions. The combined chemical and physical dimensional stacking dataset results in a single matrix (illustrated in Fig. 4.3c), with the tightest chemical and physical constraints for analysis:

$$\mathbf{D}(t,z) = \begin{bmatrix} D^{p_c=1,p_v=1}(t,z) & D^{p_c=2,p_v=1}(t,z) & D^{p_c=3,p_v=1}(t,z) \\ D^{p_c=1,p_v=2}(t,z) & D^{p_c=2,p_v=2}(t,z) & D^{p_c=3,p_v=2}(t,z) \\ \cdots & \cdots & \cdots \\ D^{p_c=1,p_v=10}(t,z) & D^{p_c=2,p_v=10}(t,z) & D^{p_c=3,p_v=10}(t,z) \end{bmatrix} \tag{4.8}$$

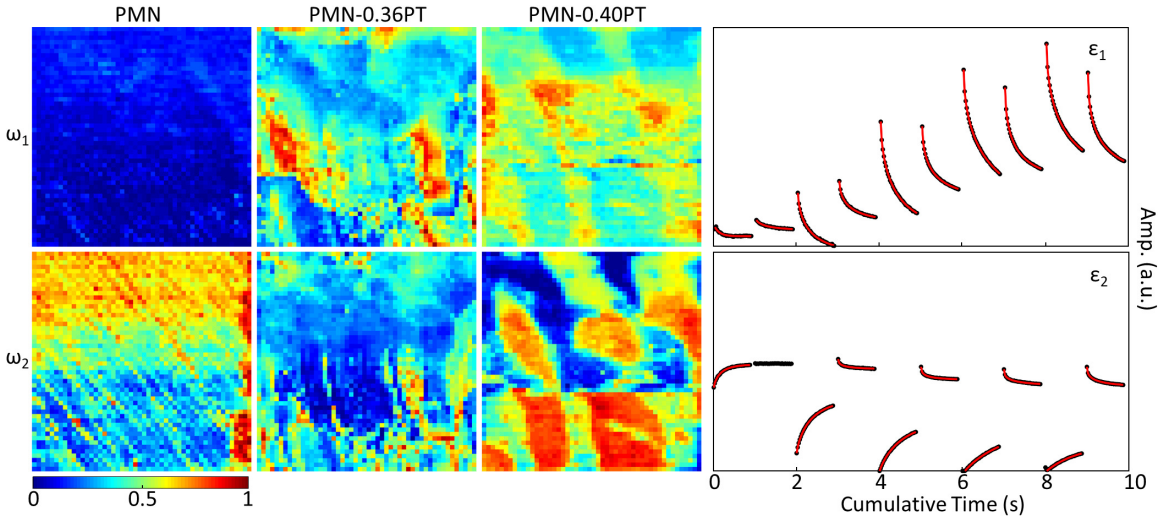

Figure 4.6: Voltage and composition dimensional stacking in NMF analysis. Components (ε_1 and ε_2) and *weight maps* (ω_1 and ω_2) are shown for a two component NMF on the voltage- and composition-dimensional stacking dataset for PMN, PMN-0.36PT, and PMN-0.40PT. The $D^{p_c,p_v}(t,z)$ slices are voltage-stacked along the time axis, resulting in the components inheriting the p_v dependence (similar to Fig. 4.5a). These slices are subsequently composition-stacked along the spatial axis, resulting in the *weight maps* inheriting the p_c dependence (similar to Fig. 4.5b). The red lines represent the KWW fitting to each curve.

Which with dimensional reduction provides:

$$D(t,z) = \sum_{i=0}^{N} w_i(z,p_c)\varepsilon_i(t,p_v) + error \tag{4.9}$$

Figure 4.6 shows the results of a two component NMF analysis of the combined voltage- and composition-dimensions stacked dataset. Component 1, ε_1, shows strong *relaxation* behavior at all voltages, somewhat tending to saturate at increasing applied voltage amplitudes. This component is notably strong in the PMN-0.36PT and PMN-0.40PT compositions and significantly absent in the pure relaxor. Conversely, the second component (ε_2), with strong *poling* at V_i^+ and weak *relaxation* at V_i^-, is observed through-

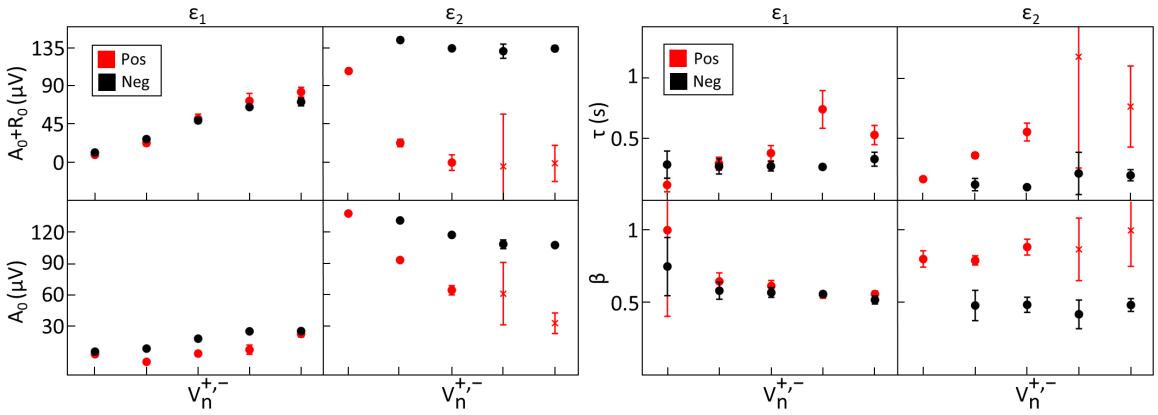

Figure 4.7: KWW functional fitting parameters for the voltage- and composition- dimensional stacking NMF *eigenvectors*. Functional parameters were extracted from the combined dimensional stacking analysis (Fig. 4.6) for both component 1 (ε_1) and component 2 (ε_2) and at each applied voltage. $A_0 + R_0$ is the total piezoresponse amplitude, A_0 is the piezoresponse amplitude at saturation, τ is the characteristic time constant, and β is the stretch exponential. The bars represent the confidence intervals

out the phase diagram, at varying intensities. Furthermore, this component is reminiscent of the averaged response of PMN shown in Figure 4.2a, in that it shows *poling* in response to positive voltages. These components are presented with Y axis values in Figure A.10 in Appendix A.

Quantitative information can also be extracted from the components by fitting the individual behaviors to the KWW functional. The resulting coefficients are plotted in Figure 4.7. For ease of fitting, the response to the highest positive voltages of the second component were considered as purely *poling*, ignoring the first three experimental data points for each curve. The error bars (representing confidence intervals) are subsequently larger for these data points, indicating a possible contribution from yet a third mechanism. The second component's response to the first negative voltage was not fitted as it showed no time dependence.

The response at saturation (A_0) and initial piezoresponse value ($A_0 + R_0$) plots confirm that the response to negative voltages in component 1 tends to saturate with increasing applied voltage amplitude. The stretch exponential β quickly approaches $\approx$0.6 in component 1 for either voltage polarity, and is approximately equal to 0.5-0.6 in response to negative voltages for the second component, showing a *relaxation* behavior. Conversely, β steadily increases with voltage amplitude from 0.75 to 1 in response to positive voltages for the second component, exhibiting a *poling* behavior.

A comparison of the different methods used to analyze the multivariate data highlights the advantages and disadvantages associated with each. Averaging and statistical distribution analysis successfully identified the presence of at least two distinct contributors, but could not directly identify these behaviors. Application of conventional DR allowed for identification of behaviors and the respective spatial mapping thereof. However, this approach could not easily provide quantitative comparisons across all the parameters, precluding correlative analysis. P_v dimensional stacking for a single composition enabled such a comparison. Stacking along the time dimension (Fig. 4.5a) generated unique voltage-correlated behaviors, while stacking along the spatial dimension tracked the evolution of shared behaviors with increasing voltage magnitudes (Fig. 4.5b). Finally, the combined voltage- and composition- stacked DR produced a quantitative correlation of piezoresponse evolution across the sampled areas, as a function of applied voltages

and probed chemical compositions.

Furthermore, regardless of the analysis method, a *poling-like* behavior was observed, most strongly correlated with the relaxor end member, PMN. Referring back to Figure 4.4, the *weight maps* for the two components (*relaxation* and *poling*) are very similar, while the actual components tend to reproduce almost symmetric local trends. Consistently with the voltage- and composition-stacked analysis shown in Figure 4.6, it is clear that only a single behavior is present in the pure PMN sample: *relaxation* in response to negative applied voltages and *poling-like* response to positive applied voltages. Hence this behavior can be considered an indisputable signature of the relaxor end member, and indeed persists even at ferroelectric addition to the solid solution. We note that these results are consistent with previous work finding that the relaxor-type behavior persists into compositions with substantial ferroelectric content, i.e. as high as PMN-0.5PT.[65]

Additionally, the dimensional stacking analysis clearly shows that two factors correlate with the appearance of a relaxation-dominated behavior: namely, introduction of the ferroelectric end member and applied field magnitude. As demonstrated in component 1 of Figure 4.6, a strong *relaxation* in the piezoresponse, reminiscent of typical ferroelectric relaxation, is observed with introduction of the ferroelectric end member. Such relaxation saturates with increasing magnitude of the applied voltage, at values well above the $V_C^{\pm}$. Furthermore, the *weight maps* in Fig. 4.5b depict an en-

hancement in the *relaxation* behavior and a decrease in the *poling* behavior when the voltage magnitude is increased.

Finally, it should be noted that *relaxations* with β values approximately equal to 0.6 have been associated with domain glasses,[153,154] or domains with glassy properties. In general, glass-like behavior is associated with complex non-equilibrium states of matter with strong disorder.[155] However, the disorder is often associated with lack of structural organization. In comparison, here glassy behavior is observed in bulk single crystals, where the disorder is observed for the functional (i.e. physical) response of the material, as a direct result of local chemical and polar heterogeneities. In fact, the glassy domain behavior is persistently observed when a ferroelectric solid solution is created with the relaxor end member. Although glassy behavior, i.e. dipolar- and spin-glass behavior, have been reported extensively in literature for relaxor materials, such reports have been limited to either pure relaxor (e.g., PMN) or relaxor-ferroelectric solid solutions with small ferroelectric content.[156] Here, the dimensional stacking analytic techniques highlight specifically that the domain glass behavior can be observed throughout the phase diagram, again consistent with Bokov and Ye.[65] Further, this domain glass behavior is a strong signature of the relaxor-ferroelectric solid solution as well as perceivably of the very large enhancement in electromechanical response observed in these materials.

In summary, a method for applying physical and chemical constraints

to machine learning techniques is presented. Through informed use of dimensional stacking, meaningful chemical and physical characteristics from multidimensional datasets can be extracted. Thanks to its intrinsically correlative nature, this method outperforms conventional dimensional reduction and statistical techniques that are limited by information loss or lack direct comparability.

To demonstrate the dimensional stacking approach, it was used for nanoscale investigations of electromechanical relaxation of (1-x)PMN-xPT relaxor-ferroelectrics across the phase diagram (x=0,0.36,0.4). Specifically, simple statistical analysis, conventional dimensional reduction, and finally dimensional stacking techniques were leveraged to identify the multiple contributors to the observed electromechanical response at different ferroelectric end member contents. All approaches identified both poling and relaxation contributors to the response, at least in some compositions. However, only the dimensional stacking technique enables a direct and quantitative comparison of the evolution of the different contributors across the phase diagram. Specifically, a *poling* behavior - signature of the presence of a relaxor component - is observed in all compositions. Additionally, the existence of a domain glass state is also identified in all the compositions containing also the ferroelectric end member.

The dimensional stacking technique is generically valid for the correlated analysis of any multidimensional dataset, in a wide range of fields. It should

prove of particular interest for the analysis of the functional response of all materials of complex compositions, as well as design of new functional materials.

CHAPTER 5

ADDRESSING ELECTROMECHANICAL SWITCHING IN FERROELECTRIC THIN FILMS WITH BETTER, FASTER, AND LESS BIASED MACHINE LEARNING

5.1 Summary

In this work, it is demonstrated that the interpretability of machine learning results in materials science, and specifically materials' functionalities, can be vastly improved through physical insights and careful data handling. The use of techniques such as dimensional stacking can provide the much needed physical and chemical constraints, while proper understanding of the assumptions imposed by model parameters can help avoid over-interpretation. These concepts are illustrated by application to recently reported ferroelectric switching experiments in $PbZr_{0.2}Ti_{0.8}O_3$ thin films. Through systematic analysis and introduction of physical constraints, it is argued that the behaviors present are not necessarily due to exotic mechanisms previously suggested, but rather well described by classical ferroelectric switching superimposed by non-ferroelectric phenomena, such as electrochemical deformation, electrostatic interactions, and/or charge injection.

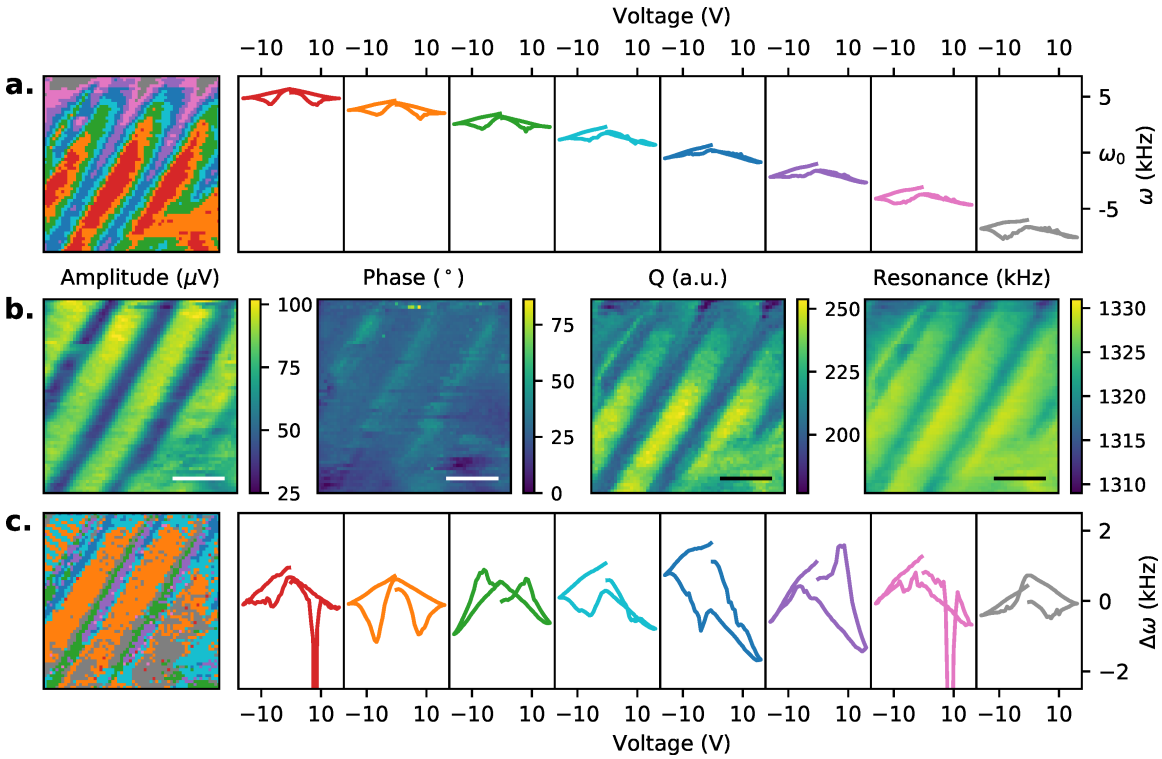

Figure 5.1: *K*-means analysis of the BE-PFM resonance frequency, ω, (a) as measured and (c) with the point-by-point mean removed, as such the y-axis represents the deviation from the mean. (b) maps of the SSPFM local mean values for amplitude (A), phase (ϕ), quality factor (Q), and resonance (ω), the micron bars represent $0.5\mu m$. In (a) and (c) the maps show the spatial locations where the correspondingly colored resonance curves occur. In part (a), ω_0 is the mean resonance value, $\omega_0 \approx 1323kHz$, for the full set of data. In part (c), components are derived for the normalized resonance curves, after removal of the local mean value, and hence shown as deviation from mean.

5.2 *K*-Means Analysis

Switching experiments probe the effects of applied DC voltage (upon its removal) on the piezoresponse and hence polarization state of the material. Given that switching events require nucleation and growth of new domains or motion of preexisting domain walls, it is expected to affect not only A and ϕ, but also ω and Q. We start with the consideration of the probed viscoelastic properties of the sample. Figure 5.1a shows the result of a sim-

ple clustering algorithm, *k*-means, applied to the cantilever resonance data for eight components. Although 8 contributions were selected, to first approximation only two unique types of behaviors are observed. The three left-most curves (red, orange, and green) all exhibit relatively symmetrical curves with softening (reduction of resonance frequency) at coercive voltages, a behavior expected of a typical ferroelectric material. The remaining components (blue, teal, purple, pink and gray) show an asymmetric behavior, with a linear and non-hysteretic branch at positive fields.

The obvious distinction between these 8 curves lies in their mean resonance values. The spatial distribution of the components in Figure 5.1a distinctly shows that the mean resonance frequency increases towards the bottom of the sampled area. By mapping the mean value at each point for A, ϕ, ω, and Q (Figure 5.1b), it becomes clear that the Q and ω gradually shift to higher values throughout the measurement, i.e. from the top left towards the bottom right of the sampled area. Such a gradual hardening (increase of resonance frequency) as the experiment progresses is often observed in samples with accumulation of (tip-)injected charges, and resulting increase in global electrostatic effects between sample surface and cantilever.[157] As the *k*-means algorithm shows substantial susceptibility to changes in the mean values, the shifts in the mean resonance value are identified as unique behaviors.

In order to account for the influence of this effect and to focus only on the

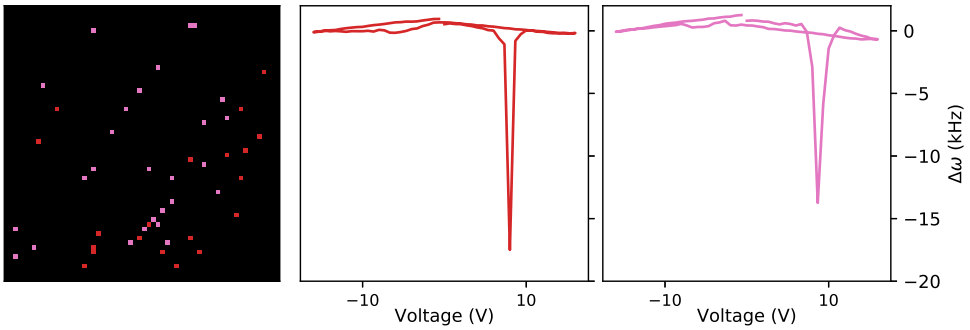

Figure 5.2: Outlier behaviors identified in Fig. 5.1 and their spatial distribution. The two contributions are identified with the corresponding color on the map of the sampled area to the right. Black pixels in the spatial map indicate absence of the two shown behaviors.

underlying materials' behaviours, the data can be *normalized* by subtracting the mean resonance at each point. This operation was also performed on the piezoresponse curves in subsequent analyses to maintain consistency. The *k*-means investigation of normalized data yields behaviors with substantially more distinct features, as shown in Figure 5.1c. Furthermore, the analysis of thus normalized data identifies the *a* and *c* domains within some of the c/a stripes (e.g., the light blue and orange bands in the top left corner), as well as relatively uniform bands corresponding to the a_1/a_2 stripes, clearly correlated with the piezoresponse amplitude, and topography.

A closer inspection of the obtained resonance components identifies two contributions with sharp softening occurring close to 10V (first and seventh components from left). Such substantial acoustic softening has been previously associated with voltage-induced phase transitions[158]. However, we note that prior reports have shown that phase-transition-induced acoustic softening, while substantial, is also expected to be symmetric with respect

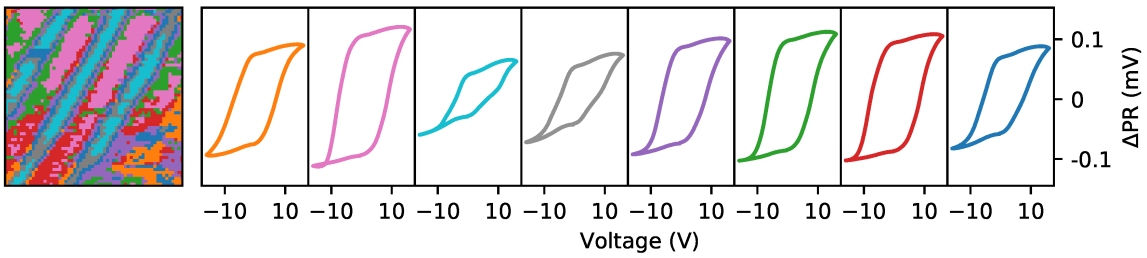

Figure 5.3: *K*-means analysis of the BE-PFM piezoresponse curves with the point-by-point mean removed, as such the y-axis represents the deviation from the mean.. The maps show the spatial locations where the correspondingly colored piezoresponse curves occur. Components are derived for the normalized piezoresponse curves, after removal of the local mean value, and hence shown as deviation from mean

to the applied voltage polarity. The spatial occurrences of these behaviors are sporadic and randomly distributed (Figure 5.2) such presence strongly suggests that these behaviors correspond to outliers, possibly due to local measurement errors and/or compromised tip-sample contact. The large variation in the resonance frequency in these curves (a variation 5 times greater than all other behaviors) and the irregular and isolated appearance of these points (spatial occurrence of less than 2%) supports their removal from consideration in the forthcoming analysis. Hereafter, these points will be shown as white pixels in all spatial maps. The *k*-means analysis as presented in Figure 5.1c was also performed for the piezoresponse and is shown in Figure 5.3. However, no notable outlier or non-ferroelectric trends are apparent in the piezoresponse analysis.

Ultimately, while the *k*-means approach successfully and quickly identifies possible systematic issues within the dataset, it is weak in terms of physical insight for two main reasons. Firstly, *k*-means is “infinitely sparse”,

meaning that each point can only exhibit a single behavior, eliminating the possibility of a superposition of contributors. Such a superposition might be expected at or near the boundaries of the two distinct ferroelectric polarization bands, where the probed volume would included both c/a and a_1/a_2 domains, as well as additional contributions to the ferroelectric polarization reversal. Secondly, performing *k*-means clustering on the resonance parameter alone ignores three quarters of the available data and does not provide direct information on the polarization state, or piezoresponse of the sample. Both of these challenges can be overcome through the use of dimensional reduction techniques supplemented with dimensional stacking. Here Dictionary Learning was chosen as the preferred DR approach, given the available control over the sparsity of the derived results.

5.3 Dictionary Learning analysis

Dictionary Learning (DL), as all other DR techniques, seeks to represent a given dataset (D) as a series of eigenvector-eigenvalue pairs. Mathematically, for a single parameter of the described dataset ($D^p(z,v)$), where $p = [A, \phi, \omega, Q]$), N separate components are derived, with eigenvectors $V(v)$, and corresponding eigenvalues, $U(z)$, by minimizing Equation 5.1.

$$(U(z), V(v)) = \frac{1}{2} \left\| D^p(z,v) - U(z)V(v) \right\|_2^2 + \alpha \left\| U(z) \right\|_1 \tag{5.1}$$

where $\|D^p(z,v) - U(z)V(v)\|_2^2$ represents the norm-squared error, and $\|U(z)\|_1$ imposes a preference towards sparse results. The relative importance between sparsity and model error can be adjusted with the user specified parameter α, which defaults to 1. Thus, Dictionary Learning allows for the identification of linearly superimposed behaviors, as might be found near the domain walls, but also contains a preference towards sparse behaviors, which might be expected in the bulk of a single domain, where a single behavior is expected to occur. Applied to this specific case, the eigenvectors are derived as a function of voltage (v) and the eigenvalues are derived as a function of space ($z = [x, y]$): hence, eigenvectors can potentially represent contributors to the switching behaviors, while eigenvalues are effective weight *maps* representing the spatial distributions of the identified contributors. In order to impart additional physical constraints, dimensional stacking is used to concatenate the piezoresponse and contact resonance data prior to the DL analysis.[22] Such concatenation implies a fundamental correlation between the electromechanical response (as probed by the piezoresponse, *PR*, which combines *A* and ϕ information), and the elastic properties of the material (as tracked by the cantilever-tip resonance) to the applied waveform, as discussed above. We note that the piezoresponse data were also processed by mean removal from each PR curve, and subsequently scaled by a constant factor such that the resulting PR dataset has a variance comparable to that of the resonance curves (for details see Appendix B).

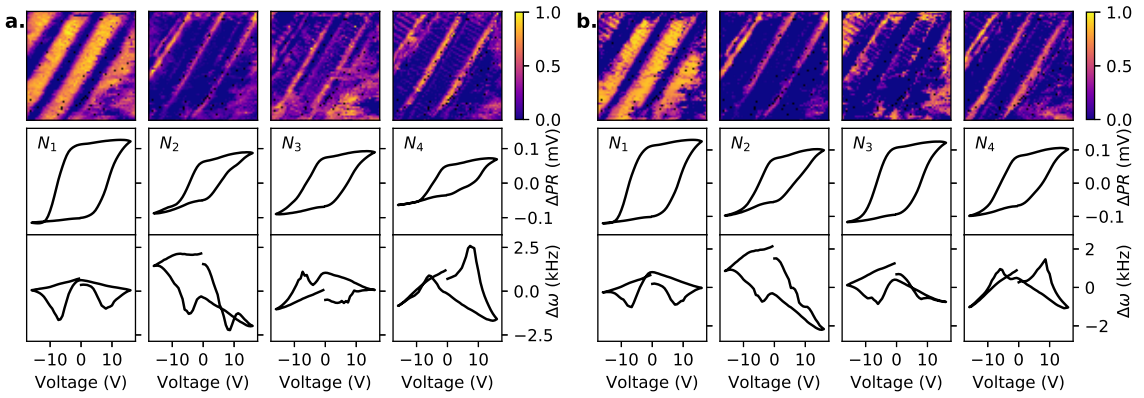

Figure 5.4: Stacked mean-subtracted piezoresponse and resonance ($PR - \omega$) Dictionary Learning analysis with $N = 4$ components and α of (a) 1 and (b) 12. At each spatial point, the observed piezoresponse and resonance behavior can be approximated as a linear superposition of the spatial weight maps (top row) and their corresponding derived behaviors (two bottom rows). Here, the middle row is the piezoresponse (PR) and the bottom row is the corresponding resonance (ω).

Proper application of Dictionary Learning requires an informed selection of two parameters: *N*, corresponding to the number of eigenvectors or contributing behaviors, and α, the sparsity parameter regulating how much overlap across behaviors is allowed at each point. Typically such parameters are either left at their default values, or chosen to be "physically reasonable". Here, for instance, scientific intuition would suggest N to be set to at least 4, as this would be the minimum number of unique contributions: c domains, *a* domains within the *c/a* and within the a_1/a_2 stripes, and any additional contributions from domain walls, boundaries between stripes, or non-ferroelectric phenomena, etc. The choice of $N = 4$ and the $\alpha = 1$ (default value) results in Figure 5.4a: the obtained (spatial) weight maps highlight either the c/a domain stripes or the a_1/a_2 stripes. Additionally, bands corresponding to *a* domains within the c/a stripes are visible

in at least one map, enabling a possible physical interpretation of the DL analysis. However, increasing α by approximately a factor of 10 forces a substantial decrease in allowed spatial overlap of different behaviors and, as shown in Figure 5.4b, results in the distinction between *a* and *c* domain within the c/a stripes to become even stronger. Moreover, the corresponding piezoresponse hysteresis and resonance curves undergo visible and at times substantial changes. Clearly, modifying the amount of allowed overlap among contributions through α yields different results with a separate physical interpretation. Conventionally, the decision on the choice of different parameters has been made with physical insights and expectations in mind, so as to yield the most "physically reasonable" result. However, this approach unavoidably introduces biases and preconceptions, and additional care and model performance metrics should be taken into account when choosing parameters.

5.3.1 Parameter Selection via Error Analysis

One such metric for measuring model performance is the root mean square (RMS) of the residuals or RMS error (see Appendix B). Figure 5.5a shows the spatial mean of the RMS error for *N* ranging from 2 to 9 components, and α values of 1, 6, and 12. Naturally, error decreases with increasing number of components, due to the enhanced model flexibility, and error increases with α, due to a decreased emphasis on model error (first term in

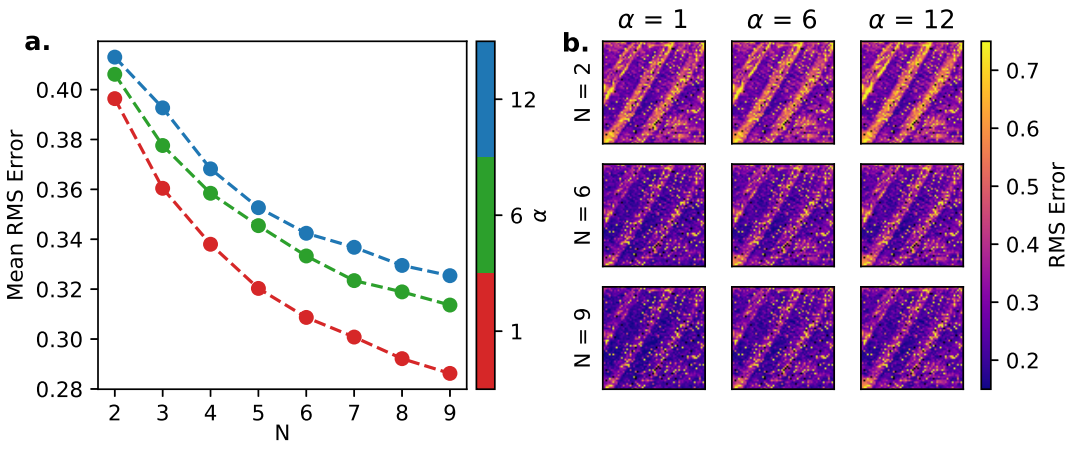

Figure 5.5: Root mean squared (RMS) error of a Dictionary Learning analysis of stacked mean-subtracted $PR - \omega$, based on 24 different $N - \alpha$ pairs. The different analyses consider a range of number of eigenvectors ($N = 2$ to 9) and α (1, 6, or 12). (a) The spatially-averaged RMS error for each combination of N and α is shown in parametric curves similar to scree plots. (b) The spatial distribution of the RMS error for $N = 2, 6, 9$ components and $\alpha = 1, 6, 12$ (i.e. increasing sparsity) is shown in order to evaluate specific locations where parameter choice might result in increased error in the obtained results.

Equation 1). However, these metrics alone offer limited information on the over-fitting that can occur when N is too large. In order to minimize over-fitting, the qualitative scree test recommends selecting N to be at or close to where saturation in error improvement begins (i.e. the "elbow"), which in Figure 5.5a is estimated to be between 5 and 7 components. To further assess proper selection of $N - \alpha$ pairs, the spatial distribution of the RMS error for $N = 2$, $N = 6$, and $N = 9$ and $\alpha = 1, 6, 12$ is plotted in Figure 5.5b. Substantial improvements in error are seen when N is increased from 2 to 6, but little to no change occurs when N is increased further. Thus, Figure 5.5a would suggest $\approx 5 - 7$ as an ideal range for choice of the number of contributing eigenvectors, consistently with the RMS error's spatial distribution in Figure 5.5b. Additionally, increase in α does not largely affect

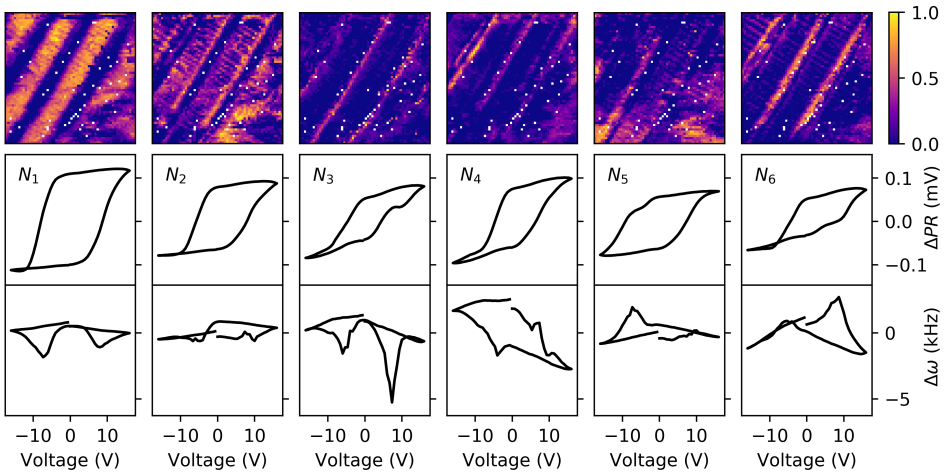

Figure 5.6: Dictionary Learning of stacked, mean-subtracted $PR - \omega$ with $\alpha = 1$ and $N = 6$. At each spatial point, the observed piezoresponse and resonance behavior can be approximated as a linear superposition of the spatial weight maps (top row) with their corresponding derived behaviors (bottom two rows). Here, the middle row shows the piezoresponse (PR) and the bottom row the corresponding resonance (ω).

the error. Hence for the below analysis, $N = 6$ was chosen as the center of the ideal range for N, and $\alpha = 1$ was selected to minimize the RMS error.

5.3.2 Dictionary Learning Results: $N = 6$ and $\alpha = 1$

Figure 5.6 shows the output of the Dictionary Learning analysis on the stacked *PR* and ω curves with $\alpha = 1$ and $N = 6$. A *k*-means analysis of the data was used to initialize Dictionary Learning, essentially providing an initial guess for the optimizer. All analyses (including the *k*-means seed, and the stacked DL) were completed within 1 to 2 hours on a commercially available ASUS laptop with an 8$^{\text{th}}$ Generation Intel Core i5 8250U 1.6GHz processor and 16Gb RAM. This can be contrasted with a typical NN analysis,[145] which needs substantially more computational power and an order of

magnitude more time to yield physically interpretable results.

The interpretation of the resulting components is as follows:

Components N_1 and N_2: Typical Ferroelectric Switching in c/a Stripes:

The first two components (N_1 and N_2) are most strongly present in the c/a stripes and their piezoresponse can be associated with a typical ferroelectric hysteresis curve. Additionally, the first component's resonance frequency exhibits softening associated with polarization switching at each coercive voltage. The second component also exhibits general resonance softening in the vicinity of coercive voltages, however, small superimposed hardening steps are also visible. From the initial amplitude scans (Figure B.1), the *c*-domains within the *c/a* stripes can be roughly identified (Figure 5.7, the identification process is discussed in Figure B.2) and compared to the maps in Figure 5.6. Through a comparison of Figures 5.6 and 5.7, it becomes evident that the first component is mostly associated with the *c*-domains, and thus represents typical 180° switching. Similarly the second component is most strongly associated with *a* domains within the c/a-stripes.

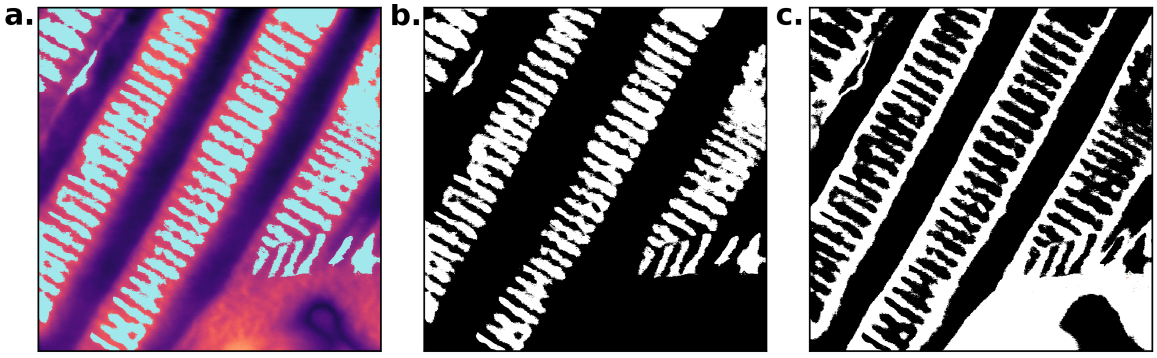

Figure 5.7: (a) The BE piezoresponse amplitude performed after the switching characterization where the blue-gray lines highlight the *c*-domains with the *c/a* stripe. The mean of each horizontal line was removed for clarity, to adjust for a slight reduction of the amplitude from the top left to the bottom right of the sampled area. This shift in amplitude is visible in Fig. B.1b. (b) part (a) in black and white, where the white corresponds to the *c*-domains within the *c/a* domain stripe. (c) the inverse of (b), i.e. the *a*-domains highlighted in white.

Component N_3: Ferroelastic-Mediated or Mechanically Constrained Behavior:

In the third component (N_3), the piezoresponse curve has a significant "notch" (at positive increasing voltages), a behavior previously assigned to charged domain walls[145] and/or ferroelastic-mediated ferroelectric switching.[144] Additionally, the PR hysteresis curve shows a significant decrease in retention from saturation to remnant values, possibly indicating a large degree of back-switching. We note that this component occurs largely in the "valleys" of the sawtooth topography (see Figure B.3 and B.4) and, thus, such back-switching could be due to increased mechanical constraints from the surrounding material. It should be noted that neither the presence of charged domains nor mechanical constraints are completely physically compatible with the substantial softening observed in ω. However, this softening is

consistent with previous reports of ferroelastic switching.[159]

Components N_5 and N_6: Electrostatic and/or Electrochemical Phenomena

The fifth and the sixth components (N_5 and N_6) show tilted piezoresponse loops, with asymmetric resonance curves. Specifically, in each component, a significant hardening is observed near one or the other coercive voltage, with near-linear behavior in response to the other applied voltage polarity. To address these components, the SSPFM characterization performed on the PZT thin film was replicated on a $\approx$ 1-mm thick soda-lime glass slide (Fig. 5.8). The mean resonance curve of Fig. 5.8a indicates that the non-ferroelectric behavior present in this sample consistently exhibits hardening when approaching 10 volts. As this glass sample could exhibit either charge injection or electrochemical deformation a specific non-ferroelectric behavior cannot be attributed with certainty. However, it is reasonable to assert that N_5 and N_6 identify contributions from either charge injection or electrochemical deformation, as: 1) N_5 and N_6 exhibit similar hardening to glass and 2) N_5 and N_6 exhibit piezoresponse behavior consistent with previous reports on these non-ferroelectric phenomena.[160,161,162] Lastly, in the spatial map of the mean resonance shown in Fig. 5.8b, the bottom exhibits slightly higher frequencies than the top. This gradual hardening is consistent with the non-ferroelectric phenomena seen in Fig. 5.1.

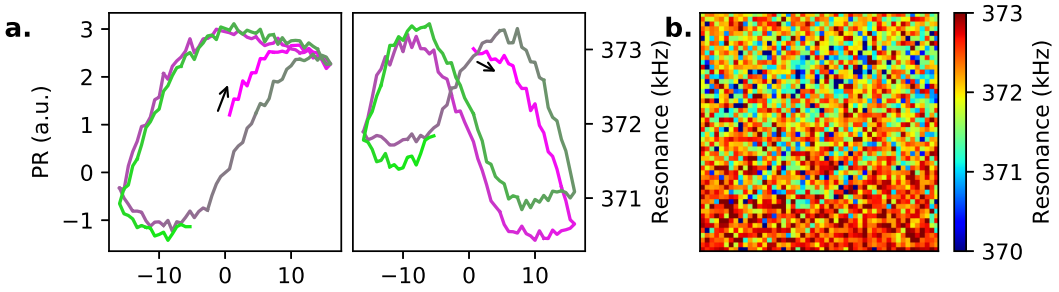

Figure 5.8: The piezoresponse and resonance frequency acquired on a $\approx$ 1-mm thick glass slide, through the same SSPFM experimental protocol as described in the main text. The probing area was 2 μm by 2 μm, with 3600 points probed on a 60x60 grid. Two cycles of a bi-polar triangular waveform similar to that reported for the PZT thin films were applied to the the sample. a) The spatial average of the resulting piezoresponse and resonance curves for both cycles. The pink to green color scaling indicates the progression from beginning (pink) to the end (green). The arrow indicates the direction of progression after the first acquisition point. b) The mean resonance value mapped over the sampled area, at each point of the 60x60 grid.

5.3.3 Component N_4: Various Non-Ferroelectric Phenomena

The fourth component (N_4) shows an asymmetric PR hysteresis curve and an even more asymmetric resonance loop. A comparison with the raw data (Figure B.5 and B.6) clearly indicates the presence of similar looking resonance and PR curves with considerably reduced amplitude compared to adjacent locations. We note that the resonance frequencies at positive voltages in N_4 could be well-described by the non-ferroelectric phenomena, similar to that seen in glass (Figure 5.8) superimposed with a small amount of ferroelectric softening at coercive values. The asymmetric response at negative voltages is tentatively assigned to Schottky barrier[163] formation between tip and sample surface in addition to possible conductive phenomena.[160] The piezoresponse curve can similarly be well-described by a superposition of

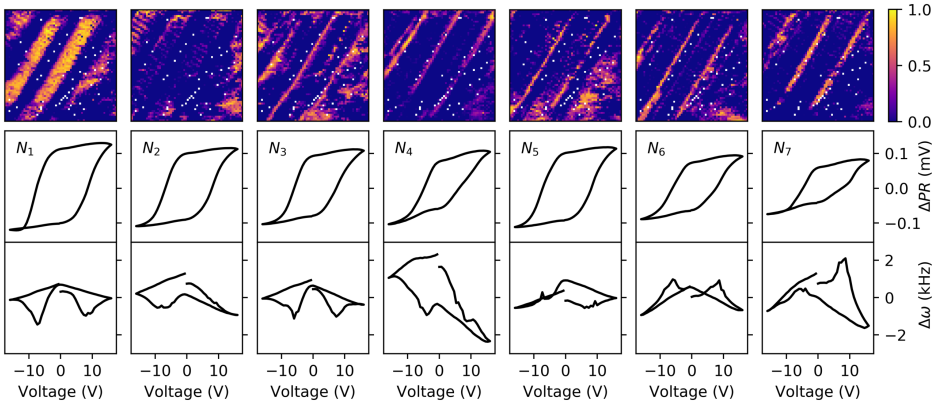

Figure 5.9: Dictionary Learning of stacked mean-subtracted $PR - \omega$ for $\alpha = 12$ and $N = 7$. The middle row is the PR and the bottom row is the corresponding ω.

different conduction-like, non-ferroelectric behaviors.[161] Further discussion of ferroelectric and non-ferroelectric contributions is provided in the Appendix B section "Review of Physical Contributors to the Switching PFM Response". Finally, we note a sizable influence of topography, which is discussed in Figures B.5 and B.6.

5.3.4 Dictionary Learning Results: $N = 7$ and $\alpha = 12$

While many of the obtained components from the above analysis can be attributed to physical phenomena, the choice of DL parameters can drastically affect the interpretation. As the model error will only slightly increase with increasing α and noting that the ideal N was found to be within a range from 5 to 7, further insight can be gained by considering additional analyses with varying α and N. The stacked Dictionary Learning analyses for all of the considered parameter pairs ($N = 5, 6, 7$ and $\alpha = 1, 6, 12$) are reported

in Figure B.7 to B.15. The stacked DL analysis for the highest values of these parameters, $N = 7$ and $\alpha = 12$, is shown in Figure 5.9.

Components N_1, N_4, and N_7 in Figure 5.9 are very similar to components N_1, N_4, and N_6 observed for $N = 6$ and $\alpha = 1$ analysis (Figure 5.6). In contrast, the new component N_3 (in Figure 5.9 and also in Figure B.11 and B.12) is significantly more consistent with polarization switching: the previously observed "notch" in the piezoresponse curve (Figure 5.6) is now absent, and the softening in the resonance frequency at coercive voltage is symmetric with respect to polarity and similar to those seen for component N_1. In fact, a detailed review of the raw data (Figure B.5 and B.6) reveals that the *PR* "notch" is observed when the evaluation of piezoresponse is largely stunted near the coercive voltages. Specifically, at the very low values of piezoresponse, correct evaluation of the functional parameters is often difficult and hence the missing data has been removed and/or interpolated in the original dataset (Figure B.5 and B.6). Additionally, the new components N_2, N_5, and N_6 in Figure 5.9 show substantial changes with respect to the analysis with lower component count and sparsity. Component N_6 shows a symmetric hardening in proximity of the coercive voltages. Such a behavior is consistent with both a non-ferroelectric hardening, as well as with ferroelectric switching with large mechanical constraints. The behaviors associated with components N_2 and N_5 are spatially complementary, and are located within the c/a stripes. For these components,

the PR curves show typical hysteresis behavior. However, the resonance curves show an asymmetry with respect to the applied voltage polarity, and the weight maps are associated with complementary spatial distributions across the c/a stripes. Specifically, the resonance frequencies show softening at negative applied voltages for N_2, and at positive voltages for N_5. The opposite polarity branch for each curve shows an almost linear behavior, indicative of limited hysteretic behavior or over-fitting.

Overall, by considering Figure 5.6, 5.9, and the other analyses (Figure B.7 to B.15) as a whole, a few overarching conclusions can be drawn. Firstly, the observed changes in components across analysis parameters suggest that some behaviors might have higher sparsity than others. Secondly, the chosen algorithm or parameters are seldom able to highlight *all* of the appropriate physical phenomena while optimizing model parameters (N and α). These observations emphasize the necessity to consider as many variations of model parameters as possible, while remaining cognizant of the limitations imposed by quantitative metrics such as RMS error. Additionally, across all of the various analyses considered here, the results are often well-explained by polarization switching, superimposed with non-ferroelectric phenomena. Specifically, *c* domain switching shows consistently recognizable features for *PR* curves, accompanied by resonance curves with substantial softening at coercive voltages. Polarization switching and piezoresponse in *a* domains is substantially suppressed, particu-

larly in depressed locations in topography. Such suppressed switching is easily justified by the large lateral constraints exercised by the "inert" volume of material surrounding these locations, specifically in consideration of the large deformations associated with ferroelastic (compared to pure ferroelectric) switching. Lastly, additional contributions from instrumentation and non-ferroelectric phenomena were consistently observed. The presence of such contributions in PFM characterizations remains a growing concern for the scientific community.[164,165,166] However, it is evident that use of dimensionally stacked datasets for DR approaches is a viable approach for identification of such phenomena, enabling reduced misinterpretation of the obtained information.

5.4 Conclusions

In summary, we reported on the physical interpretability challenges of Machine Learning techniques, illustrated through the analysis of recently reported ferroelectric switching experiments in $PbZr_{0.2}Ti_{0.8}O_3$ thin films. Firstly, the quality of obtained results corresponds directly to the quality of the dataset, as highlighted by the presence of non-ferroelectric phenomena (instrumentation related or otherwise) resulting in shifts in the mean values capable of dominating any ML analysis. Secondly, slight changes in Dimensional Reduction model parameters lead to distinct changes in obtained outputs, highlighting the need for a systematic choice of these

parameters, as well as their explicit disclosure in literature reports. Any user-based,"physically reasonable" choice of results are inherently subject to bias, possibly leading to "discovery" of nonphysical behaviors. As a possible solution to these challenges, we advocate for a careful and critical approach to the use of Machine Learning techniques, including through considering available model performance metrics, maintaining a healthy suspicion of the results, continually referring to our physical understanding in interpretation, and consideration of all thus-selected possible outcomes.

In conclusion, through the application of a careful and systematic approach to data selection and processing augmented with increased constraints provided by dimensional stacking, we have demonstrated that much of the complexity in the behavior of the previously reported polarization switching in PZT thin films can be unraveled. Specifically, classical polarization switching (augmented by locally-imposed mechanical constraints), and non-ferroelectric phenomena are sufficient to explain the observed results.

CHAPTER 6

EFFECTS OF DOMAIN WALL PROXIMITY ON POLARIZATION SWITCHING IN RELAXOR-FERROELECTRIC SINGLE CRYSTALS

6.1 Summary

In this work, the influence of proximity to *pre-existing* domain walls on the local piezoresponse in a relaxor-ferroelectric solid solution is considered. Specifically, switching behavior in a 001-cut tetragonal $0.60Pb(Mg_{1/3}Nb_{2/3})O_3-0.40PbTiO_3$ (0.60PMN-0.40PT) single crystal is investigated through use of resonant piezoresponse force microscopy (R-PFM, as described in Chapter 2). It was found that proximity to domain walls has limited impact on the piezoresponse and the switching thereof in this material. While the switching dimensionality changes from two to three at increasing distance from a domain wall, the switching voltage is only slightly increased (by $\approx 25\%$ at up to $\approx 300nm$ away). The results are in sharp contrast to non-relaxor based compositions (i.e. $LiNbO_3$[21]), where similar changes in distance from a domain wall can result in three to four times increase in the nucleation voltage.

6.2 Initial Images

The initial piezoresponse amplitude, phase, contact resonance (ω), and quality factor (Q) of a 10 μm x 10 μm probed area is shown in Figure 6.1a (further images taken after the switching experiment are shown in Figure C.1). Switching PFM response was recorded for an applied triangular electric voltage waveform, as described in Methods. The 10 μm x 10 μm area was probed with a negative voltages first waveform.

6.3 Machine Learning-based Analysis

One of the most immediate methods to identify domain wall proximity effects on the switching response is application of a clustering algorithm to the switching PFM data. As seen in Chapter 5, clustering approaches can also be used for identification of possible outliers - i.e., localized or extended areas of prevalent non-ferroelectric behavior, due to surface sample preparation or tip-sample contact issues - and eventual systematic changes introduced by the measurement. Here, a *k*-means clustering analysis is performed on stacked piezoresponse and contact resonance,[22] similar to the analysis performed in Chapter 5. In order to minimize user bias, the analysis was performed for an arbitrarily large number of components (N=*8*), as shown in 6.1b. This analysis is further discussed in Figure C.4.

Component N_8 is a low signal-to-noise ratio behavior, with limited hys-

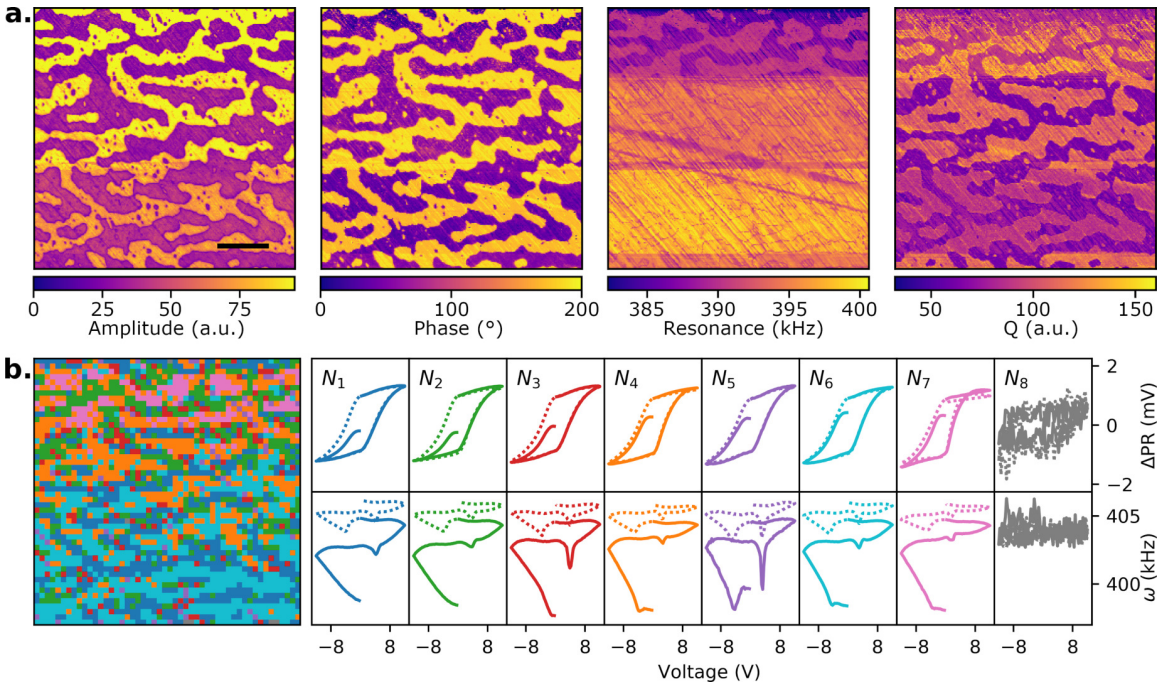

Figure 6.1: Initial PFM scan images (a) and k-means analysis of the switching piezoresponse analysis of a 10 μm x 10 μm area. a) From left to right, the initial piezoresponse amplitude (A), phase (ϕ), contact resonance (ω), and quality factor (Q) of the area. The micron bar represents $2\mu m$. b) Stacked piezoresponse and resonance k-means analysis with $N = 8$ clusters applied to the 10 μm x 10 μm SSPFM data. At each spatial point shown in the map, the piezoresponse and resonance are given by the corresponding colored component. Here, the upper row is the deviation of the piezoresponse from the mean (ΔPR) and the bottom row is the corresponding resonance (ω). The solid lines represent the results from the first cycle and the dotted lines the second cycle of a two-cycle measurement.

teresis and saturation. Furthermore, it is only observed in 5 points. These features suggest that N_8 is due to localized data acquisition challenges and possibly poor tip to surface contact. Data corresponding to this component is therefore removed from all subsequent analysis. The other components (N_1 to N_7) exhibit typical ferroelectric behavior, i.e. "classic" hysteresis curves in the piezoresponse, and resonance curves indicating softening around the coercive voltages. Components N_3 and N_5 exhibit somewhat stronger contact resonance softening at coercive voltages, and appear to be

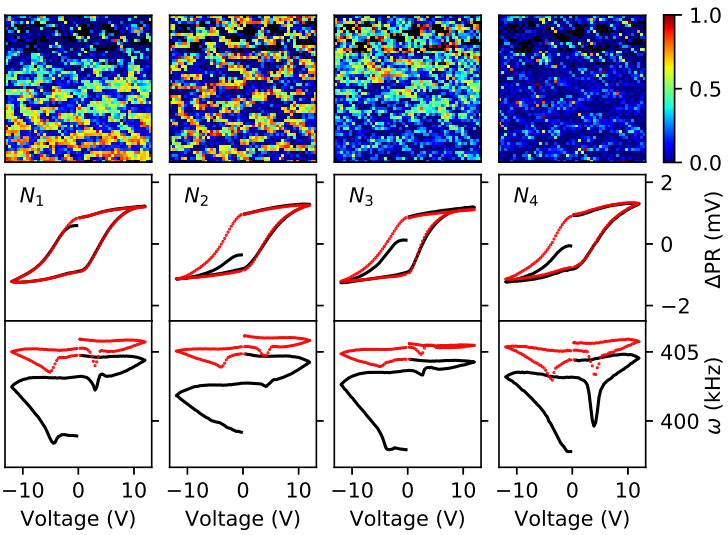

Figure 6.2: Stacked piezoresponse and resonance dictionary learning analysis with four components ($N = 4$) and default sparsity ($\alpha = 1$) for the 10 μm x 10 μm switching PFM data. At each spatial point, the piezoresponse and contact resonance can be approximated as a linear superposition of the spatial weight maps (top row) with their corresponding derived behaviors (bottom two rows). Here, the middle row is the change in the piezoresponse with respect to the global mean (ΔPR) and the bottom row is the corresponding contact resonance frequency (ω). The response to the first applied cycle is shown in continuous black lines, and to the second cycle in red dotted lines.

often localized in proximity of domain walls and at surface protrusions. However, deriving further physical information with respect to the domain wall proximity from Figure 6.1 is challenging, given that the observed behavior is not present at all domain walls.

The interpretability of the results is likely hindered by the nature of the *K*-means clustering approach where unique behaviors are assigned to each point, without any possibility for superposition. However, while sparse behaviors might be expected in the bulk of a domain, superimposed behaviors could exist at points near a domain wall (with contributions from the do-

main wall and the adjacent domains). Hence, we next use dimensionality reduction, which allows for a superposition of behaviors. In order to accommodate sparse as well as superimposed contributors, we chose Dictionary Learning as the dimensionality reduction method. For discussion of model parameter selection and additional information with respect to the sets of analyses performed, refer to Appendix C.

Figure 6.2 shows representative results for the piezoresponse and resonance stacked dictionary learning analysis with four components ($N = 4$) and default sparsity ($\alpha = 1$). The spatial maps of N_1 and N_2 appear to highlight two different domain polarities, with N_1 mostly absent at the top of the sampled area. The first quarter cycle ($V = 0$ to $-10V$) of N_1 sees a change in the sign of piezoresponse with a local softening in the contact resonance at zero *PR*, i.e. polarization switching at coercive voltage. Conversely, the piezoresponse during the same quarter cycle in N_2 does not show switching in sign, nor contact resonance softening. Thus, N_1 and N_2 highlight the *down*-polarized (switching) and the *up*-polarized (non-switching) domains, respectively. Beyond the first quarter cycle, N_1 and N_2 show similar behavior in the piezoresponse curves.

Component N_3 shows an intermediate behavior compared to N_1 and N_2, with weak switching in the first quarter cycle. Additionally, N_3's spatial distribution is more closely mapped to the *down-polarized* domains, and somewhat complimentary to the N_1's spatial distribution. The contact res-

onance softening at positive voltages is followed by slight hardening, consistent with superposition of ferroelectric switching with charge injection and/or electrochemical effects.[148,163] Finally, N_4 is mildly present in the *up*-polarized domains, with sporadically larger contributions at points that often match the topological protuberances on the surface (Figure C.3) and/or locations with higher density of domain walls. The comparatively large resonance softenings observed in this component are consistent with the reduced lateral constraint exercised by (inactive) surrounding material and/or ferroelastic switching.[159,158] However, the correlation between this component and the domain walls is not strict.

Thus, neither *k*-means nor Dictionary Learning analysis identify specific contributions or behaviors associated with domain walls. The lack of identification of a "domain wall proximity" component is in direct contrast with overfitting of other phenomena, and identification of sporadic behaviors. However, dimensionality reduction and clustering approaches are based on identification of discrete behaviors. Hence, gradual spatial changes in contributors (from domain wall to the bulk of the domain) might not be easily identifiable with such approaches, and more "traditional" statistical analysis could prove more informative.

6.4 Statistical Analysis of the Second Cycle

Statistical analysis was performed on the characteristic parameters for the switching PFM hysteresis curves, i.e., for coercive and nucleation voltages ($V_c^{\pm}$ and $V_n^{\pm}$, respectively), and saturation and remanent piezoresponse ($PR_s^{\pm}$ and $PR_0^{\pm}$, respectively), as described in Figure C.9. Domain walls were identified from the R-PFM amplitude, via local thresholding, and phase measurements, via Canney edge detection[167] (Figures 6.1a and 6.3a). Then, this wall image was used to calculate the distance to the nearest domain wall for each pixel (Figure 6.3b). The measured coercive voltages were binned every $80nm$ as a function of distance to the nearest domain wall (bin size selection is discussed in Appendix C).

The coercive voltages were analyzed according to the initial phase for each point, and separated for the initially *up*- and *down*-polarized domains (Figures 6.3c and 6.3d, respectively). Analysis of other characteristic parameters, both independent of the domain polarity and split according to polarity, are shown in Figure C.11. The initially *up*-polarized domains (Figure 6.3c) show a slight increase in V_C^+ and a slight decrease in the absolute value in V_C^- with distance from domain walls. However, the initially *down*-polarized domains (Figure 6.3d) show a very slight increase in the magnitude of both V_C^+ and V_C^- with increasing distance from domain walls, which could indicate a slight energetic preference towards switching near a

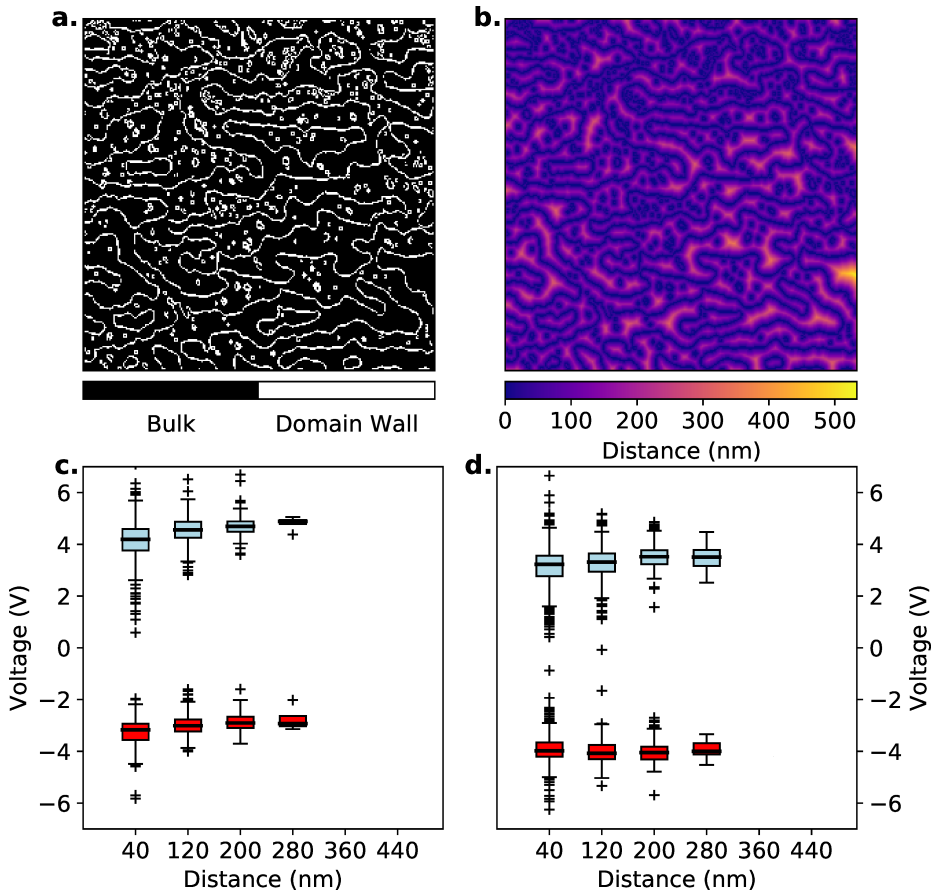

Figure 6.3: Distance from domain wall and effect on the second cycle coercive voltage for the $10\mu m$ x $10\mu m$ area. a) Domain walls are identified through Canny edge detection applied to the phase image (Figure 6.1a). b) The distance to the nearest domain wall is mapped for each pixel within the scanned area. c, d) Box-and-whisker plots of the binned V_c^+ and V_c^- values for the initially (c) *up*-polarized (*non-switching*) and (d) *down*-polarized (*switching*) domains. In all box-and-whisker plots, bin size is 80 nm, and x-axis values represent the center value for each bin.. Each box includes the first to third quartiles. The bold line within the box corresponds to the median, and the error bars coresond to 1.5 times the interquartile range or $\approx 99\%$ confidence interval for a normal distribution.

domain wall.

Three challenges remain with respect to the interpretation of the trends identified above. First, the behavioral dependence on the distance to a domain wall seen in Figure 6.3 is well within the distribution range of the reported data for the different bins. Hence, drawing conclusions on the ob-

served trends can be fraught with error. Second, the R-PFM phase images show newly created domains after the switching experiment (Figure C.1). Third, the piezoresponse curves do not indicate substantial changes between the two applied cycles, beyond the first quarter cycle as illustrated in Figure 6.1b. The above observations suggest that while the first cycle probes the response of the virgin samples, the second cycle probes the response of a new domain created in the first cycle. Hence, the distance to the domain wall can be correctly evaluated from the initial phase map only for domains which switch in response to the first quarter cycle (*down*-polarized or *switching* domains). The weak trends present in Figure 6.3c are more likely related to variations in the underlying chemistry and/or microstructure of the material, where the same variations contribute also in the creation of the virgin domains.

6.4.1 Statistical Analysis of the First Quarter Cycle

To achieve a better assessment of the proximity to the (initial) domain walls, we consider only the first quarter cycle of the piezoresponse, corresponding to changes with respect to the virgin domain configuration. However, among the functional parameters used to characterize hysteresis in ferroelectric materials, only saturation (piezoresponse) can be evaluated in the first quarter cycle. As an alternative approach, functional fitting to the Kolmogorov-Avrami-Ishibashi (KAI) polarization reversal model[168] is used henceforth.

This model is defined in Eq. 6.1:

$$PR(V) = A + Re^{-(\frac{V}{V_{sw}})^n} \tag{6.1}$$

where, $PR(V)$ is the voltage-dependent piezoresponse, A is the offset in the piezoresponse, R is the overall change in the piezoresponse, V_{sw} is related to the energy required for switching, and n is related to the dimensionality of domain wall growth (d). Specifically, the KAI model can describe both a nucleation-limited process where $d = n - 1$, and a growth-limited process where $d = n$. Additionally, based on Eq. 6.1, the initial piezoresponse value (at $V = 0$) is described by $A + R$, and the saturation *PR* value (at $V \to \infty$) is described by A. The data are plotted separately for switching and non-switching locations. It is noteworthy that as seen in Figure 1 and 2, even domains not switching within the first quarter cycle, exhibit still a voltage dependent response. Such field dependence of the response in nominally non-switching location can be due to multiple contributions:

- The piezoresponse measured is the average response of the probed volume and not necessarily monodomain. Hence, even when the average out of plane polarization of the sample is already well aligned with the applied voltage polarity, at increasing voltage, the smaller volume of ill-aligned domains can still switch to align better to the applied field;

- The intrinsic piezoelectric response of the material (i.e., in single do-

mains) still results in an increased out of plain deformation under an applied external electric field;

- Non-ferroelectric phenomena (such as electrochemical deformation and electrostatic effects) can also contribute to an observed increase in the piezoresponse under increasing applied voltage.

Hence, the KAI model can provide information with respect to both switching and non-switching domains. However, the information from switching domains is expected to more informative with respect to the domain wall proximity effects.

Figure 6.4 shows the binned distributions of the functional parameters of the first quarter cycle of the piezoresponse fitted to Eq. 6.1. Consistent with the analysis above, the initial piezoresponse ($A + R$) shows a sharp discontinuity at the domain wall, with a median of approximately $+/-$ $0.5mV$ in either domain, and no substantial dependence on domain wall proximity. Discontinuities are also observed in the other parameters across the domain wall, although more limited in the *n* and V_{sw} values than *A*.

In the *non-switching* domain, the saturated response, A, shows a slight linear increase as a domain wall is approached, while in the *switching* domain the same coefficient shows a slight linear increase at increasing distance from the domain wall. The overall observed linear trend is likely due to some external (i.e.non-ferroelectric) phenomena, such as electrostatic effects due to charge injection at the surface.[157] Specifically, we note that the

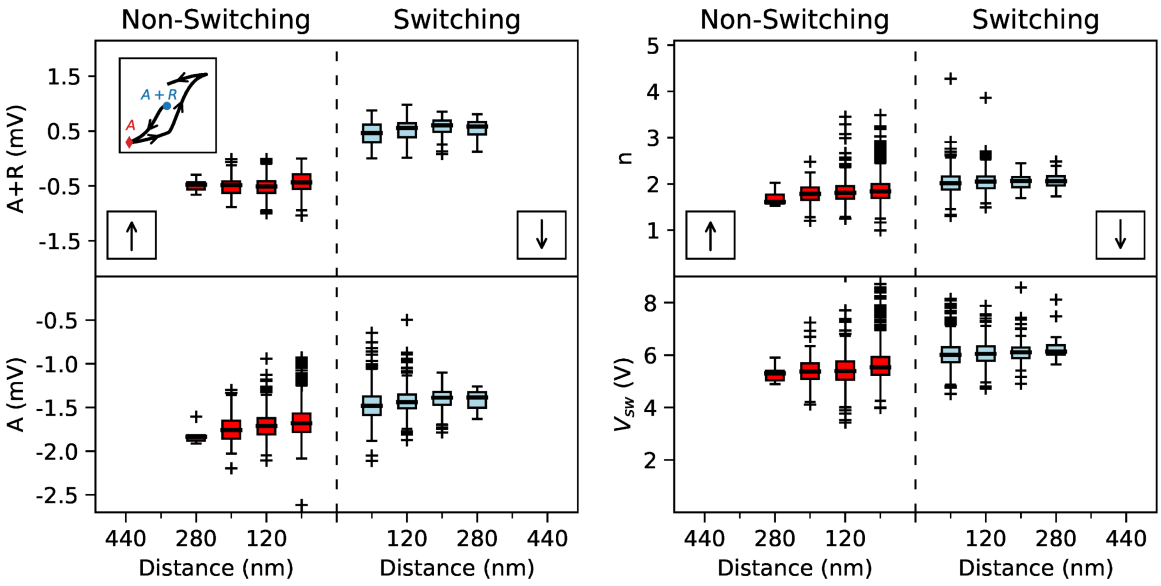

Figure 6.4: Distributions of the binned KAI fitting coefficients for the first quarter cycle of the $10\mu m$ x $10\mu m$ scan, plotted as a function of distance to the nearest domain wall. Switching and Non-Switching labels are based on the initial polarization state, i.e., as shown schematically, *down*- or *up*-polarized, respectively. The vertical dashed line in each plot represents the domain wall. As shown in the inset, $A + R$ is the initial piezoresponse value, and A is the saturation value. n is related to the growth dimensionality, and V_{sw} is the effective voltage required for switching. In all box-and-whisker plots, bin size is 80 nm, and x-axis values represent the center value for each bin. Each box includes the first to third quartiles. The bold line within the box corresponds to the median, and the error bars correspond to 1.5 times the interquartile range or $\approx 99\%$ confidence interval for a normal distribution.

first quarter cycle is probing the response to negative applied voltages. The injected electrons can accumulate on the surface or diffuse laterally. Within a *non-switching* domain, accumulation of such surface charges can result in an effective higher observed saturation piezoresponse (A). However, at closer proximity to a domain wall, such surface charges have a higher probability of attraction to and therefore motion towards the opposite polarity domains, resulting in the observed linear trend.

The exponential coefficient n is similar in both domain polarities and

≈ 2, with the median *n* slightly smaller than 2 for the *non-switching* domains. Outliers in n for the *non-switching* domains approach and at times exceed 3, potentially indicating a higher degree of dimensionality. However, if such outliers are associated with nucleation-limited variants, then the growth dimensionality would be in-line with the median value ($d = n - 1 \approx 2$). The corresponding outliers in V_{sw} suggest higher voltages required for switching. Given the immediate proximity to a domain wall in many of such outliers, a nucleation-limited process is unexpected. However, such an event could be due to strong pinning of the domain wall, due to underlying chemical or structural heterogeneities in the material. The domain wall proximity trends in Figure 6.4 are slight and well-within the range of data distributions, thus suggesting once again limited contribution from domain wall proximity.

6.5 Initial Images and *K*-means of 8μm by 8μm area

The study is next expanded to a new location with a wider range of domain sizes. The new location is probed with a waveform starting with positive applied voltages and an increased contact force (See Chapter 2), in order to reduce electrostatic effects.[169,170] Furthermore, resolution was increased by probing a smaller 8μm by 8μm area with only one applied voltage cycle.

Figure 6.5a shows the basic R-PFM scan images of the 8 μm x 8 μm area. The initial domain structure is apparent in the A and ϕ images. However,the

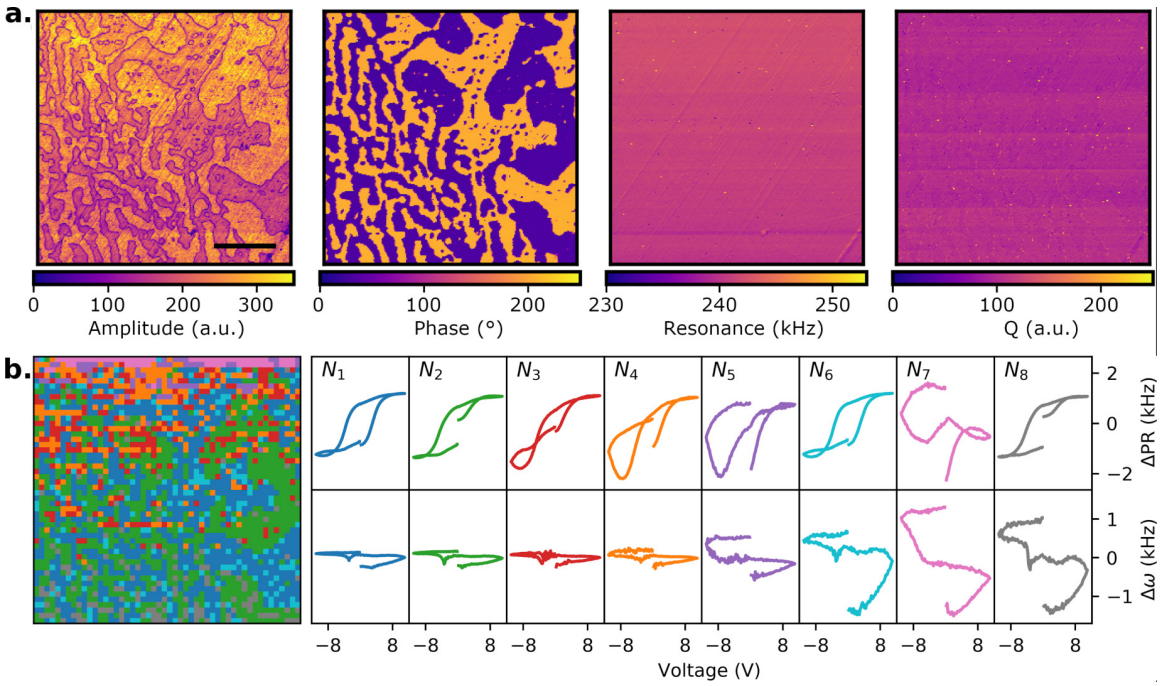

Figure 6.5: Initial PFM scan images (a) and *k*-means analysis of the switching piezoresponse analysis of the 8 μm x 8 μm area. a) From left to right, the initial piezoresponse amplitude (A), phase (ϕ), contact resonance (ω), and quality factor (Q) of the area. The micron bar represents $2\mu m$. b) Stacked piezoresponse and resonance *k*-means analysis with $N = 8$ clusters applied to the 8 μm x 8 μm switching data. At each spatial point shown in the map, the piezoresponse and resonance are given by the corresponding colored component. Here, the upper row is the deviation of the piezoresponse from the mean (ΔPR) and the bottom row is the corresponding resonance (ω).

changes to the overall domain configuration appear to be more substantial when compared to the 10 μm x 10 μm area (Figure 6.1), possibly due to the closer distance between two adjacent switched points in the grid: this distance is approximately 160nm compared to 200nm in the 10 μm x 10 μm area.

Figure 6.5b shows the *PR and* ω stacked *k*-means analysis for the 8 μm x 8 μm area and $N = 8$. All components show to varying degrees non-ferroelectric behavior at negative voltages, as evidenced by crossover in the

PR curves (N_1-N_3 and N_6), or PR behavior inconsistent with a ferroelectric hysteresis curve (N_4, N_5 and N_7). However, subsequent analyses are limited to the first quarter cycle response of the sample, i.e. only positive voltages. Hence, electro-chemical/static effects at negative voltages are not expected to directly impact the analysis. N_5 and N_7 show strong departures from typical ferroelectric hysteresis at positive voltages, as well as limited presence with respect to the number of assigned point to these behaviors. Thus, locations corresponding to N_5 and N_7 are removed from further consideration.

However, the *k*-means analysis of the 8 μm x 8 μm area shows no evidence of a switching behavior influenced by a nearby domain wall. Dictionary learning analysis was also performed on the 8 μm x 8 μm area (presented in Appendix C), but again no domain wall dependent behavior could be identified. Thus, traditional statistical analysis was again performed.

6.6 Statistical Analysis of the First Quarter Cycle of the 8 μm x 8 μm area.

Figure 6.6 shows the characteristic parameters for the KAI analysis of the first quarter cycle for the $8\mu m$ x $8\mu m$ sampled area. As the first quarter cycle is in response to positive applied voltages, the *up*-polarized domains switch and the *down*-polarized domains do not. Within each set of (*switching* or *non-switching*) domains, the median initial piezoresponse values, $A + R$,

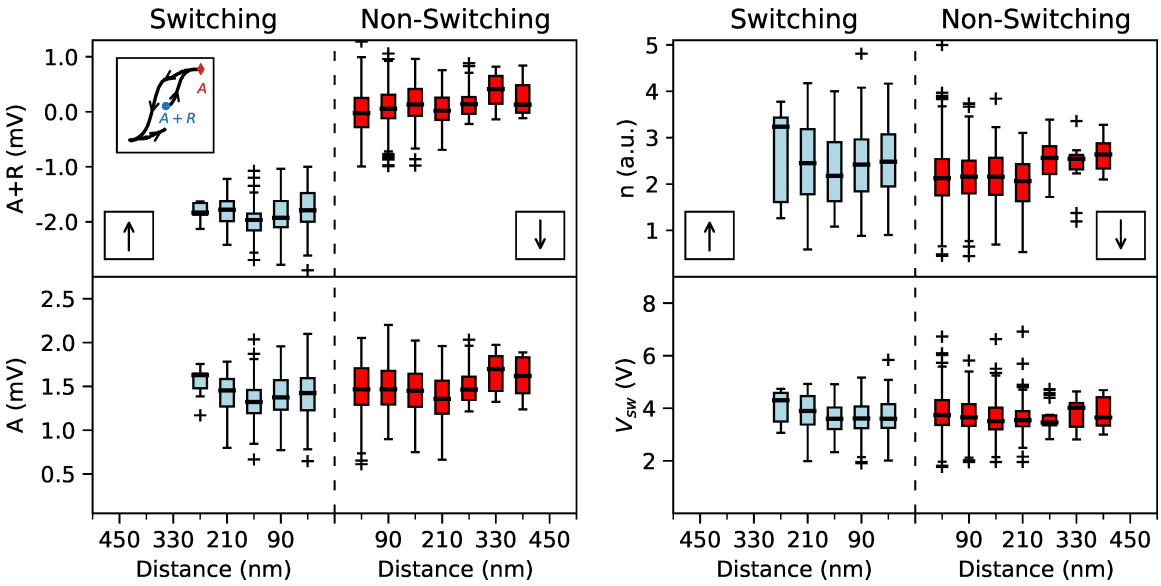

Figure 6.6: Distributions of the binned KAI fitting coefficients for the first quarter cycle of the $8\mu m$ x $8\mu m$ scan, plotted as a function of distance to the nearest domain wall. Switching and Non-Switching labels are based on the initial polarization state, i.e., as shown schematically, *up*- or *down*-polarized, respectively. The vertical dashed line in each plot represents the domain wall. As shown in the inset, $A+R$ is the initial piezoresponse value, and A is the saturation value. n is related to the growth dimensionality, and V_{sw} is the effective voltage required for switching. In all box-and-whisker plots, bin size is 60 nm, and x-axis values represent the center value for each bin.. Each box includes the first to third quartiles. The bold line within the box corresponds to the median, and the error bars correspond to 1.5 times the interquartile range or $\approx 99\%$ confidence interval for a normal distribution.

are relatively unchanged with distance from domain wall. At the domain wall, a sharp discontinuity is again observed in $A+R$, but the values are not symmetric for the two domains polarities, indicating the presence of surface charges and electrostatic effects in the new location. All other parameters do not show substantial discontinuity across the domain wall. Notably, positive injected charges have been shown to diffuse more slowly on dielectric surfaces compared to negative injected charges.[157] A lower charge mobility often results in local accumulation rather than lateral diffusion,[171] and hence

a more uniform electrostatic effect, independent of the location and distance from a domain wall, or the initial domain polarity.

In the *switching* domains, the A, n, and V_{sw} exhibit a relative increase at increasing distance from a domain wall. The median n increases from ≈ 2.5 at the domain wall to ≈ 3.4 in the farthest bin. Assuming the presence of both growth-limited ($n = d$) and nucleation-limited ($n = d + 1$) behaviors, this increase can be interpreted as predominately 2D growth, in growth-limited switching regime near domain walls, and nucleation-limited regime in the domain bulk. Alternatively, the results could be interpreted as transition from 2D domain wall motion in proximity of a domain wall, to 3D domain wall motion when farther away from the domain wall. The median V_{sw} increases by ≈ 25 percent when moving from near a domain wall to the domain bulk, indicating a limited energetic preference towards switching near a domain wall.

While the trends in Figure 6.6 are stronger than those in Figure 6.4, changes across the different bins remain well within the 99% confidence interval. Additionally, the limited changes in V_{sw} are in marked contrast with previous reports for the effects of proximity to a domain wall on the switching behavior of the uniaxial ferroelectric $LiNbO_3$ single crystals.[21,48] In the previous reports, a change in the switching regime was observed at $\approx 2 - 4\mu m$ from the domain wall and was accompanied by an order of magnitude increase in the nucleation (switching) bias. At smaller length

scales, ($\lesssim 500nm$) the nucleation voltage increased by up to 4x when moving farther from a domain wall. Here, the limited change in the V_{sw} suggests then that nucleation is not a limiting step in polarization switching in the relaxor-ferroelectric single crystal, possibly due to the presence of pervasive underlying heterogeneities, that can act as nuclei for polarization reversal. In proximity of a domain wall, application of an appropriate bias can result in motion of the domain wall, in order to grow the well-aligned domain, with a two-dimensional growth process. Conversely, at distances $> 250nm$, the switching mechanism is mostly free of the effect of the pre-existing domain walls. The switching nucleus is expected to be in a location immediately beneath the tip contact to the sample, and the growth process will be three-dimensional, following more closely the three-dimensional field distribution in an extended volume under the tip. Lastly, we note that while the switching process might change dimensionality, the effective result on the observed piezoresponse or required switching bias is minimal, indicating a "soft" piezoelectric behavior, as indeed expected from a relaxor-ferroelectric single crystal.[65]

6.7 Summary and Conclusions

In summary, we showed that proximity to a preexisting domain wall has a limited influence on the local piezoresponse and its switching behavior in a relaxor-ferroelectric single crystal. The results were consistent across

multiple analytical approaches, including machine learning techniques and binned data as a function of domain wall distance. A possible transition from 2D to 3D growth-limited regime was observed at increasing distance from a domain wall. However, the energetic impact of such transition was limited to less than 25% increase in the nucleation bias.

Lastly, our results also highlight the shortcomings of the standard multi-cycle averaging approach for analysis of switching PFM data, particularly when relating functional behavior to the virgin state of the material (e.g. initial position of domain walls). While such an approach results in increased signal-to-noise ratio, it also equally ignores the virgin domain state of the sample and is increasingly affected by the local underlying heterogeneities in the probed material.

CHAPTER 7

CONCLUSIONS AND FUTURE WORK

In this chapter, the conclusions of the thesis are briefly summarized and recommendations for future work are provided.

7.1 Summary and Conclusions

7.1.1 Multivariate Assessment of the Electromechanical Relaxation in Relaxor-Ferroelectrics

The evolution of the time- and electric field- dependent electromechanical relaxation in relaxor-ferroelectric PMN-xPT was probed for a range of compositions across the MPB. Simple statistical analysis identified two distinct behaviors, i.e., a relaxation-like and a poling-like trend. Furthermore, the poling-like behavior in response to positive voltages and relaxation-like behavior in response to negative voltages was associated with the relaxor end member. Through application of dimensional reduction techniques, these behaviors could be directly identified and spatially mapped for any given composition/voltage combination. However, correlating all of the composition/voltage combinations remained challenging.

Physical/chemical constraints were then imposed with dimensional stacking, resulting in a quantitative correlation of the piezoresponse evolution

across composition and voltage. With this correlated analysis, it became readily apparent that: 1) the poling/relaxation-like behavior is a unique signature of the relaxor end member and persists across the phase diagram, 2) as the ferroelectric end member is added a more relaxation-dominated behavior emerges, and 3) a domain glass behavior is continuously observed in all composition.

The effectiveness of the correlated analysis demonstrates that dimensional stacking is indeed a powerful tool when used appropriately. But, overall this study highlights how a wide range of analyses, including a dimensionally stacked ML approach, can build-upon and strengthen ML results. For instance, the simple statistical analysis was limited but identified at least two behaviors, which informed the non-dimensionally stacked analysis showing evidence of the glassy state. As a whole, these analyses showed a previously unreported behavioral signature of the relaxor end member and a glassy behavior present in all composition.

7.1.2 Electromechanical Switching in Ferroelectric Thin Films with Less Biased Machine Learning

Expounding upon the concepts developed in the previous study, dimensional stacking was further demonstrated on multiple functional variables (i.e. a stacked analysis of the piezoresponse and contact resonance) from previously reported polarization switching in a PZT thin film. Two strong influ-

ences on ML-results were identified. First, a direct correspondence between data set quality and results was emphasized. In particular, outlier behavior (non-ferroelectric trends due to instrumentation and/or sample issues, e.g. acoustic hardening due to electrostatic displacement) was shown to dominate ML results. Second, slight changes in ML model parameters were shown to lead to distinct changes in outputs, effectively allowing for user preconceptions to be imposed upon ML analyses.

To address these troubling aspects of ML, a methodology was formalized which minimizes the impact of biases and data set quality, thereby increasing interpretability. It was shown that through intentional and appropriate use of overfitting in clustering analysis, outlier behavior could be efficiently identified and accounted for. Furthermore, an analysis of the root-mean-squared model error was implemented as a means of quantitatively selecting a range of valid ML-model parameters, all of which were considered collectively to further minimize bias.

Through consideration of the ML-analyses as described above, a range of behaviors were identified. In brief, the results are well-explained by polarization switching, superimposed with non-ferroelectric phenomena. Specifically, the switching of *c* domains showed consistently recognizable features in *PR* curves, and an accompanied substantial softening at coercive voltages in the resonance curves. Conversely, polarization switching in *a* domains was substantially suppressed, particularly in topographically depressed lo-

cations. Such suppressed switching is easily justified by the large lateral constraints exercised by the "inert" volume of material surrounding these locations, specifically in consideration of the large deformations associated with ferroelastic (compared to pure ferroelectric) switching. Lastly, additional contributions from instrumentation and non-ferroelectric phenomena were consistently observed. The above described results stand in contrast to previously reported exotic phenomena, i.e. ferroelastic mediated switching and/or charged domain walls, the erroneous identification of which is here ascribed to instrumentation issues and non-ferroelectric phenomena improperly accounted for.

7.1.3 Effects of Domain Wall Proximity on Polarization Switching in Relaxor-Ferroelectric Single Crystals

Finally, the developed open-source R-PFM and ML-methodology, including dimensional stacking were applied to a study assessing the effect of proximity to domain walls on the polarization switching in a relaxor-FE PMN-40PT single crystal. An initial *k*-means analysis was applied to remove outlier behavior, the dimensionally stacked piezoresponse-resonance behavior was analyzed with DL, and an error analysis was used to limit user-bias. While no ML-derived behavior was found to be correlated with the domain walls, application of traditional statistical analysis identified a slight dependence on domain wall proximity of the functional switching pa-

rameters. This study once again highlighted the major limitation of ML techniques in their inherently mathematical nature, e.g., DL clearly ignored the subtle dependence on domain wall proximity, likely in favor of a reduced reconstruction error or an increased sparsity.

By application of simple statistics, a possible transition from 2D to 3D growth-limited regime was observed at increasing distance from a domain wall. However, the energetic impact of this transition was limited to less than 25% increase in the nucleation bias. This limited change in nucleation bias is in marked contrast with previous reports considering a similar study of a trigonal $LiNbO_3$ single crystals[21, 48]. The results suggest that nucleation is not a limiting step in polarization switching in this relaxor-ferroelectric single crystal, possibly due to the presence of pervasive underlying heterogeneities, which can act as nuclei for polarization reversal.

7.2 Future Work

7.2.1 Non-Ferroelectric Effects in Piezoresponse Force Microscopy

A recurring theme throughout this thesis, and widely present in literature,[164,165,166] is the effect of non-ferroelectric phenomena in PFM measurements. Specifically, the analyses presented here have often included contributions attributed to electrostatic displacement and related injected charges, as well electrochemical deformation. Yet, a consistent and complete description of the electrostatic and electrochemical phenomena's influence on electrome-

chanical deformation probed via PFM is lacking. In particular, the effects of electrostatic and electrochemical tip displacement on the contact resonance and quality factor have been often ignored in literature. This is due in part to the wide range of parameters that can influence such contributions - e.g., humidity,[157] voltage polarity,[157] contact force,[170] and cantilever stiffness[172,173] - and in part in the lack of availability of appropriate instrumentation outside Oak Ridge National Laboratory.

A systematic multi-dimensional study could shed some light upon the influence of electrostatic displacement on the electromechanical response, allowing for future PFM based studies to better account for these effects. Such studies could be achieved with R-PFM and the ML methodology outlined in this thesis.

First, a correlated ML-analysis of the switching behavior of a non-ferroelectric dielectric (e.g. soda-lime glass) and a ferroelectric single crystal (PZT or PMN-xPT) could be performed. Soda-lime glass can exhibit electrostatic displacement, given that it is a dielectric material. Additionally, electrochemical deformation is also possible in the same material, based on the disordered structures with relatively large network holes that allow ionic motion. Direct comparison of the piezoresponse hysteresis features (across all R-PFM parameters) or alternatively, ML results of switching PFM data on both sets of samples would allow effective identification of the non-ferroelectric phenomena in the ferroelectric sample.

Additional information could be gained by correlating the "in-field" (measured under an applied electric field) and "out-of-field" (measured after removal of the applied electric field) switching PFM response. In particular, the non-ferroelectric sample and the in-field and out-of-field behavior of the ferroelectric sample could be combined into to a single correlative ML-analysis. Specifically, due to the presence of large superimposed DC bias, the in-field response is expected to have a large amount of charge injection compared to the out-of-field response, even in a ferroelectric material. Thus, the ML results would track the switching behavior across four data sets with increasing non-ferroelectric contributions, i.e.: a ferroelectric with weak non-ferroelectric contributions (out-of-field), a ferroelectric with strong non-ferroelectric contributions (in-field), a non-ferroelectric sample (out-of-field), and a non-ferroelectric sample with increased charge injection (in-field).

7.2.2 Effects of Humidity and Voltage Polarity on the Piezoresponse Force Microscopy Characterization

In ambient conditions, polarization switching has been shown to result in formation of excess uncompensated charge, typically through disassociation of chemisorbed or physisorbed water molecules on the surface[174]. These charges are necessary for polarization switching to occur, as they screen the *depolarizing field* which opposes the polarization[175]. However, these

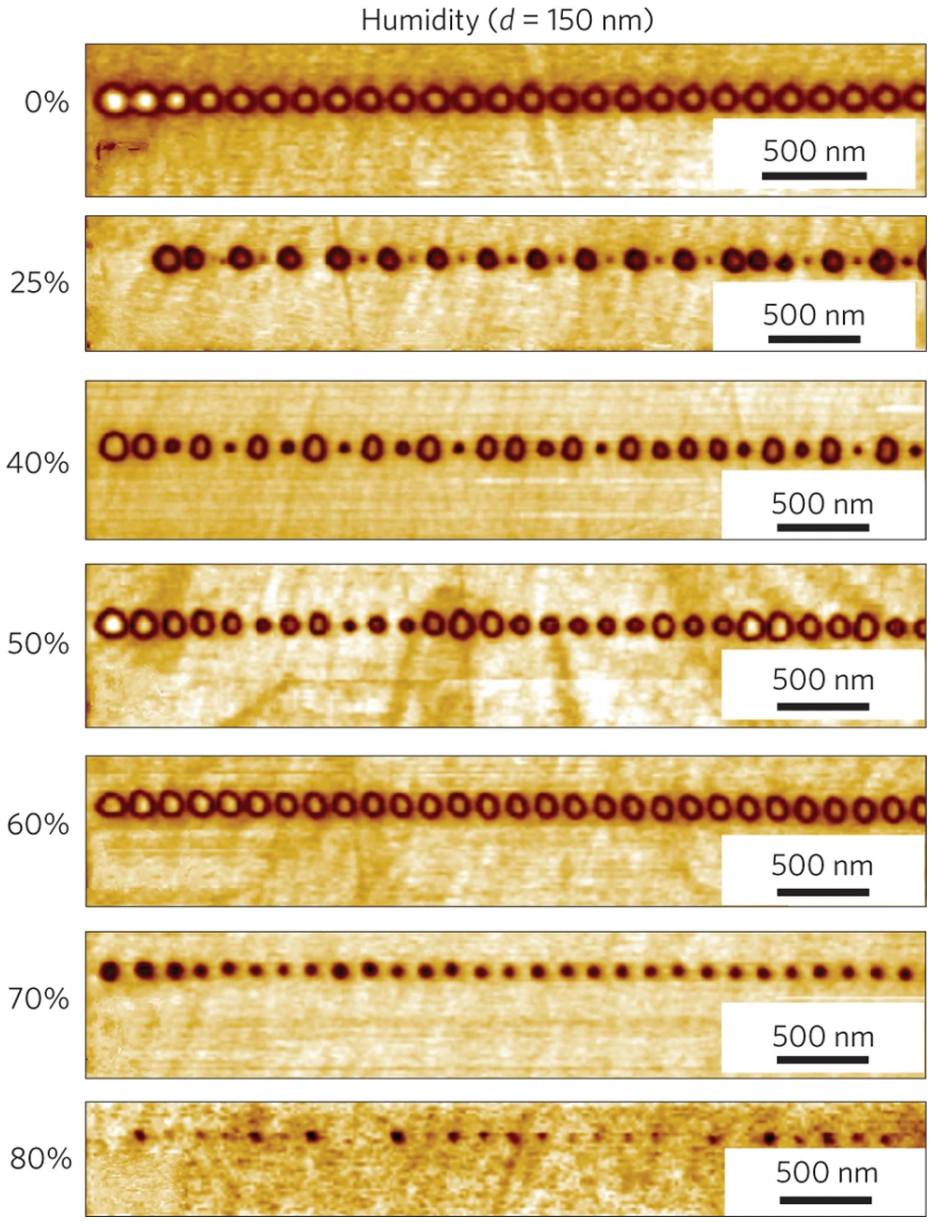

Figure 7.1: A linear series of points where the polarization was switched by application of a DC voltage through SPM and for a range of relative humidity values[176]. The value to the left of the rectangular images indicate the relative humidity The ferroelectric material was $LiNbO_3$. Reproduced from [176].

charges also diffuse laterally along the surface, at a rate that is dependent on the relative humidity, temperature, applied voltage polarity, and domain polarity[176, 157].

Lateral charge diffusion can result in chaotic behavior, specifically when

probing a ferroelectric in a series of closely spaced points, as charges yielded from previous points migrate and influence the response at other points through electrostatic phenomena. Such chaotic behavior is, in turn, strongly dependent on relative humidity, temperature, etc.. For instance, Ievlev et al. demonstrated that when nucleating domains in series of close points, the formed domains can be: uniform in size (low humidity), non-uniform in size with some periodicity (moderate humidity), or non-existent (high humidity) (Fig. 7.1)[176]. Thus, it is reasonable to expect that these parameters (e.g. humidity and voltage/domain polarity) would similarly influence the observed switching behavior probed via a grid-based PFM measurement. In particular, changes in humidity and voltage/domain polarity would be expected to result in a variation in the electrostatic influence on the probed switching behavior, given the probed points are sufficiently close.

A correlative R-PFM and ML study across humidity and voltage/domain polarity could elucidate the impact of these parameters on the observed piezoresponse and viscoelastic properties in grid-based R-PFM probings of the switching behavior. Such a study could inform on the optimal experimental parameters (e.g. relative humidity) in order to minimize electrostatic effects from injected charge. The proposed study should consider the relative humidity values used in Fig. 7.1, allowing for a point of comparison, however, it is expected that the relative humidity levels for the discussed switching discussed above will be also a function of the dielectric and fer-

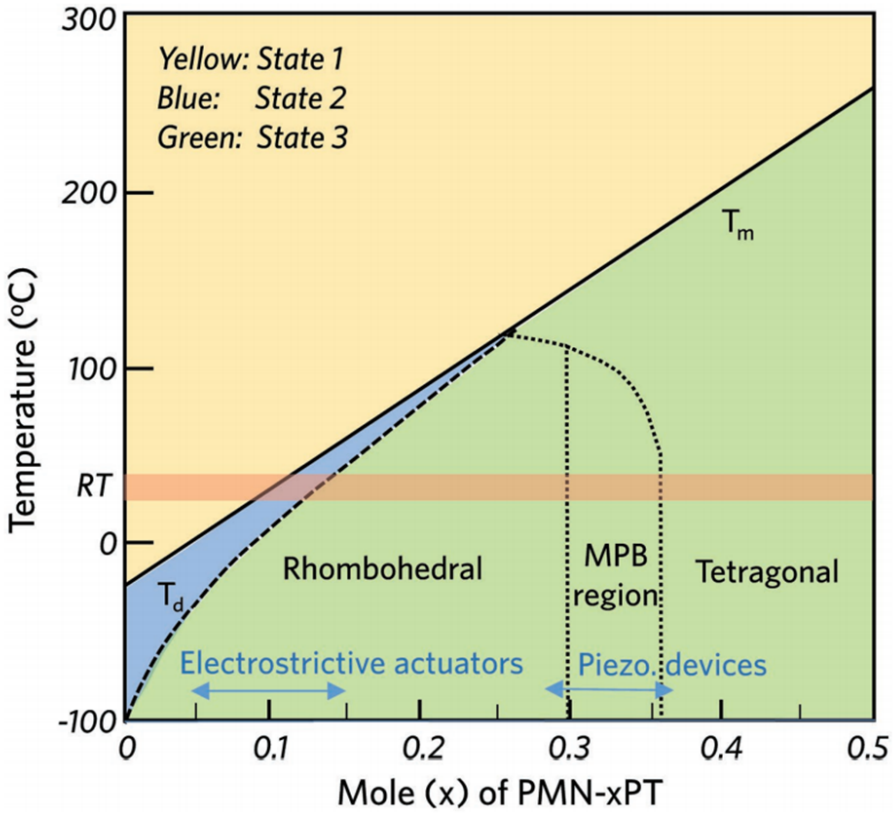

Figure 7.2: Phase diagram reproduced from [50]. T_d is the depolarizing temperature. T_m is the temperature of maximum dielectric permittivity. The pink band highlight room temperature. The Burns temperature is not shown ($T_B \approx 350\ ^\circ C$ for PMN)

roelectric properties of the material studied (charge screening is directly related to the polarization to be "screened"). Furthermore, the use of the same ferroelectric materials probed in the in/out-of field study (PZT or PMN-PT) of the previous section would enable identification of the non-ferroelectric components (e.g. electrostatic displacement).

7.2.3 Temperature Dependence of the Electromechanical Response in Relaxor-Ferroelectrics

As discussed in Chapter 1, one of the defining features of relaxors is there unique temperature-dependence. In particular, while all ferroelectric perovskites exist in a non-ferroelectric state at high temperatures and transition to a ferroelectric state upon cooling, relaxors exhibit no well-defined transition. However, in relaxors, three temperatures are of unique importance (e.g. Fig. 7.2): the Burns temperature T_B ($T_B \approx 350\ ^\circ C$ for PMN), the temperature of maximum dielectric permittivity T_m, and the depolarization temperature T_d. To review, above T_B relaxors behave similarly to typical ferroelectrics at high temperature, but below T_B (State 1 in Fig. 7.2) ergodic PNRs begin to form and relaxors begin to exhibit their unique properties. Then, as a relaxor is further cooled, frequency dispersion in the dielectric response can be observed (State 2 in Fig. 7.2, near T_m). Finally, below T_d (State 3 in Fig. 7.2) PNRs freeze into a non-ergodic state and relaxors can be forced into a ferroelectric state via poling.

These temperature-dependent changes combined with the composition dependent ones assessed in Chapter 4, yield a complete phase diagram (Fig. 7.2). Thus, the study in Chapter 4 essentially only considered a slice of the phase diagram describing the unique behavior of relaxor-ferroelectrics. A temperature-dependent correlative R-PFM and ML-study could be used to

expand the previous composition-based work.

Such a study could consider PMN-xPT with $x \approx 15$, which at room temperature is a rhombohedral ferroelectric, around $50\ ^{\circ}C$ is in State 2 (below T_m and above T_d), and exhibits a dielectric peak at $\approx 75\ ^{\circ}C$. By applying R-PFM and the ML process developed here, the evolution of the piezoresponse and viscoelastic properties could be correlated across these states. Specifically, PMN-15PT could be probed at: room temperature (State 3, ferroelectric), $60\ ^{\circ}C$ (State 2, ergodic PNRs and below dielectric peak), and $100\ ^{\circ}C$ (State 1, ergodic PNRs and above dielectric peak). In order to reveal characteristic switching behavior associated with ergodic and non-ergodic behavior, or ferroelectric, short-range polar and nonpolar behavior in these materials.

Appendices

APPENDIX A

DIMENSIONAL STACKING AND ELECTROMECHANICAL RELAXATION

A.1 Spatially Averaged Response

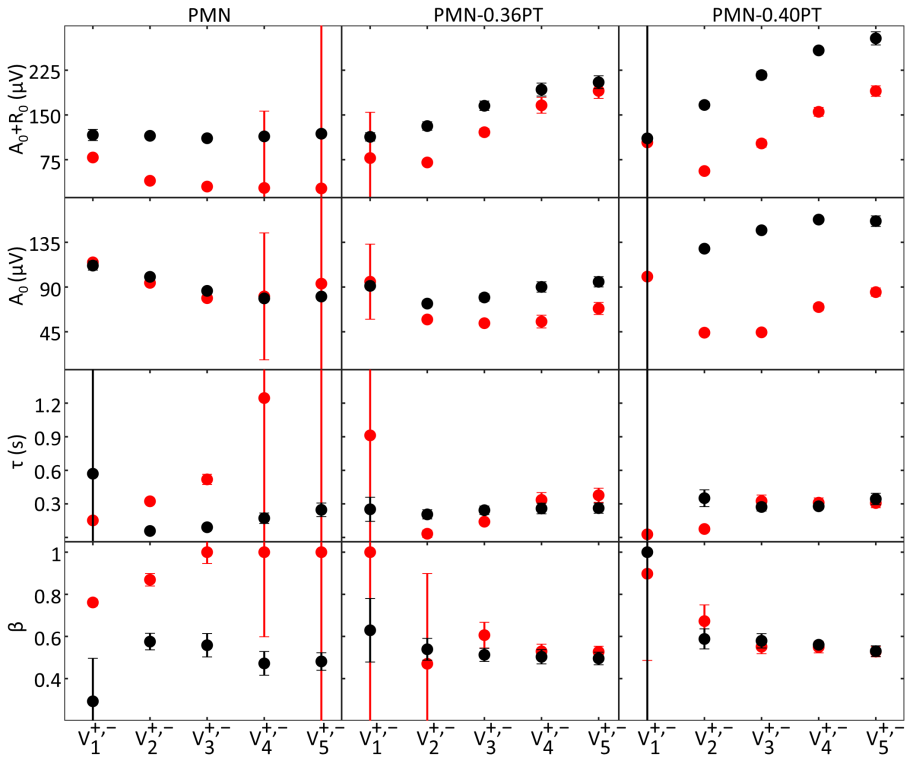

Figure A.1: KWW fitting coefficients of the average response amplitude for each voltage and composition combination (i.e. fitting coefficients of the curves plotted in Fig. 4.1). A_0 is the response at saturation, R_0 is the amplitude of the change over time, τ is the characteristic time constant, and β is the stretch exponential.

The spatially averaged piezoresponse amplitudes (in Figure 4.1) were fit to Kohlrausch-William-Watts (KWW, $KWW(t) = A_0 + R_0 e^{(-(t/\tau)^{\beta})}$). Figure A.1 shows the $A_0 + R_0$, A_0, τ, and β for these fittings, where A_0 is

the piezoresponse amplitude at saturation, R_0 is total piezoresponse change over time, τ is the characteristic time constant, and β is the stretch exponential, describing the width of the time constant distribution.

A.1.1 Distributions of Point-by-Point Fitting Coefficients

Fitting can be applied without spatially averaging the response, i.e. fitting each voltage/composition combination at each spatial point. The distributions of the KWW coefficients for a point-by-point fitting of each voltage-composition combination are plotted in Figures A.2-A.7. Curves that did not follow a strict monotonic trend were not considered for fitting. Such curves were predominantly those corresponding to removal of sub-coercive/near-coercive DC voltages. At lower applied voltages, some samples showed bimodal distributions in their characteristic parameters, e.g. R_0 at V_2^+ for PMN-0.36PT and V_4^+ for PMN-0.40PT. It should be noted that positive R_0 values correspond to relaxation, while negative R_0 values correspond to poling-like behavior. Lastly, we note that a large number of sampled location's responses can be fit to a simple exponential ($\beta = 1$), consistent with a simple homogeneous behavior. The observed distributions suggest that homogeneous and heterogeneous behaving locations are mixed and that homogeneous behavior is reduced at increasing magnitude of applied voltage.

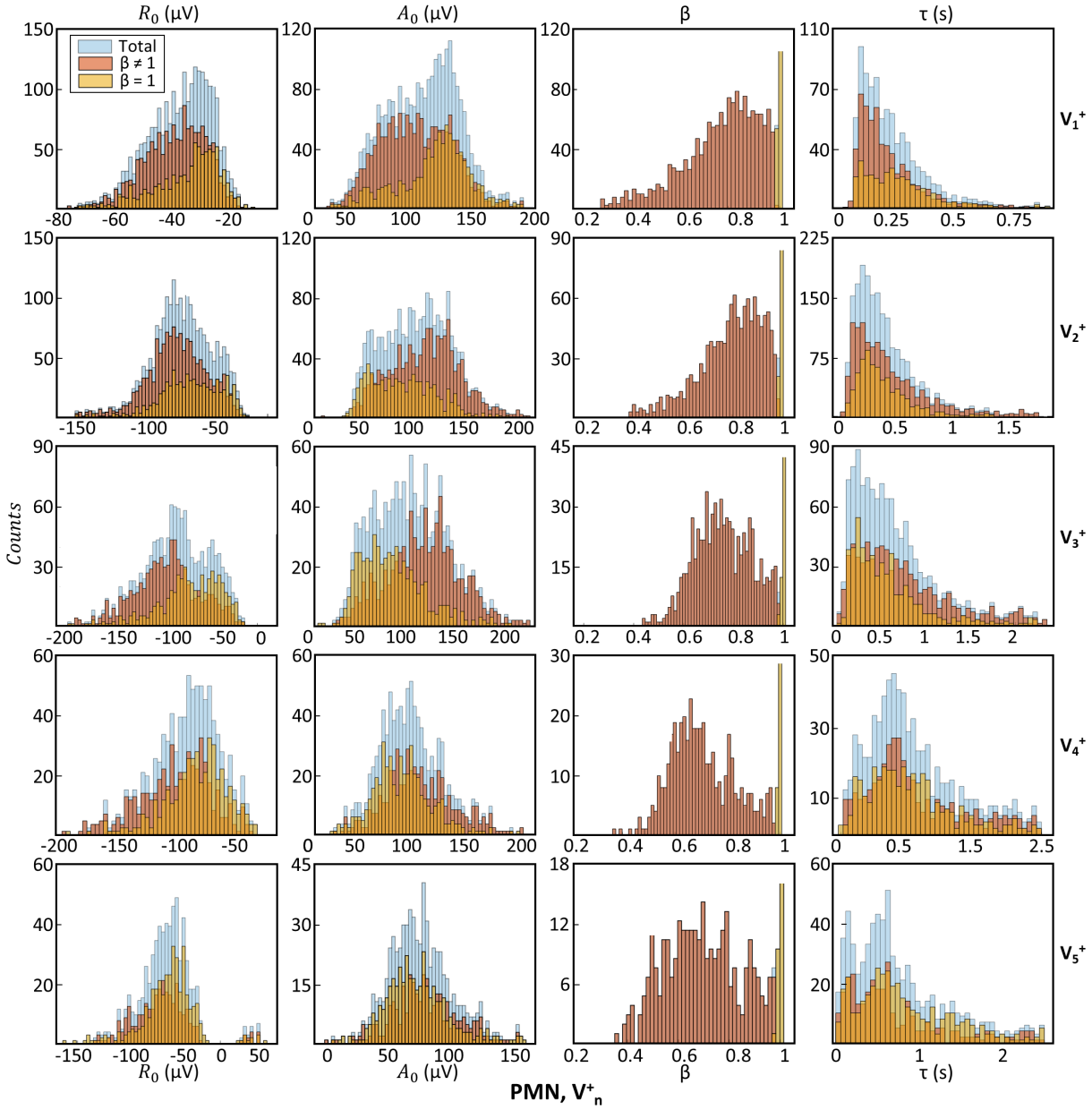

Figure A.2: Histograms of the characteristic parameters for a point-by-point KWW fitting of PMN's response to positive applied voltages. A_0 is the piezoresponse amplitude at saturation, R_0 is the overall amplitude change over time, τ is the characteristic time constant, and β is the stretch exponential.

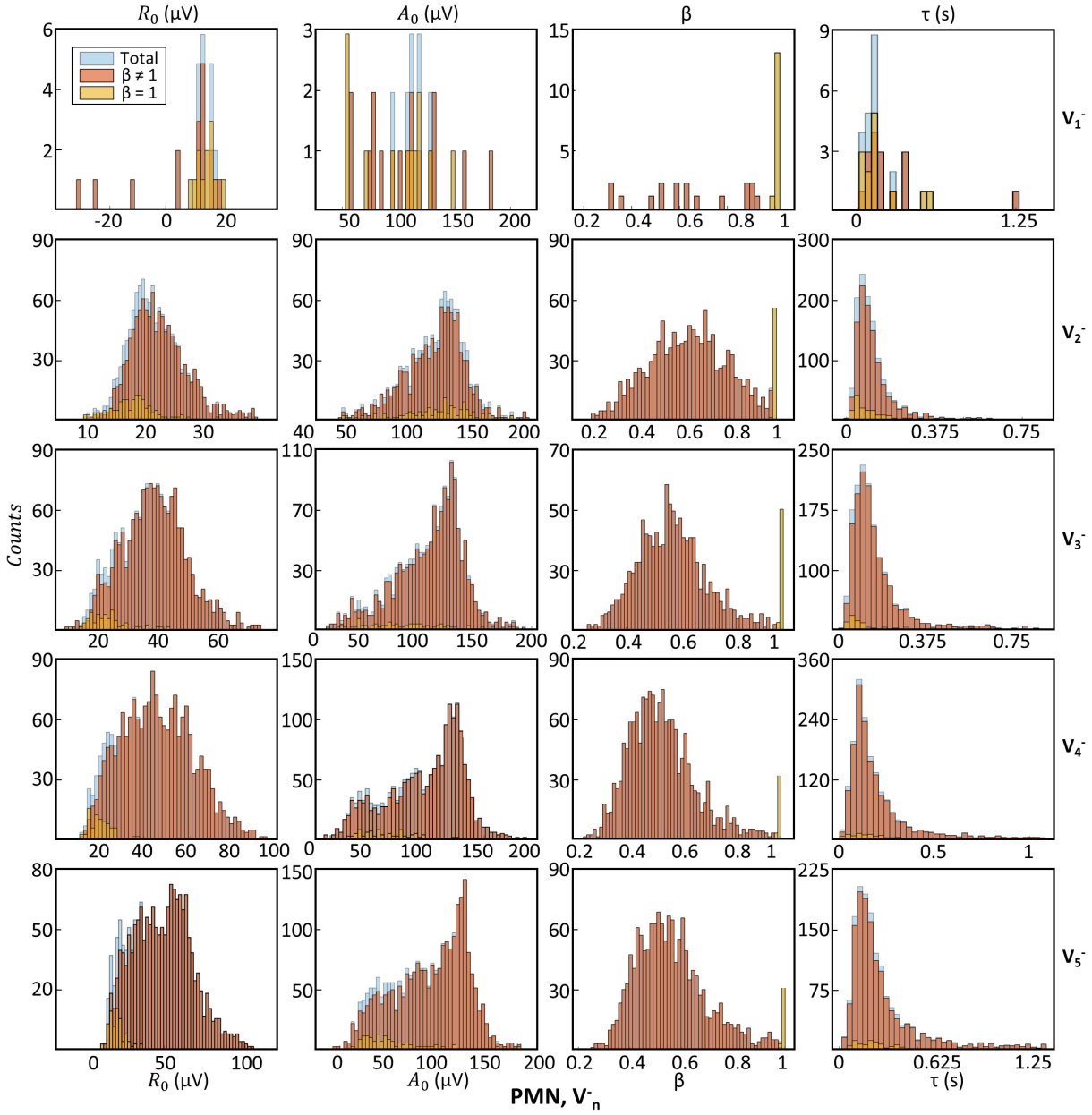

Figure A.3: Histograms of the characteristic parameters for a point-by-point KWW fitting of PMN's response to negative applied voltages. A_0 is the piezoresponse amplitude at saturation, R_0 is the overall amplitude change over time, τ is the characteristic time constant, and β is the stretch exponential.

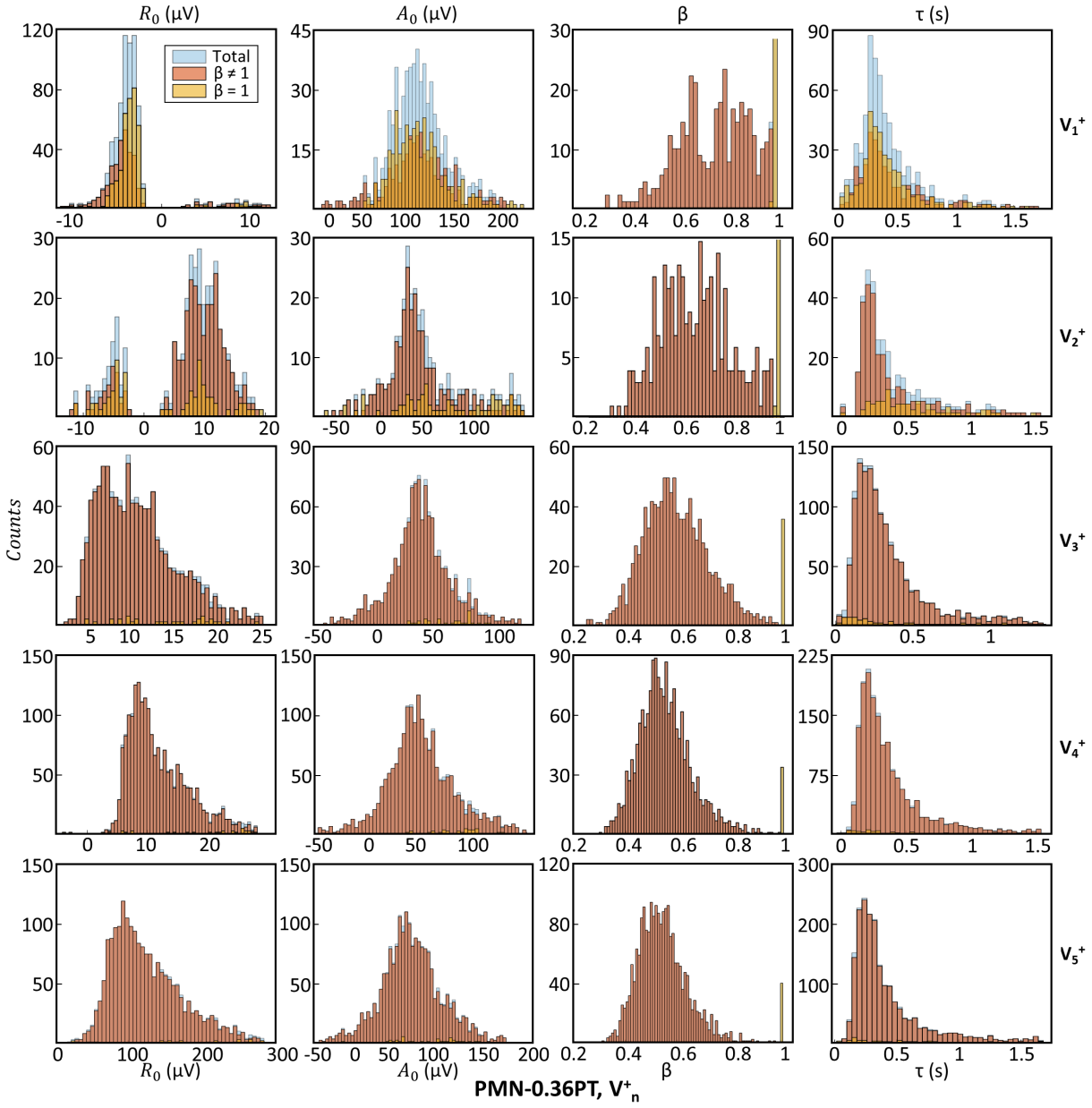

Figure A.4: Histograms of the characteristic parameters for a point-by-point KWW fitting of PMN-0.36PT's response to positive applied voltages. A_0 is the piezoresponse amplitude at saturation, R_0 is the overall amplitude change over time, τ is the characteristic time constant, and β is the stretch exponential.

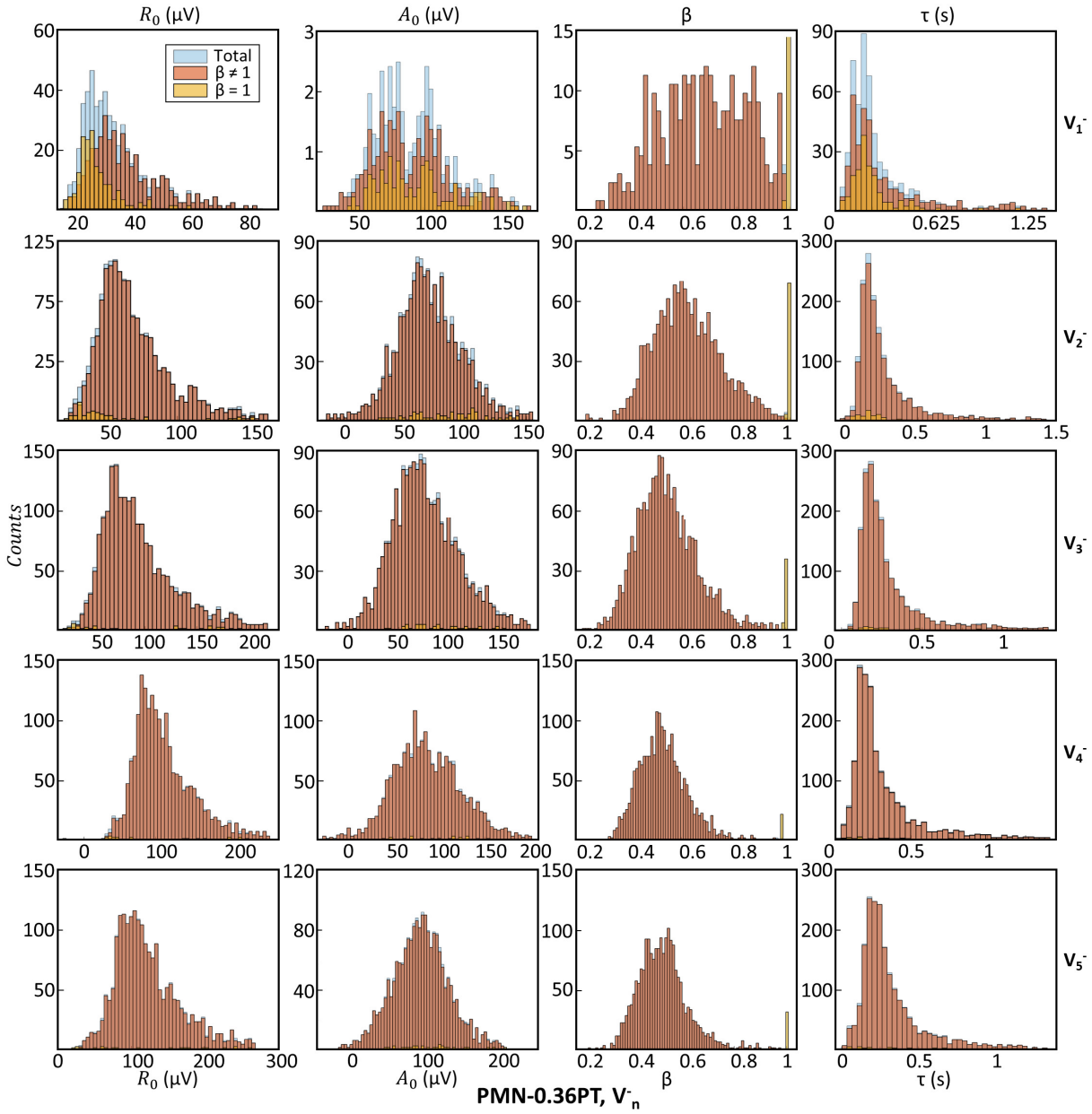

Figure A.5: Histograms of the characteristic parameters for a point-by-point KWW fitting of PMN-0.36PT's response to negative applied voltages. A_0 is the piezoresponse amplitude at saturation, R_0 is the overall amplitude change over time, τ is the characteristic time constant, and β is the stretch exponential.

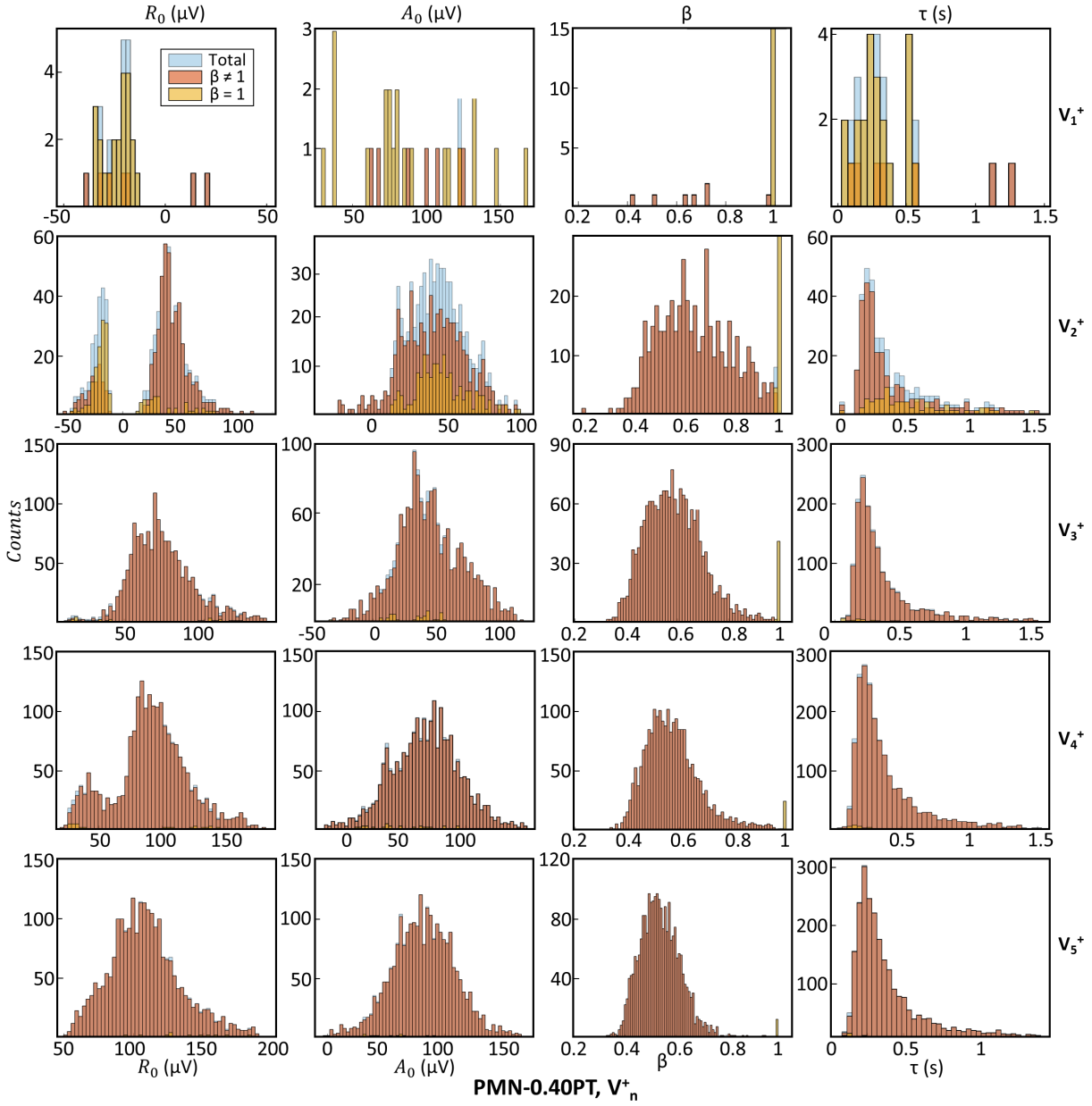

Figure A.6: Histograms of the characteristic parameters for a point-by-point KWW fitting of PMN-0.40PT's response to positive applied voltages. A_0 is the piezoresponse amplitude at saturation, R_0 is the overall amplitude change over time, τ is the characteristic time constant, and β is the stretch exponential.

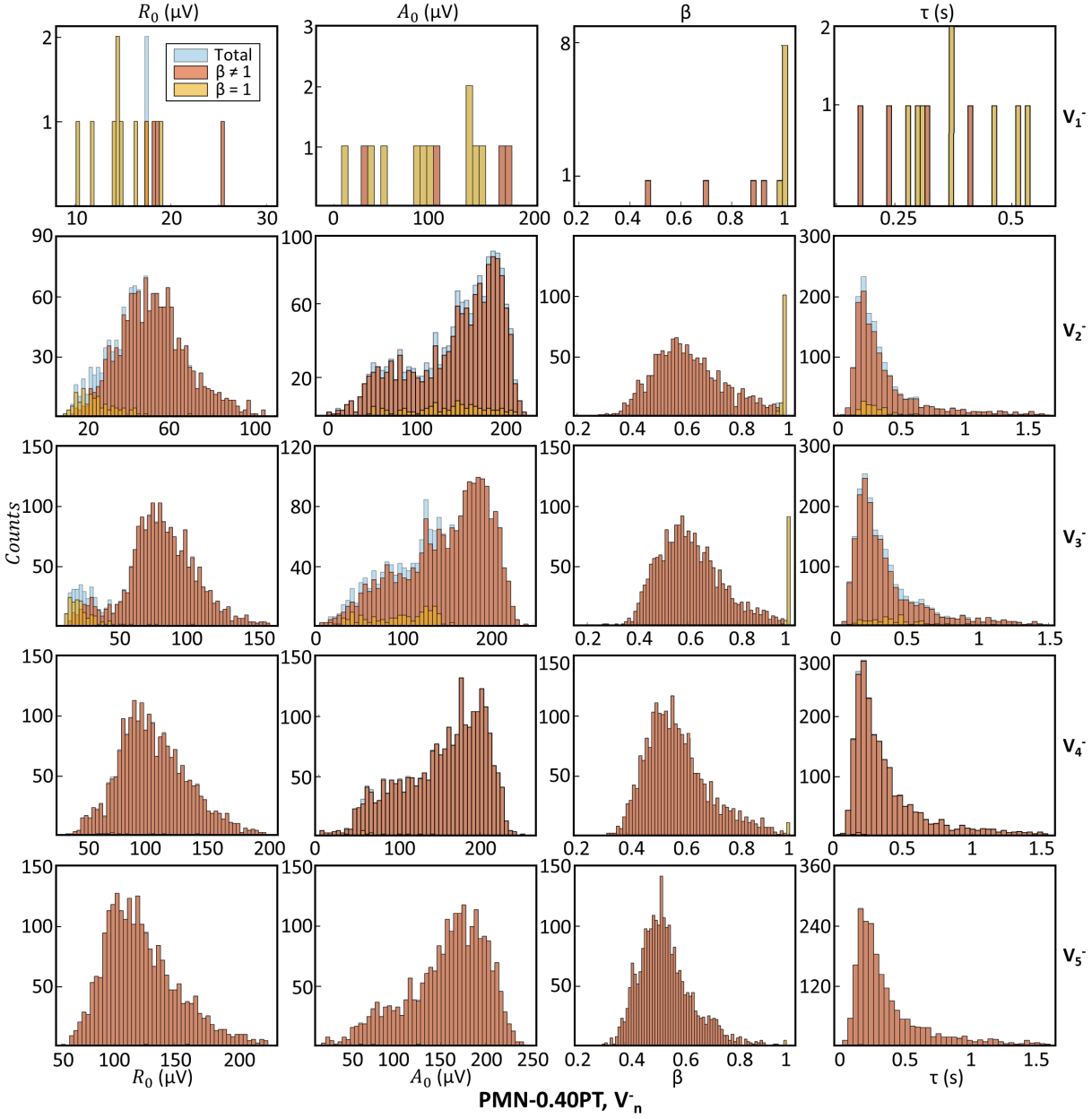

Figure A.7: Histograms of the characteristic parameters for a point-by-point KWW fitting of PMN-0.36PT's response to negative applied voltages. A_0 is the piezoresponse amplitude at saturation, R_0 is the overall amplitude change over time, τ is the characteristic time constant, and β is the stretch exponential.

A.2 Dimensional Reduction

Dimensional reduction was applied to the dataset in two forms, without stacking (the conventional method) and with stacking. The latter approach was introduced in this study and has a distinct advantage in its ability to impose physical and chemical constraints onto the analysis. The desired outcome of dimensional reduction was to identify time-dependent fundamental piezoresponse behaviors (e.g. relaxation or poling trends) and generate spatial weightings of those behaviors (illustrated in Fig. 2a). This goal is complicated by the fact that the obtained dataset was measured as a function of 4 parameters: space (X and Y), time (t), applied voltage (p_v), and composition (e.g. p_c or PMN, PMN-0.36PT, and PMN-0.40PT). The conventional solution to this issue is to slice the dataset according to measurement parameters and analyze the slices independently, illustrated in the top arrow of Fig. 2b. In dimensional stacking, these slices are instead concatenated together either along the spatial dimension or along the temporal dimension, illustrated by the bottom two arrows in Fig. 2b.

A.2.1 Conventional Dimensional Reduction: Fitting Coefficients

The conventional method of dimensional reduction was performed on all compositions and voltages, i.e. independent application to each voltage/composition slice (the top arrows in Fig. 2b). Figure 3 shows the NMF analysis results

for all compositions and for a voltage approximately 2-3 times the negative coercive. Tables A.1 and A.2 report representative coefficients for the KWW fitting of the two components identified in the conventional NMF analysis shown in Figure 3.

Table A.1: Fitting coefficients for component 1 of the conventional NMF decomposition shown in Figure 3

Coeff.	PMN	PMN-0.36PT	PMN-0.40PT
A_0	70 ± 9	23 ± 5	36 ± 3
R_0	183 ± 17	325 ± 6	235 ± 4
τ	0.25 ± 0.03	0.23 ± 0.01	0.21 ± 0.01
β	1 ± 0.2	0.56 ± 0.01	0.63 ± 0.01

Table A.2: Fitting coefficients for component 2 of the conventional NMF decomposition shown in Figure 3

Coeff.	PMN	PMN-0.36PT	PMN-0.40PT
A_0	132 ± 13	210 ± 4	229 ± 5
R_0	-146 ± 21	-160 ± 6	94 ± 5
τ	0.27 ± 0.05	0.19 ± 0.02	0.48 ± 0.08
β	1 ± 0.2	0.61 ± 0.04	0.5 ± 0.02

A.2.2 Dimensional Reduction with Stacking: Quantitative Values

Introduction of physical and chemical constraints into dimensional reduction analysis can be achieved through concatenation or stacking of the $D^{p_v,p_c}(t,z)$ datasets prior to analysis. If individual $D^{p_v,p_c}(t,z)$ datasets for different p_v and/or p_c values are stacked together along the temporal or spatial dimension, the results will inherit the p_v and/or p_c dependence after the DR process. This approach can thus be used to impose constraints to the DR analysis: stacking of datasets along the temporal dimension will impose a spatial constraint, and an stacking along the spatial dimension will impose temporal correlation.

Results from the NMF analysis of the voltage stacked PMN-0.36PT data is shown in Figure 4a for stacking along the temporal axis and Figure 4b for

stacking along the spatial axis. Figures A.8 and A.9 show a recreation of the results in Figures 4a and b respectively. Both Figures now report quantitative values for the components. Figure A.10 shows the components from the NMF analysis of the combined voltage- and composition-stacking of the entire dataset (originally shown in Figure 5). However, here we report quantitative values for the amplitude of the components. Additionally, Figures A.8 and A.10 label each of the trends in the components with respect to the corresponding applied voltage pulse.

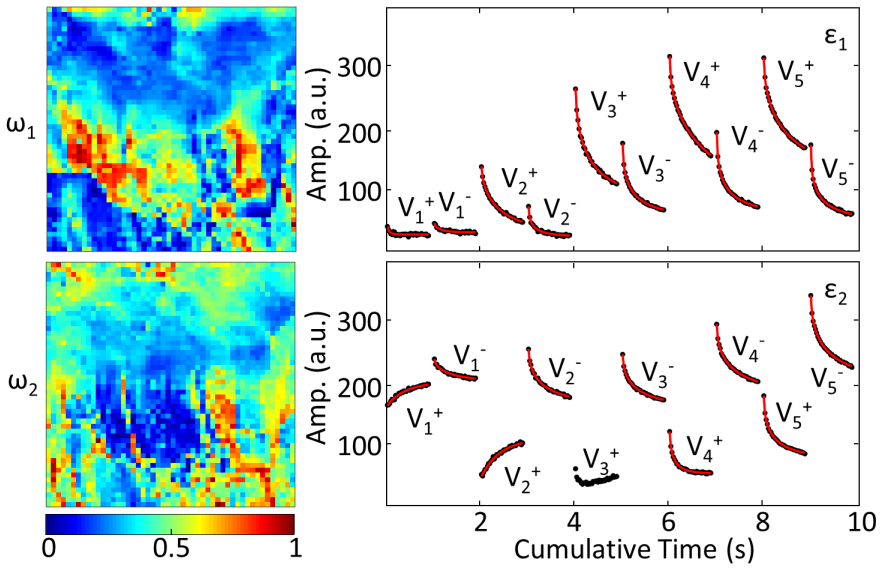

Figure A.8: The results of voltage stacking along the temporal axis for PMN-0.36PT now including quantitative information for the components and labels for each trend indicating which of the applied pulses the trend corresponds to. Red lines indicate the KWW fit to each curve.

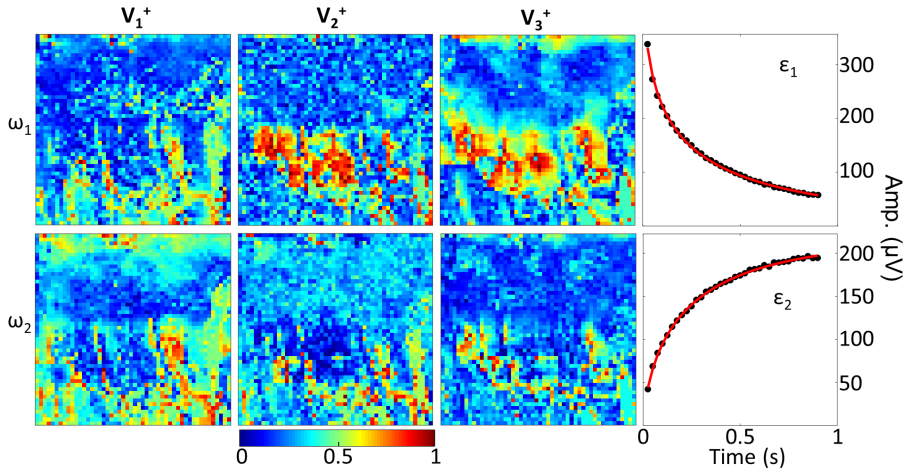

Figure A.9: The results of voltage stacking along the spatial axis for PMN-0.36PT now including quantitative information for the components. Red lines indicate the KWW fit to each curve.

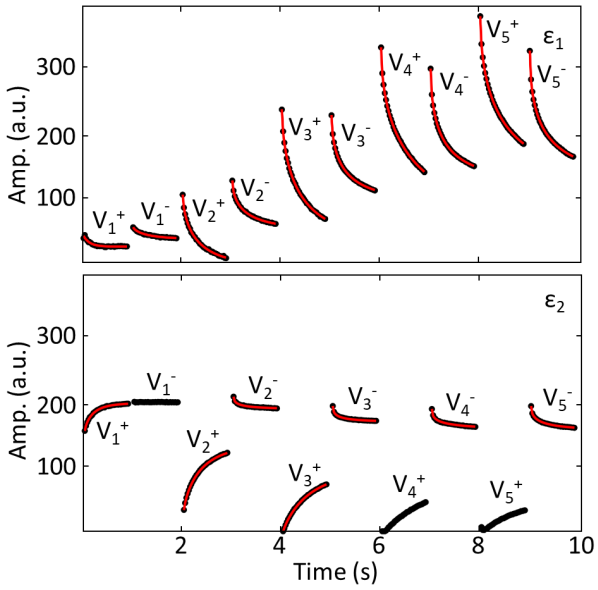

Figure A.10: Components obtained from a combined voltage- and composition-stacking NMF analysis of the entire dataset with quantitative Y axis (piezoresponse amplitude) values. Each trend is labeled with the corresponding applied voltage pulse. These components were originally reported without quantitative information in Figure 5, here the components are plotted without the weight maps for simplicity.

APPENDIX B

ELECTROMECHANICAL SWITCHING IN FERROELECTRIC THIN FILMS

B.1 Experimental Set Up: BE-PFM and SSPFM Characterization

Fig. B.1 shows the basic PFM scan images of the probed area. Fig. B.1a and B.1b show the out-of-plane piezoresponse amplitude (A), phase (ϕ), and height prior and post to polarization switching characterization, respectively. The in-plane phase information was not included in previous reports [144, 145], and hence assignment of specific locations to *a* or *c* domains is simply based on the amplitude characteristics. The amplitude images show large bands with strong out-of-plane response, representing the *c/a* domain stripes, and bands with limited out-of-plane response, representing the a_1/a_2 domain stripes. The *c/a* domain stripes shows local variations in amplitude and phase, with no or very limited out-of-plane piezoresponse. Similar to previous reports, we identify these striations as *a*-domains within the *c/a* band. The before (”initial”) and after (”final”) phase images confirm switching and, further, striations due to the *a* domains within the *c/a* domains are again visible in the initial image. Finally, the height images highlight the sawtooth topography of the sample area.

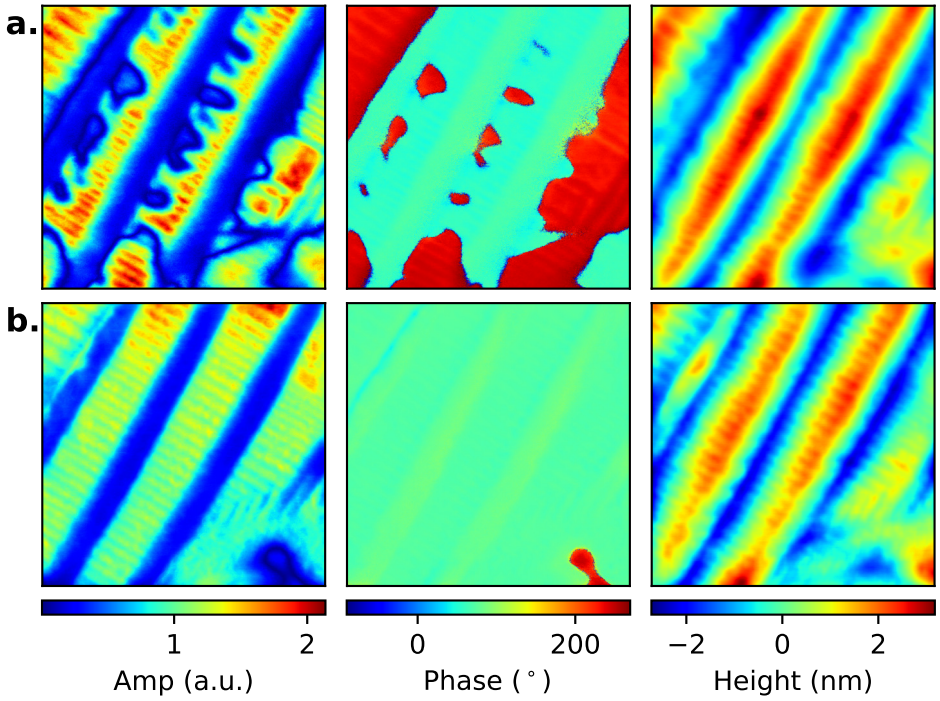

Figure B.1: (Left to right) The (a) "initial" and (b) "final" out-of-plane piezoresponse amplitude and phase, and height of the sampled area, characterized (a) before and (b) after switching spectroscopy.

B.2 Pre-Processing of Data

The previous reports [144, 145] on the data set include a number of operations performed on the data both before and after analysis: data cleaning, interpolation, removal of bad points, normalization, and rotations. Rotations apply also additional interpolations after all the prior operations have been performed. We do not comment on the above operations, as the authors do not fully discuss the motivation for all operations performed. Furthermore, the raw data or specifics of fitting to the simple harmonic oscillator

(SHO) model have not been reported by the authors. However, data quality has a strong impact on the results of ML analysis: hence, handling of the data must be carefully scrutinized. Thus, for this work, we began with the un-processed as-provided data and adopted only the pre-processing steps (previously applied and reported) that we found to be reasonable and necessary. Below we briefly describe the rationale for the operations that were performed on the data in our work.

B.2.1 Resonance Data

Following previous analysis of this data set, the contact resonance data was first subjected to a hard limit, i.e. resonance values less then 1300 kHz and greater than 1340 kHz were removed from consideration. We assume that such outliers cannot correspond to realistic changes in the material's properties, but more probably can be assigned to local tip-sample contact variations. Alternatively, very low piezorepsonse (and hence low signal-to-noise ratio) could result in incorrect identification of the resonance peak and hence extracted peak parameters. We underline once again that the original publication of the data set in [144, 145] does not discuss this choice. Thus, in choosing to apply these hard limits in the current work, we defer to the researchers who performed the measurement and are familiar with the specific acquisition tool's and used fitting algorithm's limitations. Next, non-numerical values, which typically represent points where the SHO fitting

has failed, were interpolated with a spline fitting as in the previous reports. We note that most machine learning techniques cannot operate on data sets with undefined values. An alternative option for removal of "nil" or "inf" values would be to replace the these with the mean value or zero. However, such choices are not always consistent with the underlying physics of the probed sample. Finally, as outlined in the manuscript, in order to account for the gradual shifts in the resonance frequency during the scan, the mean value for each curve was removed for each point's switching response.

B.2.2 Piezoresponse Data

While the piezoresponse data, *PR*, has been provided within the data set, it was recalculated here through application of Equation 2.1. The optimal rotation angle is an arbitrary angle used to maximize the cosine function for each point. While the original data set provides an optimal rotation angles for each *PR* point, we believe that such an arbitrary rotation may remove important spatial information by applying an unnecessary normalization across the spatial points. As such, we used the average of the provided optimal rotation angles, and applied it equally to all points in Equation 2.1. Subsequently, the mean value of the piezoresponse at each point was removed to maintain consistency with the resonance data.

In order to create comparable data sets for dimensional stacking, the range of values in the piezoresponse data must be made analogous to the

range of values in the resonance data. Specifically, ω values range in the hundreds or thousands of kHz, whereas *PR* values are in the tens of μV range. As ML techniques are essentially mathematical optimizations, minimizing the error in the representation of the larger variable (resonance frequency) will be prioritized due its larger value. The local mean removal process obviates in part to this problem by centering all data series around zero. However, to ensure that the Dictionary Learning algorithm weights the piezoresponse and resonance equally, the piezoresponse is multiplied by a constant factor (3), before stacking to resonance, in order to offer comparable standard deviation for both set of data. The same factor is removed once the components are obtained from Dictionary Learning output. Thus, the stacked piezoresponse and resonance ($PR - \omega$) data have each a mean of 0 (due to the point-by-point mean removal) and comparable standard deviations (≈ 0.6).

B.3 Root Mean Squared Error Evaluation

When comparing various dimensional reduction (DR) results, a metric for goodness-of-fit should be considered. Here, we use the root mean squared error (RMS) or the root mean squared of the residuals. Given a data set D and a set of DR-derived eigenvectors (V) with corresponding eigenvalues (U) approximating D, the root mean squared error (RMS) can be calculated

with Equ. B.1.

$$E_{RMS} = \sqrt{\frac{\sum_{t=0}^{L}(D - UV)^2}{L}} \tag{B.1}$$

Here, the squared error of the dimensional reduction ($(D - UV)^2$) is averaged over some dimension L and its square root is calculated. In the present work, the squared errors are calculated at each spatial point for each value of the piezoresponse/resonance curves and then averaged over the piezoresponse/resonance curves. This results in spatial maps of the RMS error (examples shown in Fig. 5.5). In addition, these RMS error spatial maps are also averaged into a single RMS error metric (Fig. 5.5).

B.4 Comparing 6 component dictionary learning results with amplitude scans

Fig. B.2 compares the resulting weight maps from Fig. 5.6 to the *c* and *a* domains within the *c/a* stripes. Due to the lack of a lateral PFM image and cross-talk between piezoresponse and topography, the identification of *c* and *a* domains in Figure B.2 is non-exhaustive and simply a best approximation. Specifically, to identify the *c*-domains and the *a*-domains within the *c/a* stripes, we use the out-of-plane *amplitude* images. Within the *c/a* stripes, striations corresponding to comparatively stronger and weaker piezoresponse amplitude can be observed. The *c*-domains are expected to exhibit the strongest out-of-plane piezoresponse, and indeed were seem-

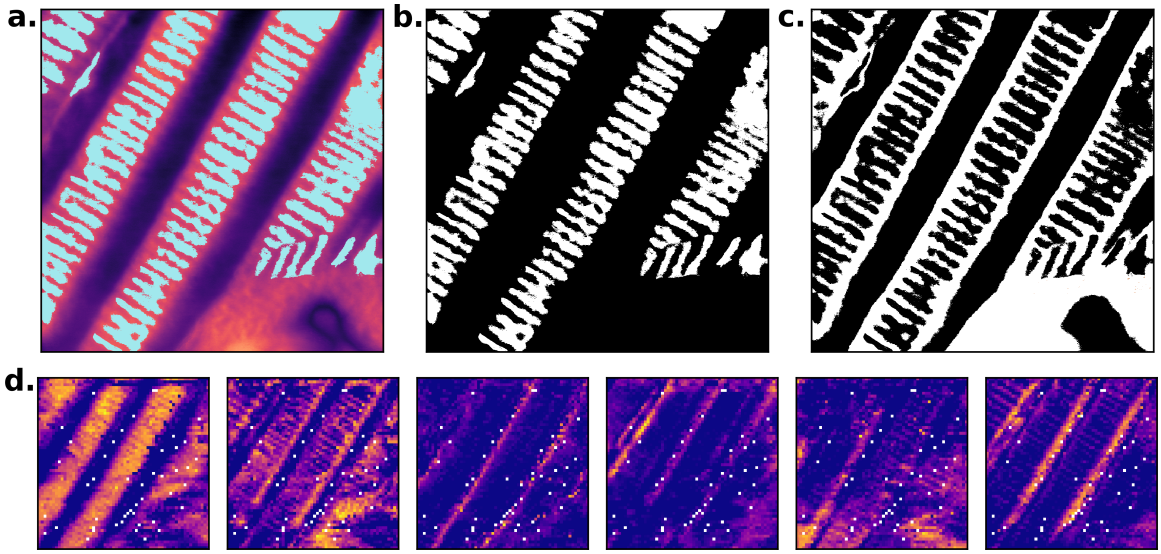

Figure B.2: A comparison of the results obtained in Fig. 5.6 and the identified *c*- and *a*- domains. (a) The BE piezoresponse amplitude performed after the switching characterization where the blue-gray lines highlight the *c*-domains with the *c/a* stripe. The mean of each horizontal line was removed for clarity, to adjust for a slight reduction of the amplitude from the top left to the bottom right of the sampled area. This shift in amplitude is visible in Fig. 5.4. (b) part (a) in black and white, where the white corresponds to the *c*-domains within the *c/a* domain stripe. (c) the inverse of (b), i.e. the *a*-domains highlighted in white. (d) The weight maps obtained for the $N = 6$ and $\alpha = 1$ analysis, as shown in Fig. 5.6. The first component from left shows strong presence in locations corresponding to mostly *c* domains in parts (a) and (b).

ingly assigned in the original data set analysis also to *c* domains[144]. In Fig. B.2a and b, the *c* domains were identified by applying a local threshold to the amplitude image. The *a* domains (Fig. B.2c) were identified by inverting the *c* domain image (Fig. B.2b). By comparing Fig. B.2b to the weight maps obtained from the Dictionary Learning analysis, we can identify components most closely related to the *c* domains, such as the leftmost weight map in Figure B.2d.

B.5 Dictionary Learning - Components' Correlation with Topography

Figs. B.3 and B.4 show the resulting weight maps from Figs. 5.6 and 5.9 projected onto the topography. In Fig. B.3 it is apparent that N_3 is almost entirely limited to the regions within the valleys of the topography. As stated in the main text, increased mechanical constraints from the surrounding materials could result in the presence of backswitching as evidenced in the piezoresponse curve of N_3.

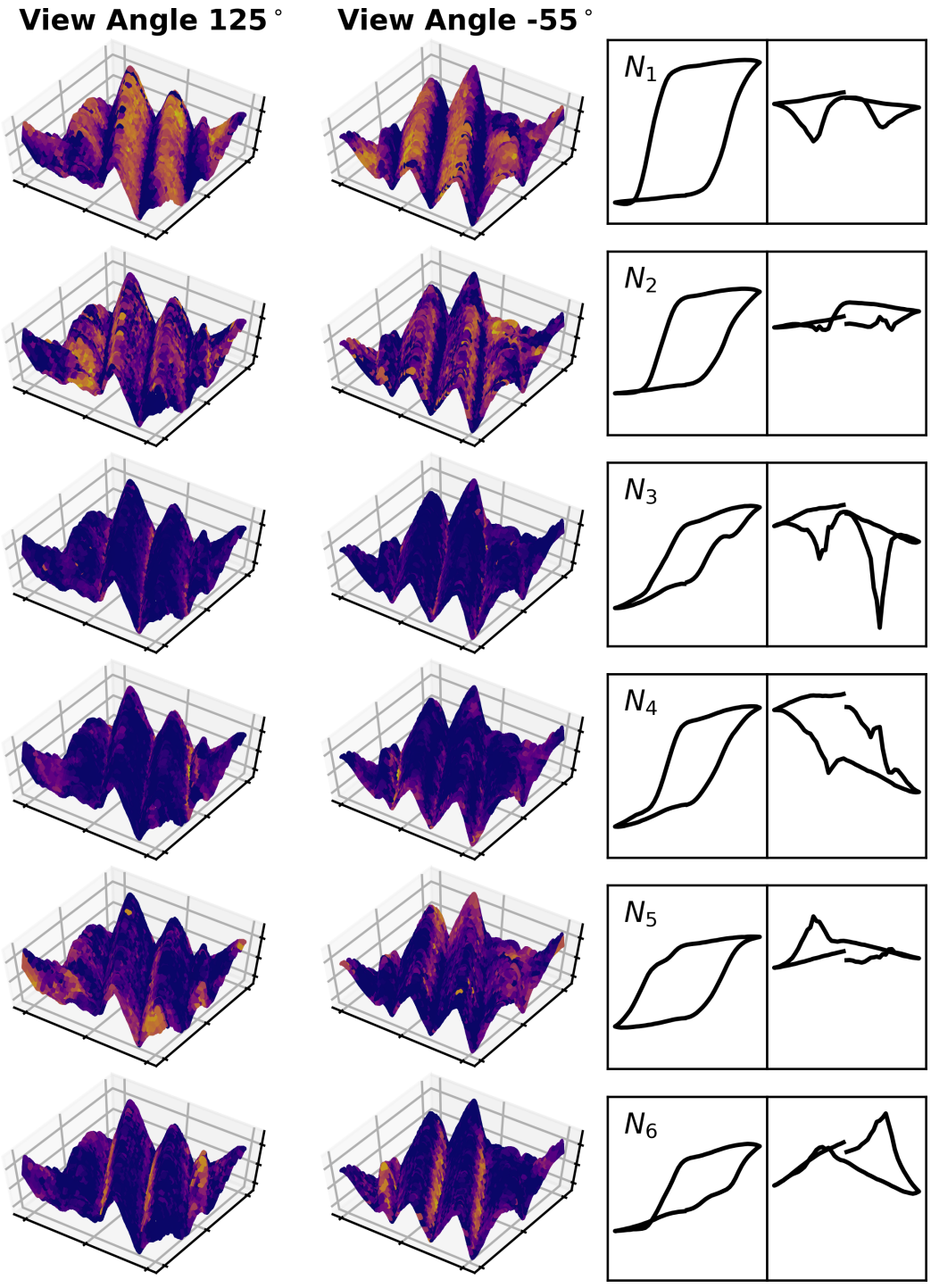

Figure B.3: The weight maps and components from Fig. 5.6 with the maps projected onto the topography of the sample area and viewed from two angles

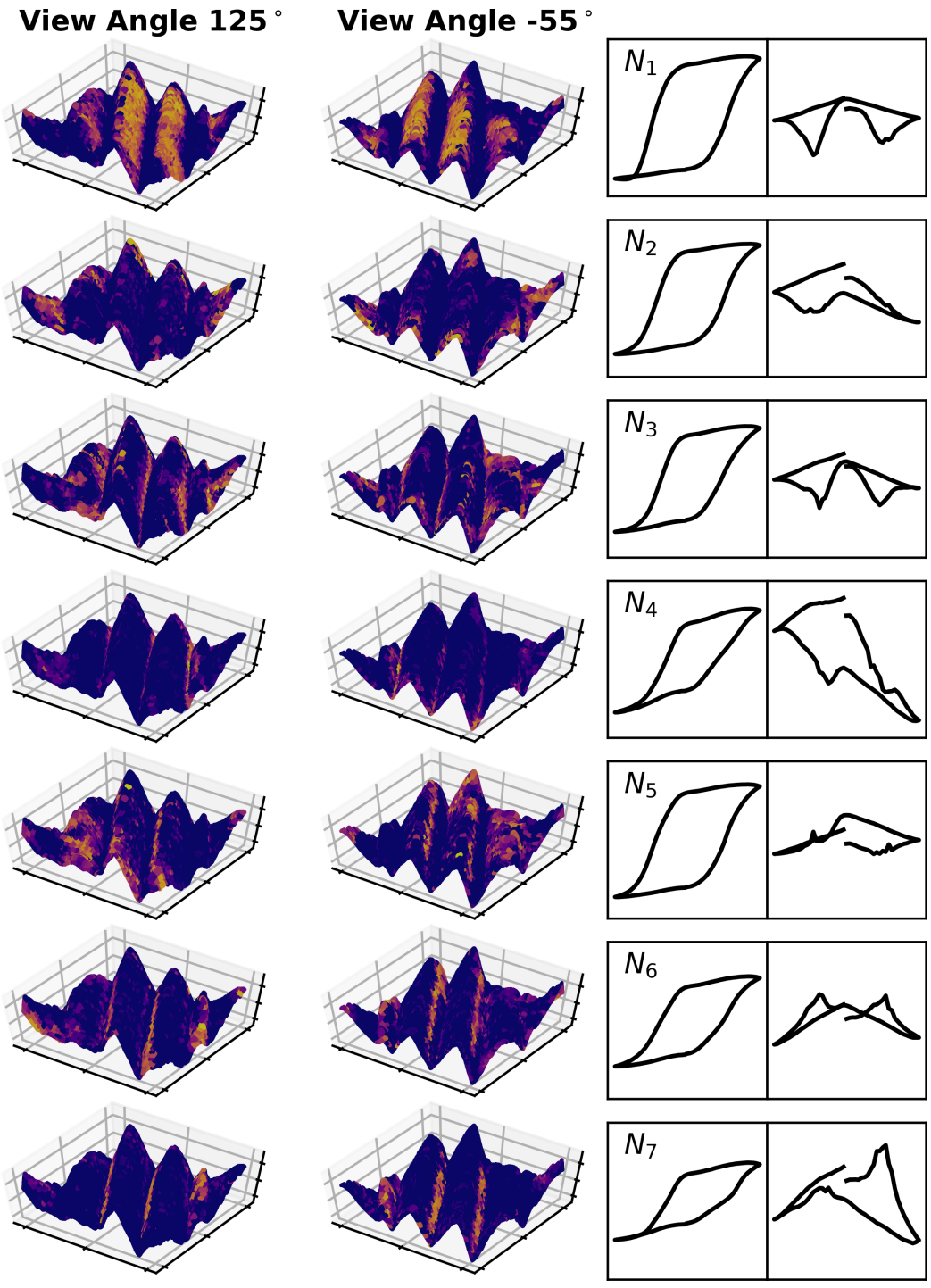

Figure B.4: The weight maps and components from Fig. 5.9 with the maps projected onto the topography of the sample area and viewed from two angles

B.6 Review of Physical Contributors to the Switching PFM Response

In our discussion, various behaviors are attributed to electrostatic/electrochemical effects (e.g. N_5 and N_6 in Figure 5.6), Shottky-like barrier behavior (e.g. N_4 in Figure 5.6), and ferroelastic-mediated switching. Specifically:

- The behaviors attributed to electrostatics/electrochemical effects (e.g. N_5 and N_6 in Figure 5.6) exhibit a significant contact resonance hardening at near-coercive voltages, consistent with the glass data (Figure S8), and piezoresponse behavior consistent with previously reported studies[160, 161, 162].

- The highly asymmetric behavior (e.g. N_4 in Figure 5.6) is attributed to a combination of a Shottky barrier, conduction, and non-ferroelectric (glass-like) behavior. Specifically:

  - the piezoresponse curve of N_4 can be approximated by considering a superposition of reported electrochemical and conduction contributors as in Balke and coworkers[160], or combined PFM response of glass and ceria in Collins et al.[161].

  - similar highly asymmetric contact resonance curves have been reported via PFM of piezoelectrically-active but not ferroelectric ZnO[163] thin films. Such an asymmetry can therefore be associated largely with Shottky barrier type behaviors, given the semi-

conducting nature of the films.

- Previous studies have shown that ferroelastic switching can results in substantial electromechanical softening in proximity of the coercive voltages.[159] This is consistent with the resonance behavior observed in N_3 in Figure 5.6. However, this significant softening is not observed in analyses with higher α values, suggesting that this behavior is possibly non-physical.

B.7 Sampled Raw Data and Topography Correlation

The functional response of the film is strongly correlated with the topography, as illustrated in Figure B.5, likely due to non-flat tip-surface contact during probing. Fig. B.5 and Fig. B.6 show the topography of four selected sub-areas of the sample, overlaid with individual piezoresponse, resonance, amplitude, and phase curves at their (approximate) corresponding probing locations. In general, the overall change in amplitude increases across the *c/a* stripes and is smallest in a_1/a_2, particularly in proximity of the vallyes in the topography. Similarly, phase curves with missing numerical values and/or with unphysical values (phase differing from saturation at one voltage or the other) are most common in a_1/a_2 stripes. The overall outcome is that stunted and skewed piezoresponse loops (e.g. Fig. B.6d and e and associated with the "notch" seen in Figs. 5.6 and 5.9) are mostly correlated with the a_1/a_2 stripes and the topography valleys. Additionally, a sharp

transition in the piezoresponse curves occurs at topographic ”peaks” and ”valleys”. For instance, typical piezoresponse curves transition to stunted (i.e., substantially suppressed) curves at the ”peak” in Fig. B.5b and from stunted to typical curves at the ”valleys” in Fig. B.5b and Fig. B.6c. We note that phase curves missing numerical data near coercive voltages appear to be more common in and around the valley's in Fig. B.5e. Such missing values are often due to a failed extraction of functional parameters from the simple harmonic oscillator (SHO) model. Considering that missing or unphysical points predominately occur near coercive voltages, it is reasonable to suggest that the reduced piezoresponse, resulting in poor signal-to-noise ratio, can lead to a failed SHO fitting, or selection of a resonance peak in the acquired data, which does not correspond to the actual electromechanical response of the sample. Finally, we highlight the substantial changes in the resonance behavior seen in component N_4 of Figs. 5.6 and 5.9 is observed in Fig. B.5c and Fig. B.6c, confirming that this component is *not* due to overfitting.

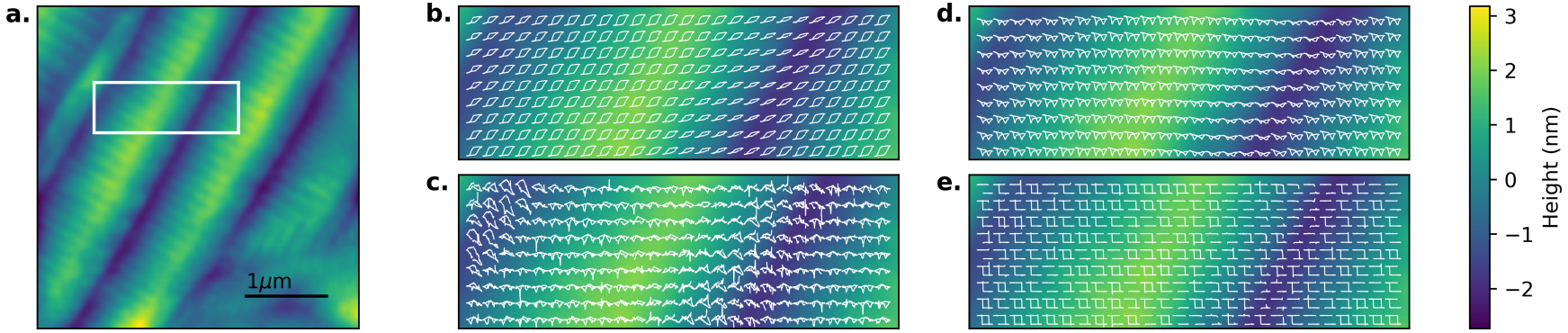

Figure B.5: Sampled piezoresponse, resonance, amplitude, and phase correlated to topography. a) The topography of the 2 μm by 2 μm square area, the white box represents the sampled area. b, c, d, and e) The piezoresponse, resonance, amplitude and phase overlaid the topography within the area corresponding to the white square in (a). The individual variables are all plotted on a identical axis scales, allowing assessment of vertical shifts, and point-to-point variations in the data.

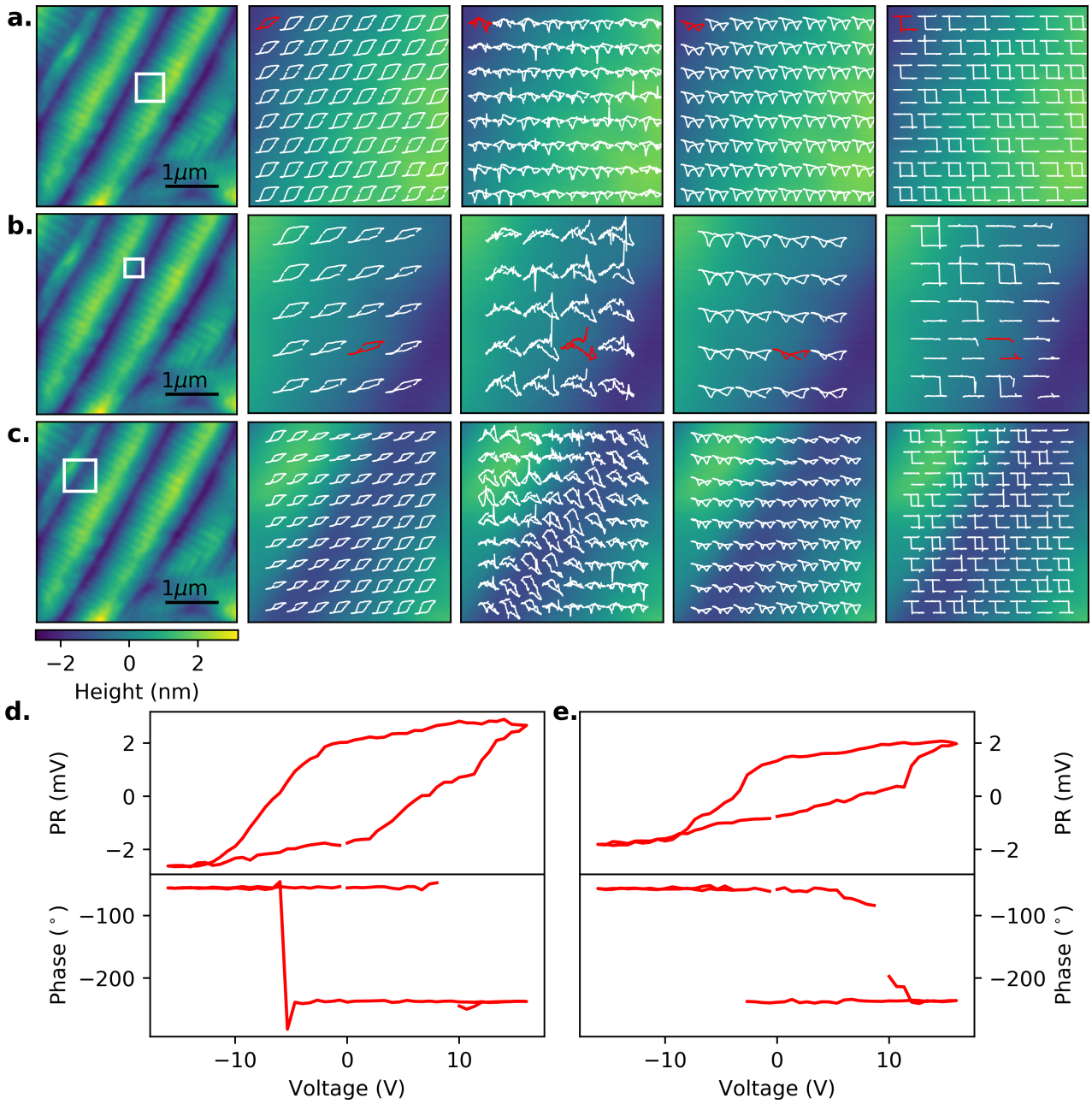

Figure B.6: Sampled piezoresponse, resonance, amplitude, and phase correlated to topography for (a) the *c/a* domain stripe, (b) the a_1/a_2 domain strip, and (c) an intermediate region overlapping both. a, b, and c) From left to right: topography of sampled areas, followed by piezoresponse, resonance, amplitude and phase overlaid on the topography of the area marked by the corresponding white square. These sampled areas lie within: (a) the *c/a* domain stripe, (b) the a_1/a_2 domain stripe, and (c) an area overlapping both. d) The individual variables are all plotted on a identical axis scales, allowing assessment of vertical shifts, and point-to-point variations in the data. d) Piezoresponse and phase curves for point identified in (a) in red. The piezoresponse is on the top and the phase is on the bottom. e) Piezoresponse and phase curves for point identified in (b) in red. The piezoresponse is on the top and the phase is on the bottom.

B.8 Dictionary Learning - Effects of N and α

As illustrated in Fig. 5.5, the ideal number of components (N) and α parameter for this data set are $N = 5 - 7$ and $\alpha = 1$, with a comparatively weak effect of α, as seen in Fig. 5.5. Figs. B.7-B.15 shows the results of a $PR - \omega$ stacked dictionary learning analysis for $N = 5, 6,$ and 7 and for $\alpha = 1, 6,$ and 12. Most analyses consistently show the same 4 components. First, component N_1 of all analyses are very similar and indicate typical ferroelectric switching within the *c*-domain stripes of the *c*-*a* domains. Second, the behavior with the highly asymmetric resonance curve occurs in component N_3 in the N=5 analyses (Figs. B.7, B.8, and B.9) and component N_4 in N=6 (Figs. B.10, B.11, and B.12) and N=7 (Figs. B.13, B.14, and B.15) analyses. Finally, the two behaviors with complementary asymmetric hardening, associated with a non-ferroelectric phenomena, are persistently the last two components of all analyses, except for the $N = 7$ and $\alpha = 12$ analysis (Fig. B.15).

Additional behaviors are present depending on the particular parameters used. The asymmetric behavior in component N_2 of Figs. B.8 and B.9, Figs. B.11 and B.12, and Figs. B.13, B.14, and B.15 tends to appear with increased α and there is often a spatially complimentary behavior, e.g. component N_5 in Figs. B.11 and B.12 and Figs. B.14 and B.15. The piezoresponse curves for these two behaviors (N_2 and N_5) are typical and change

little when increasing α from 6 to 12. For N_2, the resonance curves are also fairly consistent across model parameters, i.e. an almost linear trend at positive voltages and a somewhat typical ferroelectric softening at negative voltages. However, the resonance curve for N_5 shows more substantial changes. At high α and N (Fig. B.15), N_5 has a resonance behavior complimenting N_2, i.e. an almost linear trend at negative voltages and softening at positive voltages, but at lower N/α the resonance behavior is drastically different, showing hardening at negating voltages. The drastic behavioral changes and complimentary spatial maps of N_5 support that it is sensitive to over-fitting and perhaps combines the behavior from various other components. Meanwhile, N_2 is more consistent and could represent limited hysteretic behavior, but, being complimentary with N_5, could also represent some degree of overfitting. Finally, the atypical notched piezoresponse curve seen in N_3 in Fig. B.10 and Fig. B.13, notably becomes a classic ferroelectric piezoresponse loop as α is increased. In fact, the notched behavior is likely related to measurement and data processing errors as illustrated in Fig. B.5 and B.6.

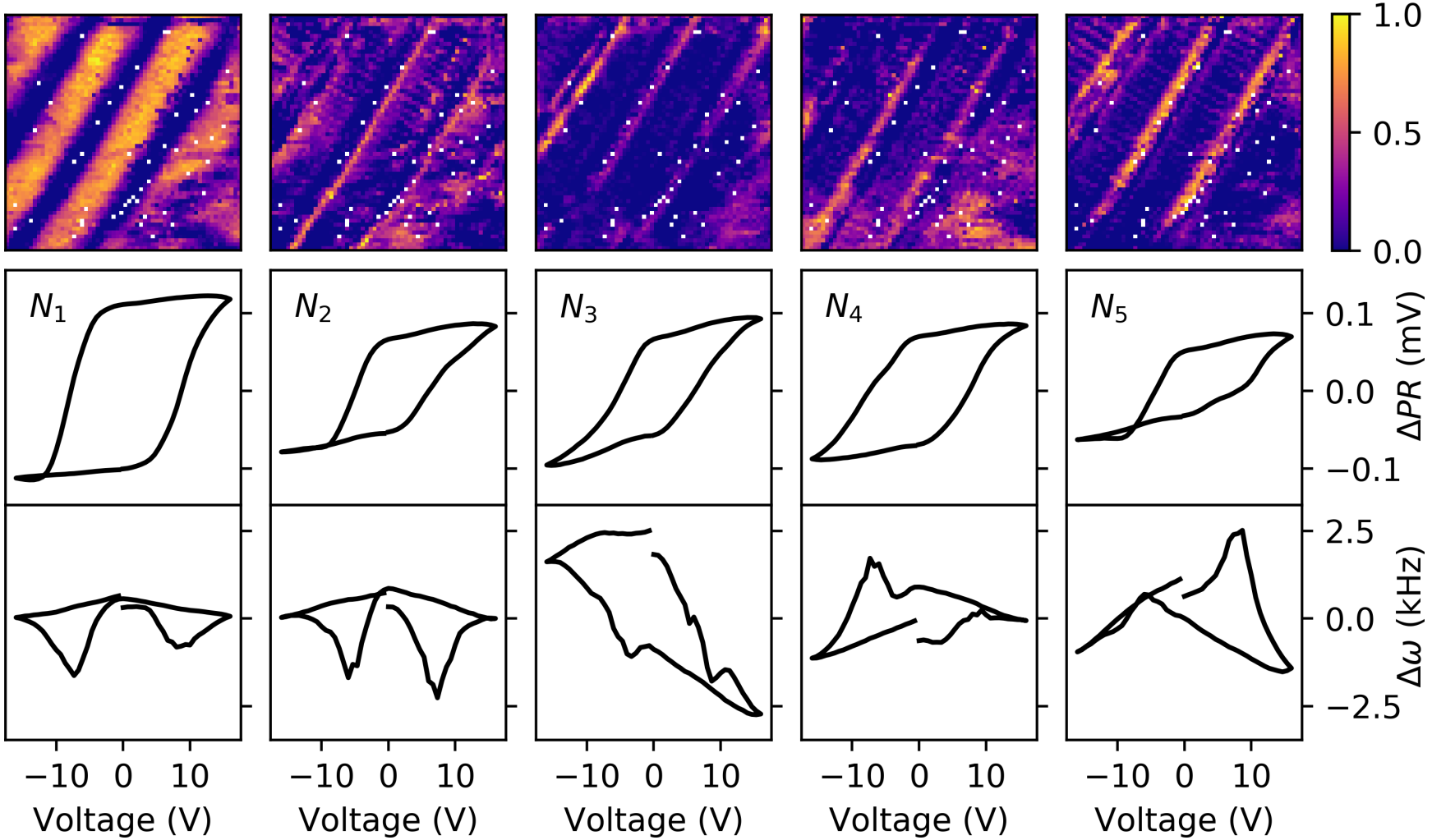

Figure B.7: Dictionary learning of stacked mean-subtracted $PR - \omega$ for $N = 5$ and for $\alpha = 1$. At each spatial point, the observed piezoresponse and resonance behavior can be approximated as a linear superposition of the spatial weight maps (top row) multiplied by the corresponding derived behaviors. Here, the middle row is the piezoresponse behavior and the bottom row is the corresponding resonance behavior. Prior to analysis, the point-by-point mean was removed from both the resonance and piezoresponse data. Further, the piezoresponse was multiplied by a constant factor such that the values were comparable to that of the mean removed resonance values (See Supplemental Note 1).

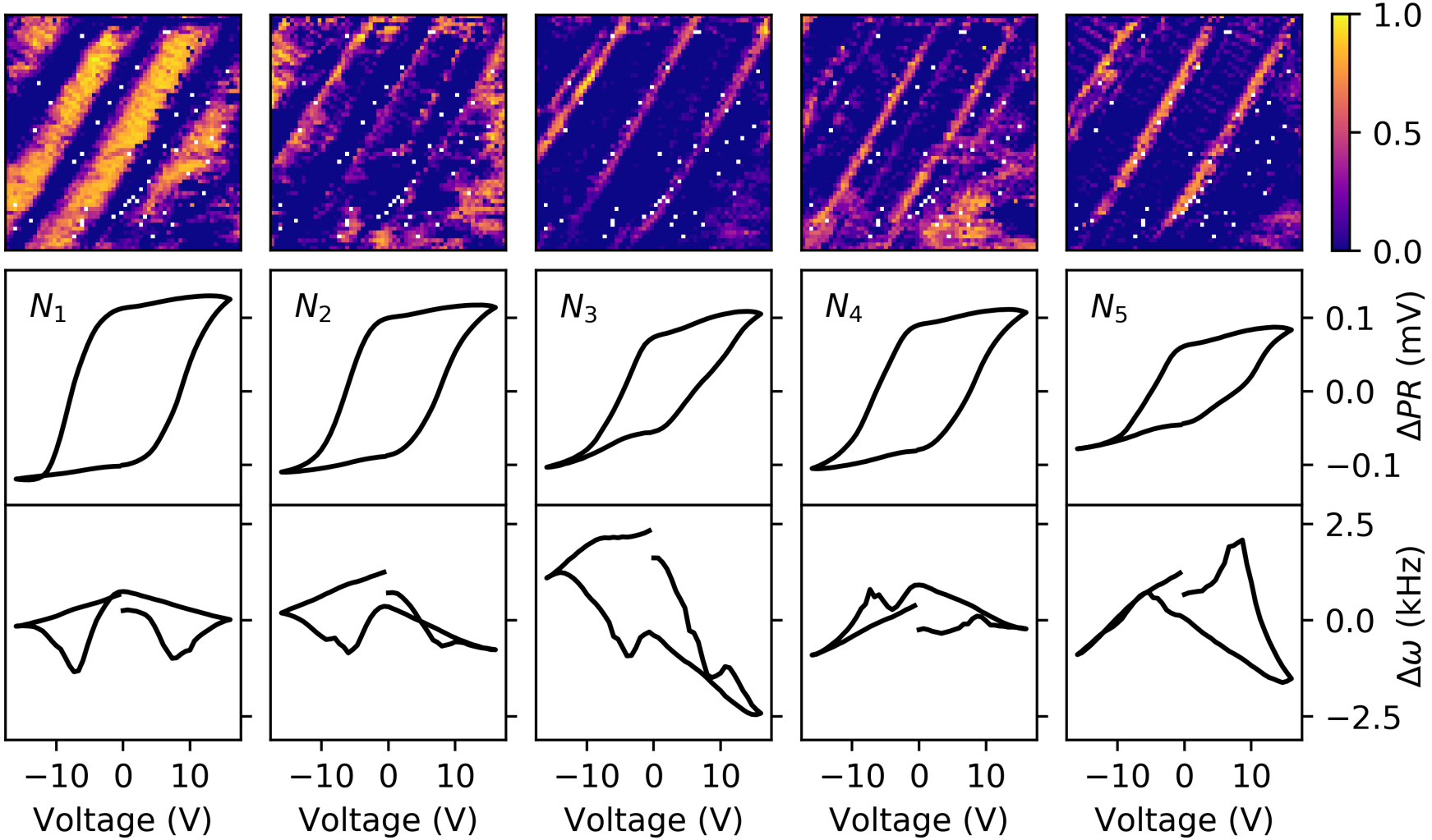

Figure B.8: Dictionary learning of stacked mean-subtracted $PR - \omega$ for $N = 5$ and for $\alpha = 6$. At each spatial point, the observed piezoresponse and resonance behavior can be approximated as a linear superposition of the spatial weight maps (top row) multiplied by the corresponding derived behaviors. Here, the middle row is the piezoresponse behavior and the bottom row is the corresponding resonance behavior. Prior to analysis, the point-by-point mean was removed from both the resonance and piezoresponse data. Further, the piezoresponse was multiplied by a constant factor such that the values were comparable to that of the mean removed resonance values (See Supplemental Note 1).

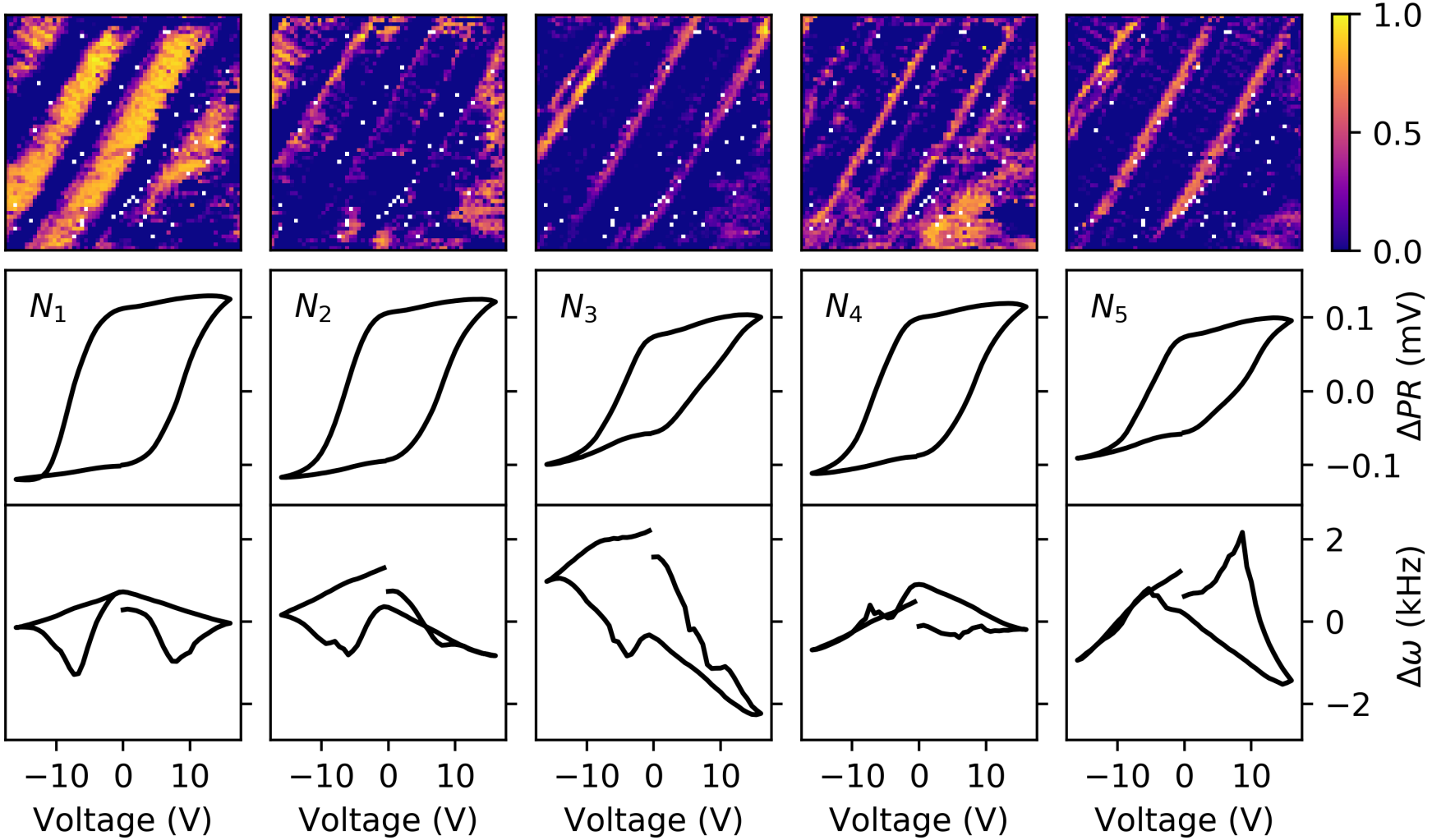

Figure B.9: Dictionary learning of stacked mean-subtracted $PR - \omega$ for $N = 5$ and for $\alpha = 12$. At each spatial point, the observed piezoresponse and resonance behavior can be approximated as a linear superposition of the spatial weight maps (top row) multiplied by the corresponding derived behaviors. Here, the middle row is the piezoresponse behavior and the bottom row is the corresponding resonance behavior. Prior to analysis, the point-by-point mean was removed from both the resonance and piezoresponse data. Further, the piezoresponse was multiplied by a constant factor such that the values were comparable to that of the mean removed resonance values (See Supplemental Note 1).

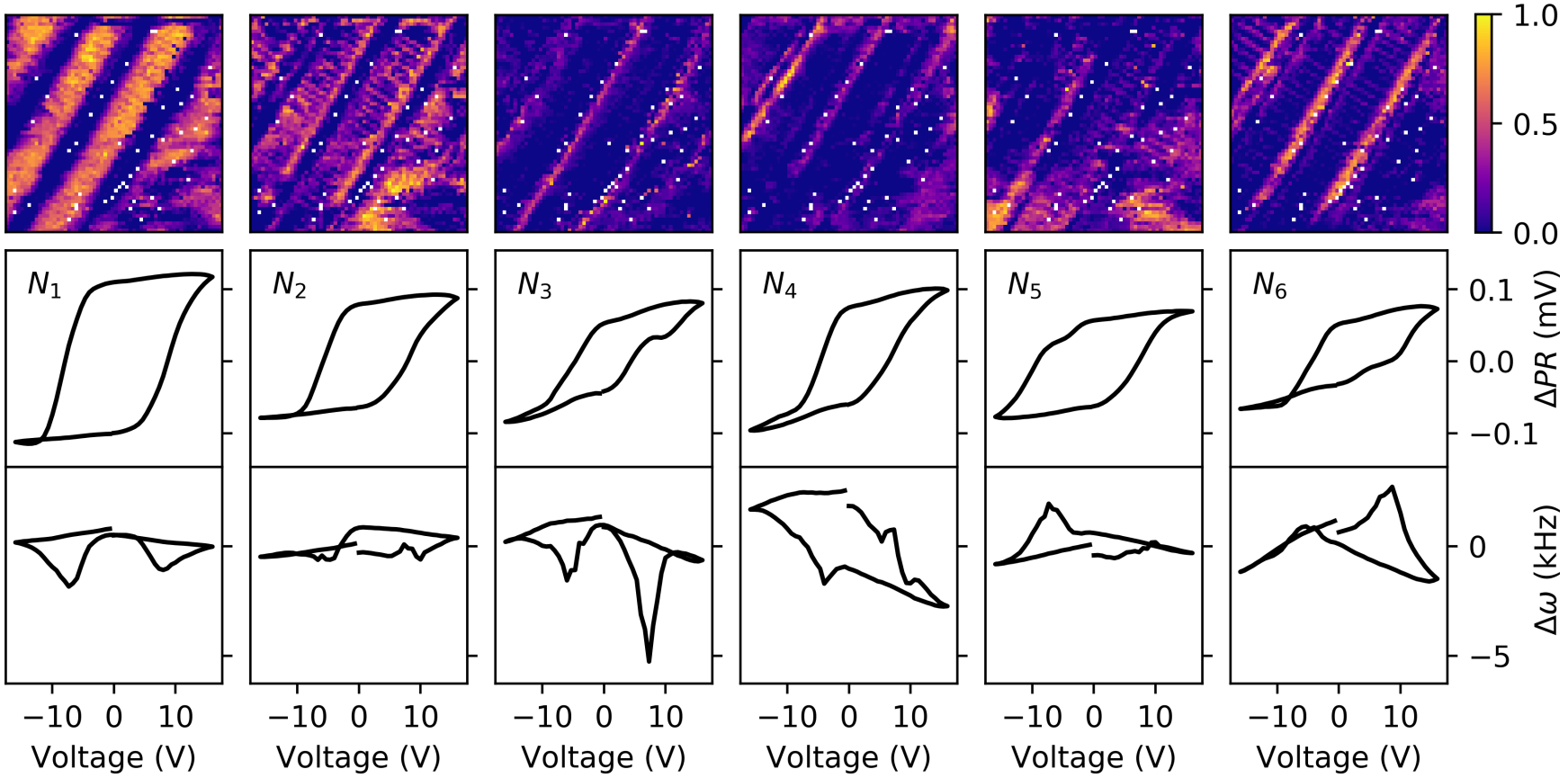

Figure B.10: Dictionary learning of stacked mean-subtracted $PR - \omega$ for $N = 6$ and for $\alpha = 1$. At each spatial point, the observed piezoresponse and resonance behavior can be approximated as a linear superposition of the spatial weight maps (top row) multiplied by the corresponding derived behaviors. Here, the middle row is the piezoresponse behavior and the bottom row is the corresponding resonance behavior. Prior to analysis, the point-by-point mean was removed from both the resonance and piezoresponse data. Further, the piezoresponse was multiplied by a constant factor such that the values were comparable to that of the mean removed resonance values (See Supplemental Note 1).

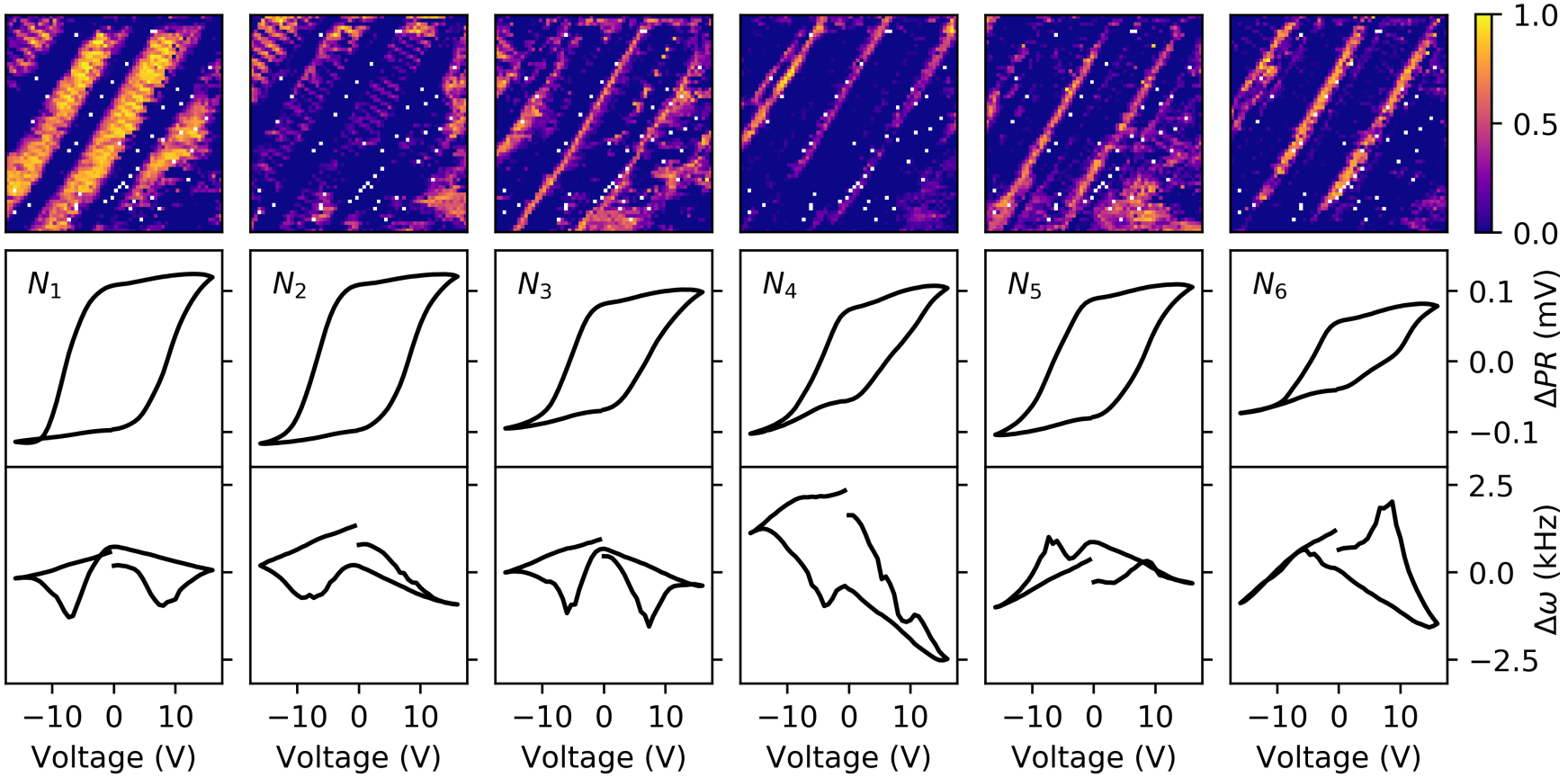

Figure B.11: Dictionary learning of stacked mean-subtracted $PR - \omega$ for $N = 6$ and for $\alpha = 6$. At each spatial point, the observed piezoresponse and resonance behavior can be approximated as a linear superposition of the spatial weight maps (top row) multiplied by the corresponding derived behaviors. Here, the middle row is the piezoresponse behavior and the bottom row is the corresponding resonance behavior. Prior to analysis, the point-by-point mean was removed from both the resonance and piezoresponse data. Further, the piezoresponse was multiplied by a constant factor such that the values were comparable to that of the mean removed resonance values (See Supplemental Note 1).

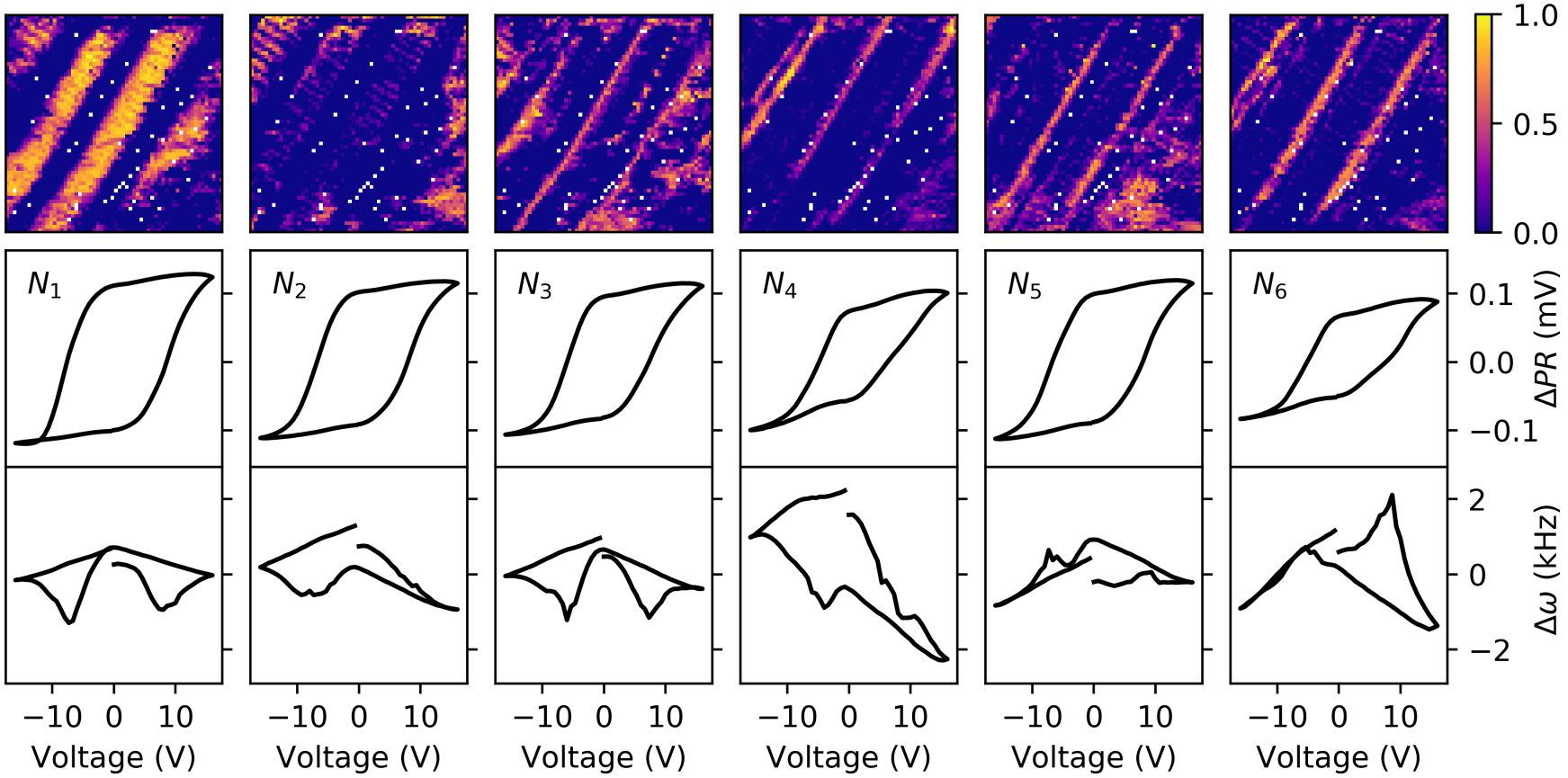

Figure B.12: Dictionary learning of stacked mean-subtracted $PR - \omega$ for $N = 6$ and for $\alpha = 12$. At each spatial point, the observed piezoresponse and resonance behavior can be approximated as a linear superposition of the spatial weight maps (top row) multiplied by the corresponding derived behaviors. Here, the middle row is the piezoresponse behavior and the bottom row is the corresponding resonance behavior. Prior to analysis, the point-by-point mean was removed from both the resonance and piezoresponse data. Further, the piezoresponse was multiplied by a constant factor such that the values were comparable to that of the mean removed resonance values (See Supplemental Note 1).

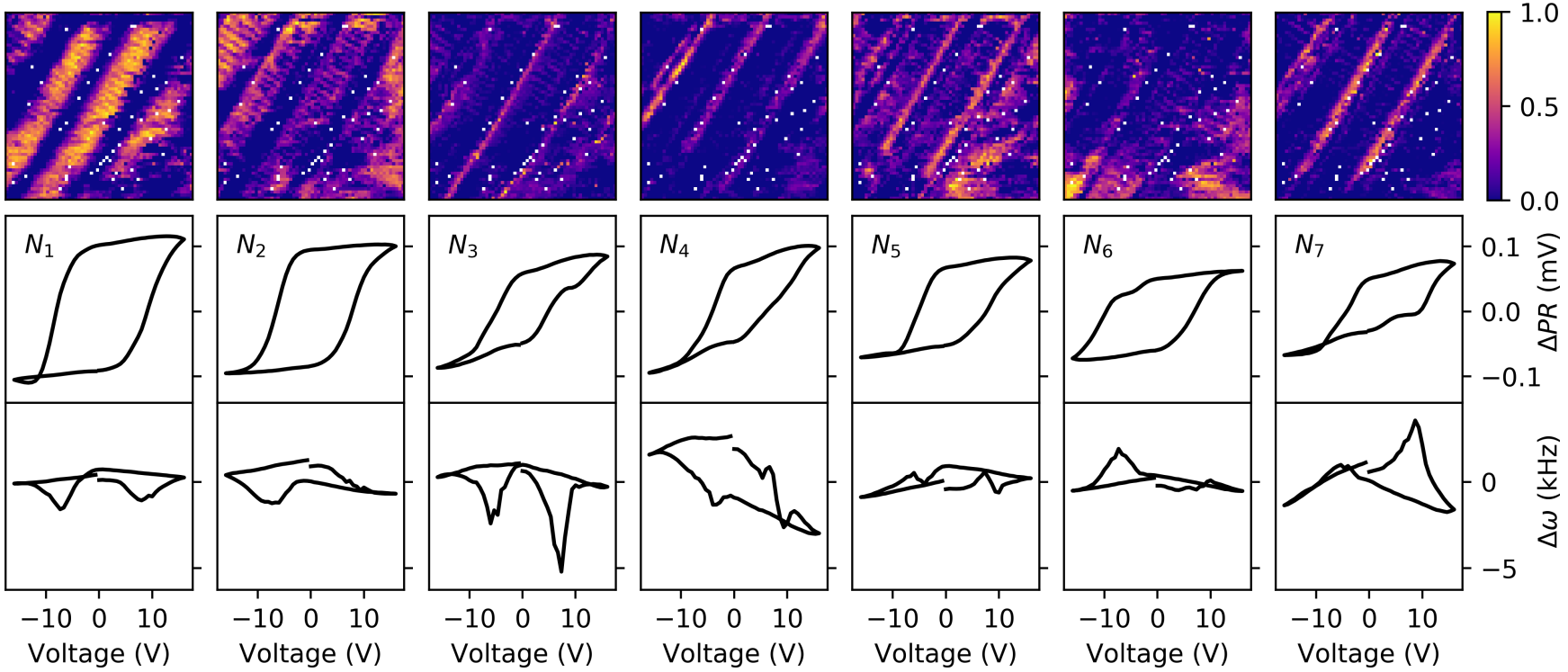

Figure B.13: Dictionary learning of stacked mean-subtracted $PR - \omega$ for $N = 7$ and for $\alpha = 1$. At each spatial point, the observed piezoresponse and resonance behavior can be approximated as a linear superposition of the spatial weight maps (top row) multiplied by the corresponding derived behaviors. Here, the middle row is the piezoresponse behavior and the bottom row is the corresponding resonance behavior. Prior to analysis, the point-by-point mean was removed from both the resonance and piezoresponse data. Further, the piezoresponse was multiplied by a constant factor such that the values were comparable to that of the mean removed resonance values (See Supplemental Note 1).

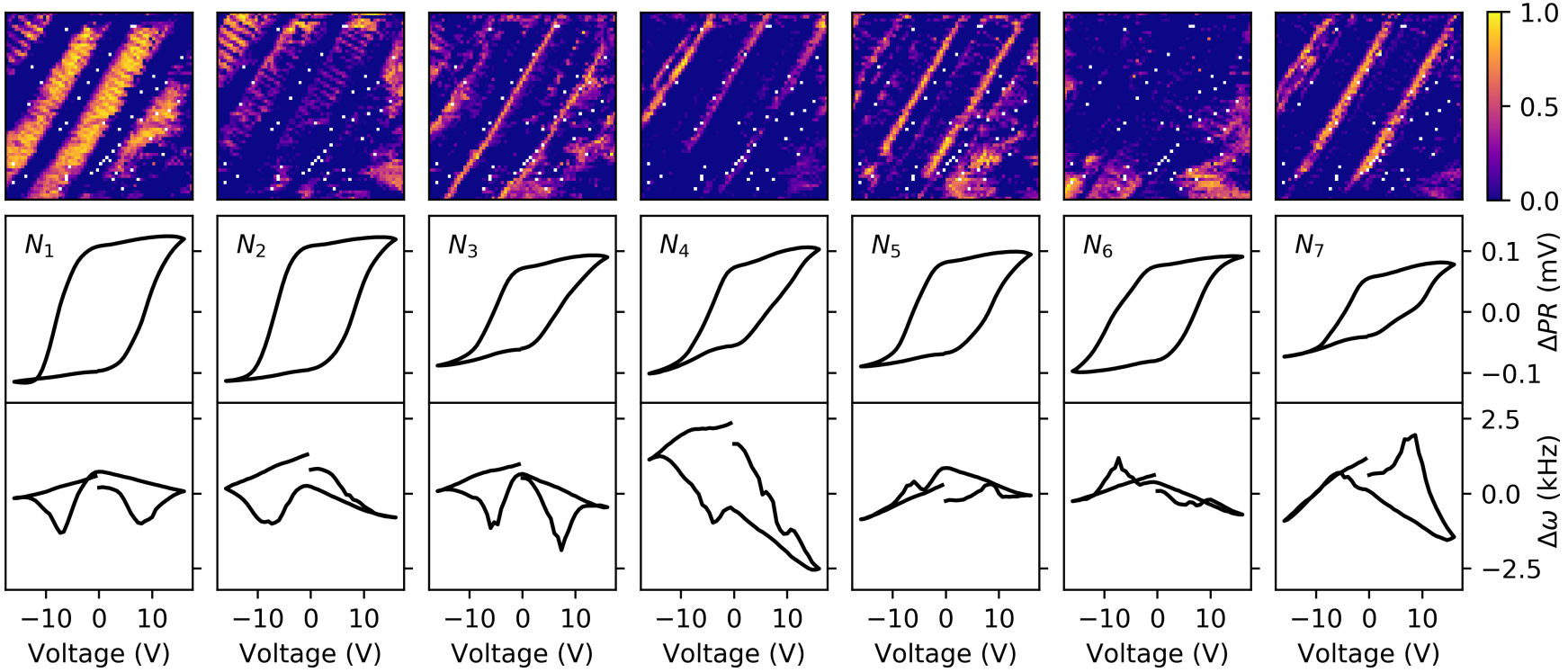

Figure B.14: Dictionary learning of stacked mean-subtracted $PR - \omega$ for $N = 7$ and for $\alpha = 6$. At each spatial point, the observed piezoresponse and resonance behavior can be approximated as a linear superposition of the spatial weight maps (top row) multiplied by the corresponding derived behaviors. Here, the middle row is the piezoresponse behavior and the bottom row is the corresponding resonance behavior. Prior to analysis, the point-by-point mean was removed from both the resonance and piezoresponse data. Further, the piezoresponse was multiplied by a constant factor such that the values were comparable to that of the mean removed resonance values (See Supplemental Note 1).

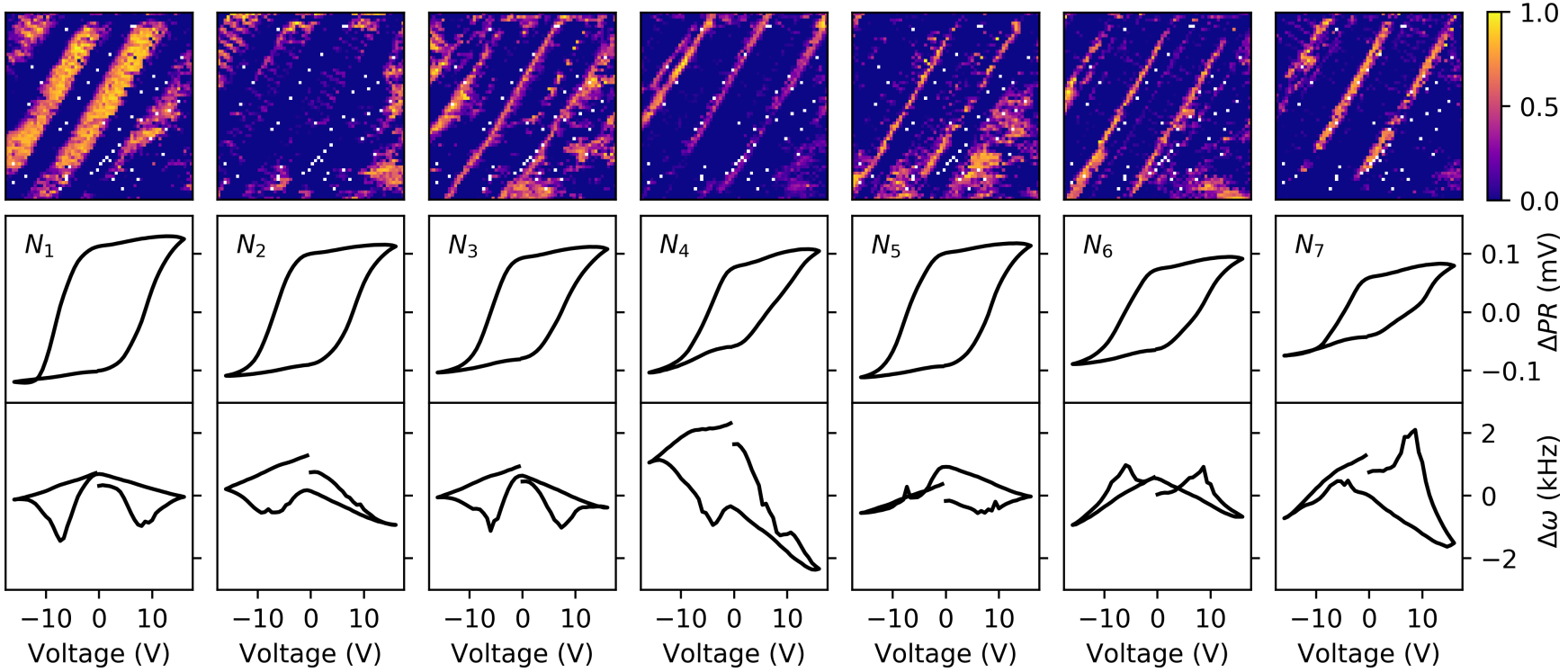

Figure B.15: Dictionary learning of stacked mean-subtracted $PR - \omega$ for $N = 7$ and for $\alpha = 12$. At each spatial point, the observed piezoresponse and resonance behavior can be approximated as a linear superposition of the spatial weight maps (top row) multiplied by the corresponding derived behaviors. Here, the middle row is the piezoresponse behavior and the bottom row is the corresponding resonance behavior. Prior to analysis, the point-by-point mean was removed from both the resonance and piezoresponse data. Further, the piezoresponse was multiplied by a constant factor such that the values were comparable to that of the mean removed resonance values (See Supplemental Note 1).

APPENDIX C

DOMAIN WALL PROXIMITY ON POLARIZATION SWITCHING

C.1 Experimental Set Up

C.1.1 R-PFM: Scan and Switching PFM

In this work, we discuss the sample response after the removal of the DC bias voltage ("off-field" or "read" cycle), and the obtained hysteresis curves are reported as a function of the DC voltage immediately preceding the recorded response. When calculating the PR for switching PFM experiments, a unique optimal rotation angle (θ_{opt}) can be found for each point/hysteresis curve. However, given the conceptual meaning for the rotation angle, a single and constant $\overline{\theta}_{opt} \approx 270^{\circ}$ was used for all hysteresis loops, corresponding to approximately the mean value of the θ_{opt} across the analyzed points.

C.1.2 R-PFM Scans

R-PFM scans were performed before and after switching experiments for both sample areas. Figure C.1 shows the A, ϕ, ω, and Q before and after the switching characterization for the 10 μm x 10 μm area. The initial domain structure is apparent in the initial A ϕ images (Figure C.1a). Furthermore, much of the initial domain structure persists after the switching experiments

(Figure C.1b), with the notable addition of small "dots", corresponding to newly nucleated domains within a single domain polarity. The initial ω map shows two step-wise increases in the contact resonance as the measurement progresses (from the top towards the bottom of the sampled area). Conversely, after the switching experiments, the contact resonance is consistent within each domain polarity, and relatively constant across the scanned area.

Figure C.2 shows the basic R-PFM scan images of the 8 μm x 8 μm area. Again, the initial domain structure is apparent in the "before" (i.e. acquired before the switching experiment) A and ϕ images (Figure C.2a). Much of the initial domain structure is still visible in the A and ϕ images after the switching experiments. The before and after ω images show limited change in the average contact resonance, indicating stable measurement setup with

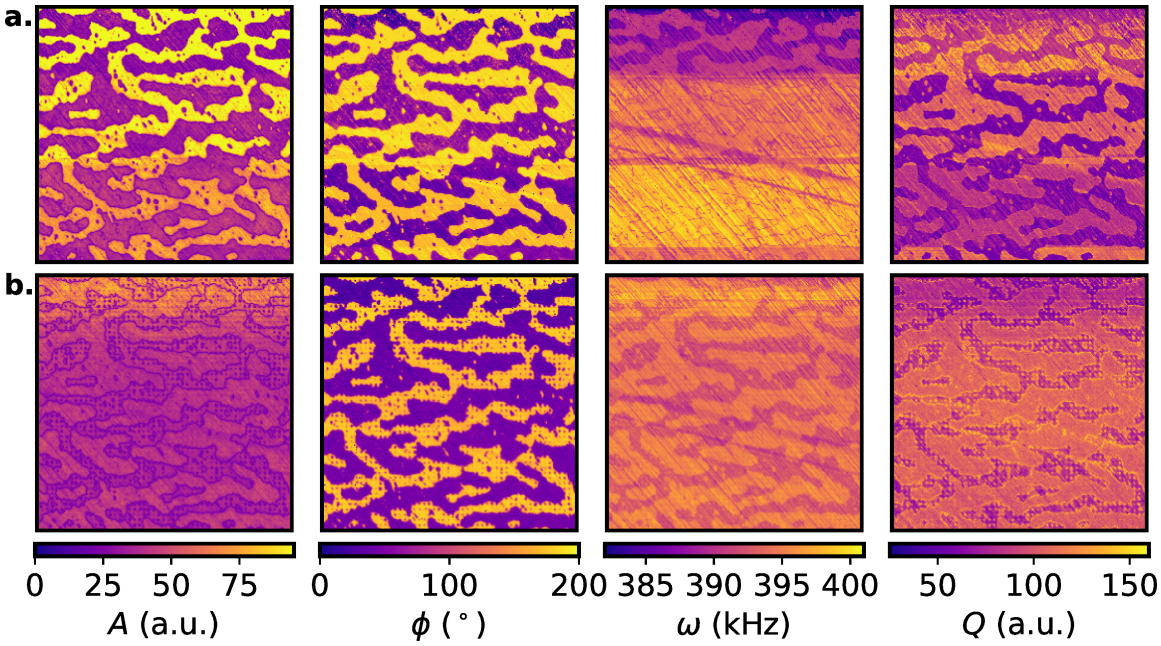

Figure C.1: (Left to right) The out-of-plane piezoresponse A, ϕ, ω, and Q of the 10 μm x 10 μm area (a) before and (b) after switching PFM measurements.

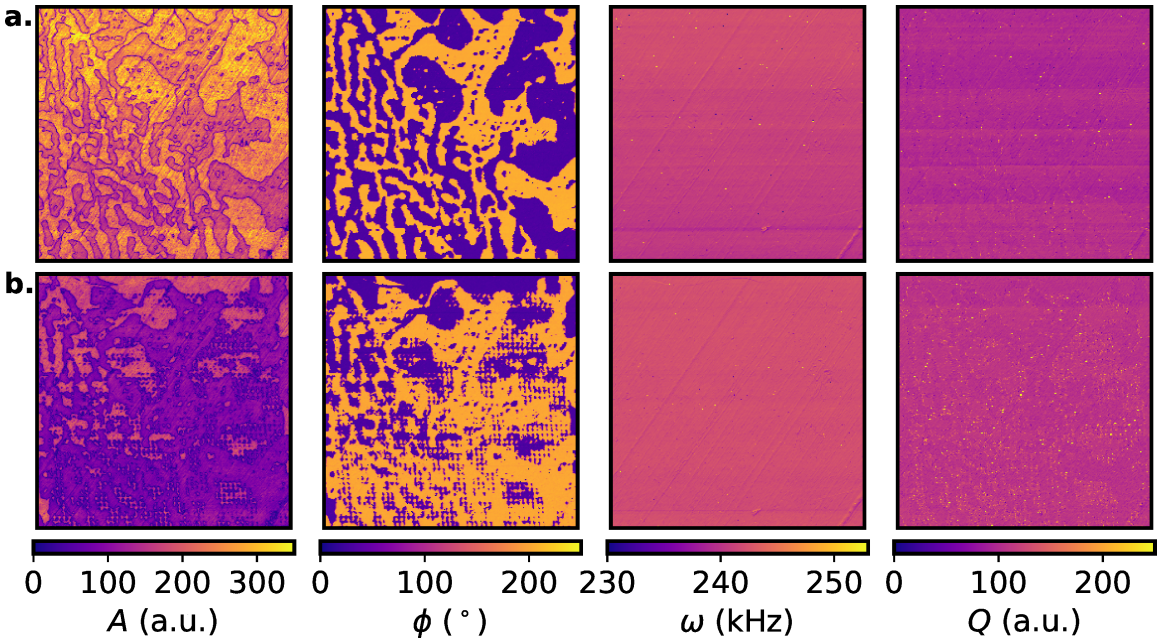

Figure C.2: (Left to right) The out-of-plane piezoresponse A, ϕ, ω, and Q of the 8 μm x 8 μm area, (a) before and (b) after switching PFM experiments.

limited tip changes or viscoelastic tip-sample changes. Conversely, a closer perusal of Figure C.2b shows a spatial shift between the initial scanned area the post-switching scan and that the grid points are shifted with respect to the original orthogonal grid.

The original R-PFM scans were collected with a resolution of 256x308 and are interpolated down to 256x256 in Figures 1, C.1, and C.2, for ease of comparison to the 50x50 point *k*-means and Dictionary learning maps. The interpolation was performed with a 2D linear spline, specifically, the function *resize* provided by the Python package scikit-image.

C.1.3 Topography of the Sampled Areas

Figure C.3 shows the topography of the two probed areas from before and after the switching experiments. In both locations the topography is dominated by striations from polishing: in the 10 μm x 10 μm area these run from the top left to the bottom right corner, and in the 8 μm x 8 μm area from top right to bottom left. The 10 μm x 10 μm area lines match some but not all the lines observed in the ω and Q scans, shown in Figure C.1. Additionally, the spatial map of N_4 in Figure 2 match some of the topographical feature identified in Figure C.3a. Hence, this component could, in part, be related to the topographical features.

Lastly, we note that a sizable spatial shift is apparent in the 8 μm x 8 μm area between the before and after images, resulting in a challenge for direct correlation of domain wall distances calculated with the before image in Figure C.2 to the data obtained from the switching experiments. This shift (and the progressive "drift" down the sample area, observed in Figure C.2b) were accounted for by manually assessing the location of the domain "dots" in Figure C.2b. This process is described below.

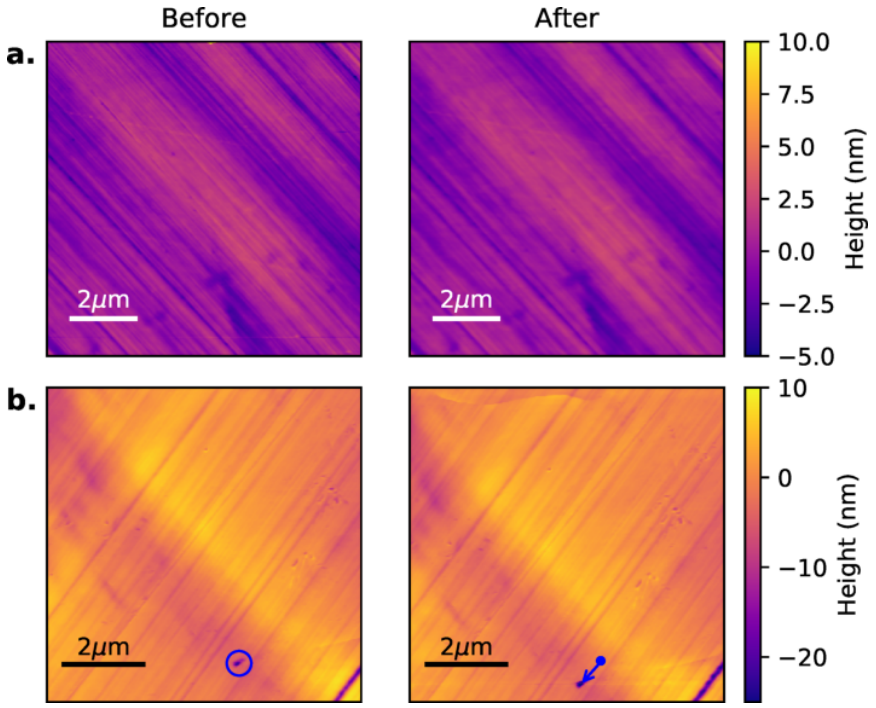

Figure C.3: The topography of the a) 10 μm x 10 μm and b) 8 μm x 8 μm ares probed (left) before and (right) after the switching experiments. To highlight the spatial shift during measurements in (b), the before image shows a highlighted topographical feature with a blue circle, while the after image identified with a vector the change in the feature's position between the two images.

C.2 Machine Learning Approaches

Machine learning (ML) techniques were applied to the PR and ω curves obtained from the switching experiments in an attempt to identify the impact of domain walls on the switching behavior. However, a few pre-processing steps were performed prior to ML analysis. First, for both the PR and ω data, the point-by-point mean was removed and the data was divided by the standard deviation (z-normalization). Second, ω values greater than 4 standard deviations away from the mean were removed and back-filled, using the previous data point in the curve. Finally, the PR and ω response data sets were dimensionally stacked along the time-axis[22], implying a spatial correlation between the local electromechanical response and the viscoelastic contact properties.

C.2.1 *K*-Means Analysis

The PR and ω stacked data was analyzed by *k*-means, grouping spatial points that share similar PR and ω behavior together, and identifying the average behavior for the group. The number of groups or clusters derived (N) is user-specified and was chosen to be arbitrarily large ($N = 8$), in order to minimize user bias, and identify possible outliers.

The output of the ***PR and*** ω stacked *k*-mean analysis for the 10 μm x 10 μm area and $N = 8$ is shown in Figure 1b and reproduced in Figure C.4 for

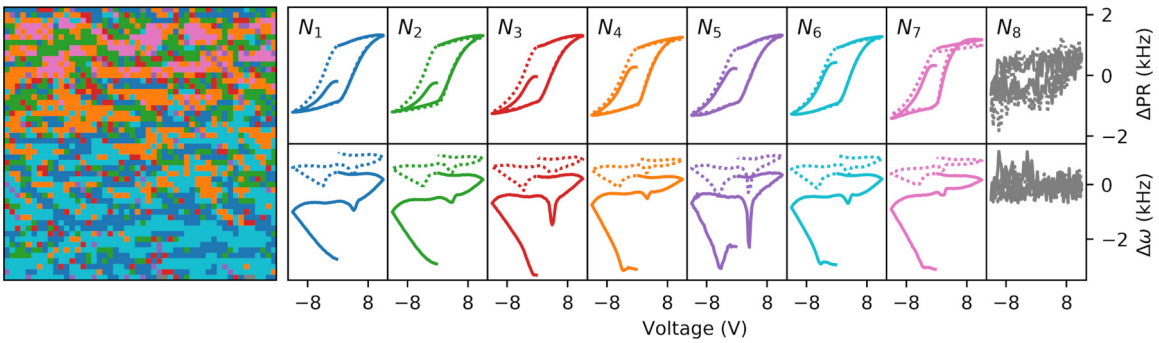

Figure C.4: Stacked piezoresponse and contact resonance *k*-means analysis for eight clusters ($N = 8$), applied to the 10 μm x 10 μm switching PFM data. At each spatial point shown in the map, the piezoresponse and contact resonance hysteresis curves are best described by the corresponding colored behavior. Here, the top row is the piezoresponse (PR) and the bottom row is the corresponding contact resonance (ω).

convenience. An inspection of Figure C.4 reveals an atypical "crossover" in the piezoresponse curves for N_7 at positive voltages. Additionally, this component is present in confined locations within a single domain polarity ($\approx$ 140 points), mostly at the beginning of the scan (top third of the scanned area). The cross-over feature has been previously assigned to presence of non-ferroelectric contributions (e.g., electrochemical or electrostatic displacement, due to charge injection)[166]. The limited amount of cross-over behavior and the similarity in the resonance curves with other components was the basis to *not exclude* these points from subsequent analysis. However, we note that inclusion of these points could affect the number of outliers with respect to subsequent statistical calculations, but not necessarily ML approaches.

C.3 Dictionary Learning

Dictionary Learning seeks to decompose a given data set (D) into a number (N) of component (W) and weight map (U) pairs. Here, D is the probed PR and ω data, which was measured as a function of applied electric field (v) and spatial coordinate within the sampled area ($z = [x, y]$), i.e. $D = D^p(z, v)$ where $p = [PR, \omega]$. For this data set and the analysis of a single parameter (e.g. $p = PR$), DL derives the components (eigenvectors) and corresponding weight maps (eigenvalues), by minimizing Eq. 5.1.

Here, $\|D^p(z, v) - U(z)W(v)\|_2^2$ represents the norm-squared error and $\|U(z)\|_1$ imposes a preference towards sparse results. The user can specify the relative importance of sparsity as compared to model error by adjusting the parameter α, which otherwise defaults to 1. As such, DL can identify linearly superimposed behaviors, as might be found near the domain walls, or sparse behaviors, which might be expected in the domain bulk. In this work, the components are derived as a function of voltage (v) and the weight maps are derived as a function of space ($z = [x, y]$). Thus, the components represent different contributors to the switching behavior, and the weight maps represent the spatial distributions of the identified contributors. As in the *k*-means analysis, the PR and ω data are dimensionally stacked prior to analysis, allowing for DL to derive correlated PR and ω behavior (i.e. components, $W(v, p)$).

C.3.1 N and α Selection: Error Analysis

To perform the DL analysis, the parameters N and α must be provided by the user. As previously reported by Griffin et. al.[148], selection of these parameters should be informed by a quantitative and reproducible methodology. Following the procedure introduced in reference [148], to select parameters, we ran dictionary learning (DL) analysis over a wide range of model parameters and compared the results in terms of residual error. The particular error metric used was root mean squared error (RMS) or the root mean squared of the residuals. Given a data set D and a set of DR-derived components (W) with corresponding spatial weight maps (U) approximating D, the root mean squared error (RMS) can be calculated with Equ. B.1. Here, the squared errors ($(D - UW)^2$) are averaged over some arbitrary dimension L and square rooted. In this work, the squared errors are calculated at each spatial point for each value of the piezoresponse-resonance curves and then averaged over the piezoresponse-resonance curves, resulting in spatial maps of RMS error. The thus-obtained RMS error spatial maps are subsequently averaged into a single RMS error metric.

Figure C.5a and b plot the resulting average spatial RMS error for a number of N and α combinations for the 10 μm x 10 μm and 8μm x 8μm areas, respectively. The analyses were performed with N's ranging from 2 to 9 components and α values of 1, 1.15, and 1.3. A choice of higher α values

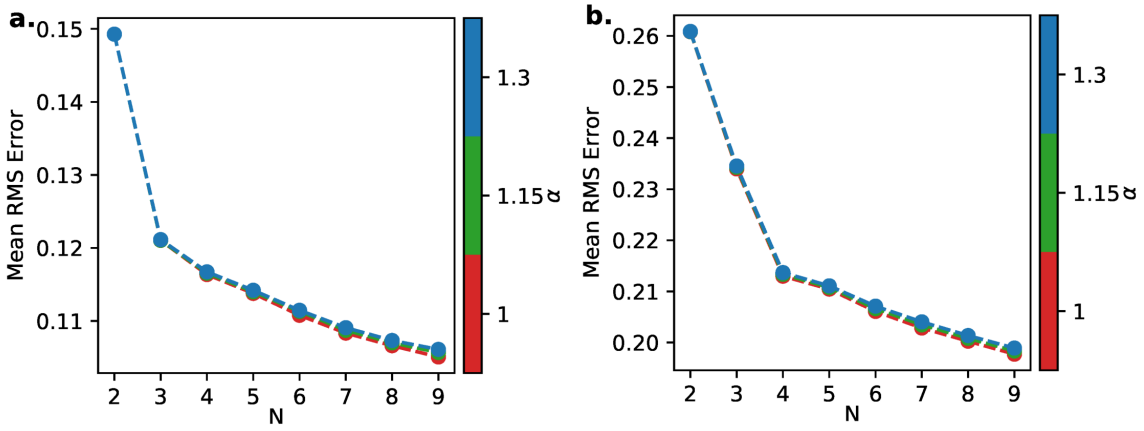

Figure C.5: The spatially-averaged root mean squared (RMS) error for various combinations of N and α, shown in parametric curves similar to scree plots, for both (a) the 10 μm x 10 μm area and (b) the 8 μm x 8 μm area. The different analyses consider a range of number of components ($N = 2$ to 9) and α (1, 1.15, or 1.3).

resulted in identification of noise components. The α parameter has indeed very limited impact on the error. Conversely, the number of components (N) has a more significant effect on the error, with a change in the curves' slope observed at $\approx$3 or 4 components, depending on the data set. As N is increased beyond these values, error decreases somewhat linearly, with a slight curvature at higher N for higher α values. In order to avoid overfitting, the scree test recommends N to be at or close to the "elbow" of Figure C.5, i.e. where saturation in error improvement begins. Overall, based on the model error, the recommended dictionary learning parameters are $\alpha = 1$ and $N = 3$ or $N = 4$ for the 10 μm x 10 μm area and $\alpha = 1$ and $N = 4$ or $N = 5$ for the 8 μm x 8 μm area.

C.3.2 Dictionary Learning Output Analysis

In the above section, a range of valid DL parameters were identified via an error analysis. To reduce user bias, the output of the DL analysis should be considered for the range of the identified parameters[148]. Additionally, we report also the extreme case of $\alpha = 1.3$, in order to verify the effects of the sparsity parameter. Figure C.6 shows the results of a piezoresponse and resonance stacked dictionary learning analysis applied to the 10 μm x 10 μm SSPFM data for $N = [3, 4]$ and $\alpha = [1, 1.3]$.

Increasing sparsity has a slight influence on the spatial weight maps of N_1 and N_3 and minimal impact on the resonance curves, for $N = 3$ (Figures C.6a and b). In particular, higher sparsity (Figure C.6b) results in N_1 and N_3 appearing to be more "spatially distinct" (i.e. more sparse) at lower number of components, e.g. N_3 is more constrained to the top of the sample area and N_1 to the bottom. α's impact is more limited in the $N = 4$ analyses (Figures C.6c and d) in either spatial weight maps or piezoresponse/resonance behaviors. The primary difference between the $N = 3$ and the $N = 4$ analyses is in component N_4 with very distinct PR and ω curves and sporadic presence in the sampled area. Overall, the physical interpretation of the different components in all analyses can be thus-described:

- N_2 represents the behavior in the domains that do not switch in the first quarter cycle;

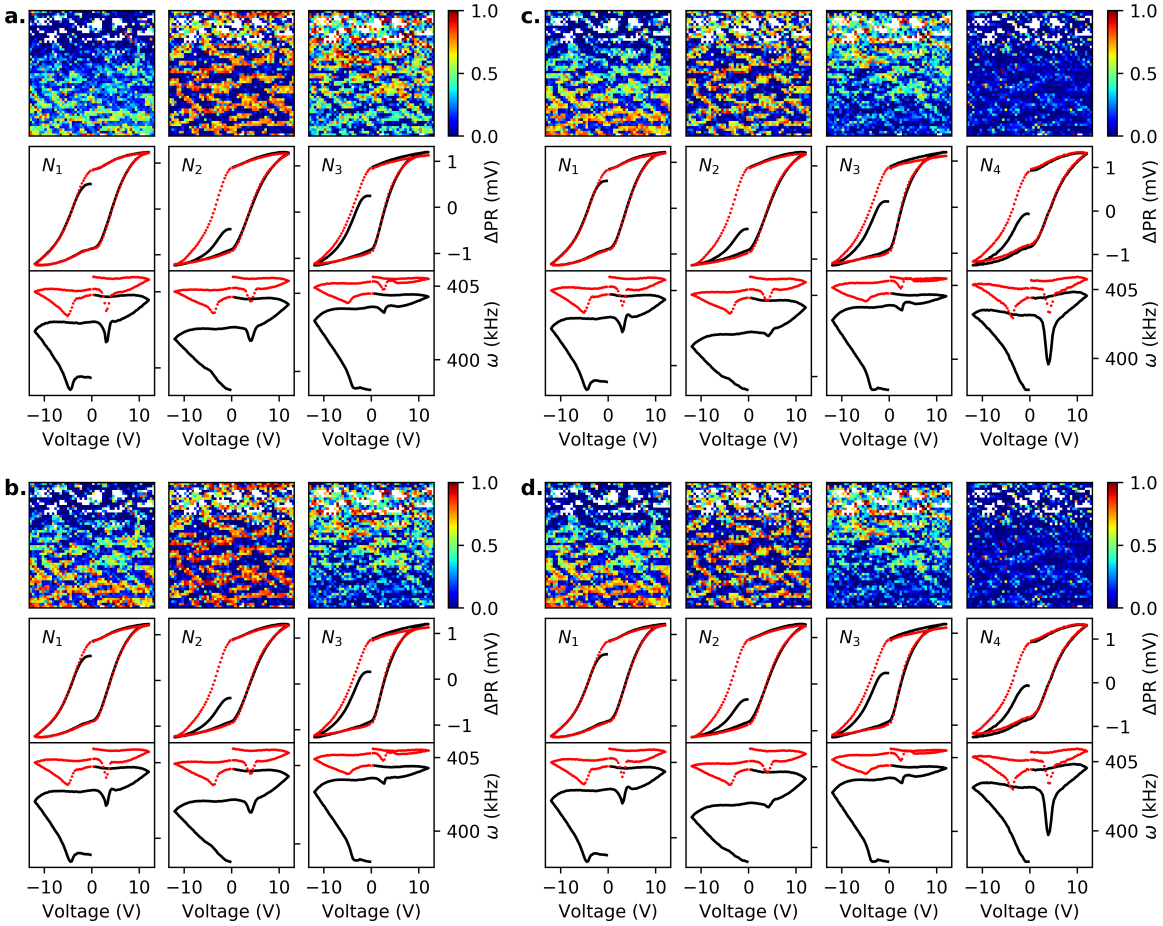

Figure C.6: Piezoresponse and resonance stacked dictionary learning analyses for various model parameters applied to the 10 μm x 10 μm switching PFM data. The model parameters used here are a) $N = 3$ and $\alpha = 1$, b) $N = 3$ and $\alpha = 1.3$, c) $N = 4$ and $\alpha = 1$, and d) $N = 4$ and $\alpha = 1.3$

- N_1 and N_3 represent domains that do switch within the first quarter cycle and are spatially complimentary to each other (while within a single polarity of domains).

- N_4 is present within a single domain polarity, however, based on the substantial contact resonance softening in proximity of the coercive voltages, it could be assigned to reduced lateral constraint exercised by (inactive) surrounding material and/or ferroelastic switching in points

corresponding to surface protuberances[159, 158]. Alternatively, the spatial map of this behavior seems to highlight some points near a domain wall and, thus, this behavior could be due to the influence of a domain wall.

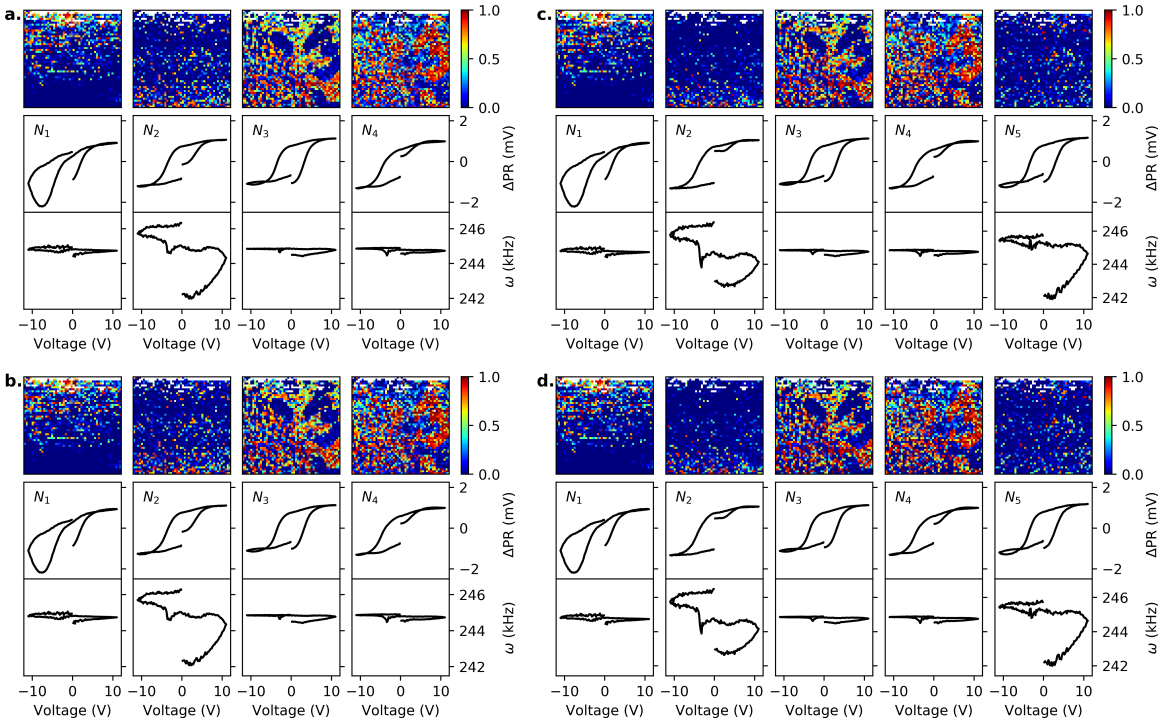

Figure C.7: Piezoresponse and resonance stacked dictionary learning analyses for various model parameters applied to the 8 μm x 8 μm switching PFM data. The model parameters used here are a) $N = 4$ and $\alpha = 1$, b) $N = 4$ and $\alpha = 1.3$, c) $N = 5$ and $\alpha = 1$, and d) $N = 5$ and $\alpha = 1.3$

Figure C.7 shows the results of the dictionary learning analysis of the piezoresponse and contact resonance stacked data set from the 8 μm x 8 μm area for $N = [4, 5]$ and $\alpha = [1, 1.3]$. For this data set, α has particularly limited impact, with barely perceptible differences when α is increased. Furthermore, N_1, N_3, and N_4 identified eigenvectors are mostly independent of the choice of N or α. Component N_1 is present predomi-

nately at the top of the sampled area and shows typical switching at positive voltages and substantial non-ferroelectric behavior at negative voltages. The spatial map of N_3 shows that this behavior is limited to a single domain and the piezoresponse and contact resonance curves exhibit behavior consistent with ferroelectric switching within the first quarter cycle (positive voltages), indicating that this component represents the *up*-polarized domains. Conversely, N_4 is associated with the *down*-polarized domains, i.e. the piezorepsonse and contact resonance behavior show no signs of polarization switching within the first quarter cycle (positive voltages).

N_2 in Figure C.7a seemingly corresponds to different combinations of N_2 and N_5 in Figure C.7c). This suggests that either the $N = 5$ analysis is overfitting and splitting a single behavior into two non-physical behaviors, or $N = 4$ is combining two or more physical behaviors into a single behavior. Notably, N_2 in Figure C.7a has a piezoresponse behavior that exhibits switching but has an initial piezoresponse value near-zero, while N_2 and N_5 in Figure C.7c show clear non-switching and switching behaviors, respectively. Additionally, N_5 exhibits a stronger cross-over of the *PR* at negative voltages than either N_2 components. All of the associated behaviors are physically possible and, as such, neither analysis (N= 4 or 5) can be considered as more accurately representing the physical contributors to the material's response. In Figure C.7a, N_2 could represent behavior near a domain wall, where the probed material volume would include both domains

and, thus, on average a lower initial piezoresponse. In Figure C.7c, N_2 and N_5 could represent the behaviors of the "dot-domains" widely present within the two larger domains.

Overall, the dictionary learning analyses of the two data sets are fairly consistent. In both data sets, the predominant behaviors describe the two polarization domains (i.e a non-switching and switching first-quarter cycle behavior), with at times addition of non-ferroelectric contributors.

C.4 Evaluation of Distance from Domain Walls

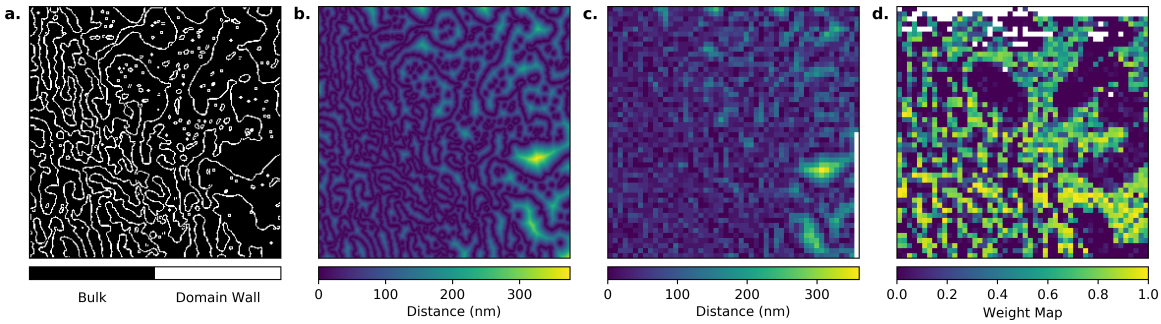

Figure C.8: Illustration of the distance from a domain wall extraction procedure for the 8 μm x 8 μm area. a) The domain walls were identified from the phase image, Figure C.2. b) The distance to the nearest domain wall was calculated for each pixel in the phase image. c) The distance from domain walls was mapped to the 50x50 switching spectroscopy points. d) A spatial weight map yielded by the dictionary learning analysis of the 8 μm x 8 μm area, which highlights a domain polarity.

The distance from a domain wall distance extraction procedure described in the main text for the 10 μm x 10 μm area was applied to the 8 μm x 8 μm area, as shown in Figures C.8. However, as seen in Figures C.2 and C.3, a sizable spatial shift occurred during the switching PFM measurement in the 8 μm x 8 μm area. Specifically, a progressive drift is apparent in the

"after-switching" phase image (Figure C.2b), where the newly nucleated domain "dots" progressively shift right-wards during consecutive scanned lines, from the top towards the bottom of the area.Additionally, the starting point of the grid did not match the exact location identified in the original, "before-switching" scan. Both issues were instrumentation related and randomly present during experiments, not fixable by the vendor. These instrumental challenges have been hence addressed through the methodology described below.

The newly created domains ("dot-shaped" domains) in the "after-switching" phase image (Figure C.2b) were used to quantify the vertical and lateral drift during the switching experiments as well as with respect to the starting point of the measurement. The calculated drift was subsequently applied to the extracted domain wall distance map (Figure C.2c).

C.4.1 Binning by Distance

In the phase images in Figures C.1 and C.2, domains are discernible with transitions shown across multiple pixels, implying an uncertainty in the distances calculated above. For instance, close inspection of the phase image in Figure C.1 shows that transition from the orange domain to the purple domains is diffused and often $\approx 1-2$ pixels wide. Given the resolution of this scan (≈ 39nm per pixel), such diffused transition corresponds to a possible variation in the distance to a domain wall of 39 to 78nm for the 10 μm x 10

μm area. Similarly, for the 8 μm x 8 μm area, the distance values could vary by ≈ 30 to 60nm. Here, we account for this uncertainty by binning points according to their distance values. Consistently with the diffused domain walls discussed above, bin sizes of 80nm and 60nm were used in Figures 3 and 4 (10 μm x 10 μm area), and Figure 5 (8 μm x 8 μm area), respectively. These bin sizes approximate the largest observed "domain wall thickness" in each area. Within this Supplemental File and for reference, Figures 4 and 5 of the main manuscript are reproduced using also 40nm and 30nm, or the smallest observed "domain wall thickness" (Figures C.14b and C.15b).

C.5 Functional Parameters for Switching PFM

The second cycle piezoresponse curve of the 10 μm by 10 μm data set was analyzed by extraction of the functional parameters associated with a ferroelectric hysteresis curve: the positive and negative nucleation and coercive voltages (V_n and V_c, respectively), and saturation and remanent piezoresponse values (PR_s and PR_r, respectively). Figure C.9 schematically illustrate these parameters with respect to a sample hysteresis curve. The coercive voltages are the positive and negative x-intercepts (corresponding to

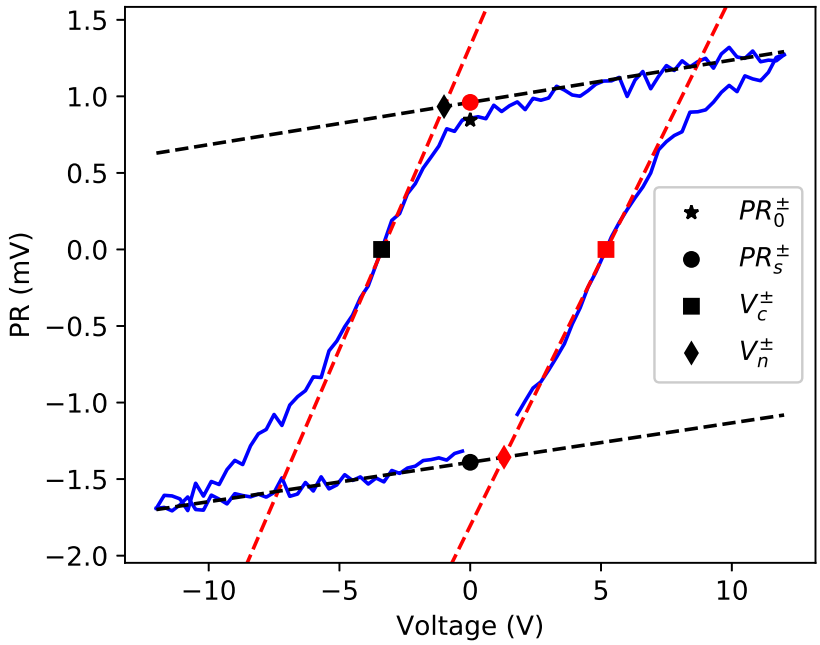

Figure C.9: Illustration of the second cycle parameter extraction. Stars denote the remnant piezoresponse values ($PR_0^{\pm}$), circles the saturation piezoresponse values ($PR_s^{\pm}$), squares the coercive voltages ($V_c^{\pm}$), and diamonds the nucleation voltages ($V_n^{\pm}$). Red markers show the positive extracted values (V_c^{+}) and black markers shows the negative extracted values (V_c^{-}). The dashed black lines show the linear fits used to find $PR_s^{\pm}$. The dashed red lines show the linear fits used to find $V_n^{\pm}$, i.e., the voltage corresponding to the intersection of the red and black dashed lines.

zero PR), and represent the critical voltages necessary to switch the probed piezoresponse. The remanent piezoresponse are the positive and negative y-intercepts (corresponding to zero volts) and inform on the polarization that is retained after applied voltages are removed. The saturation piezoresponse represents the maximum contribution of the ferroelectricity to the measured piezoresponse. The positive saturation piezoresponse value is found by linearly extrapolating the response at high voltages (7 to 11 V) in the "upper branch" to a voltage of 0 (using the upper black dashed line in Figure C.9). Likewise, the negative saturation piezoresponse value is calculated by linearly extrapolating the response in the "lower branch" to a voltage of 0. The nucleation voltages correspond to the inflection points at reducing the voltage after saturation or the "corners" of an idealized perfectly rectangular hysteresis loop. As loops are often non-ideal, the nucleation voltages are obtained by linear extrapolation of the branches of the hysteresis loop and finding the intersection of these linear approximations.

C.6 Second Cycle Switching PFM

Figure C.10 shows the second cycle binning analysis of $PR_s^{\pm}$, $PR_0^{\pm}$, and $V_n^{\pm}$ in the 10 μm x 10 μm area, and without omitting any bins. When the data is considered as a whole (Figures C.10a, d, and g), there are limited and somewhat inconsistent trends. For instance, PR_s^{+} and PR_0^{+} show a slight increase in magnitude but PR_s^{-} and PR_0^{-} a slight decrease. While, the

median $V_n^{\pm}$ does seems to increase as distance is increased, the two farthest bins contain a limited number of points, with the farthest bin contains only one point. Separating the data according to the initial polarization state (Figures C.10b and c for $PR_s^{\pm}$, Figures C.10e and f for $PR_0^{\pm}$, and Figures C.10h and i for $V_n^{\pm}$) yields similarly limited trends.

Most notably, the median $V_n^{\pm}$ in the initially *up*-polarized domains remains fairly invariant with respect to the distance from a domain wall (except for the farthest bin, which consists of data from a single point). In the *down*-polarized domains, the distributions of $V_n^{\pm}$ suggests a possible increase in magnitude with increased distance from a domain wall, even when not considering the final two bins.

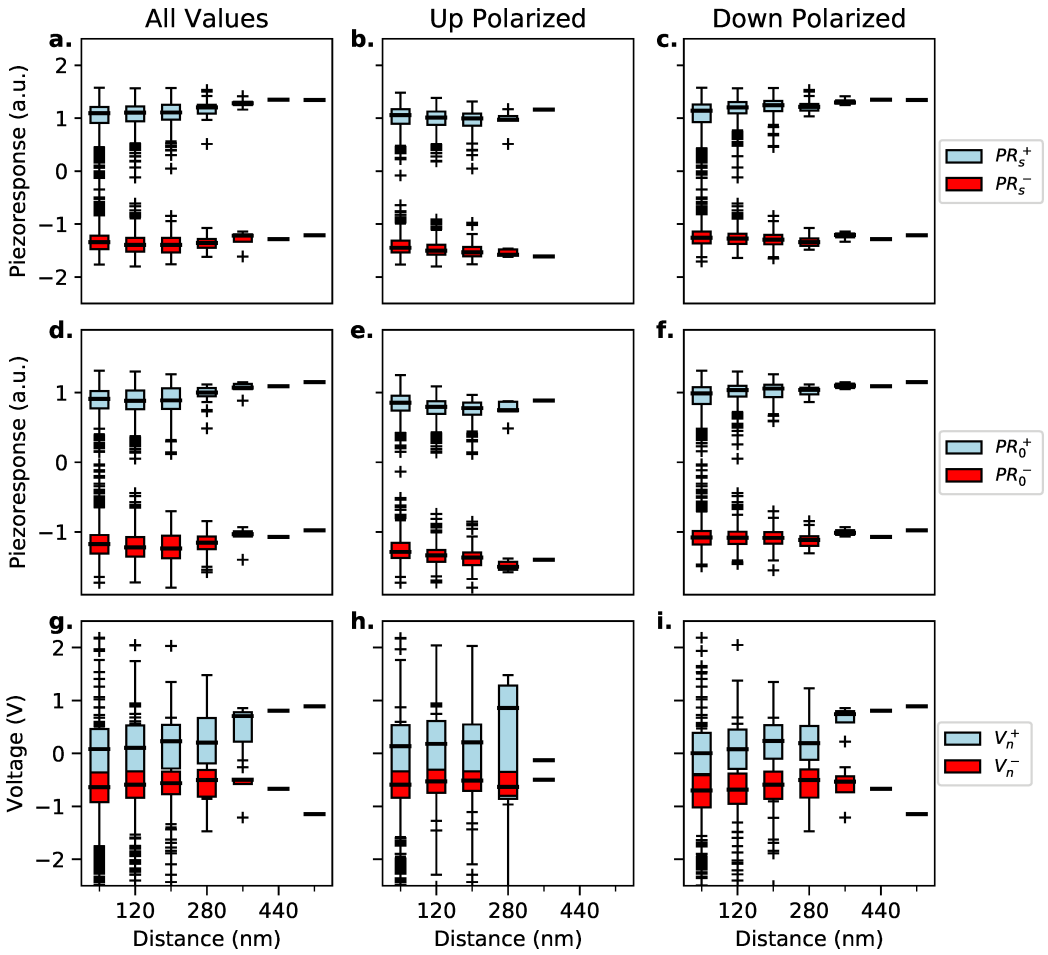

Figure C.10: (a,c) The saturation piezoresponse ($PR_s^{\pm}$, a-c), remanent piezoresponse ($PR_0^{\pm}$, g-i), and nucleation voltages ($V_n^{\pm}$, d-f), extracted from the $10\mu m$ by $10\mu m$ switching experiments and binned according to distance from the nearest domain wall. a), d), and g) Box-and-whisker plots of *all* the binned $PR_s^{\pm}$, $V_n^{\pm}$, and $PR_0^{\pm}$ values, respectively. b), e), and h) Box-and-whisker plots of the binned $PR_s^{\pm}$, $V_n^{\pm}$, and $PR_0^{\pm}$ values for the initially *up*-polarized domains only, respectively. c), f), and i) Box-and-whisker plots of the binned $PR_s^{\pm}$, $V_n^{\pm}$, and $PR_0^{\pm}$ values for the initially *down*-polarized domains only, respectively. In all box-and-whisker plots, bin size is 80 nm, and x-axis values represent the center value for each bin. Each box includes the first to third quartiles. The bold line within the box corresponds to the median, and the error bars correspond to 1.5 times the interquartile range or $\approx 99\%$ confidence interval for a normal distribution.

C.6.1 Second Cycle Switching PFM: All Data

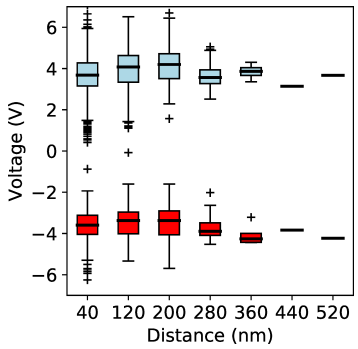

Figure C.11: Box-and-whisker plots of the binned V_c^+ and V_c^- values for the second cycle of the 10 μm x 10 μm data set.In all box-and-whisker plots, bin size is 80 nm, and x-axis values represent the center value for each bin. Each box includes the first to third quartiles. The bold line within the box corresponds to the median, and the error bars correspond to 1.5 times the interquartile range or $\approx 99\%$ confidence interval for a normal distribution.

Figure C.11 shows an analysis of the coercive voltages as a function of distance from a domain walls, similar to that shown in Figure 3, but without consideration given to the initial polarization state of the probed locations. The changes in the median values are not monotonic with increasing distance from domain walls, and well within experimental error for both parameters. Hence, there is no specific effect of the proximity to a domain wall on the switching voltages for the proved area.

C.7 Median Behavior as a Function of Distance From a Domain Wall

For additional insight, the median piezoresponse behavior for each of the bins in Figures 3, 4, and 5 are reported in Figures C.12 and C.13, respectively. In the 10 μm x 10 μm data set (Figure C.12), at increasing distance from a domain wall, the entire hysteresis curve shifts upwards (and

hence both positive and negative saturation piezoresponse values shift very slightly towards more positive values) for *switching* domains. However, in *non-switching* domains, the hysteresis curves seemingly rotate counter-clockwise at increasing distance from a domain wall (and hence, saturation and remanent piezoresponse values increase in absolute value at both positive and negative applied voltages). A closer observation of curves ob-

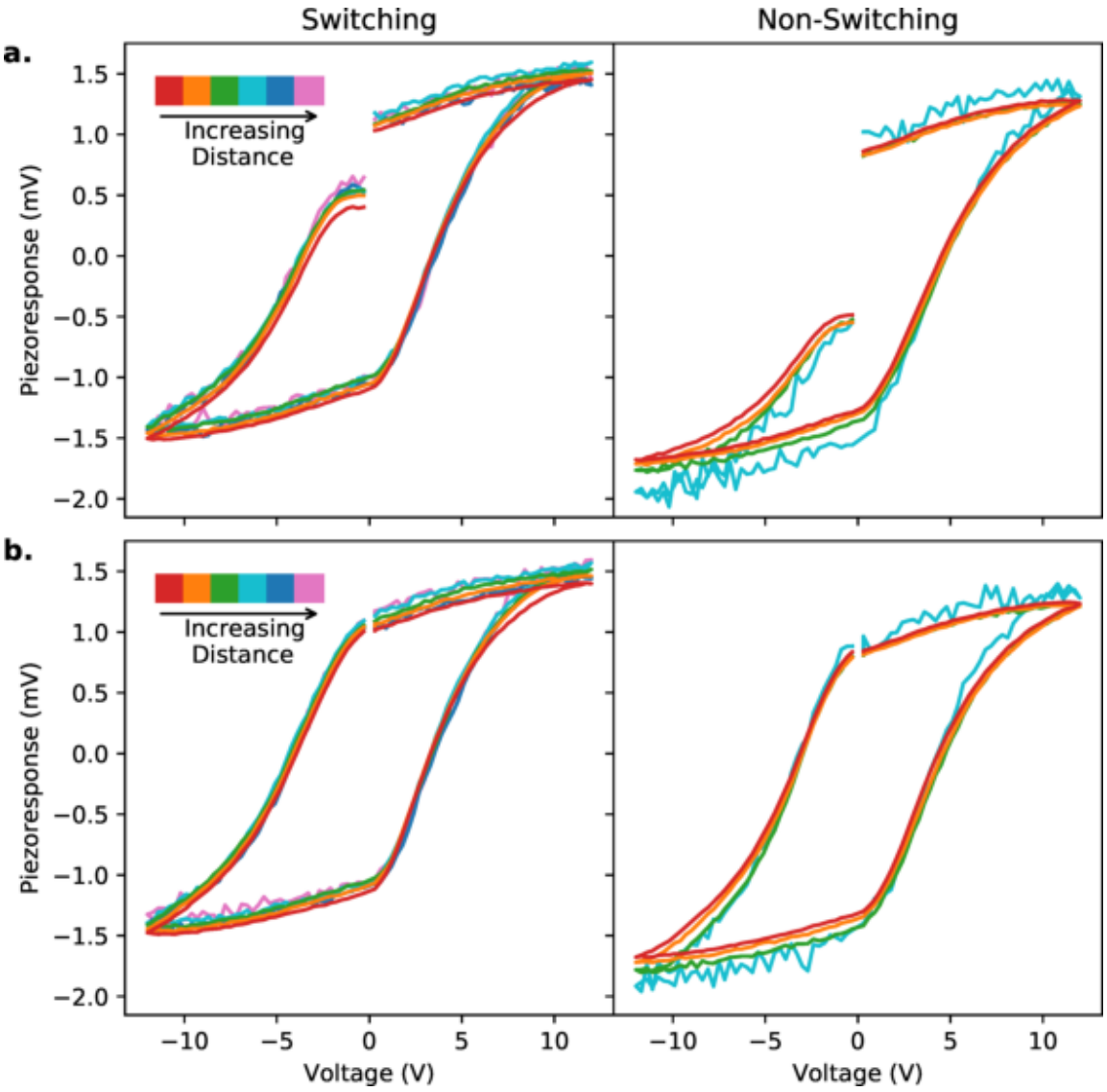

Figure C.12: The median behavior of each bin in the *Switching* and *Non-Switching* domains for the 10 μm x 10 μm and for both the (a) first and (b) second cycle.

tained from the switching locations, suggest that such counterclock-wise rotation of the hystersis curves is also observed in these location, albeit somewhat limited to the response at positive applied voltages. Additionally, the curves for *non-switching* locations are vertically shifted towards more negative piezoresponse values compared to the *switching* location, an indication of stronger electrostatic effects in *non-switching* domains. In both domain polarities, the coercive voltage is mostly unaffected by the distance from the domain wall. An exception is presented by the response of *Switching* domains during the first quarter cycle (Figure C.12a): the V_c^- shifts towards slightly higher negative voltages with increasing distance, for the first 3 bins, i.e. red, orange, and green. Such a behavior is consistent with higher polar-

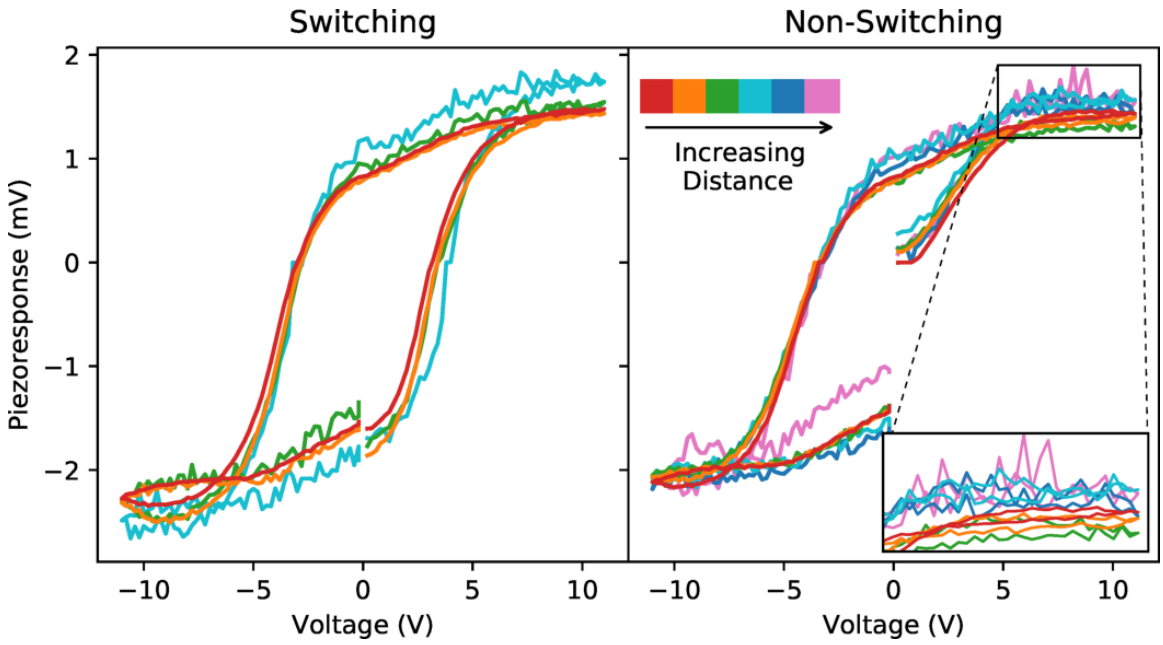

Figure C.13: The median piezoresponse behavior of each bin in the *Switching* and *Non-Switching* domains for the 8 μm x 8 μm. An inset provides a zoomed view of the *Non-Switching* curves around the positive saturation.

ization switching energy through domain wall nucleation and growth than domain wall motion. Beyond the first quarter cycle, the subsequent switching in the same locations is expected to be dominated by the creation of new "written" domains in each location and indeed the coercive voltages are independent of the (original) distance from a domain wall. A similar effect is expected in *Non-switching* domains with respect to V_c^+ for the second half cycle. However, the domain wall effects are mitigated by the electrostatic and charge injection effects clearly observed at negative and positive applied voltages.

Similar trends are observed for increasing V_c^+ away from a domain wall within a first quarter cycle of "switching" locations, for the 8 μm x 8 μm sampled area (Figure C.13). However, stronger electrostatic and charge injection contributions are highlighted by the presence of "nose"-like features at negative applied voltages, where the hysteresis curve changes from a counter-clockwise to a clockwise shape. Considering the increased contact force in the 8 μm x 8 μm measurement with respect to the 10 μm x 10 μm measurement, the "nose" feature could be also due to reduction of the ferroelastic domain variants and hence the relative increase in the ferroelectric switching contributions[45]. Allow, this explanation is limited, as the "nose" would be expected to appear symmetrically in response to positive voltages as well. Consistent with the 10 μm x 10 μm data, increasing distance typically does not have an effect on the near-coercive behavior, except

for in the first quarter of the *Switching* domain. Here, the first quarter again shows an increase in the coercive voltage with increasing distance. Furthermore, the *Switching* domain shows a similar "tilt" or counter-clockwise rotation of the piezoresponse as seen in the *Non-Switching* domain in Figure C.12. Notably, these both represent Up-oriented domains, suggesting this tilting is related on the initial polarization state.

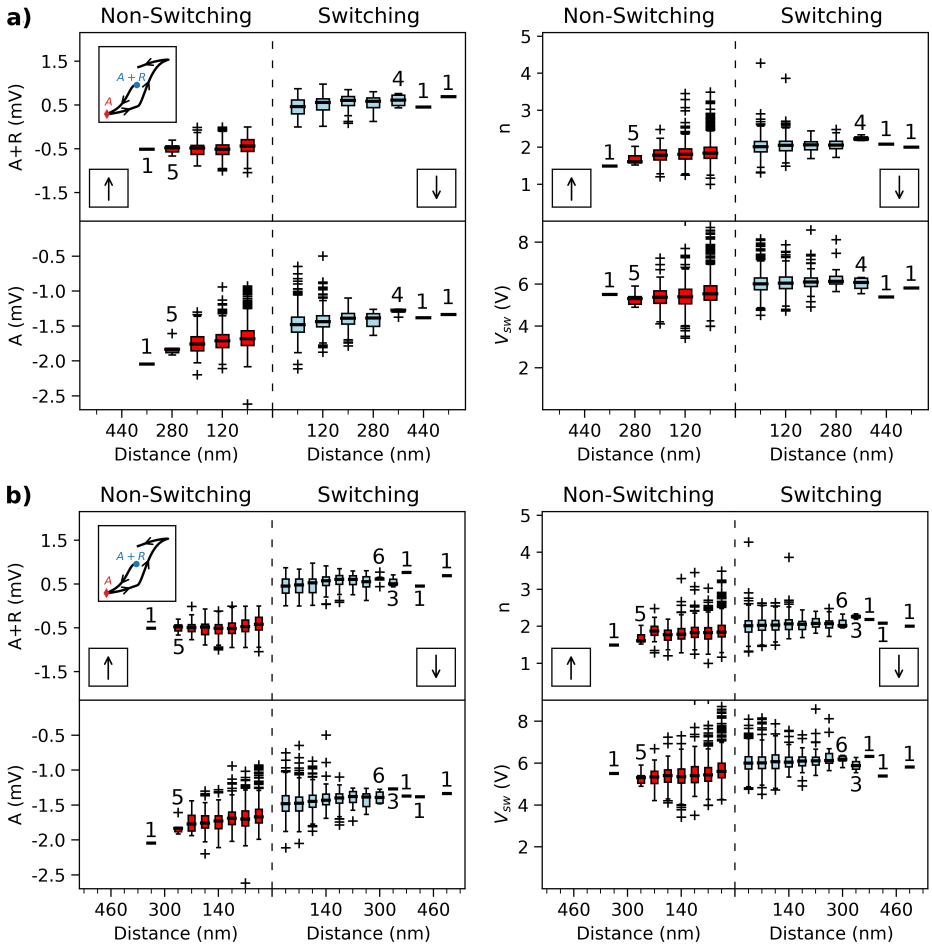

Figure C.14: Distributions of the binned functional fitting coefficients for the first quarter cycle of the $10\mu m$ by $10\mu m$ switching measurement, plotted against distance to nearest domain wall, for bin sizes of a) $80\ nm$ and b) $40\ nm$. Switching and Non-Switching are based on the point's initial polarization state, *down*- or *up*-polarized, respectively. The vertical dashed lines represent the domain wall. As shown in the inset, $A + R$ is the initial piezoresponse value, A is the saturation value, n is the effective dimensionality of growth, and V_{sw} is the effective voltage required for switching. The whisker and box plots represent the median, the first through third quartile of data (box), and $\approx 99\%$ confidence interval for a normal distribution (whiskers). Additional outliers for each bin are shown in symbols. The distance from domain wall are calculated in a) $80\ nm$ bins and b) $40\ nm$, with center value used to represent the bin. For bins with less than 10 points, the number of points within the bin is reported above/below the bin.

C.8 First Quarter Cycle Switching PFM

C.8.1 All Bins

In Figures 4 and 5 of the main text, bins with less than 5 points were removed, as they contain limited statistical information due to the small amount of representative points. In Figures C.14a and C.15a, respectively, these figures are reproduced with all bins shown. As seen, inclusion of the low density data bins (less than 5 points) results in no significant changes in the overall trends.

In the sub-section "Binning by Distance" above, we discussed the rationale behind binning the data, relating the bin size to the observed "domain wall thickness". Here, we reproduce the data used for Figures 4 and 5 (Figures C.14b and C.15b, respectively), plotted using a bin size corresponding to the smallest observed "domain wall thickness", or 40nm and 30nm, respectively. Generally, Figures C.14b and C.15b reproduce the trends seen in Figures 4 and 5. The notable exception is the second-to-last bin in the switching domain of Figure C.15b, which shows a decrease in A, n, and V_{sw} around 285nm not seen in Figure 5. However, we note that this bin contains only 2 points and ignoring bins with less the 5 points yields trends fairly similar to those seen in Figure 5.

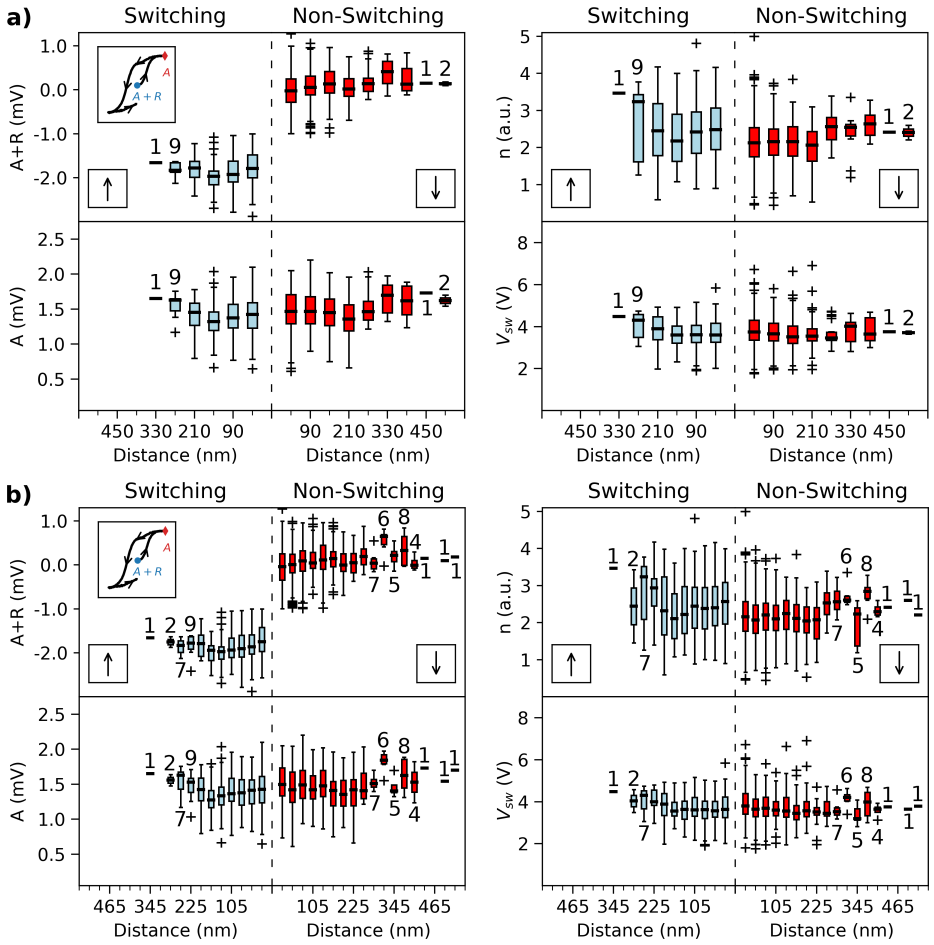

Figure C.15: Distributions of the binned functional fitting coefficients for the first quarter cycle of the $8\mu m$ by $8\mu m$ switching measurement, plotted against distance to nearest domain wall, for bin sizes of a) $60\ nm$ and b) $30\ nm$. Switching and Non-Switching are based on the point's initial polarization state, *down*- or *up*-polarized, respectively. The vertical dashed lines represent the domain wall. As shown in the inset, $A + R$ is the initial piezoresponse value, A is the saturation value, n is the effective dimensionality of growth, and V_{sw} is the effective voltage required for switching. The whisker and box plots represent the median, the first through third quartile of data (box), and $\approx 99\%$ confidence interval for a normal distribution (whiskers). Additional outliers for each bin are shown in symbols. The distance from domain wall are calculated in a) $60\ nm$ bins and b) $30\ nm$, with center value used to represent the bin. For bins with less than 10 points, the number of points within the bin is reported above/below the bin.

APPENDIX D

FURTHER IINFORMATION ON RESONANT PIEZORESPONSE FORCE MICROSCOPY

D.1 Hardware

D.1.1 Complete Hardware List

The physical components of RPFM are: the National Instruments PXIe-1082, the National Instruments BNC-2110, and a computer monitor, keyboard, and mouse. The National Instruments (NI) PXIe-1082 (Fig. D.1a) is a chassis that houses various modules. The PXIe-1082 contains 5 modules:

- PXIe-8880: An embedded controller that runs Windows 10. It is connected to the computer monitor, mouse, and keyboard.
- PXIe-5122: An oscilloscope/digitizer that is currently unused. It could possibly be used for data collection.
- HDD-8261: The hard drives for the system.
- PXIe-5412: A waveform generator that is currently unused. It could be used as an alternative means of waveform generation.
- PXIe-6124: A multifunction I/O module. This module is the workhorse

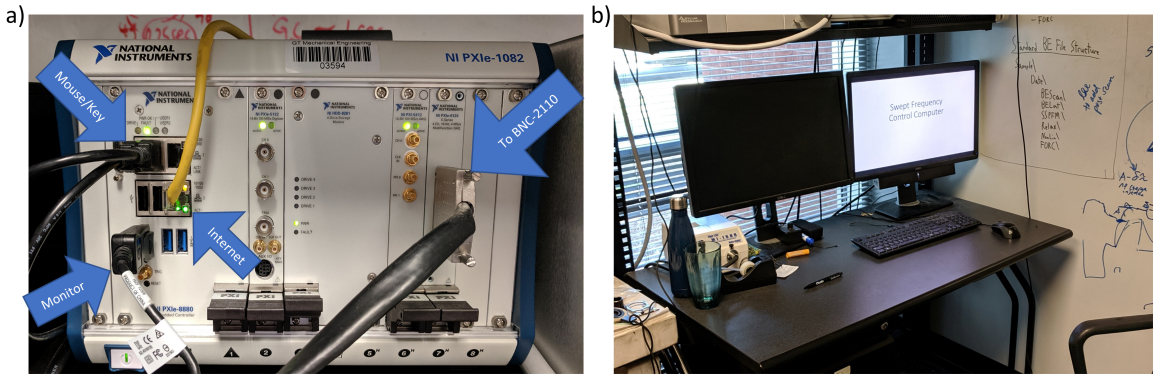

Figure D.1: a) Picture of the NI PXIe-1082. The arrows indicate the various connections. b) The monitor that is connected to the PXIe-8880 and is used to control the RPFM system.

of the RPFM system. It is used for waveform generation and collection. This module is connected to the BNC-2110.

The National Instruments (NI) BNC-2110 (Fig. D.2) is connected to the PXIe-6124 multifunction I/O module and is used for signal input/output for the PXIe-6124.

D.1.2 Comments on Hardware

The hardware for RPFM only serves two purposes: generating the measurement waveform during the application path and acquiring the raw response in the collection path. Thus, the only necessary hardware is an arbitrary waveform generator, for application, and an analog-to-digital converter, for data collection. The NI PXIe-6124 and the connected BNC-2110 fulfills both of these roles. For the application path, the waveform is calculated in the software (described below) and is generated by the PXIe-6124. The generated waveform is output on one of the channels of the BNC-2110 (the

default channel is AO 0, see Fig. D.2) and the user accordingly directs the signal to the PFM tip (see, for instance, the procedure for the Cypher AFM). For the collection path, the analog-to-digital converter collects the raw AC deflections of the tip and all of the post processing to obtain the material response is achieved in the software. The analog-to-digital converter used here is an input channel of the PXIe-6124 (the default channel is AI 0, see Fig. D.2). The user must direct the raw AC deflections of the tip to the PXIe-6124 to facilitate data collection.

Note that the PXIe-6124 has a maximum sample rate of 4 MHz, restricting the frequency range of the measurement waveform to < 2 MHz according to Nyquist-Shannon sampling theory [CITE], and a maximum voltage amplitude of ± 10 V. This limit on the voltage amplitude is an *absolute* limit and no point in the waveform can go beyond this limit. Thus, if the excitation chirp has an amplitude of 1.5 V then the maximum DC voltage that can be added to the chirp is 8.5 V.

As a final note on hardware, the above discussed trigger signal is provided to the PXIe-6124 through a trigger channel (the default channel is PFI 12, see Fig. D.2). When a rising edge is applied to the trigger channel, the PXIe-6124 will send the measurement waveform, once and only once, on the selected output channel and will sample the response on the selected input channel.

In summary, for proper operation of RPFM, three signals must properly

routed through the PXIe-6124: the measurement waveform, the trigger signal, and the response. The measurement waveform is the waveform that is generated by the PXIe-6124 and is applied to the material through the PFM tip. The trigger signal is what prompts the PXIe-6124 to output the probing waveform and begin data collection. The response is the acquired material response that the AFM outputs to the PXIe-6124. These three signals are communicated to/from the PXIe-6124 through the BNC-2110.

D.2 Comments on Nyquist-Shannon Sampling Theory

In brief, the Nyquist-Shannon Sampling theorem [CITE] states that when either generating or digitizing an analog signal the sample rate must be greater than twice the highest frequency in the signal. The upper limit on the sampling rate is typically a practical limitation imposed by either the hardware or memory usage, as higher sample rates will result in more sample points and, thus, more memory. For instance, consider a typical RPFM measurement with $f_L = 250\ kHz$ and $f_H = 300\ kHz$, here a sample rate of at least $600\ kHz$ necessary. However, the Nyquist limit is merely a minimum recommendation and using a sample rate of $600\ kHz$ will eliminate the possibility of probing the higher order harmonics. Thus, it is recommended to use a reasonably high sample rate. In this case, a sample rate of $2\ MHz$ will allow for the extraction of the fundamental, second, and third harmonic if desired.

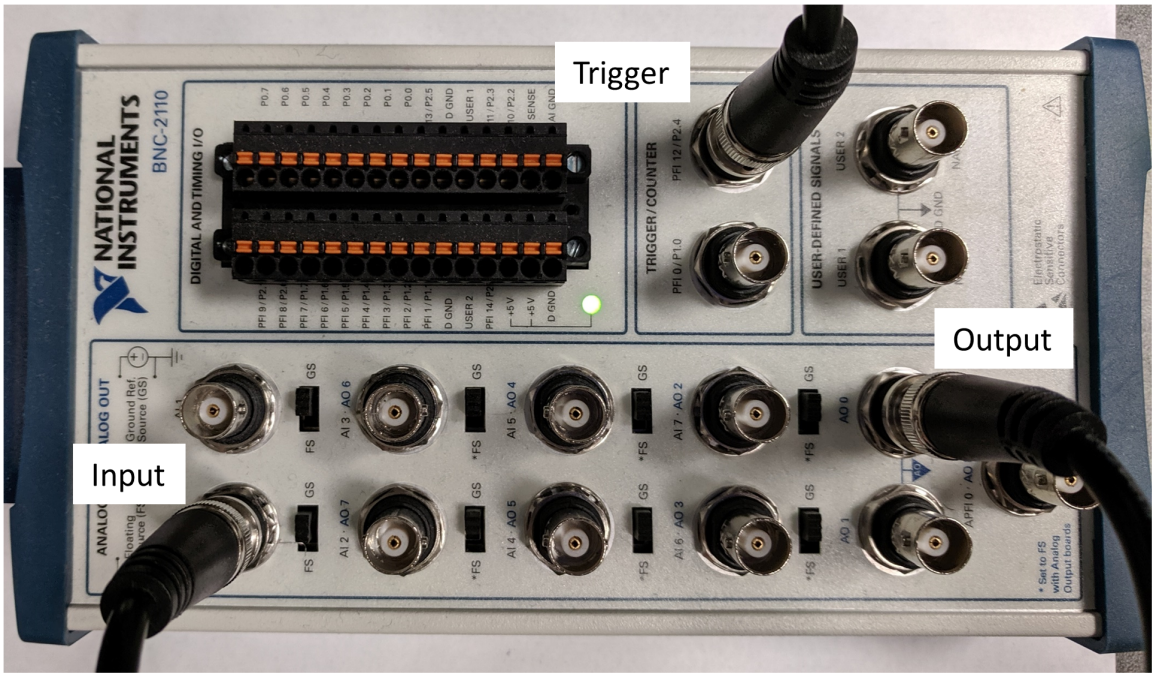

Figure D.2: Picture of the NI BNC-2110. White boxes label the signal paths.

D.3 Software

The software that runs RPFM is called Excite and is shown in its initial state in Fig. D.3. This is the software that will run in concert with the PFM and handles: managing the PXIe-6124, calculating the measurement waveform, some initial post-processing, and more. This software is divided into two components the python app and the labview app. The python app collects the user inputs, passes them to the Labview, generates supplementary files, and performs some post processing as the raw data is received from the PXIe-6124. The Labview app receives the user's specifications from python, calculates the measurement waveform, manages the PXIe-6124, and saves the raw data in the specified folder. During typical operation of Excite, the

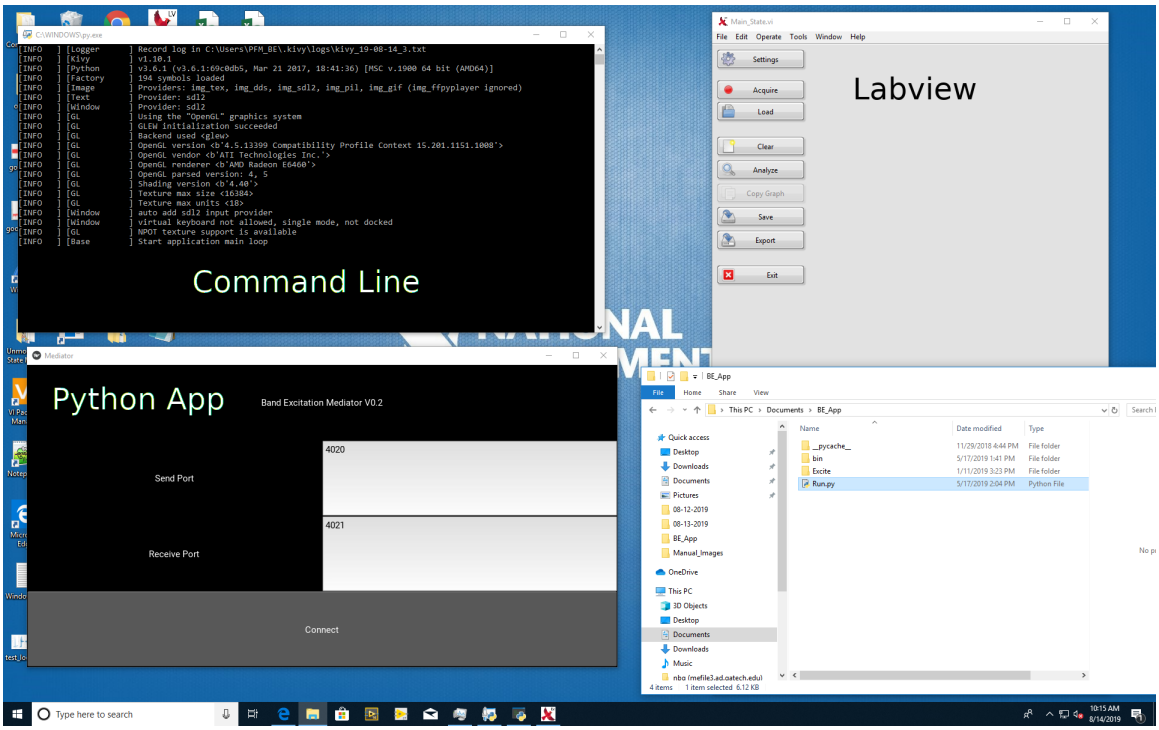

Figure D.3: Excite software upon initially launching software. Large text within the various windows labels the which component of the software the window is from

user should only interface with the python app. The Labview app only needs to be used if the user wishes to change options related to the hardware (e.g. change the output port). An overview of the operation of Excite and RPFM is provided in the next Appendix.

APPENDIX E

EXCITE/RPFM OVERVIEW OF OPERATION

When operating Excite, there are three task: prepare the physical connections between the AFM and the BNC-2110, prepare the Excite software, and prepare the AFM. Here, we will walk-through all three for a generic AFM. This overview is not intended as strict instructions, but as a means of illustrating how Excite operates. For these specific instructions see Chapter 5, which describes how Excite is operated with an Asylum MFP-3D and Cypher.

E.1 Types of Measurements

For the purpose of discussion, we can roughly classify the type of measurements typically performed on a AFM into two categories: scans, which raster over the surface while probing the response and point-by-point measurements, which probe the response at a single point or at a series of individual points over time and typically in response to some additional applied field.

E.2 The Physical Connections

As discussed above, proper operation of Excite requires the appropriate routing of three signals. First, the measurement waveform (by default channel *AO 0* of the BNC-2110) must be routed to the AFM tip and, second, the raw AC deflections of the tip must be routed to the analog-to-digital converter (by default channel *AI 0* of the BNC-2110). These signals are covered in Chapter 3. The final signal is the trigger signal which should be routed from the AFM to the trigger channel of the PXIe-6124 (by default channel *PFI 12* of the BNC-2110).

E.3 Excite Software

E.3.1 Starting Excite Software and Connecting Python and Labview

To start Excite, double click *Run.py* located in the *1Acquisition* folder. This launches both the python app and the labview app and should bring up the three windows shown in Fig. D.3. Prior to operation, the python and labview app must first be connected through TCP/IP. Connecting the two apps simply involves specifying the send and receive port numbers and clicking *Connect* in the python app. It is through this TCP/IP connection that the python app transmits the user inputs (send port) to Labview and the Labview app responds (receive port). The default port numbers are 4020 for the send port and 4021 for the receive port. Note, that the user should not

change these port numbers without a basic understanding of networking and, if these numbers are changed, corresponding changes must be made within the Labview app (in the file INFONEEDED FILE) and the python app (in the file INFONEEDED FILE).

A successful connection is shown in Fig. E.1. Note that the Command Line window now has 5 new lines: "$Sending\ connection\ message\ to\ 4020$" and "$sent\ \{"message\_name";"connect"\}$" indicating that python sent a "connect" message to Labview, "$Connection\ from\ \{127.0.0.1,\ S0312\}$" and "$\{"message\_name";"connectAck"\}$" indicating that python received a connectAck (or connection acknowledgement) from Labview, and "Connected" indicating that the connection has been established. Also, note that the python app has updated to the parameter specification screen. Now that the python and Labview apps are connected, the user can begin to input the measurement specifications.

Troubleshooting

- *Failure to connect:* When attempting to connect, if the command line shows that python sent a connect message but shows that no acknowledgement message was received, then the connection has failed. The user should check: first, that the correct port numbers were used and, second, that only one instance of each app is open.

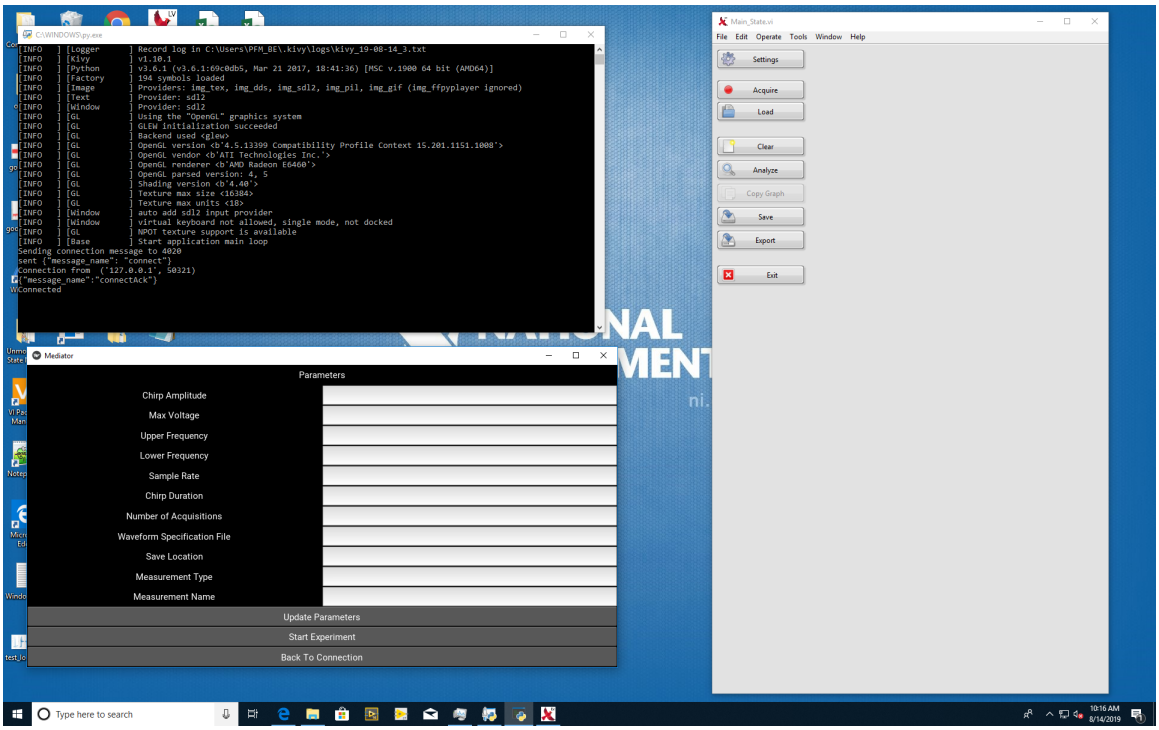

Figure E.1: Excite software upon initially launching software. Large text within the various windows labels the which component of the software the window is from

E.3.2 Specifying the Excitation Waveform

First, the user should specify the excitation waveform (i.e. the chirp). The parameters specified by the user in python are the Chirp Amplitude, Lower Frequency, Upper Frequency, Sampling Rate, and Chirp Duration. These parameters are input to the python app, transmitted to Labview over TCP/IP, and used to calculate the excitation waveform in Labview according to Eqs. 3.1 and 3.2. Appropriate values for Chirp Amplitude, Lower Frequency, and Upper Frequency are strongly dependent on the sample and PFM tip in question. It is best to empirically obtain these values by performing some initial frequency sweeps, such sweeps can be performed in via a lock-in

sweep typically available in any single frequency PFM mode.

A note regarding Chirp Amplitude: If a voltage amplifier external to the PXIe-6124 and BNC-2110 is being used, the user should account for the amplification here. For example, if the waveform being output by the PXIe-6124 is being amplified by a 10X voltage amplifier and the user desires a 1.5 V chirp, then the user must specify a chirp amplitude of 0.15 V in Python.

E.3.3 Specifying the Measurement waveform

Next, the user can specify a measurement waveform. As discussed in Band Excitation Theory in Chapter 2, the excitation waveform can be overlaid an arbitrary waveform, enabling voltage- and time- dependent spectroscopic measurements. This arbitrary waveform is specified in a waveform specification file (WSF). The WSF is a comma separated values (.csv) file with a specific structure, consisting of an arbitrary number of rows and 5 columns. From left to right, the columns in the WSF correspond to *Duration*, *DC Offset*, *Multiplier*, *Harmonic*, and *Plot Group*. A path to this file is input in the python app at the Waveform Specification File entry and python passes this path to the Labview app. Labview then reads the WSF row by row, from top to bottom. At each row, Labview constructs a series of excitation chirps based off the *Duration*, *DC Offset*, *Multiplier*, *Harmonic*, and *Plot Group* for that row, appending the chirp series together as it works down the rows.

A description of what the individual columns specify follows.

- *Duration:* The *Duration* is the number of consecutive chirps in the series for the row and must be an integer. For example, a *Duration* of 3 would result in a series of three consecutive chirps.

- *DC Offset:* The *DC voltage* value is a constant value added to the chirp series for this row, and is specified in volts. Continuing the previous example, a *Duration* of 3 and a *DC Offset* of 1 would result in a series of three consecutive chirps with a 1V DC offset added.

- *Multiplier:* The *Multiplier* is an arbitrary value to multiply the excitation chirp series by for this row, and is unit-less. This is the parameter that the user can use to vary the AC-Field (or Chirp Amplitude) throughout the measurement waveform. This value **DOES NOT** affect the DC offset, just the amplitude of the chirps. For instance, a Chirp Amplitude of 2V, a *Duration* of 3, a *DC Offset* of 1, and a *Multiplier* of 2 would result in a series of three consecutive chirps with a Chirp Amplitude of 4V and with a 1V DC offset added.

- *Harmonic:* The *Harmonic* option can be either 1, 2, or 3 and specifies which harmonic of the frequency response is of interest for this row. This option is not actually used in the generation of the measurement waveform, but specifies over which frequency range the functional fitting to Eq. 1.4 should be performed. For instance, consider if the chirp

frequency parameters are: $f_L = 250\ kHz$ and $f_H = 300\ kHz$. A *Harmonic* value of 1 for a row would result in the functional fitting being applied over the frequency range $250\ kHz$ to $300\ kHz$, while a harmonic value of 2 would result in the fitting being applied over $500\ kHz$ to $600\ kHz$. Note, be sure to use and appropriate sample rate. In the example here, at least $2 \times 600\ kHz = 1.2\ MHz$ would be required.

- *Plot Group:* The *Plot Group* is an arbitrary identifier for this row, provided for the user. This option is never used in the measurement waveform generation or during fitting. However, the final results will retain their associated *Plot Group* value and the user is welcome to use this option to allow for easy extraction of a particular subset of results. Note, that *Plot Group* can take any numerical value outside of 9 which is reserved.

Understanding the WSF files is best done through examples. Thus, a few examples follow. For these examples, we will only consider the Duration and DC Offset columns. First, an illustration of the proper WSF format is provided in Table 4.1 for the simplest measurement waveform, a single unaltered excitation chirp. As discussed, Labview constructs the measurement waveform by reading the WSF row by row, thus consider the first (and only) row in Table 4.1. A duration of 1 indicates that single chirp is desired for this row and a DC Offset of zero corresponds to no additional bias being

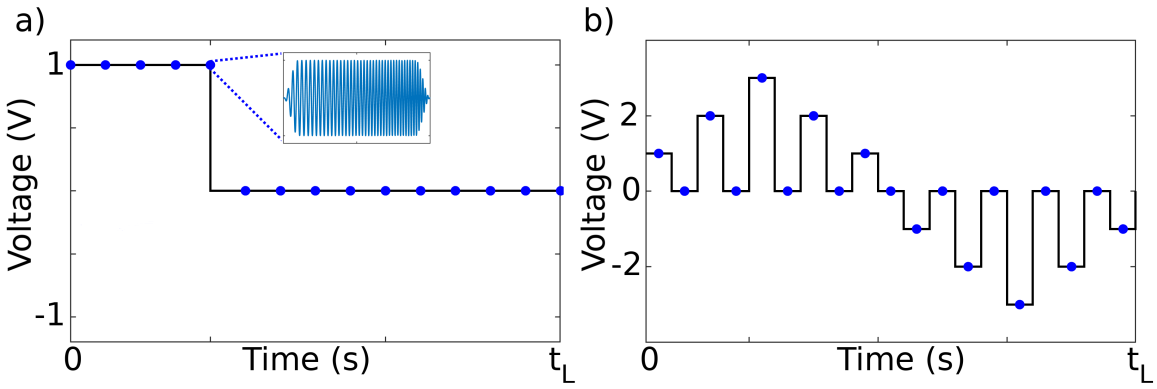

Figure E.2: Illustrations of a) a relaxation measurement waveform specified by Table E.2 and b) a switching spectroscopy measurement waveform specified by Table E.3. a) A simple relaxation measurement waveform where five consecutive chirps are applied with an added DC voltage of 1V and a subsequent 10 consecutive chirps are applied with no DC bias. In this way, the material is probed for five points while being poled by 1V and the resulting electromechanical relaxation upon removal of the 1V is probed for 10 points. b) A simple switching spectroscopy measurement waveform where the materials is probed from -3V to 3V in the typical SS-PFM fashion. Blue dots represent a single chirp and the black line represents the DC voltage.

added to the chirp. Thus, this WSF specifies a single excitation chirp with no modifications (Fig. 3.3) .

Table E.1: Simple example of a waveform specification file. A file like this would specify a single chirp with no alterations.

Duration	DC Offset	Multiplier	Harmonic	Plot Group
1	0	1	1	0

In Table 4.2, a WSF for a simple relaxation measurement is illustrated. Beginning with the first row, a duration of 5 indicates a series of 5 excitation chirps and a DC offset of 1 indicates that the 5 excitation chirp will be offset by a DC value of 1 V. In the next row, a duration of 10 indicates a series of 10 excitation chirps and a DC offset of 0 indicates no offset by a DC value. These two rows are generated consecutively. Thus, in total,

the measurement waveform will consist of 5 consecutive chirps of probing under a 1V bias (in-field), followed by 10 consecutive chirps of probing under no bias (out-of-field). This waveform is plotted in Fig. E.2a, where blue dots represent the individual chirps and the black line represents the DC voltage.

Table E.2: Simple example of a relaxation waveform specification file. A file like this would specify 5 chirps under a 1V bias, followed by 30 chirps under no bias.

Duration	DC Offset	Multiplier	Harmonic	Plot Group
5	1	1	1	0
10	0	1	1	0

In Table 4.3, a WSF for a simple SS-PFM measurement is illustrated. First, note that each row has a Duration of only 1 and, thus, each row only represents a single chirp. Further, the DC Offset column has the structure of a typical SS-PFM measurement ranging from -3 to $3\ V$. That is to say, the DC Offsets show a positive voltage triangle, followed by a negative voltage triangle, with zero DC field points in between each step. This waveform is illustrated in Fig. E.2b.

E.3.4 Number of Acquisitions

Once the user has specified the excitation and measurement waveform, they must next specify the number of *Acquisitions*. As stated above, an *Acquisition* is a single application of the measurement waveform and subsequent acquisition of the material's response and is triggered anytime a rising edge

Table E.3: Simple example of a PFM-based switching spectroscopy waveform specification file. A file like this would specify a typical -3V to 3V SS-PFM measurement and probed the response by in-field (during the applied DC voltage) and out-of-field (upon removal of the DC voltage).

Duration	DC Offset	Multiplier	Harmonic	Plot Group
1	1	1	1	0
1	0	1	1	0
1	2	1	1	0
1	0	1	1	0
1	3	1	1	0
1	0	1	1	0
1	2	1	1	0
1	0	1	1	0
1	1	1	1	0
1	0	1	1	0
1	-1	1	1	1
1	0	1	1	1
1	-2	1	1	1
1	0	1	1	1
1	-3	1	1	1
1	0	1	1	1
1	-2	1	1	1
1	0	1	1	1
1	-1	1	1	1
1	0	1	1	1

is applied to the trigger channel of the PXIe-6124. In the Python app, the user must specify the number of *Acquisitions*, or the number of triggers, that Excite should expect. For instance, if a user wanted to apply some arbitrary measurement waveform (e.g. an SS-PFM waveform, Fig. E.2b) at 100 points on a surface area, then *Number of Acquisitions* must be specified as 100. Consider another example, typical PFM scan has a resolution of 256 by 256 points and is acquired by scanning the PFM tip over the surface area collecting 256 point per line for 256 lines (illustrated in FIG). To incorpo-

rate into this measurement is the user has two options: specify *Number of Acquisitions* as $256 \times 256 = 65536$ and provide a trigger signal for each point in the 256 by 256 grid or specify *Number of Acquisitions* as 256, use a WSF to specify a train of 256 chirps (Table E.4, and provide a trigger signal for each line. Note that the latter is the recommended approach.

Table E.4: Waveform specification file for capturing a single line of a PFM scan with 256 points per line.

Duration	DC Offset	Multiplier	Harmonic	Plot Group
256	0	1	1	0

E.3.5 Remaining Measurement Parameters

The remaining measurement parameters are: Max Voltage, Save Location, Measurement Type, and Measurement Name. Max voltage is the voltage limit on the measurement and is the maximum allowable voltage output of the PXIe-6124. Note that the hardware limits the voltage out of the PXIe-6124 to $\pm 10\ V$. However, with this option, the user can impose a software limit if desired. Save Location is the folder in which all of the raw data, processed data, and supplementary files will be saved. Measurement Type and Measurement Name are only used by the tool bepy, which is a supplemental tool for plotting, data organization, and analysis. However, neither of these parameters is necessary for Excite to operate properly. Measurement Type is a tag used by the tool bepy and should be set to either Scan, Relax, SSPFM

or NonLin, which correspond to a basic RPFM domain imaging measurement, a relaxation measurement, a switching spectroscopy measurements, and a non-linear measurement. Naturally, when performing one of these four measurements the corresponding tag should be used for Measurement Type. However, if the measurement is none of these, one of these four tags must still be chosen. In this case, the user should choose whichever tag is appropriate for the measurement. Note that bepy by default plots Scan-types as an image of the individual *Acquisitions*, Relax-types as a function of time, SSPFM-types as a function of the DC Offset in the WSF, and the NonLin-types as a function of the Multiplier in the WSF. Finally, the Measurement Name parameter is used by bepy as a unique identifier for the measurement and can be any string of characters, numbers, and/or special characters.

E.3.6 Confirming Measurement Parameters

Once all of the above parameters have been specified, the user must click *Update Parameters* which sends all of the necessary parameters from the Python app to the Labview app. At this point the Excite software should resemble Fig. E.3. Note that the Command Line window now has numerous new lines consisting of: "$Connection\ from\ \{127.0.0.1,\ S0312\}$" indicating the connection, sent $\{"message\_name" : "setParam", "param\_name" : "paramIdentifier", "param\_value" : "3"\}$ indicating that Python has told Labview to update the parameter named "paramIdentifier" to the some

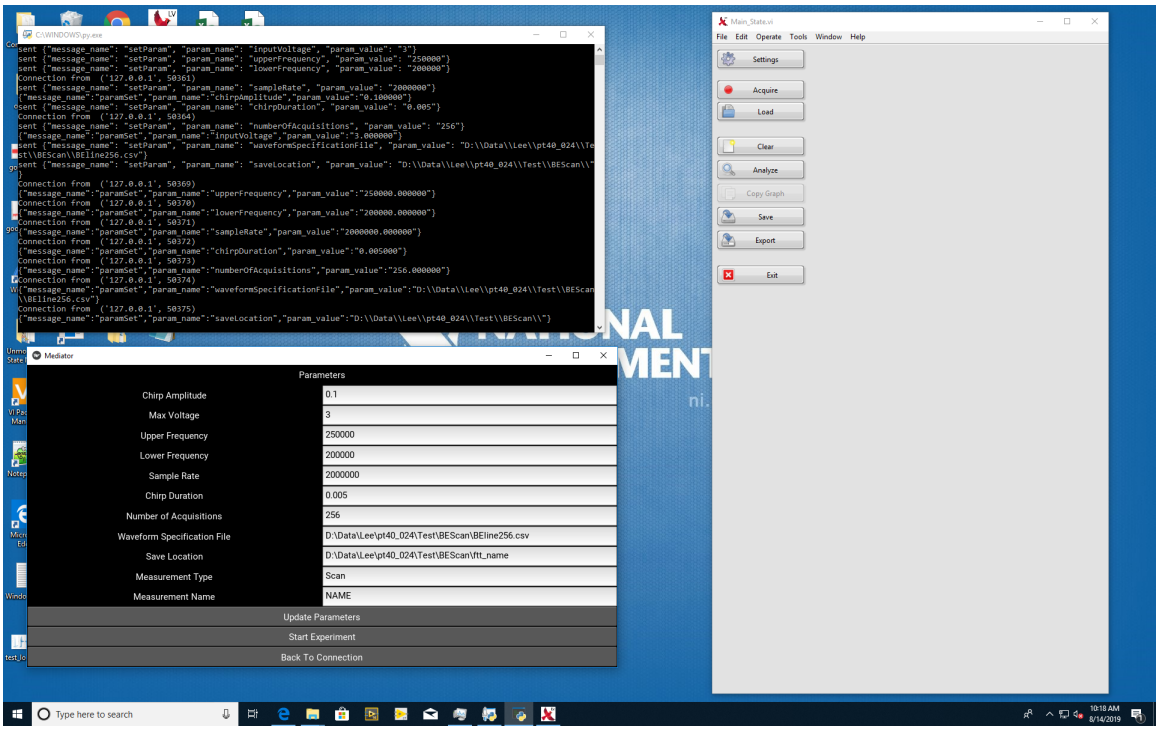

Figure E.3: Excite software with arbitrary parameters and after clicking *Update Parameters*.

value (here "3"), and $\{"message\_name" : "paramSet", "param\_name" : "paramIdentifier", "param\_value" : "3"\}$ indicating that Labview has updated the parameter named "paramIdentifier" to the requested value.

E.3.7 Summary

Once all of the parameters have been specified and confirmed, the Excite software is ready to begin the specified measurement. At this point, clicking *Start Experiment* will cause Excite to begin listening for triggers from the AFM. However, it is recommended that the user prepare the AFM before clicking *Start Experiment*, as Excite will time-out if a trigger isn't received within 2 minutes.

E.4 Preparing the AFM

E.4.1 Syncing

To reiterate, a side effect of Excite's AFM-agnosticism is that Excite has no control or knowledge of the tip movements. Thus, it falls to the user to ensure that the Cypher is properly "synced" with Excite. In other words, when the Cypher provides a trigger to Excite to begin application and acquisition, the user must ensure that the Cypher provides adequate time for the application and acquisition to finish. In a scan measurement, this typically means specifying an appropriate scan rate and accounting for any overscan the AFM might do automatically when scanning. In a point-by-point measurement, this typically means ensuring that the tip dwells long enough at the surface for the application and acquisition to finish. The specifics of syncing will depend on the particular AFM used and, thus, will be more completely discussed in Chapter 5 for the Cypher and MFP3d.

REFERENCES

[1] J. F. Scott and C. A. Paz de Araujo, "Ferroelectric Memories," *Science*, vol. 246, no. 4936, pp. 1400 –1405, Dec. 1989.

[2] H. Goesmann and C. Feldmann, "Nanoparticulate Functional Materials," *Angewandte Chemie International Edition*, vol. 49, no. 8, pp. 1362–1395, 2010.

[3] J. Kim, P. Gutruf, A. M. Chiarelli, S. Y. Heo, K. Cho, Z. Xie, A. Banks, S. Han, K.-I. Jang, J. W. Lee, K.-T. Lee, X. Feng, Y. Huang, M. Fabiani, G. Gratton, U. Paik, and J. A. Rogers, "Miniaturized Battery-Free Wireless Systems for Wearable Pulse Oximetry," *Advanced Functional Materials*, vol. 27, no. 1, p. 1 604 373, 2017.

[4] W. Zeng, L. Shu, Q. Li, S. Chen, F. Wang, and X.-M. Tao, "Fiber-Based Wearable Electronics: A Review of Materials, Fabrication, Devices, and Applications," *Advanced Materials*, vol. 26, no. 31, pp. 5310–5336, 2014.

[5] M. Amjadi, K.-U. Kyung, I. Park, and M. Sitti, "Stretchable, Skin-Mountable, and Wearable Strain Sensors and Their Potential Applications: A Review," *Advanced Functional Materials*, vol. 26, no. 11, pp. 1678–1698, 2016.

[6] K. S. Ramadan, D Sameoto, and S Evoy, "A review of piezoelectric polymers as functional materials for electromechanical transducers," *Smart Materials and Structures*, vol. 23, no. 3, p. 33 001, 2014.

[7] K. C. Cheng, H. L. W. Chan, C. L. Choy, Q. Yin, H. Luo, and Z. Yin, "Single crystal PMN-0.33PT/epoxy 1-3 composites for ultrasonic transducer applications," *IEEE Transactions on Ultrasonics, Ferroelectrics, and Frequency Control*, vol. 50, no. 9, pp. 1177–1183, 2003.

[8] L. M. Ewart, E. A. Mclaughlin, H. C. Robinson, J. J. Stace, and A Amin, "Mechanical and electromechanical properties of pmnt single crystals for naval sonar transducers," *IEEE Transactions on Ultrasonics, Ferroelectrics, and Frequency Control*, vol. 54, no. 12, pp. 2469–2473, 2007.

[9] M. J. Haun, E Furman, S. J. Jang, and L. E. Cross, "Thermodynamic theory of the lead zirconate-titanate solid solution system, part I: Phenomenology," *Ferroelectrics*, vol. 99, no. 1, pp. 13–25, Nov. 1989.

[10] D. Damjanovic, "Ferroelectric, dielectric and piezoelectric properties of ferroelectric thin films and ceramics," *Reports on Progress in Physics*, vol. 61, no. 9, pp. 1267–1324, 1998.

[11] L. W. Martin and A. M. Rappe, "Thin-film ferroelectric materials and their applications," *Nature Reviews Materials*, vol. 2, no. 2, p. 16 087, 2016.

[12] "An american national standard IEEE standard definitions of terms associated with ferroelectric and related materials," *IEEE Transactions on Ultrasonics, Ferroelectrics, and Frequency Control*, vol. 50, no. 12, pp. 1–32, 2003.

[13] N. Bassiri-Gharb, "Dielectric and piezoelectric nonlinearities in oriented Pb(Yb1/2Nb1/2)O3-PbTiO3 thin films," PhD thesis, The Pennsylvania State University, 2005.

[14] S. J. Brewer, "RADIATION HARDNESS IN FERROELECTRIC THIN FILMS FOR MEMS APPLICATIONS," PhD thesis, Georgia Institute of Technology, 2017.

[15] T. Horikawa, N. Mikami, T. Makita, J. Tanimura, M. Kataoka, K. Sato, and M. Nunoshita, "Dielectric Properties of (Ba, Sr)TiO3Thin Films Deposited by RF Sputtering," *Japanese Journal of Applied Physics*, vol. 32, no. Part 1, No. 9B, pp. 4126–4130, 1993.

[16] B. Wul and I. M. Goldman, "Dielectric constants of titanates of metals of the second group," *Compt.Rend.Acad.Sci.URSS*, vol. 46, p. 177, 1945.

[17] B. J. Rodriguez, R. J. Nemanich, A Kingon, A Gruverman, S. V. Kalinin, K Terabe, X. Y. Liu, and K Kitamura, "Domain growth kinetics in lithium niobate single crystals studied by piezoresponse force microscopy," *Applied Physics Letters*, vol. 86, no. 1, p. 12 906, Dec. 2004.

[18] A Agronin, M Molotskii, Y Rosenwaks, G Rosenman, B. J. Rodriguez, A. I. Kingon, and A Gruverman, "Dynamics of ferroelectric domain growth in the field of atomic force microscope," *Journal of Applied Physics*, vol. 99, no. 10, p. 104 102, May 2006.

[19] A Gruverman, B. J. Rodriguez, C Dehoff, J. D. Waldrep, A. I. Kingon, R. J. Nemanich, and J. S. Cross, "Direct studies of domain switching dynamics in thin film ferroelectric capacitors," *Applied Physics Letters*, vol. 87, no. 8, p. 82 902, Aug. 2005.

[20] D. M. Marincel, H. Zhang, A. Kumar, S. Jesse, S. V. Kalinin, W. M. Rainforth, I. M. Reaney, C. A. Randall, and S. Trolier-McKinstry, "Influence of a Single Grain

Boundary on Domain Wall Motion in Ferroelectrics," *Advanced Functional Materials*, vol. 24, no. 10, pp. 1409–1417, Mar. 2014.

[21] V. R. Aravind, A. N. Morozovska, S. Bhattacharyya, D Lee, S Jesse, I Grinberg, Y. L. Li, S Choudhury, P Wu, K Seal, A. M. Rappe, S. V. Svechnikov, E. A. Eliseev, S. R. Phillpot, L. Q. Chen, V. Gopalan, and S. V. Kalinin, "Correlated polarization switching in the proximity of a $180ˆ\circ$ domain wall," *Physical Review B*, vol. 82, no. 2, p. 24 111, Jul. 2010.

[22] L. A. Griffin, I. Gaponenko, S. Zhang, and N. Bassiri-Gharb, "Smart machine learning or discovering meaningful physical and chemical contributions through dimensional stacking," *npj Computational Materials*, vol. 5, no. 1, p. 85, 2019.

[23] F. Li, S. Zhang, Z. Xu, X. Wei, J. Luo, and T. R. Shrout, "Composition and phase dependence of the intrinsic and extrinsic piezoelectric activity of domain engineered (1-x)Pb(Mg1/3Nb2/3)O3-xPbTiO3 crystals," *Journal of Applied Physics*, vol. 108, no. 3, p. 34 106, Aug. 2010.

[24] S. V. Kalinin, B. J. Rodriguez, J. D. Budai, S Jesse, A. N. Morozovska, A. A. Bokov, and Z. G. Ye, "Direct evidence of mesoscopic dynamic heterogeneities at the surfaces of ergodic ferroelectric relaxors," *Physical Review B*, vol. 81, no. 6, p. 64 107, 2010.

[25] P. Finkel, K. Benjamin, and A. Amin, "Large strain transduction utilizing phase transition in relaxor-ferroelectric Pb(In1/2Nb1/2)O3–Pb(Mg1/3Nb2/3)O3–PbTiO3," *Applied Physics Letters*, vol. 98, no. 19, p. 192 902, 2011.

[26] M. E. Manley, J. W. Lynn, D. L. Abernathy, E. D. Specht, O Delaire, A. R. Bishop, R Sahul, and J. D. Budai, "Phonon localization drives polar nanoregions in a relaxor ferroelectric," *Nature Communications*, vol. 5, 2014.

[27] F. Jiang, S. Kojima, C. Zhao, and C. Feng, "Chemical ordering in lanthanum-doped lead magnesium niobate relaxor ferroelectrics probed by {A}1g Raman mode," *Applied Physics Letters*, vol. 79, no. 24, pp. 3938–3940, 2001.

[28] G. H. Blackwood and M. A. Ealey, "Electrostrictive behavior in lead magnesium niobate (PMN) actuators. I. Materials perspective," *Smart Materials and Structures*, vol. 2, no. 2, pp. 124–133, 1993.

[29] B Lewis, "Energy Loss Processes in Ferroelectric Ceramics," *Proceedings of the Physical Society*, vol. 73, no. 1, pp. 17–24, 1959.

[30] L. Rayleigh, "XXV. Notes on electricity and magnetism.—III. On the behaviour of iron and steel under the operation of feeble magnetic forces," *The London, Edinburgh, and Dublin Philosophical Magazine and Journal of Science*, vol. 23, no. 142, pp. 225–245, Mar. 1887.

[31] C. Ang and Z. Yu, "Dielectric behavior of PbZr0.52Ti0.48O3 thin films: Intrinsic and extrinsic dielectric responses," *Applied Physics Letters*, vol. 85, no. 17, pp. 3821–3823, Oct. 2004.

[32] Z. Q. Zhuang, M. J. Haun, S. Jang, and L. E. Cross, "Composition and temperature dependence of the dielectric, piezoelectric and elastic properties of pure PZT ceramics," *IEEE Transactions on Ultrasonics, Ferroelectrics, and Frequency Control*, vol. 36, no. 4, pp. 413–416, 1989.

[33] O Kersten, M Hofmann, and G Schmidt, "Dielectric dispsrsion of Mn doped ceramics," *Ferroelectrics Letters Section*, vol. 6, no. 3, pp. 75–80, Sep. 1986.

[34] U Böttger and G Arlt, "Dielectric microwave dispersion in PZT ceramics," *Ferroelectrics*, vol. 127, no. 1, pp. 95–100, Mar. 1992.

[35] G Arlt, H Dederichs, and R Herbiet, "90°-domain wall relaxation in tetragonally distorted ferroelectric ceramics," *Ferroelectrics*, vol. 74, no. 1, pp. 37–53, Aug. 1987.

[36] R Herbiet, H Tenbrock, and G Arlt, "The aging behaviour of the complex material parameters ϵ, d and s in ferroelectric PZT ceramics," *Ferroelectrics*, vol. 76, no. 1, pp. 319–326, Dec. 1987.

[37] W. J. Merz, "Switching Time in Ferroelectric BaTiO3 and Its Dependence on Crystal Thickness," *Journal of Applied Physics*, vol. 27, no. 8, pp. 938–943, Aug. 1956.

[38] E. Sun and W. Cao, "Relaxor-based ferroelectric single crystals: Growth, domain engineering, characterization and applications," *Progress in Materials Science*, vol. 65, pp. 124–210, Aug. 2014.

[39] Y. Xiang, R. Zhang, and W. Cao, "Optimization of piezoelectric properties for [001]c poled 0.94PZN–0.06PT single crystals," *Applied Physics Letters*, vol. 96, no. 9, p. 92 902, Mar. 2010.

[40] H. Takenaka, I. Grinberg, S. Liu, and A. M. Rappe, "Slush-like polar structures in single-crystal relaxors," *Nature*, vol. 546, p. 391, Jun. 2017.

[41] R. K. Vasudevan, S. Zhang, J. Ding, M. B. Okatan, S. Jesse, S. V. Kalinin, and N. Bassiri-Gharb, "Mesoscopic harmonic mapping of electromechanical response in a relaxor ferroelectric," *Applied Physics Letters*, vol. 106, no. 22, p. 222 901, 2015.

[42] Y. Kim, A. Kumar, A. Tselev, I. I. Kravchenko, H. Han, I. Vrejoiu, W. Lee, D. Hesse, M. Alexe, S. V. Kalinin, and S. Jesse, "Nonlinear Phenomena in Multiferroic Nanocapacitors: Joule Heating and Electromechanical Effects," *ACS Nano*, vol. 5, no. 11, pp. 9104–9112, Nov. 2011.

[43] S. Jesse, H. N. Lee, and S. V. Kalinin, "Quantitative mapping of switching behavior in piezoresponse force microscopy," *Review of Scientific Instruments*, vol. 77, no. 7, p. 73 702, Jul. 2006.

[44] P. Paruch, T. Giamarchi, T. Tybell, and J.-M. Triscone, "Nanoscale studies of domain wall motion in epitaxial ferroelectric thin films," *Journal of Applied Physics*, vol. 100, no. 5, p. 51 608, Sep. 2006.

[45] D. Edwards, S. Brewer, Y. Cao, S. Jesse, L.-Q. Chen, S. V. Kalinin, A. Kumar, and N. Bassiri-Gharb, "Local Probing of Ferroelectric and Ferroelastic Switching through Stress-Mediated Piezoelectric Spectroscopy," *Advanced Materials Interfaces*, vol. 3, no. 7, p. 1 500 470, Apr. 2016.

[46] C Borderon, A. E. Brunier, K Nadaud, R Renoud, M Alexe, and H. W. Gundel, "Domain wall motion in Pb(Zr0.20Ti0.80)O3 epitaxial thin films," *Scientific Reports*, vol. 7, no. 1, p. 3444, 2017.

[47] S. V. Kalinin, B. J. Rodriguez, A. Y. Borisevich, A. P. Baddorf, N. Balke, H. J. Chang, L.-Q. Chen, S. Choudhury, S. Jesse, P. Maksymovych, M. P. Nikiforov, and S. J. Pennycook, "Defect-Mediated Polarization Switching in Ferroelectrics and Related Materials: From Mesoscopic Mechanisms to Atomistic Control," *Advanced Materials*, vol. 22, no. 3, pp. 314–322, Jan. 2010.

[48] A. N. Morozovska, S. V. Kalinin, E. A. Eliseev, V. Gopalan, and S. V. Svechnikov, "Interaction of a \$180\ifmmodeˆ\circ\else\textdegree\fi{}\$ ferroelectric domain wall with a biased scanning probe microscopy tip: Effective wall geometry and thermodynamics in Ginzburg-Landau-Devonshire theory," *Physical Review B*, vol. 78, no. 12, p. 125 407, Sep. 2008.

[49] R. K. Vasudevan, S. Zhang, M. B. Okatan, S. Jesse, S. V. Kalinin, and N. Bassiri-Gharb, "Multidimensional dynamic piezoresponse measurements: Unraveling local relaxation behavior in relaxor-ferroelectrics via big data," *Journal of Applied Physics*, vol. 118, no. 7, p. 72 003, 2015.

[50] F. Li, S. Zhang, D. Damjanovic, L.-Q. Chen, and T. Shrout, "Local Structural Heterogeneity and Electromechanical Responses of Ferroelectrics: Learning from Relaxor Ferroelectrics," *Advanced Functional Materials*, vol. 0, no. 0, p. 1 801 504, 2018.

[51] S. Zhang, R. Xia, and T. R. Shrout, "Lead-free piezoelectric ceramics vs. PZT?" *Journal of Electroceramics*, vol. 19, no. 4, pp. 251–257, 2007.

[52] M. Otonicar, H. Ursic, M. Dragomir, A. Bradesko, G. Esteves, J. Jones, A. Bencan, B. Malic, and T. Rojac, "Multiscale field-induced structure of (1-x)Pb(Mg1/3Nb2/3)O3–xPbTiO3 ceramics from combined techniques," *Acta Materialia*, vol. 154, pp. 14–24, Aug. 2018.

[53] D. A. Berlincourt, C Cmolik, and H Jaffe, "Piezoelectric Properties of Polycrystalline Lead Titanate Zirconate Compositions," *Proceedings of the IRE*, vol. 48, no. 2, pp. 220–229, 1960.

[54] B. Jaffe, W. R. Cook, and H. L. Jaffe, *Piezoelectric ceramics*. 1971, ISBN: 0123795508 9780123795502.

[55] M. Davis, "Picturing the elephant: Giant piezoelectric activity and the monoclinic phases of relaxor-ferroelectric single crystals," *Journal of Electroceramics*, vol. 19, no. 1, pp. 25–47, 2007.

[56] D. Damjanovic, "A morphotropic phase boundary system based on polarization rotation and polarization extension," *Applied Physics Letters*, vol. 97, no. 6, p. 62 906, Aug. 2010.

[57] H. Fu and R. E. Cohen, "Polarization rotation mechanism for ultrahigh electromechanical response in single-crystal piezoelectrics," *Nature*, vol. 403, p. 281, Jan. 2000.

[58] D. Damjanovic, "Contributions to the Piezoelectric Effect in Ferroelectric Single Crystals and Ceramics," *Journal of the American Ceramic Society*, vol. 88, no. 10, pp. 2663–2676, Oct. 2005.

[59] H. Liu, J. Chen, L. Fan, Y. Ren, Z. Pan, K. V. Lalitha, J. Rödel, and X. Xing, "Critical Role of Monoclinic Polarization Rotation in High-Performance Perovskite Piezoelectric Materials," *Physical Review Letters*, vol. 119, no. 1, p. 17 601, Jul. 2017.

[60] F. Li, S. Zhang, Z. Xu, X. Wei, and T. R. Shrout, "Critical Property in Relaxor-PbTiO3 Single Crystals – Shear Piezoelectric Response," *Advanced Functional Materials*, vol. 21, no. 11, pp. 2118–2128, Jun. 2011.

[61] Z. Wu and R. E. Cohen, "Pressure-Induced Anomalous Phase Transitions and Colossal Enhancement of Piezoelectricity in PbTiO3," *Physical Review Letters*, vol. 95, no. 3, p. 37 601, Jul. 2005.

[62] Y. Nahas, A. Akbarzadeh, S. Prokhorenko, S. Prosandeev, R. Walter, I. Kornev, J. Íñiguez, and L Bellaiche, "Microscopic origins of the large piezoelectricity of leadfree (Ba,Ca)(Zr,Ti)O3," *Nature Communications*, vol. 8, p. 15 944, Jun. 2017.

[63] S. E. Park and T. R. Shrout, "Ultrahigh strain and piezoelectric behavior in relaxor based ferroelectric single crystals," *Journal of Applied Physics*, vol. 82, no. 4, pp. 1804–1811, 1997.

[64] S. Nomura and K. Uchino, "Electrostrictive effect in Pb(Mg1/3Nb2/3)O3-type materials," *Ferroelectrics*, vol. 41, no. 1, pp. 117–132, May 1982.

[65] A. A. Bokov and Z.-G. Ye, "Recent progress in relaxor ferroelectrics with perovskite structure," *Journal of Materials Science*, vol. 41, no. 1, pp. 31–52, 2006.

[66] I. K. Jeong, T. W. Darling, J. K. Lee, T. Proffen, R. H. Heffner, J. S. Park, K. S. Hong, W Dmowski, and T Egami, "Direct Observation of the Formation of Polar Nanoregions in $\mathrm{Pb}({\mathrm{Mg}}_{1/3}{\mathrm{Nb}}_{2/3}){\mathrm{O}}_
Using Neutron Pair Distribution Function Analysis," *Physical Review Letters*, vol. 94, no. 14, p. 147 602, 2005.

[67] G. Xu, G Shirane, J. R. D. Copley, and P. M. Gehring, "Neutron elastic diffuse scattering study of $\mathrm{Pb}({\mathrm{Mg}}_{1/3}{\mathrm{Nb}}_{2/3}){\mathrm{O}}_{
Physical Review B, vol. 69, no. 6, p. 64 112, Feb. 2004.

[68] M. E. Manley, D. L. Abernathy, R. Sahul, D. E. Parshall, J. W. Lynn, A. D. Christianson, P. J. Stonaha, E. D. Specht, and J. D. Budai, "Giant electromechanical coupling of relaxor ferroelectrics controlled by polar nanoregion vibrations," *Science Advances*, vol. 2, no. 9, e1501814, Sep. 2016.

[69] D. Phelan, C. Stock, J. A. Rodriguez-Rivera, S. Chi, J. Leão, X. Long, Y. Xie, A. A. Bokov, Z.-G. Ye, P. Ganesh, and P. M. Gehring, "Role of random electric fields in relaxors," *Proceedings of the National Academy of Sciences*, vol. 111, no. 5, 1754 LP –1759, Feb. 2014.

[70] G. Xu, J. Wen, C Stock, and P. M. Gehring, "Phase instability induced by polar nanoregions in a relaxor ferroelectric system," *Nature Materials*, vol. 7, p. 562, May 2008.

[71] D. Fu, H. Taniguchi, M. Itoh, S.-y. Koshihara, N Yamamoto, and S. Mori, "Relaxor Pb(Mg1/3Nb2/3)O3: A Ferroelectric with Multiple Inhomogeneities," *Physical Review Letters*, vol. 103, no. 20, p. 207 601, Nov. 2009.

[72] F. Li, S. Zhang, T. Yang, Z. Xu, N. Zhang, G. Liu, J. Wang, J. Wang, Z. Cheng, Z.-G. Ye, J. Luo, T. R. Shrout, and L.-Q. Chen, "The origin of ultrahigh piezoelectricity in relaxor-ferroelectric solid solution crystals," *Nature Communications*, vol. 7, p. 13 807, 2016.

[73] S. Miao, J. Zhu, X. Zhang, and Z.-Y. Cheng, "Electron diffraction and HREM study of a short-range ordered structure in the relaxor ferroelectric Pb(Mg1/3Nb2/3)O3," *Physical Review B*, vol. 65, no. 5, p. 52 101, Dec. 2001.

[74] A. D. Hilton, D. J. Barber, C. A. Randall, and T. R. Shrout, "On short range ordering in the perovskite lead magnesium niobate," *Journal of Materials Science*, vol. 25, no. 8, pp. 3461–3466, 1990.

[75] A. A. Bokov, M. A. Leshchenko, M. A. Malitskaya, and I. P. Raevski, "Dielectric spectra and Vogel-Fulcher scaling in Pb(In0.5Nb0.5)O3relaxor ferroelectric," *Journal of Physics: Condensed Matter*, vol. 11, no. 25, pp. 4899–4911, 1999.

[76] Y.-H. Chen, S. Hirose, D. Viehland, S. Takahashi, and K. Uchino, "Mn-Modified Pb(Mg1/3Nb2/3)O3-xPbTiO3 Ceramics: Improved Mechanical Quality Factors for High-Power Transducer Applications," *Japanese Journal of Applied Physics*, vol. 39, no. 8R, p. 4843, 2000.

[77] Z. Feng, O. K. Tan, W. Zhu, Y. Jia, and H. Luo, "Aging-induced giant recoverable electrostrain in Fe-doped 0.62Pb(Mg1/3Nb2/3)O3-x0.38PbTiO3 single crystals," *Applied Physics Letters*, vol. 92, no. 14, p. 142 910, 2008.

[78] S. Zhang, J. Luo, W. Hackenberger, and T. R. Shrout, "Characterization of Pb(In1/2Nb1/2)O3-Pb(Mg1/3Nb2/3)O3-PbTiO3 ferroelectric crystal with enhanced phase transition temperatures," *Journal of Applied Physics*, vol. 104, no. 6, p. 64 106, 2008.

[79] F. Li, D. Lin, Z. Chen, Z. Cheng, J. Wang, C. Li, Z. Xu, Q. Huang, X. Liao, L.-Q. Chen, T. R. Shrout, and S. Zhang, "Ultrahigh piezoelectricity in ferroelectric ceramics by design," *Nature Materials*, vol. 17, no. 4, pp. 349–354, 2018.

[80] S. Wada, H. Kakemoto, and T. Tsurumi, "Enhanced Piezoelectric Properties of Piezoelectric Single Crystals by Domain Engineering," *MATERIALS TRANSACTIONS*, vol. 45, no. 2, pp. 178–187, 2004.

[81] C. Qiu, B. Wang, N. Zhang, S. Zhang, J. Liu, D. Walker, Y. Wang, H. Tian, T. R. Shrout, Z. Xu, L.-Q. Chen, and F. Li, "Transparent ferroelectric crystals with ultrahigh piezoelectricity," *Nature*, vol. 577, no. 7790, pp. 350–354, 2020.

[82] D. Viehland, M. Kim, Z Xu, and J. Li, "Long-time present tweedlike precursors and paraelectric clusters in ferroelectrics containing strong quenched randomness," *Applied Physics Letters*, vol. 67, no. 17, pp. 2471–2473, Oct. 1995.

[83] F. Li, S. Zhang, Z. Xu, and L.-Q. Chen, "The Contributions of Polar Nanoregions to the Dielectric and Piezoelectric Responses in Domain-Engineered Relaxor-PbTiO3 Crystals," *Advanced Functional Materials*, vol. 27, no. 18, p. 1 700 310, May 2017.

[84] M Wallace, R. L. Johnson-Wilke, G Esteves, C. M. Fancher, R. H. T. Wilke, J. L. Jones, and S Trolier-McKinstry, "In situ measurement of increased ferroelectric/ferroelastic domain wall motion in declamped tetragonal lead zirconate titanate thin films," *Journal of Applied Physics*, vol. 117, no. 5, p. 54 103, Feb. 2015.

[85] J Karthik, A. R. Damodaran, and L. W. Martin, "Effect of 90\ifmmodeˆ\circ\else\textdegree\fi{} Domain Walls on the Low-Field Permittivity of ${\mathrm{PbZr}}_{0.2}{\mathrm{Ti}}_{0.8}{ Thin Films," *Physical Review Letters*, vol. 108, no. 16, p. 167 601, Apr. 2012.

[86] C.-L. Jia, S.-B. Mi, K. Urban, I. Vrejoiu, M. Alexe, and D. Hesse, "Atomic-scale study of electric dipoles near charged and uncharged domain walls in ferroelectric films," *Nature Materials*, vol. 7, p. 57, Dec. 2007.

[87] M.-W. Chu, I. Szafraniak, D. Hesse, M. Alexe, and U. Gösele, "Elastic coupling between 90\ifmmodeˆ\circ\else\textdegree\fi{} twin walls and interfacial dislocations in epitaxial ferroelectric perovskites: A quantitative high-resolution transmission electron microscopy study," *Physical Review B*, vol. 72, no. 17, p. 174 112, Nov. 2005.

[88] Y.-H. Shin, I. Grinberg, I.-W. Chen, and A. M. Rappe, "Nucleation and growth mechanism of ferroelectric domain-wall motion," *Nature*, vol. 449, p. 881, Oct. 2007.

[89] Z. Chen, Q. Huang, F. Wang, S. P. Ringer, H. Luo, and X. Liao, "Stress-induced reversible and irreversible ferroelectric domain switching," *Applied Physics Letters*, vol. 112, no. 15, p. 152 901, 2018.

[90] Z. Chen, L. Hong, F. Wang, X. An, X. Wang, S. Ringer, L.-Q. Chen, H. Luo, and X. Liao, "Kinetics of Domain Switching by Mechanical and Electrical Stimulation in Relaxor-Based Ferroelectrics," *Phys. Rev. Applied*, vol. 8, no. 6, p. 64 005, 2017.

[91] J. Kling, X. Tan, W. Jo, H.-J. Kleebe, H. Fuess, and J. Rödel, "In Situ Transmission Electron Microscopy of Electric Field-Triggered Reversible Domain Formation in Bi-Based Lead-Free Piezoceramics," *Journal of the American Ceramic Society*, vol. 93, no. 9, pp. 2452–2455, 2010.

[92] Z. Chen, L. Hong, F. Wang, S. P. Ringer, L.-Q. Chen, H. Luo, and X. Liao, "Facilitation of Ferroelectric Switching via Mechanical Manipulation of Hierarchical Nanoscale Domain Structures," *Phys. Rev. Lett.*, vol. 118, no. 1, p. 17 601, 2017.

[93] C Ma and X Tan, "In situ Transmission Electron Microscopy Study on the Phase Transitionsin Lead-Free (1-x)(Bi1/2Na1/2)TiO3-BaTiO3 Ceramics," *Journal of the American Ceramic Society*, vol. 94, no. 11, pp. 4040–4044, 2011.

[94] R. A. Cowley, S. N. Gvasaliya, S. G. Lushnikov, B Roessli, and G. M. Rotaru, "Relaxing with relaxors: a review of relaxor ferroelectrics," *Advances in Physics*, vol. 60, no. 2, pp. 229–327, Apr. 2011.

[95] P. M. GEHRING, "NEUTRON DIFFUSE SCATTERING IN LEAD-BASED RELAXOR FERROELECTRICS AND ITS RELATIONSHIP TO THE ULTRA-HIGH PIEZOELECTRICITY," *Journal of Advanced Dielectrics*, vol. 02, no. 02, p. 1 241 005, Apr. 2012.

[96] C. Gerber and H. P. Lang, "How the doors to the nanoworld were opened," *Nature Nanotechnology*, vol. 1, p. 3, 2006.

[97] V. V. Shvartsman, B Dkhil, and A. L. Kholkin, "Mesoscale Domains and Nature of the Relaxor State by Piezoresponse Force Microscopy," *Annual Review of Materials Research*, vol. 43, no. 1, pp. 423–449, 2013.

[98] R. Dittmer, D. Gobeljic, W. Jo, V. V. Shvartsman, D. C. Lupascu, J. L. Jones, and J. Rödel, "Ergodicity reflected in macroscopic and microscopic field-dependent behavior of BNT-based relaxors," *Journal of Applied Physics*, vol. 115, no. 8, p. 84 111, 2014.

[99] Y. Wang, G. Yuan, H. Luo, J. Li, and D Viehland, "Phase Transition in the Near-Surface Region of Ternary $\mathrm{Pb}({\mathrm{In}}_{1/2}{\mathrm{Nb}}_{1/2}){\math
}}\mathrm{Pb}({\mathrm{Mg}}_{1/3}{\mathrm{Nb}}_{2/3}){\mathrm{O}}_{3}\text{\ens
}}{\mathrm{PbTiO}}_{3}$ R," *Phys. Rev. Applied*, vol. 8, no. 3, p. 34 032, 2017.

[100] L. M. Garten, M. Burch, A. S. Gupta, R. Haislmaier, V. Gopalan, E. C. Dickey, and S. Trolier-McKinstry, "Relaxor Ferroelectric Behavior in Barium Strontium Titanate," *Journal of the American Ceramic Society*, vol. 99, no. 5, pp. 1645–1650, 2016.

[101] L. V. Simagina, T. R. Volk, Y. V. Bodnarchuk, R. V. Gainutdinov, and L. I. Ivleva, "Backswitching effect in relaxor SBN crystals, studied by PFM-spectroscopy," *Ferroelectrics Letters Section*, vol. 44, no. 4-6, pp. 65–72, 2017.

[102] A. Kholkin, A. Morozovska, D. Kiselev, I. Bdikin, B. Rodriguez, P. Wu, A. Bokov, Z.-G. Ye, B. Dkhil, L.-Q. Chen, M. Kosec, and S. V. Kalinin, "Surface Domain Structures and Mesoscopic Phase Transition in Relaxor Ferroelectrics," *Advanced Functional Materials*, vol. 21, no. 11, pp. 1977–1987, 2011.

[103] V. V. Shvartsman and A. L. Kholkin, "Evolution of nanodomains in 0.9Pb(Mg1/3Nb2/3)O3-0.1PbTiO3 single crystals," *Journal of Applied Physics*, vol. 101, no. 6, p. 64 108, 2007.

[104] F. Bai, J. Li, and D Viehland, "Domain engineered states over various length scales in (001)-oriented Pb(Mg1/3Nb2/3)O3-x%PbTiO3 crystals: Electrical history dependence of hierarchal domains," *Journal of Applied Physics*, vol. 97, no. 5, p. 54 103, Feb. 2005.

[105] M Abplanalp, D Barošová, P Bridenbaugh, J Erhart, J Fousek, P Günter, J Nosek, and M Šulc, "Ferroelectric domain structures in PZN–8%PT single crystals studied by scanning force microscopy," *Solid State Communications*, vol. 119, no. 1, pp. 7–12, 2001.

[106] I. K. Bdikin, V. V. Shvartsman, and A. L. Kholkin, "Nanoscale domains and local piezoelectric hysteresis in Pb(Zn1/3Nb2/3)O3-4.5\%PbTIO3 single crystals," *Applied Physics Letters*, vol. 83, no. 20, pp. 4232–4234, Nov. 2003.

[107] M. Iwata, K. Katsuraya, S. Tachizaki, J. Hlinka, I. Suzuki, M. Maeda, N. Yasuda, and Y. Ishibashi, "Domain Wall Structure in Pb(Zn1/3Nb2/3)O3-PbTiO3-Mixed Crystals by Atomic Force Microscopy," *Japanese Journal of Applied Physics*, vol. 43, no. 9B, pp. 6812–6815, 2004.

[108] Q. Li, Y. Liu, R. L. Withers, Y. Wan, Z. Li, and Z. Xu, "Piezoresponse force microscopy studies on the domain structures and local switching behavior of Pb(In1/2Nb1/2)O3-Pb(Mg1/3Nb2/3)O3-PbTiO3 single crystals," *Journal of Applied Physics*, vol. 112, no. 5, p. 52 006, 2012.

[109] B. J. Rodriguez, S Jesse, A. N. Morozovska, S. V. Svechnikov, D. A. Kiselev, A. L. Kholkin, A. A. Bokov, Z.-G. Ye, and S. V. Kalinin, "Real space mapping of polarization dynamics and hysteresis loop formation in relaxor-ferroelectric Pb(Mg1/3Nb2/3)O3-PbTiO3 solid solutions," *Journal of Applied Physics*, vol. 108, no. 4, p. 42 006, 2010.

[110] B. J. Rodriguez, S Jesse, A. A. Bokov, Z.-G. Ye, and S. V. Kalinin, "Mapping bias-induced phase stability and random fields in relaxor ferroelectrics," *Applied Physics Letters*, vol. 95, no. 9, p. 92 904, Aug. 2009.

[111] R. Proksch and S. V. Kalinin, "Energy dissipation measurements in frequency-modulated scanning probe microscopy," *Nanotechnology*, vol. 21, no. 45, p. 455 705, 2010.

[112] R. Garcı'a and R. Pérez, "Dynamic atomic force microscopy methods," *Surface Science Reports*, vol. 47, no. 6, pp. 197–301, 2002.

[113] R. Proksch, "Multifrequency, repulsive-mode amplitude-modulated atomic force microscopy," *Applied Physics Letters*, vol. 89, no. 11, p. 113 121, Sep. 2006.

[114] A. Gannepalli, A. Sebastian, J. Cleveland, and M. Salapaka, "Thermally driven non-contact atomic force microscopy," *Applied Physics Letters*, vol. 87, no. 11, p. 111 901, Sep. 2005.

[115] A. B. Kos and D. C. Hurley, "Nanomechanical mapping with resonance tracking scanned probe microscope," *Measurement Science and Technology*, vol. 19, no. 1, p. 15 504, 2007.

[116] R. Proksch and E. D. Dahlberg, "A detection technique for scanning force microscopy," *Review of Scientific Instruments*, vol. 64, no. 4, pp. 912–916, 1993.

[117] M. Stark, R. Guckenberger, A. Stemmer, and R. W. Stark, "Estimating the transfer function of the cantilever in atomic force microscopy: A system identification approach," *Journal of Applied Physics*, vol. 98, no. 11, p. 114 904, 2005.

[118] S. Jesse and S. V. Kalinin, "Band excitation in scanning probe microscopy: sines of change," *Journal of Physics D: Applied Physics*, vol. 44, no. 46, p. 464 006, 2011.

[119] S. Jesse and S. V. Kalinin, "Band excitation in scanning probe microscopy: sines of change," *Journal of Physics D: Applied Physics*, vol. 44, no. 46, p. 464 006, 2011.

[120] M. Ceriotti, "Unsupervised machine learning in atomistic simulations, between predictions and understanding," *The Journal of Chemical Physics*, vol. 150, no. 15, p. 150 901, Apr. 2019.

[121] A. Ludwig, "Discovery of new materials using combinatorial synthesis and high-throughput characterization of thin-film materials libraries combined with computational methods," *npj Computational Materials*, vol. 5, no. 1, p. 70, 2019.

[122] P. C. Jennings, S. Lysgaard, J. S. Hummelshøj, T. Vegge, and T. Bligaard, "Genetic algorithms for computational materials discovery accelerated by machine learning," *npj Computational Materials*, vol. 5, no. 1, p. 46, 2019.

[123] H. Huo, Z. Rong, O. Kononova, W. Sun, T. Botari, T. He, V. Tshitoyan, and G. Ceder, "Semi-supervised machine-learning classification of materials synthesis procedures," *npj Computational Materials*, vol. 5, no. 1, p. 62, 2019.

[124] A. Cecen, H. Dai, Y. C. Yabansu, S. R. Kalidindi, and L. Song, "Material structure-property linkages using three-dimensional convolutional neural networks," *Acta Materialia*, vol. 146, pp. 76–84, Mar. 2018.

[125] J. Carrasquilla and R. G. Melko, "Machine learning phases of matter," *Nature Physics*, vol. 13, no. 5, pp. 431–434, 2017.

[126] Y. Hui and Y. Liu, "Volumetric Data Exploration with Machine Learning-Aided Visualization in Neutron Science BT - Advances in Computer Vision," K. Arai and S. Kapoor, Eds., Cham: Springer International Publishing, 2020, pp. 257–271, ISBN: 978-3-030-17795-9.

[127] V. H. C. de Albuquerque, P. C. Cortez, A. R. de Alexandria, and J. M. R. S. Tavares, "A new solution for automatic microstructures analysis from images based on a backpropagation artificial neural network," *Nondestructive Testing and Evaluation*, vol. 23, no. 4, pp. 273–283, Dec. 2008.

[128] K. T. Butler, D. W. Davies, H. Cartwright, O. Isayev, and A. Walsh, "Machine learning for molecular and materials science," *Nature*, vol. 559, no. 10, 547–555, 2018.

[129] E. Strelcov, A. Belianinov, Y.-H. Hsieh, Y.-H. Chu, and S. V. Kalinin, "Constraining Data Mining with Physical Models: Voltage- and Oxygen Pressure-Dependent Transport in Multiferroic Nanostructures," *Nano Letters*, vol. 15, no. 10, pp. 6650–6657, 2015.

[130] S Jesse, M Chi, A Belianinov, C Beekman, S. V. Kalinin, A. Y. Borisevich, and A. R. Lupini, "Big Data Analytics for Scanning Transmission Electron Microscopy Ptychography," *Scientific Reports*, vol. 6, no. 26348, 2018.

[131] A. Belianinov, P. Ganesh, W. Lin, B. C. Sales, A. S. Sefat, S. Jesse, M. Pan, and S. V. Kalinin, "Research Update: Spatially resolved mapping of electronic structure on atomic level by multivariate statistical analysis," *APL Materials*, vol. 2, no. 12, p. 120 701, 2014.

[132] E. Strelcov, A. Belianinov, Y.-H. Hsieh, S. Jesse, A. P. Baddorf, Y.-H. Chu, and S. V. Kalinin, "Deep Data Analysis of Conductive Phenomena on Complex Oxide Interfaces: Physics from Data Mining," *ACS Nano*, vol. 8, no. 6, p. 6449, 2014.

[133] G. F. Nataf, N Barrett, J Kreisel, and M Guennou, "Raman signatures of ferroic domain walls captured by principal component analysis," *Journal of Physics: Condensed Matter*, vol. 30, no. 3, p. 35 902, 2018.

[134] L. Li, Y. Yang, D. Zhang, Z.-G. Ye, S. Jesse, S. V. Kalinin, and R. K. Vasudevan, "Machine learning-enabled identification of material phase transitions based on experimental data: Exploring collective dynamics in ferroelectric relaxors," *Science Advances*, vol. 4, no. 3, 2018.

[135] M. Ziatdinov, A. Maksov, and S. V. Kalinin, "Learning surface molecular structures via machine vision," *npj Computational Materials*, vol. 3, no. 1, p. 31, 2017.

[136] L. M. Ghiringhelli, J. Vybiral, S. V. Levchenko, C. Draxl, and M. Scheffler, "Big Data of Materials Science: Critical Role of the Descriptor," *Physical Review Letters*, vol. 114, no. 10, p. 105 503, Mar. 2015.

[137] S. R. Johnson, "The Trouble with QSAR (or How I Learned To Stop Worrying and Embrace Fallacy)," *Journal of Chemical Information and Modeling*, vol. 48, no. 1, pp. 25–26, Jan. 2008.

[138] A. Belianinov, R. Vasudevan, E. Strelcov, C. Steed, S. M. Yang, A. Tselev, S. Jesse, M. Biegalski, G. Shipman, C. Symons, A. Borisevich, R. Archibald, and S. Kalinin, "Big data and deep data in scanning and electron microscopies: deriving functionality from multidimensional data sets," *Advanced Structural and Chemical Imaging*, vol. 1, no. 1, p. 6, 2015.

[139] J. Schmidt, M. R. G. Marques, S. Botti, and M. A. L. Marques, "Recent advances and applications of machine learning in solid-state materials science," *npj Computational Materials*, vol. 5, no. 1, p. 83, 2019.

[140] B. S. S. Pokuri, S. Ghosal, A. Kokate, S. Sarkar, and B. Ganapathysubramanian, "Interpretable deep learning for guided microstructure-property explorations in photovoltaics," *npj Computational Materials*, vol. 5, no. 1, p. 95, 2019.

[141] Y. Iwasaki, R. Sawada, V. Stanev, M. Ishida, A. Kirihara, Y. Omori, H. Someya, I. Takeuchi, E. Saitoh, and S. Yorozu, "Identification of advanced spin-driven thermoelectric materials via interpretable machine learning," *npj Computational Materials*, vol. 5, no. 1, p. 103, 2019.

[142] P. W. Bridgman, "Certain Physical Properties of Single Crystals of Tungsten, Antimony, Bismuth, Tellurium, Cadmium, Zinc, and Tin," *Proceedings of the American Academy of Arts and Sciences*, vol. 60, no. 6, pp. 305–383, May 1925.

[143] D. C. Stockbarger, "The Production of Large Single Crystals of Lithium Fluoride," *Review of Scientific Instruments*, vol. 7, no. 3, pp. 133–136, Mar. 1936.

[144] J. C. Agar, Y. Cao, B. Naul, S. Pandya, S. van der Walt, A. I. Luo, J. T. Maher, N. Balke, S. Jesse, S. V. Kalinin, R. K. Vasudevan, and L. W. Martin, "Machine Detection of Enhanced Electromechanical Energy Conversion in PbZr0.2Ti0.8O3 Thin Films," *Advanced Materials*, vol. 30, no. 28, p. 1 800 701, Jul. 2018.

[145] J. C. Agar, B. Naul, S. Pandya, S. van der Walt, J. Maher, Y. Ren, L.-Q. Chen, S. V. Kalinin, R. K. Vasudevan, Y. Cao, J. S. Bloom, and L. W. Martin, "Revealing ferroelectric switching character using deep recurrent neural networks," *Nature Communications*, vol. 10, no. 1, p. 4809, 2019.

[146] S. Jesse, A. P. Baddorf, and S. V. Kalinin, "Switching spectroscopy piezoresponse force microscopy of ferroelectric materials," *Applied Physics Letters*, vol. 88, no. 6, p. 62 908, Feb. 2006.

[147] S. J. Brewer, S. C. Williams, C. Z. Deng, A. B. Naden, S. M. Neumayer, B. J. Rodriguez, A. Kumar, and N. Bassiri-Gharb, "Functional and structural effects of layer periodicity in chemical solution-deposited Pb(Zr,Ti)O3 thin films," *Journal of the American Ceramic Society*, vol. 100, no. 12, pp. 5561–5572, Dec. 2017.

[148] L. A. Griffin, I. Gaponenko, and N. Bassiri-Gharb, "Better, Faster, and Less Biased Machine Learning: Electromechanical Switching in Ferroelectric Thin Films," *Manuscript Submitted*, 2020.

[149] E. W. Weisstein, *Sweep Signal.*

[150] J. W. Tukey, "An introduction to the calculations of numerical spectrum analysis," *Spectral Analysis of Time Series*, pp. 25–46, 1967.

[151] J. Garcia-Barriocanal, A. Rivera-Calzada, M. Varela, Z. Sefrioui, M. R. Díaz-Guillén, K. J. Moreno, J. A. Díaz-Guillén, E. Iborra, A. F. Fuentes, S. J. Pennycook, C. Leon, and J. Santamaria, "Tailoring Disorder and Dimensionality: Strategies for Improved Solid Oxide Fuel Cell Electrolytes," *ChemPhysChem*, vol. 10, no. 7, pp. 1003–1011, May 2009.

[152] J Trzmiel, K Weron, J Janczura, and E Placzek-Popko, "Properties of the relaxation time distribution underlying the Kohlrausch–Williams–Watts photoionization of the DX centers in Cd1-xMnxTe mixed crystals," *Journal of Physics: Condensed Matter*, vol. 21, no. 34, p. 345 801, 2009.

[153] E. K. H. Salje, X Ding, Z Zhao, T Lookman, and A Saxena, "Thermally activated avalanches: Jamming and the progression of needle domains," *Phys. Rev. B*, vol. 83, no. 10, p. 104 109, 2011.

[154] E. K. H. Salje, X Ding, and O Aktas, "Domain glass," *physica status solidi (b)*, vol. 251, no. 10, pp. 2061–2066, 2014.

[155] Y. Fan, T. Iwashita, and T. Egami, "Energy landscape-driven non-equilibrium evolution of inherent structure in disordered material," *Nature Communications*, vol. 8, p. 15 417, May 2017.

[156] G. A. Samara, "The relaxational properties of compositionally disordered ABO3perovskites," *Journal of Physics: Condensed Matter*, vol. 15, no. 9, R367–R411, 2003.

[157] N. Domingo, I. Gaponenko, K. Cordero-Edwards, N. Stucki, V. Pérez-Dieste, C. Escudero, E. Pach, A. Verdaguer, and P. Paruch, "Surface charged species and electrochemistry of ferroelectric thin films," *Nanoscale*, vol. 11, no. 38, pp. 17 920–17 930, 2019.

[158] R. K. Vasudevan, H Khassaf, Y Cao, S. J. Zhang, A Tselev, B Carmichael, M. B. Okatan, S Jesse, L. Q. Chen, S. P. Alpay, S. V. Kalinin, and N Bassiri-Gharb, "Acoustic Detection of Phase Transitions at the Nanoscale," *Advanced Functional Materials*, vol. 26, no. 4, pp. 478–486, 2016.

[159] J. Yin and W. Cao, "Polarization reversal study using ultrasound," *Applied Physics Letters*, vol. 79, no. 27, pp. 4556–4558, Dec. 2001.

[160] N. Balke, S. Jesse, Q. Li, P. Maksymovych, M Baris Okatan, E. Strelcov, A. Tselev, and S. V. Kalinin, "Current and surface charge modified hysteresis loops in ferroelectric thin films," *Journal of Applied Physics*, vol. 118, no. 7, p. 72 013, Aug. 2015.

[161] L. Collins, Y. Liu, O. S. Ovchinnikova, and R. Proksch, "Quantitative Electromechanical Atomic Force Microscopy," *ACS Nano*, vol. 13, no. 7, pp. 8055–8066, Jul. 2019.

[162] Q. Li, S. Jesse, A. Tselev, L. Collins, P. Yu, I. Kravchenko, S. V. Kalinin, and N. Balke, "Probing Local Bias-Induced Transitions Using Photothermal Excitation Contact Resonance Atomic Force Microscopy and Voltage Spectroscopy," *ACS Nano*, vol. 9, no. 2, pp. 1848–1857, Feb. 2015.

[163] Y. Liu, Y. Sun, W. Lu, H. Wang, Z. Wang, B. Yu, T. Li, and K. Zeng, "Variation of contact resonance frequency during domain switching in PFM measurements for ferroelectric materials," *Journal of Materiomics*, vol. 6, no. 1, pp. 109–118, 2020.

[164] R. K. Vasudevan, N. Balke, P. Maksymovych, S. Jesse, and S. V. Kalinin, "Ferroelectric or non-ferroelectric: Why so many materials exhibit "ferroelectricity" on the nanoscale," *Applied Physics Reviews*, vol. 4, no. 2, p. 21 302, May 2017.

[165] N. Balke, P. Maksymovych, S. Jesse, I. I. Kravchenko, Q. Li, and S. V. Kalinin, "Exploring Local Electrostatic Effects with Scanning Probe Microscopy: Implications for Piezoresponse Force Microscopy and Triboelectricity," *ACS Nano*, vol. 8, no. 10, pp. 10 229–10 236, Oct. 2014.

[166] N. Balke, P. Maksymovych, S. Jesse, A. Herklotz, A. Tselev, C.-B. Eom, I. I. Kravchenko, P. Yu, and S. V. Kalinin, "Differentiating Ferroelectric and Nonferroelectric Electromechanical Effects with Scanning Probe Microscopy," *ACS Nano*, vol. 9, no. 6, pp. 6484–6492, Jun. 2015.

[167] J Canny, "A Computational Approach to Edge Detection," *IEEE Transactions on Pattern Analysis and Machine Intelligence*, vol. PAMI-8, no. 6, pp. 679–698, 1986.

[168] Y. Ishibashi and Y. Takagi, "Note on Ferroelectric Domain Switching," *Journal of the Physical Society of Japan*, vol. 31, no. 2, pp. 506–510, Aug. 1971.

[169] C Harnagea, M Alexe, D Hesse, and A Pignolet, "Contact resonances in voltage-modulated force microscopy," *Applied Physics Letters*, vol. 83, no. 2, pp. 338–340, Jul. 2003.

[170] S. V. Kalinin and D. A. Bonnell, "Imaging mechanism of piezoresponse force microscopy of ferroelectric surfaces," *Physical Review B*, vol. 65, no. 12, p. 125 408, Mar. 2002.

[171] I. Gaponenko, L. Musy, S. V. Kalinin, N. Domingo, N. Stucki, A. Verdaguer, N. Bassiri-Gharb, and P. Paruch, *Local and correlated studies of humidity-mediated ferroelectric thin film surface charge dynamics*.

[172] S. Hong, J. Woo, H. Shin, J. U. Jeon, Y. E. Pak, E. L. Colla, N. Setter, E. Kim, and K. No, "Principle of ferroelectric domain imaging using atomic force microscope," *Journal of Applied Physics*, vol. 89, no. 2, pp. 1377–1386, Dec. 2000.

[173] N. Balke, S. Jesse, P. Yu, B. Carmichael, S. V. Kalinin, and A. Tselev, "Quantification of surface displacements and electromechanical phenomena via dynamic atomic force microscopy," *Nanotechnology*, vol. 27, no. 42, p. 425 707, 2016.

[174] S. V. Kalinin and D. A. Bonnell, "Screening Phenomena on Oxide Surfaces and Its Implications for Local Electrostatic and Transport Measurements," *Nano Letters*, vol. 4, no. 4, pp. 555–560, Apr. 2004.

[175] A. Tagantsev, L. E. Cross, and J. Fousek, *Domains in Ferroic Crystals and Thin Films*. New York: Springer International Publishing, 2010.

[176] A. V. Ievlev, S Jesse, A. N. Morozovska, E Strelcov, E. A. Eliseev, Y. V. Pershin, A Kumar, V. Y. Shur, and S. V. Kalinin, "Intermittency, quasiperiodicity and chaos in probe-induced ferroelectric domain switching," *Nature Physics*, vol. 10, no. 1, pp. 59–66, 2014.